Cerchar abrasivity test – laboratory testing and numerical simulation

To the Faculty of Geosciences, Geoengineering and Mining
of the Technischen Universität Bergakademie Freiberg
approved

THESIS

to attain the academic degree of
Doctor of Engineering
Dr.-Ing.
submitted

by Dipl.-Ing. Guangzhe Zhang
born on the June 28, 1982 in Shenyang, PR China

Reviews: Prof. Dr.-Ing. habil. Heinz Konietzky, TU Bergakademie Freiberg, Germany
Prof. Dr. Michael Alber, Ruhr-Universität Bochum, Germany

Date of the award: 17.06.2020

Declaration

I, Guangzhe Zhang, declare that the Ph.D. thesis entitled “Cerchar abrasivity test – laboratory testing and numerical simulation” contains no material that has been submitted previously, in whole or in part, for the award of any other academic degree or diploma. Except where otherwise indicated, this thesis is my own work.

Place, Date, Signature

Acknowledgements

Having struggled and been perseverant. The long and laborious journey would not be finished without the help of a number of people.

I would like to express my sincere gratitude to Prof. Heinz Konietzky, my supervisor, for his invaluable guidance, helpful advice, patience and continuous support through my doctoral study at the Chair for Rock Mechanics, Geotechnical Institute, Technical University Bergakademie Freiberg.

I would like to thank Prof. Shouding Li at the Institute of Geology and Geophysics at the Chinese Academy of Sciences, Dr. Reinhard Kleeberg at the Institute for Mineralogy, Dr. Klinger Mathias at the Institute for Energy Process Engineering and Chemical Engineering, Dr. Patrick Gehre at the Institute for Ceramic, Glass and Construction Materials for their technical support.

Acknowledge is extended to the colleagues and friends at the Geotechnical Institute for the encouragement and support during my stay here. I specially mention Prof. Wengang Dang, Dr. Thomas Frühwirt, Dr. Martin Herbst, Dr. Zhengyang Song, Dr. Fei Wang, Mr. Gerd Münzberger, Mrs. Beatrice Tauch, Mr. Yufeng Zhao, Mr. Vishal Vilas Yadav and Mr. Jian Zhao.

I would like to express appreciation to the China Scholarship Council (CSC) for the financial support of my study.

Deepest gratitude is expressed to my family, my father Xuechao Zhang, my mother Xin Guan and my wife Dr. Jin Zhao for their selfless love, understanding and support. My sweet heart daughter Shuyu Zhang, I love you.

Abstract

Abrasivity is a characteristic property of rocks. Rock abrasivity has influence on tool wear, energy consumption and construction time and is therefore an important parameter in rock engineering. Over the years, a number of testing methods have been developed to define and quantify the abrasive potential of rocks. Due to simple design and convenient handling, Cerchar abrasivity test and its index, Cerchar abrasivity index, are most commonly used to assess the rock abrasivity.

Besides the abrasivity index, various parameters can be derived from the Cerchar test thanks to the development of a special designed testing device. Diverse parameters like scratching force, applied work and specific energy can be used to estimate the cutting efficiency. Moreover, a new composite parameter named Cerchar abrasion ratio is proposed, which considers both, the wear on the stylus tip and the material removal on the rock surface and can be regarded as an indicator to evaluate the cutting effectivity.

Since the development of Cerchar abrasivity test, major attentions are focused on the abrasion of the stylus, but minor attentions are paid to investigate the mechanical behavior of rocks against the action of the stylus during the scratching process. The scratch groove produced on the rock surface is observed under a scanning electron microscope. The Cerchar wear mechanism can be explained as follows: mineral grains are detached from damaged surface by fracturing after plastic deformation on stressed surface. Transition from plastic deformation-induced to cracking-induced wear are related to the rock microstructure.

For the Cerchar test, various factors affecting the Cerchar abrasivity index have been studied, which can be divided into testing condition-based and geotechnical-based factors. The influence of some dominant testing condition-based factors including surface condition, testing distance and velocity on the test result is investigated by using the new designed testing device, in which the sliding distance and scratching velocity can be exactly controlled during the test. Results show that the surface condition can affect the result of Cerchar index, especially for hard and inhomogeneous rocks, while the testing distance and velocity have no obvious influence on the Cerchar index.

As far as it is known, in rock mechanics, anisotropic features of rocks can affect the experimental results significantly. In the original Cerchar specification, testing procedure for stratified or foliated rocks is not specially discussed. Due to this, the influence of rock anisotropy on the Cerchar abrasivity index is investigated based on two intact metamorphic rocks of slate and gneiss. However, no significant dependency is found.

Cerchar scratch test is simulated based on a quasi-homogeneous model made of sandstone with respect to its mineralogical-mechanical properties. The numerical simulation is conducted by using the discrete element method-based particle flow code of PFC^{3D}. As a result, the simulated scratching force shows a good agreement with the experimental result. A gap between numerical and experimental studies can be attributed to the testing condition-based factors, such as rock mineralogy and microstructure, scratching velocity and depth of scratch, tool abrasion and temperature.

Based on the calibrated sandstone model, numerical simulations of rock cutting are conducted under different testing conditions. The influence of tool geometry like tip shape, tip angle and tip wear, and cutting parameters including cutting velocity, depth of cut and rake angle on the cutting force and crack pattern is studied.

Table of contents

List of figures

List of tables

Nomenclature

A	Particle
A_i	Percentage of individual mineral
AMC	Abrasive mineral content
AV	Abrasion value on tungsten carbide
AVS	Abrasion value on cutter steel
b	Particle
B	Particle
BEM	Boundary element method
BTS	Brazilian tensile strength
c	Cohesion
CAI	Cerchar abrasivity index
CAR	Cerchar abrasion ratio
$Cerchar$	Centre d'Études et Recherches des Charbonnages
d	Distance between two particles or between a particle and a wall
$damp$	Mechanical/Local damping coefficient
d_s	Sliding distance
D_c	Depth of cut
D_s	Depth of scratch
D_D	Disc diameter
DEM	Discrete element method
$E - modulus$	Young's modulus
E^*	Effective modulus
EQC	Equivalent quartz content
F_i	Contact force vector / Resultant force acting on the particle
F_i^n	Normal component vector
F_i^S	Shear component vector
F_n	Normal contact force
F_s	Scratching force
F_s^{max}	Maximum shear contact force

F_s^{new}	Updated shear contact force
F_s^{old}	Shear contact force of the previous timestep
FC	Cutting force
FC^*	Peak cutting force
FDM	Finite difference method
FEM	Finite element method
FN	Normal force
FSi	Sideway force
g_i	Body force acceleration vector (i.e. gravitational acceleration)
GS	Average size of quartz grain
HRC	Rockwell hardness number of scale C
I	Moment of inertia of the particle
ISRM	International society for rock mechanics
k^*	Ratio of normal-to-shear stiffness
k_1	Water jet factor
k_2	Cutting speed factor
k_s	Shear contact stiffness
K_n	Normal contact stiffness
LAC	LCPC abrasivity coefficient
LCPC	Laboratoire Central des Ponts et Chausées
LF	Linear feet of cutter travel on the face
m	Total mass of the particle
m_0	Mass of the impeller before the LCPC test
m_1	Mass of the impeller after the LCPC test
m_{ra}	Mass of the rock aggregates
M_i	Resultant moment acting on the particle
MCAI	Modified Cerchar abrasivity index
MCF	Mean cutting force
MHN	Mohs scratch hardness number
MNF	Mean normal force
MPSF	Mean peak scratching force

MSF	Mean scratching force
MSiF	Mean sideway force
n_i	Normal unity vector
n	Number of constituent minerals
n_{shear}	Number of shear-induced cracks
$n_{tension}$	Number of tension-induced cracks
n_{total}	Total number of cracks
P	Confining pressure
PC	Pick consumption
PFC	Particle flow code
QC	Quartz content
r_{max}	Maximum particle radius
r_{min}	Minimum particle radius
$R^{[A]}$, $R^{[B]}$, $R^{[b]}$	Particle radius
RAI	Rock abrasivity index
RHN	Rosiwal grinding hardness number
R^2	Coefficient of determination
SE	Scratching energy
SEM	Scanning electron microscopy
SSE	Specific scratching energy
SWI	Schimazek wear index
t	Calculation/Computational time or testing duration
TBM	Tunnel boring machine
U_n	Overlap of two particles in the normal direction
U^n	Overlap of two particles or between a particle and a wall in normal direction
UCS	Uniaxial compressive strength
v_c	Cutting velocity
v_i	Indentation velocity
v_p	P-wave velocity
v_s	Scratching velocity

v_s	Velocity in the shear direction
V_m	Material removal volume
V_s	Tip wear volume
VHN	Vickers indentation hardness number
VHNR	Vickers hardness number of rock
w	Wall
W_f	Specific disc wear
W_t	Diameter of the wear flat on the pick/stylus tip
$x_i^{[A]}, x_i^{[B]}, x_i^{[b]}$	Position vectors of the particle center
$x_i^{[c]}$	Position vector of the contact point
$x_i, \dot{x}_i, \ddot{x}_i$	Position, translational velocity, translational acceleration
XRD	X-Ray diffraction
ΔF_s	Shear contact force increment
Δt	Timestep
Δu_s	Contact displacement increment in the shear direction

α	Rake angle
β	Clearance angle
γ	Attack angle
θ	Pick/Stylus tip angle
μ	Coefficient of friction
ν	Poisson's ratio
ρ	Density
σ_c	Compressive strength
σ_t	Tensile strength
σ_m	Mean stress
σ_1	Maximum stress
σ_2	Intermediate stress
σ_3	Minimum stress
φ	Friction angle

$\omega_i, \dot{\omega}_i$	Angular velocity, angular acceleration
$\emptyset$	Porosity
$\emptyset_B$	Bottom diameter of the conical pick

1. Background and introduction

1.1 Definition and determination of rock hardness

In geology and mineralogy, hardness is a characteristic property of mineral. It is not a fundamental physical quantity, but can be related to the local strength of rocks. Atkinson (1993) stated: rock hardness can be considered as a behavioral characterization rather than a physical property of the rock. Its magnitude can be affected by many rock intrinsic properties, particularly important are type of minerals, grain size and shape, cohesion of grain boundaries, as well as rock strength including plastic behavior and elastic modulus.

There are three fundamental hardness scales: (1) Mohs scratch hardness scale (Mohs 1824), (2) Rosiwal grinding hardness scale (Rosiwal 1896), and (3) Vickers indentation hardness scale (Smith and Sandland 1925). The geologist-mineralogist's approach to quantify the hardness of a rock is firstly to measure the content of individual minerals within the rock and then to calculate the composite hardness in proportion to the mineral constituents. In rock mechanics, various testing methods have been developed to determine the hardness of rocks. These methods can be divided into indentation and rebound methods. Among these, Brinell (Brinell 1900), Rockwell (Rockwell 1914), Vickers (Smith and Sandland 1925) and Knoop (Knoop 1939) hardness tests, which are based on the metallurgical hardness testing method, are regarded as indentation method, while Shore scleroscope (Shore 1907) and Schmidt hammer (Schmidt 1946) hardness tests are regarded as rebound method.

1.2 Definition and determination of rock abrasivity

Different from hardness, abrasivity is a characteristic property of rocks which leads to the wear of tools during rock excavations. Rock abrasivity is defined as wear or loss of material that rocks produce on another material (Atkinson 1993), especially on the mechanical tools like drill bits, roadheader picks and TBM disc cutters. Its magnitude can be affected by mineral-scaled and rock-scaled parameters, very important parameters are mineral composition and content, grain size, shape and hardness, type and cementation degree of cementing materials, as well as rock properties including strength, brittleness and fracture toughness.

Over the years, many parameters have been proposed to defined and quantify the abrasivity of rocks based on mineralogical, mechanical and geotechnical methods. The from mineralogical analysis method derived indexes, such as silica content (West 1981), quartz content (West 1986), abrasive mineral content associated with Mohs hardness scale (West 1981), equivalent quartz content referred to Rosiwal hardness scale (West 1981) and Vickers hardness number of rock related to Vickers hardness scale (Bruland 1998), can be referred to as an indicator of rock abrasivity. However, such indexes take no account of cementing materials with respect to their hardness or abrasiveness and ignore the effect of grain size and shape. Therefore, they are not very accurate to assess the rock abrasivity. On the other hand, a number of mechanical testing methods have been developed to determine and classify the rock abrasivity. Among these, Cerchar abrasivity test (Valantin 1973, Cerchar 1986, NF P94-430-1 2000, ASTM D7625-10 2010, Alber et al. 2014), LCPC abrasimeter test (NF P18-579 1990) and abrasion value tungsten carbide and abrasion value cutter steel tests (Bruland and Nilsen 1995) are widely used. In addition, geotechnical indexes like Schimazek wear index (Schimazek and Knatz 1970, 1976) and rock abrasivity index (Plinninger 2002) calculated as a composite index from fundamental rock mechanical parameters can be used to estimate the abrasive potential of rocks.

1.2.1 Silica content

Silica (SiO_2) content can be referred to as an indicator of rock abrasivity (West 1981). It reflects not only how much quartz is present within a rock but also the amount of silicate minerals like micas, feldspars and clay minerals. In general, the greater the silica content in a rock, the more abrasive this rock.

1.2.2 Quartz content

Quartz content can be used to give a measure of rock abrasivity (West 1981, 1986). If quartz is the dominant abrasive mineral within a rock, quartz content may be a more reasonable and reliable indicator than silica content. Overall, the abrasive potential of rocks increases with increased quartz content. Note that the quartz content is quite different from the silica content. Table 1-1 gives a comparison between silica content and quartz content for some typical rocks.

Table 1-1 Comparison between silica content and quartz content (West 1981)

Rock type	**Silica content [%]**	**Quartz content [%]**
Basalt	47	0
Granite	72	31
Sandstone	80	70
Shale	59	32

1.2.3 Abrasive mineral content

As far as it is known, as the hardness of tool steel is about 5.5 in the Mohs hardness scale, all minerals with hardness over this value can be treated as abrasive. Therefore, not only quartz with Mohs hardness number of 7 but also other hard minerals like fluorite, apatite, orthoclase and feldspar with Mohs hardness number ranging from 4 to 6 have abrasive potential.

The abrasive mineral content (AMC) associated with Mohs hardness scale was proposed by West (1981), which is calculated by multiplying the percentage of individual mineral with its Mohs hardness number.

$$\mathrm{AMC} = \sum_{i=1}^{n} \mathrm{A_i} \cdot \mathrm{MHN_i} \qquad (1\text{-}1)$$

where AMC [-] is the abrasive mineral content, $\mathrm{A_i}$ [%] and $\mathrm{MHN_i}$ [-] represent the percentage of individual mineral and its Mohs hardness number, respectively, and n [-] denotes the number of constituent minerals present within the rock. Overall, the greater the percentage of hard minerals within a rock, the higher the AMC, and then the more abrasive this rock.

1.2.4 Equivalent quartz content

The equivalent quartz content (EQC) was proposed by West (1981) in consideration of hard minerals referred to Rosiwal hardness scale. The EQC is calculated by multiplying the percentage of individual mineral with its Rosiwal hardness number.

$$EQC = \sum_{i=1}^{n} A_i \cdot RHN_i \quad (1\text{-}2)$$

where EQC [%] is the equivalent quartz content, A_i [%] and RHN_i [-] represent the percentage of individual mineral and its Rosiwal hardness number, respectively, and n [-] denotes the number of constituent minerals present within the rock. A classification of rock abrasivity according to the EQC is summarized in Table 1-2.

Table 1-2 Abrasive classification according to equivalent quartz content (Plinninger 2002)

EQC [%]	**Abrasive classification**
< 10	not abrasive
10 - 25	slightly abrasive
25 - 50	abrasive
50 - 75	very abrasive
> 75	extremely abrasive

1.2.5 Vickers hardness number of rock

The Vickers hardness number of rock (VHNR) related to Vickers hardness scale was proposed by Bruland (1998). This index is calculated by multiplying the percentage of individual mineral with its Vickers hardness number.

$$VHNR = \sum_{i=1}^{n} A_i \cdot VHN_i \quad (1\text{-}3)$$

where VHNR [-] denotes the Vickers hardness number of the rock, A_i [%] and VHN_i [-] represent the percentage of individual mineral and its Vickers hardness number, respectively, and n [-] is the number of constituent minerals present within the rock. Overall, the higher the VHNR, the more abrasive the rock. The ten standard minerals and their Mohs scratch, Rosiwal grinding and Vickers indentation hardness numbers are compared in Table 1-3.

Table 1-3 Mohs, Rosiwal and Vickers hardness number of ten standard minerals (West 1981, Aktinson 1993)

Mineral	**Mohs scratch hardness number**	**Rosiwal grinding hardness number**	**Vickers indentation hardness number**
Talc	1	0.03	14
Gypsum	2	0.25	40
Calcite	3	4.5	125
Fluorite	4	5	188
Apatite	5	6.5	530
Orthoclase/Feldspar	6	37	788
Quartz	7	120	1413
Topaz	8	175	1745
Corundum	9	1000	2428
Diamond	10	140000	-

1.2.6 LCPC abrasivity coefficient

The LCPC abrasimeter test was originally developed by the Laboratoire Central des Ponts et Chausées (LCPC) to determine the abrasivity of soil or rock aggregates. A detailed description of this test is published in the French standard NF P18-579 (1990).

The LCPC abrasivity coefficient (LAC) is defined as the mass loss of a steel impeller divided by the broken rock of about 500 g with the grain fraction of 4 - 6.3 mm.

$$\mathrm{LAC} = \frac{(m_0 - m_1)}{m_{ra}} \tag{1-4}$$

where LAC [g/t] denotes the LCPC abrasivity coefficient, m_0 [g] and m_1 [g] represent the mass of the impeller before and after testing, respectively, and m_{ra} [t] is the mass of rock aggregates. A classification of rock abrasivity according to the LAC is summarized in Table 1-4.

Table 1-4 Abrasive classification according to LCPC abrasivity coefficient (Thuro et al. 2006)

LAC [g/t]	**Abrasive classification**
0 - 50	Not abrasive
50 - 100	Not very abrasive
100 - 250	Slightly abrasive
250 - 500	(Medium) abrasive
500 - 1250	Very abrasive
1250 - 2000	Extremely abrasive

1.2.7 Abrasion value

The NTNU (Norwegian University of Science and Technology), or NTH (Norwegian Institute of Technology, a predecessor of today's NTNU), or SINTEF (founded by NTH), testing method was particularly developed to evaluate the drillability of rocks by percussive drilling. Today, this method is mainly used to predict the performance of TBM. This testing method consists of various laboratory tests including brittleness test, Sievers' J-value miniature drill test and abrasion value test and its variation, abrasion value cutter steel test.

The abrasion value test developed by Selmer-Olsen and Lien (1960) gives a measure of time-dependent abrasion of crushed rock powder on tungsten carbide test piece (i.e. the ability of the rock that causes the wear of tungsten carbide). Crushed rock powder finer than 1 mm passes under the loaded tungsten carbide test piece. The abrasion value (AV) is defined as the mass loss of the test piece in milligrams after 100 revolutions of the rotation steel disc in 5 minutes. The development of abrasion value cutter steel test is based on the abrasion value test. The difference between these two tests is that the abrasion value test is conducted by using a tungsten carbide, while the abrasion value cutter steel test by using a TBM cutter steel. The abrasion value on cutter steel (AVS) is defined as the mass loss of the test piece in milligrams after 20 revolutions of the rotation steel disc in 1 minute. A classification of rock abrasivity according to the AV and AVS is summarized in Table 1-5.

Table 1-5 Abrasive classification according to abrasion value (Dahl et al. 2012)

AV [mg]	**AVS [mg]**	**Abrasive classification**
≥ 58.0	≥ 44.0	Extremely high abrasive
42.0 - 57.9	36.0 - 43.9	Very high abrasive
28.0 - 41.9	26.0 - 35.9	High abrasive
11.0 - 27.9	13.0 - 25.9	Medium abrasive
4.0 - 10.9	4.0 - 12.9	Low abrasive
1.1 - 3.9	1.1 - 3.9	Very low abrasive
≤ 1.0	≤ 1.0	Extremely low abrasive

1.2.8 Schimazek wear index

The Schimazek wear index (SWI) was firstly introduced by Schimazek and Knatz (1970, 1976) to estimate the pick consumption for the German coal mining industry. A small-scale simplified wear test was conducted on sedimentary rocks using a pin-on-disc. Then, the wear of the pick is related to the percentage and grain size of quartz minerals within the rock and the tensile strength of the rock.

$$\mathrm{SWI} = 10 \cdot \mathrm{QC} \cdot \mathrm{GS} \cdot \mathrm{BTS} \tag{1-5}$$

where SWI [N/mm] denotes the Schimazek wear index, QC [%] is the quartz content, GS [mm] is the average size of quartz grains, and BTS [MPa] is the Brazilian tensile strength of the rock. A classification of rock abrasivity according to the SWI is summarized in Table 1-6.

Table 1-6 Abrasive classification according to Schimazek wear index (Bilgin et al. 2014)

SWI [N/mm]	**Abrasive classification**	**Pick consumption [m^3/pick]**
< 0.05	Nonabrasive	90 - 110
0.05 - 0.07	Low abrasive	50 - 90
0.07 - 1.00	Abrasive	30 - 50
1.00 - 1.05	Very abrasive	10 - 30
> 1.05	Very hard and abrasive	1 - 10

1.2.9 Rock abrasivity index

A composite index called rock abrasivity index (RAI) was originally introduced by Plinninger (2002) in consideration of two main parameters of the rock: (1) the content of abrasive minerals within the rock which is relevant for abrasive wear of the tool, and (2) the strength of the rock which is relevant for both, abrasive wear and impact failure of the tool. This index is calculated by multiplying the equivalent quartz content with the uniaxial compressive strength of the rock.

$$\mathrm{RAI} = \mathrm{EQC} \cdot \mathrm{UCS} \tag{1-6}$$

where RAI [-], EQC [%] and UCS [MPa] represent the rock abrasivity index, equivalent quartz content and uniaxial compressive strength of the rock, respectively. A classification of rock abrasivity according to the RAI is summarized in Table 1-7.

Table 1-7 Abrasivity classification according to rock abrasivity index (Plinninger 2002)

RAI [-]	**Abrasive classification**
< 10	Not abrasive
10 - 30	Slightly abrasive
30 - 60	Abrasive
60 - 120	Very abrasive
> 120	Extremely abrasive

2. State of the art

2.1 Cerchar abrasivity test

Cerchar abrasivity test was originally developed by the Centre d'Études et Recherches des Charbonnages (Cerchar) de France for the French coal mining industry. The Cerchar abrasivity index is mainly used to assess the abrasivity of rocks and then to estimate the wear of tools. A detailed description of this test is presented by Valantin (1973) and Cerchar (1986), as well as published in the French standard NF P94-430-1 (2000) and ASTM D7625-10 (2010). Recently, a new study issued by Alber et al. (2014) provides generalized guideline for determining the rock abrasivity using the Cerchar testing method.

Two basic testing apparatuses are most commonly applied for testing: (1) the original Cerchar apparatus fabricated at the Cerchar center (Cerchar, 1986), and (2) the West apparatus designed by West (1989), as illustrated in Figure 2-1. For these two apparatuses, the testing procedure is quite different: in Cerchar apparatus the stylus slides on a fixed rock sample for 1 second, while in West apparatus the rock sample moves under the fixed stylus for 10 seconds. Note that all other apparatuses are modification of these two apparatuses.

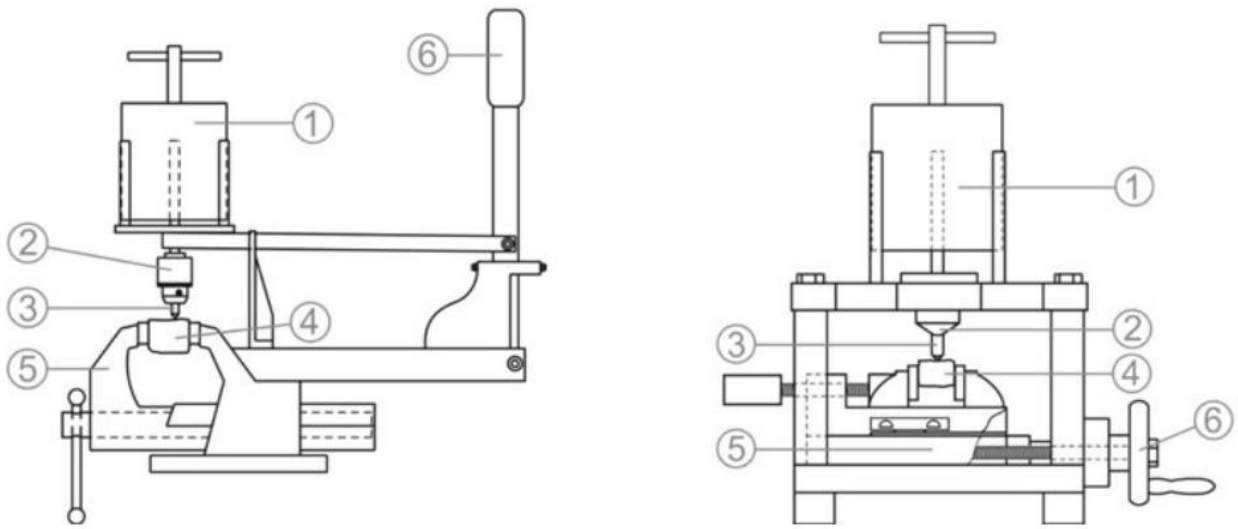

Figure 2-1 Original Cerchar apparatus (left) versus West apparatus (right) (①: weight; ②: stylus guide; ③: stylus; ④: rock sample; ⑤: vice; ⑥: hand crank/wheel) (Alber et al. 2014)

The testing procedure is described as follows: under a normal load of 7 kg a sharp steel stylus with 90° conical tip angle moves 10 mm over a rock surface within 1 s or 10 s, depending on the applied apparatus. The wear flat on the stylus tip measured in millimeter multiplied by a factor of 10 is defined as the Cerchar abrasivity index (CAI) which indicates the rock abrasivity.

$$\mathrm{CAI} = \mathrm{W_t} \cdot 10 \tag{2-1}$$

where CAI [-] represents the Cerchar abrasivity index, and $\mathrm{W_t}$ [mm] denotes the diameter of wear flat on the stylus tip. A classification of rock abrasivity according to the CAI is summarized in Table 2-1.

Table 2-1 Abrasive classification according to Cerchar abrasivity index (Alber et al. 2014)

CAI [-]	**Abrasive classification**
0.1 - 0.4	Extremely low abrasive
0.5 - 0.9	Very low abrasive
1.0 - 1.9	Low abrasive
2.0 - 2.9	Medium abrasive
3.0 - 3.9	High abrasive
4.0 - 4.9	Very high abrasive
≥ 5.0	Extremely high abrasive

Recently, with the aid of new designed Cerchar testing device, the applied scratching force generated on the stylus and the corresponding penetration depth of the stylus into the rock can be measured and recorded during the test. Then, a modified Cerchar abrasivity index (MCAI), which is calculated by dividing the wear flat by the scratching force, is proposed and used to quantify the rock abrasivity (Hamzaban et al. 2014). A classification of rock abrasivity according to the MCAI is summarized in Table 2-2.

Table 2-2 Comparison between Cerchar abrasivity index and modified Cerchar abrasivity index (Cerchar 1986, Hamzaban et al. 2014)

CAI [-]	**Abrasive classification**	**MCAI [mm/N]**	**Abrasive classification**
0.1 - 0.3	Non-abrasive	0 - 0.05	Non-abrasive
0.3 - 0.5	Not very abrasive	0.05 - 0.15	Slightly abrasive
0.5 - 1.0	Slightly abrasive	0.15 - 0.5	Abrasive
1.0 - 2.0	Medium abrasive to abrasive	0.5 - 0.8	Very abrasive
2.0 - 4.0	Very abrasive	> 0.8	Extremely abrasive
4.0 - 6.0	Extremely abrasive	-	-

2.2 Influence of various factors on Cerchar abrasivity index

Since the development of Cerchar abrasivity test, influence of various factors on the result of CAI has been studied by many researchers. These factors can be divided into two categories: (1) testing condition-based factors, such as testing apparatus, stylus metallurgy and hardness, testing distance and velocity, as well as tip wear measurement, and (2) geological-geotechnical-based factors which are related to mineral composition and content, grain size and shape, quartz content and its equivalence, as well as rock properties including strength, hardness and fracture toughness.

2.2.1 Testing apparatus

Käsling et al. (2007) compared the CAI results obtained from both, Cerchar and West apparatuses. No great difference was found for homogeneous rocks, while the CAI value measured on Cerchar apparatus is lower than that on West apparatus for heterogeneous rocks. They concluded that West apparatus is more stable than Cerchar apparatus for testing heterogeneous rocks. The accuracy of CAI can be attributed to the testing velocity assigned to different apparatuses. A scratching velocity of 10 mm/s is used for the Cerchar apparatus. Therefore, a jump of the stylus from the sample surface may occur by rapid and uncontrolled moving of the hand handle and due to a higher roughness grade on the surface of heterogeneous rocks. In contrast, the testing with West apparatus is much slower within 1 mm/s so that the stylus can better be controlled.

2.2.2 Applied load

Accordingly, the applied load acting on the stylus is defined to be 70 N. To see how CAI varies with changed loading force, Jacobs and Hagan (2009) as well as Ghasemi (2010) studied the correlation of the CAI values with the applied loads. It was found that CAI increases linearly with increased normal force.

2.2.3 Stylus metallurgy and hardness

Over the years, various steel types have been used for the Cerchar measurements by different researchers. Plinninger (2003) suggested to utilize the 115CrV4 tool steel which is heat-treated to the Rockwell hardness number of scale C (HRC) of 55 ± 1. Standford and Hagan (2009) compared the CAI results after testing seven different metallurgic types (Silver steel, H13, M340, Calmax, Sverker3, Rigor and S600) with the same hardness level of HRC 50 -55. They concluded that the CAI value does not vary by changing the type of steel, as long as their hardness is equal.

According to the French Standard NF P94-430-1 (2000), the stylus must be hardened to HRC 54 - 56. However, steel hardness used in different laboratories varies in a wide range. Suana and Peters (1982), Alber (2008) and Yarali et al. (2008) followed this recommendation. West (1989) stated: as the steel suggested in the original specification was not available in UK, an alternative stylus made from EN24 steel hardened to HRC 40 is used. However, Al-Ameen and Waller (1994) pointed out that the hardness of EN24 stylus is higher than materials constructed for the mining equipment. Therefore, they used a softer stylus made from EN3 (mild steel with Vickers hardness number of 225). Standford and Hagan (2009) compared the CAI results measured by using one steel type but with nine different hardness levels of HRC 15, 24, 29, 35, 40, 45, 50, 55 and 60. It was found that CAI decreases linearly with increased hardness number. Michalakopoulos et al. (2006) studied the relation of two most commonly used hardness levels: HRC 40 versus 55 and obtained a linear relationship ($\mathrm{CAI}_{\mathrm{HRC55}} = 0.59 \cdot \mathrm{CAI}_{\mathrm{HRC40}} + 0.11$). A similar result was identified by Käsling and Thuro (2010).

2.2.4 Surface condition

In Cerchar (1986), surface condition of rock samples was not specially discussed. West (1989) stated: for hard rocks a flat surface should be produced by cutting the sample with a diamond saw and for soft rocks a flat surface should be prepared with a file. The influence of surface condition on the CAI was investigated by Al-Ameen and Waller (1994), Plinninger et al. (2003) and Rostami et al. (2005), respectively. Al-Ameen and Waller (1994) concluded that a CAI value measured on rough surface is almost identical to that on polished surface, but the rocks used for their tests were mainly soft rocks. Plinninger et al. (2003) found that CAI on rough surface is about 0.5 times higher than that on sawn surface ($\mathrm{CAI}_{\mathrm{rough}} = 0.99 \cdot \mathrm{CAI}_{\mathrm{sawn}} + 0.48$). Rostami et al. (2005) compared the CAI values taken from different references and came to similar conclusions.

2.2.5 Sliding distance

As defined in Cerchar (1986), the stylus has to move 10 mm over the rock surface. The effect of sliding distance on the CAI was examined by Al-Ameen and Waller (1994), Plinninger et al. (2003) and Yarali et al. (2013), respectively. Al-Ameen and Waller (1994) found that about 70% of the stylus wear occurs in the first 1 mm, 85% of the final CAI value is achieved after 2 mm and only 15% of the final CAI value is due to the final 8 mm. Plinninger et al. (2003) confirmed this finding and stated that there is no substantial deviation in CAI when sliding distance varies between 9.5 mm and 10.5 mm so that a lengthening of the distance seems to be not necessary. Yarali et al. (2013) lengthened the standard testing distance to 20 mm with every increment of 2 mm. It was found that 87% of the CAI value after 10 mm and 97% after 15 mm are reached corresponding to the testing distance of 20 mm. They suggested a lengthening up to 15 mm to get a satisfactory result.

2.2.6 Scratching velocity

Accordingly, the sliding distance of 10 mm is finished within 1 second on Cerchar apparatus, while the scratching velocity is 1 mm/s on West apparatus. Plinninger et al. (2004) pointed out that, although there is a great velocity difference between the two apparatuses, the CAI results seem to be equal. The influence of scratching velocity on the CAI was investigated by Rostami et al. (2014) by moving 10 mm standard testing distance within four different durations (5 s, 10 s, 30 s and 60 s)

using a West apparatus: However, no significant dependency was found, which indicates that the CAI is not affected by the testing velocity.

2.2.7 Testing repetition

Cerchar (1986) suggested to perform two to three single tests for fine-grained homogeneous rocks and five or more tests for rocks with grain sizes larger than 1 mm. West (1989) pointed out that five single tests should be representative for a rock sample. Thiele (2006) examined the numbers of single tests affecting the accuracy of the CAI value based on four different rock types (granite, quartz sandstone, limestone, quartz crystal). It was found that, overall, the predefined five single tests are insufficient for testing heterogeneous rocks. He suggested that the CAI value of a rock could be measured from a total of four to five rock samples and for each rock sample with five single tests.

2.2.8 Tip wear measurement

The accuracy of CAI is mainly dependent on the measurement approach of wear flat on the stylus tip. West (1989) found that a burr is present occasionally on the downstream side of the wear flat of the stylus tip. Then, he suggested to remove it before the measuring or ignore it during the measuring. Rostami et al. (2005) proposed a method to determine the wear flat from the side of the stylus that the correct angle of 90° on the tip is reproduced before a measurement begins, which provides for correct determination of the start and end point of the wear flat. Käsling (2009) stated: various wear flats could be formed depending on the rock mineralogy and strength, as well as surface condition of the rock sample. A single test is invalid and should be repeated when a rounded or asymmetric tip wear is formed.

2.2.9 Mineral grain size

The study of Suana and Peters (1982) showed that mineral grain size has no obvious influence on the CAI when its value varies between 50 µm and 100 µm. This finding was confirmed by Lassnig et al. (2008).

2.2.10 Quartz-based index

West (1986) correlated the Cerchar abrasivity with the quartz content of rocks. He concluded that an increase of quartz content leads to an increase of rock abrasivity. Thuro and Käsling (2009) studied the relation between the Cerchar index and equivalent quartz content. It was found that the CAI increases linearly with increased quartz equivalence.

2.2.11 Rock porosity

Alber (2008) considered that the Cerchar abrasivity could be related to the porosity of rocks. However, it was only found that the CAI value of a rock seems to be high when its porosity is low, and vice versa. This reflects that the stylus is able to plough through the rock much easier and without being strongly abraded when many pores are present within the rock.

2.2.12 Rock moisture

Jacobs and Hagan (2009) studied the dependency of Cerchar abrasivity on the moisture of rocks. Tests were carried out with three levels of water content from oven dried condition (0.0%) via natural condition (2.6%) to fully saturated condition (6.6%). It was found that about two-thirds of the CAI value is reduced from dry condition to saturated condition. CAI decreases when the rock moisture is increased. A similar result is identified by Abu Bakar et al. (2016) that the CAI value in saturated rock is about 79% of that in dry rock.

2.2.13 Rock anisotropy

The testing procedure for stratified or foliated rocks was not specially discussed in Cerchar (1986). Käsling et al. (2007) stated: Cerchar measurements in layered rocks should be conducted three times to obtain the final CAI value: the sliding direction of the stylus is orthogonal and parallel, respectively, to the foliated surface, and sliding on the foliation surface. Alber et al. (2014) suggested to scratch orthogonal to as well as on the anisotropic surface of layered rock samples. Moradizadeh et al. (2016) performed their tests orthogonal and parallel to schistosity direction of metamorphic rocks.

2.2.14 Rock strength

Altindag et al. (2009) studied the correlation of Cerchar abrasivity with strength properties of the rock. It was found that CAI increases as both, UCS and BTS increase. This conclusion was confirmed by Ghasemi (2010).

2.2.15 Rock toughness

Alber (2008) studied the dependency of Cerchar abrasivity on the fracture toughness (K_{IC}) of rocks. He concluded that, although rock abrasivity is considered to be related to its toughness, no meaningful relationship was found.

2.2.16 Stress condition

Alber (2008) pointed out that the stress state of the rock sample with standard CAI value might be different from that of the rock in underground excavations. Results of his study showed that the CAI value measured with a confining pressure is higher than that without confining pressure. Moreover, by performing Cerchar measurements with a Hoek's cell, linear relationships between the CAI and the mean stress ($\sigma_m = (\sigma_1 + \sigma_2 + \sigma_3)/3$) were derived for four tested rocks, as summarized in Table 2-3.

Table 2-3 Relation of Cerchar abrasivity index and mean stress (Alber 2008)

Rock type	**Equation**
Sandstone	$\mathrm{CAI} = 1.1 + 0.13\sigma_m$
Greywacke	$\mathrm{CAI} = 1.0 + 0.06\sigma_m$
Granite	$\mathrm{CAI} = 4.2 + 0.12\sigma_m$
Mica schist	$\mathrm{CAI} = 4.0 + 0.11\sigma_m$

2.3 Cerchar mechanism

2.3.1 Tribology and wear mechanism

Tribology is the science of interacting surfaces in relative motion (Arnell et al. 1991). Friction and wear occur within a tribosystem. Wear is defined as the unwanted removal of solid material from rubbing surfaces (Burwell 1957/58). There are four basic wear mechanisms: adhesive wear, abrasive wear, fatigue wear and corrosive wear. The abrasive wear occurs when there is friction between a hard and sharp material and a relatively soft material and the harder material penetrates into the softer one. It can be divided into two-body or three-body abrasion with respect to the involved materials, as illustrated in Figure 2-2. The two-body abrasive wear occurs when abrasive particles are fixed to one body, while the second one slides over it, scratching or removing material, as, for example, in the pin-on-disc cutting test.

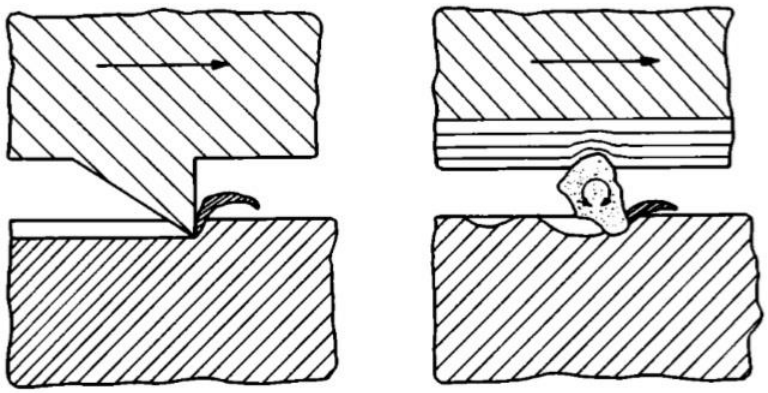

Figure 2-2 Two-body wear (left) versus three body wear (right) (Zum Gahr 1987)

Moore and King (1980) stated: both, plastic deformation mechanism and fracture mechanism result in material removal during abrasive wear of brittle materials. Zum Gahr (1987) defined the abrasive wear as a grooving wear. A model was developed to describe it by distinguishing four types of interactions between an abrasive material and a wearing material: micro-ploughing, micro-cutting, micro-fatigue and micro-cracking, as illustrated in Figure 2-3.

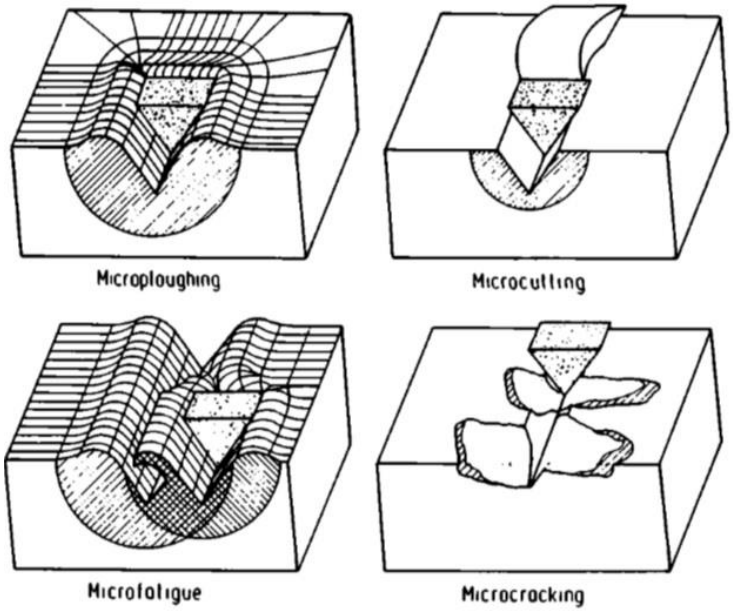

Figure 2-3 Physical interactions between abrasive particles and surfaces of materials (Zum Gahr 1987)

In material sciences, fracture behavior of rock-like materials (ceramics and glasses) subjected to the indenting and scratching of a mechanical tool has been studied by many researches. Ruff et al. (1995) investigated the damage process by simultaneously indenting and scratching brittle material like ceramics using a pyramidal cutting tool. Morphology of damage including surface cracking, spalling, grain pull-out and plastic deformation are identified, as can be seen in Figure 2-4.

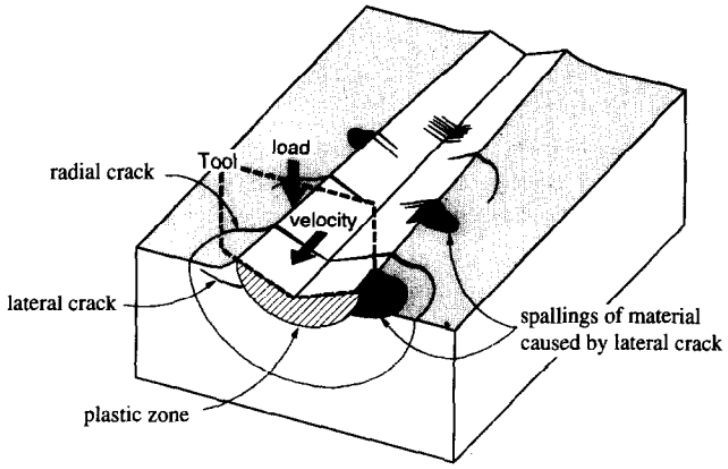

Figure 2-4 Damage morphology on brittle material subjected to indenting and scratching of a pyramidal cutting tool (Ruff et al. 1995)

Konstanty (2002) investigated the rock cutting mechanism, which can be explained by the formation of indentation with plastic deformation and breaking mechanism of rock. When the cutting depth is deep enough, cracks and chips are formed due to brittle fracture of the rock. As can be seen in Figure 2-5, there is a plastic deformation zone beneath the groove, which is formed by the horizontal movement of the wedge-like tool along the abraded surface. Two main crack systems (radial and lateral) can be caused: (1) radial cracks are formed by the action of the wedge by applying the high normal force and continue to propagate due to the residual tensile strength at the tip of the crack after the normal force is removed, and (2) lateral cracks are initiated when the applied load is removed and continue to propagate within the residual stress relaxation process.

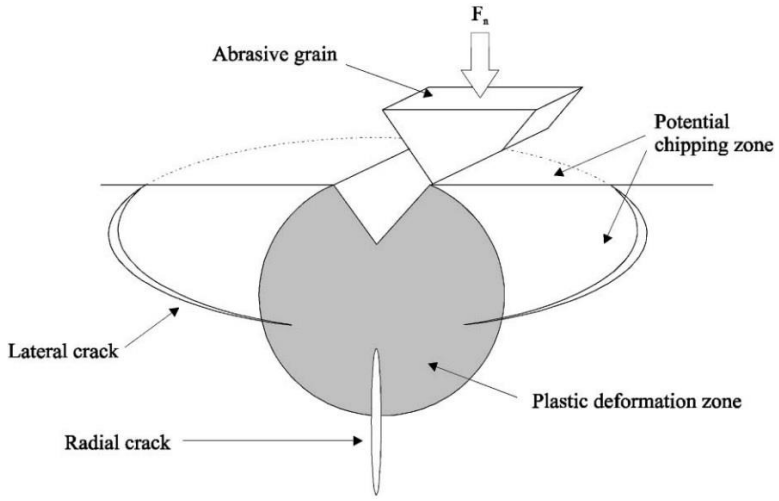

Figure 2-5 Schematic representation of the plastic deformation zone, radial and lateral cracks produced by cutting brittle materials with a wedge-like cutting tool (Konstanty 2002)

Wang and Clausen (2002) performed an indenting-cutting test on marble by using a single point cutting tool. They concluded that plastic deformation and fracture chipping of material are the dominant damage and material removal processes. Figure 2-6 illustrates the fracture formation and propagation beneath the rock surface formed by a sharp indenter and a blunt indenter, respectively.

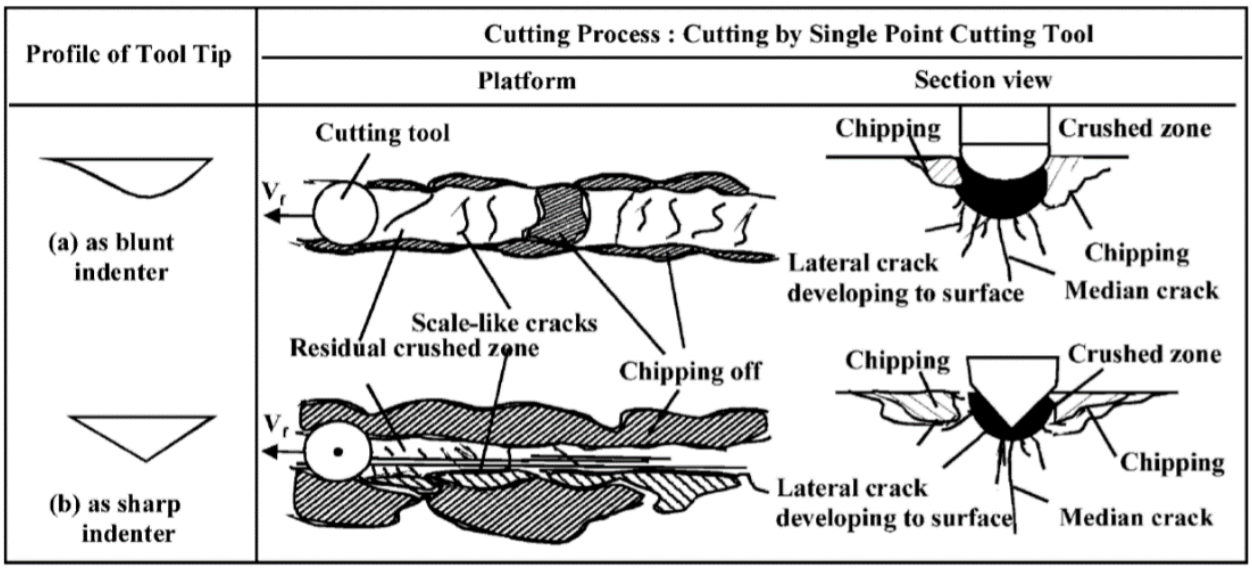

Figure 2-6 Damage morphology on marble subjected to indenting and cutting of a single point cutting tool (Wang and Clausen 2002)

2.3.2 Cerchar abrasive wear mechanism

According to the testing setup, Cerchar scratch test can be referred to as a two-body abrasion test. Abrasive wear occurs on both, stylus tip and rock surface. Over the years, however, the wear mechanism during the Cerchar scratching process has been studied by few researchers.

Suana and Peters (1982) selected different rock types and divided them into three groups: (1) granite, gneiss and metamorphic schist, (2) sandstone with silicate, carbonate and clay matrixes, and (3) basaltic rocks, in consideration of mineralogy and petrology of the rocks. They interpreted the testing mechanism based on these three rock groups and concluded that the rock abrasivity is mainly dependent on the petrological and mineralogical properties of the rock.

Al-Ameen and Waller (1994) interpreted the Cerchar mechanism based on hard rocks (igneous rocks, metamorphic rocks and some sedimentary rocks such as ironstone, chert, dolomite and some sandstone with cement material of quartz) and soft rocks (all sedimentary rocks without those categorized in hard rocks). They stated: the stylus movement and abrasion is firstly dependent on the rock type and strength and then on the degree of surface roughness and constituent minerals.

Hamzaban et al. (2014) observed the light micrographs of damaged surface on various rock types and discussed the material removal process according to their abrasive classifications. However, a detailed identification of cracking and fracturing in the scratch groove is not possible due to relatively low resolution of the pictures.

On the other hand, Piazzetta et al. (2018) studied the abrasive wear occurring on the applied stylus. They classified the wear regime into two extremes (mild and severe) with a transition region in-between and related it to the corresponding CAI values. Conclusions are summarized in Table 2-4.

Table 2-4 Relation of stylus wear regime, rock material removal and Cerchar abrasivity index (Piazzetta et al. 2018)

CAI [-]	**Wear regime**	**Wear mechanism**
0.1 - 1.8	Mild	Polishing, flattening and micro-plowing (low material loss)
1.8 - 3.1	Transitional	Micro-plowing and micro-fatigue
> 3.1	Severe	Micro-cutting with formation of well-defined grooves and microchips (high material volume removal)

2.4 Prediction of tool wear using Cerchar abrasivity index

As far as it is known, Cerchar abrasivity index is primarily used to assess the rock abrasivity. For this purpose, a classification is available in the original recommendation (Cerchar 1986). Another main application of this index is to estimate the tool wear or lifetime during rock excavations. For decades, relations or empirical formulas have been established between the tool consumption and CAI or a combination of CAI with other rock mechanical parameters like UCS.

2.4.1 Pick consumption

According to Rostami et al. (2005), the pick consumption of a medium- to heavy-duty roadheader can be estimated by the following formula:

$$PC = \frac{CAI}{4} \cdot k_1 \cdot k_2 \qquad (2\text{-}2)$$

where PC [bits/ton] is the pick consumption, k_1 [-] is between 0.75 and 1 for cutter heads with water jet spray and effectiveness of the jets, and k_2 [-] is a constant related to cutter head speed and varies from 0.9 to 1.2 for axial low speed cutter heads to transverse high speed heads.

Figure 2-7 shows the consumption of a point-attack pick ([picks/m^3]) related to the UCS and CAI, which is developed by the Australia Voestalpine Ltd. for rocks with relatively lower strength and low to medium-high abrasive properties.

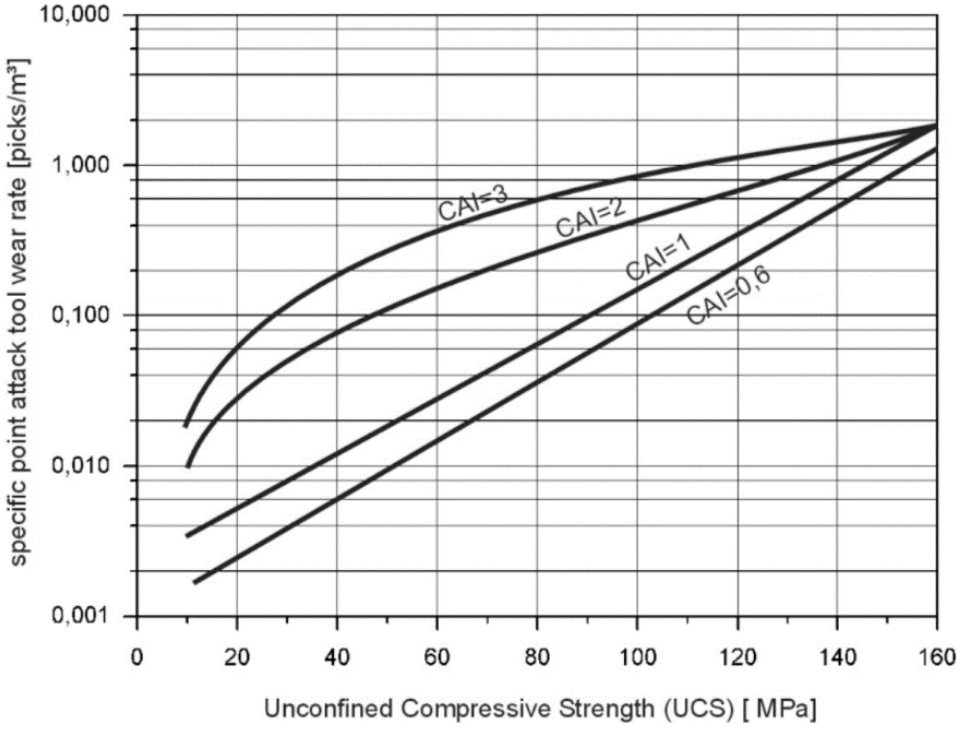

Figure 2-7 Relation of point-attack pick consumption and combined CAI and UCS (Plinninger et al. 2004)

Based on the trans-Alpine project of Mont Cenis tunnel supported by the Sweden Sandvik Group, the specific pick consumption ([picks/m^3]) of a tunnel miner MT620 can be estimated by means of the combined UCS and CAI. Seen from Figure 2-8, for example, in the case of an UCS value of 60 MPa and a CAI value of 1.3, the specific pick consumption is calculated to be about 0.04 picks per solid cubic meter of cut material.

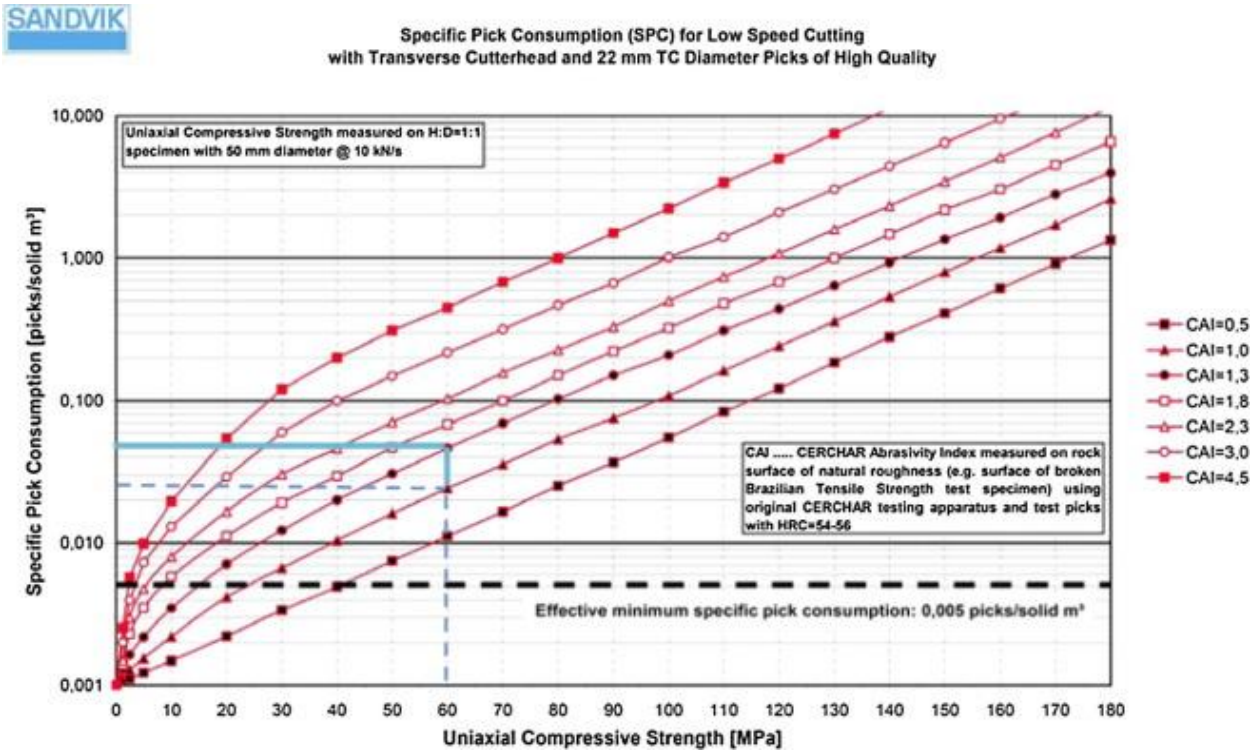

Figure 2-8 Relation of specific pick consumption and combined CAI and UCS for tunnel miner MT620 (Restner and Pichler 2007)

2.4.2 Disc cutter consumption

Gehring (1995) derived a formula for estimating the specific disc wear as a function of Cerchar abrasivity index (see Figure 2-9). A power relationship is obtained:

$$W_f = 0.74 \cdot CAI^{1.93} \quad (2\text{-}3)$$

where W_f [mg/m] is the specific disc wear, and CAI [-] is the Cerchar abrasivity index.

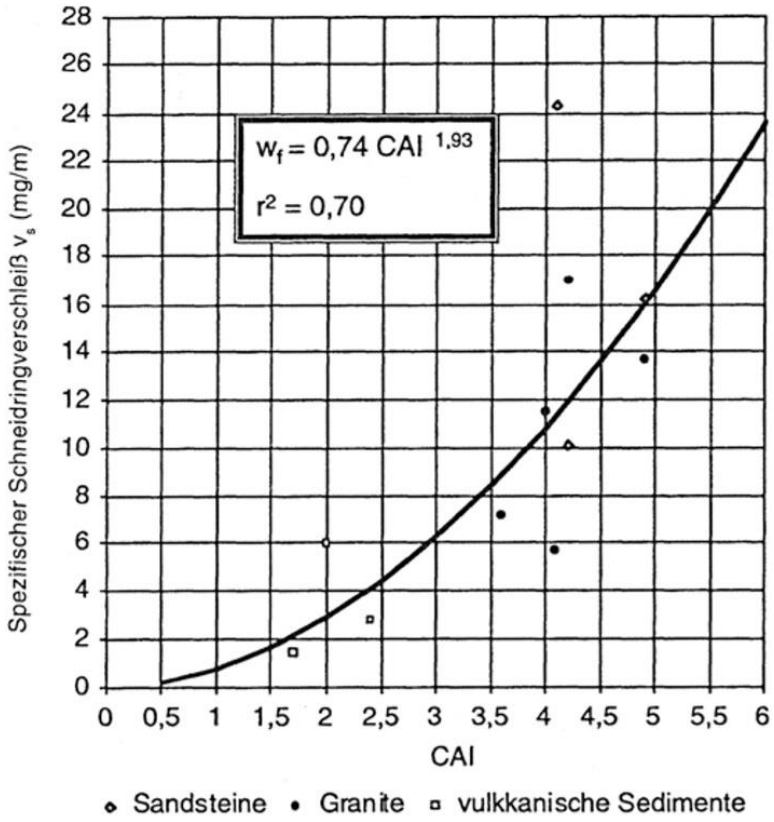

Figure 2-9 Relation of specific disc wear and CAI (Gehring 1995)

In Maidl et al. (2001), the specific wear rate ([m^3/disc]) of a 17 inch disc cutter is correlated with the combined UCS and CAI based on the five rock groups (see Figure 2-10). It is obvious that the higher the UCS and CAI of a rock, the greater the wear rate of a disc cutter.

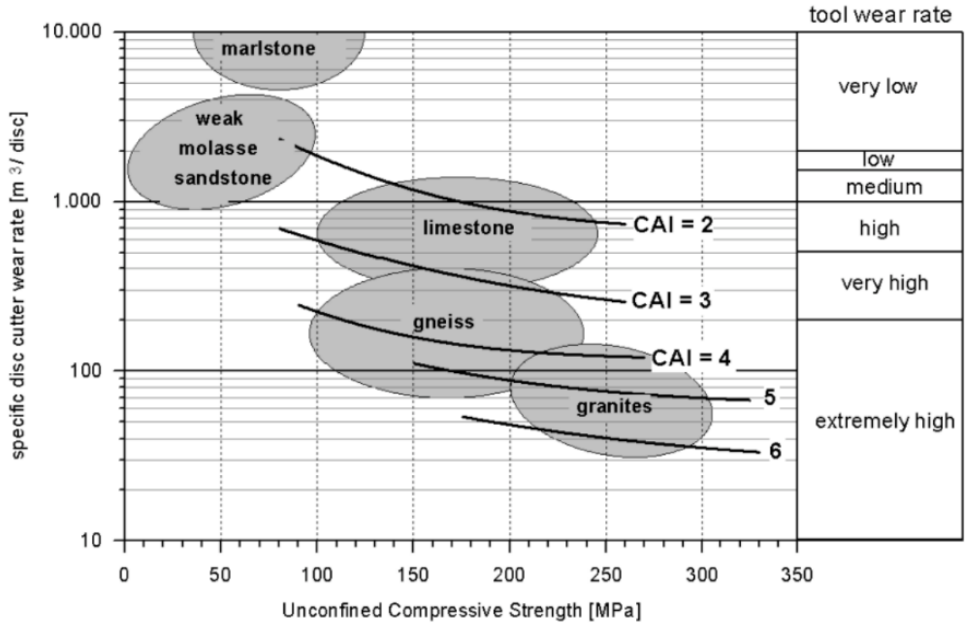

Figure 2-10 Relation of specific disc cutter wear rate and combined CAI and UCS (Maidl et al. 2001)

Study of Rostami et al. (2005) indicates that, for disc cutters, the cutter life has an inverse proportion to the CAI. The formula for cutter life of a hard rock TBM is described as follows:

$$LF = \frac{6.75 \cdot D_D}{17 \cdot CAI} \tag{2-4}$$

where LF [10^6·feet] is the linear feet of cutter travel on the face, and D_D [inch] is the disc diameter.

3. Cerchar abrasivity test

3.1 Laboratory experiment

In total, eight types of igneous, sedimentary and metamorphic rocks are selected for testing in this work. They are diorite, granite, dolomite, limestone, greywacke, sandstone, slate and gneiss. Laboratory experiments are carried out at the Technical University Bergakademie Freiberg to determine the petrological-mineralogical and physical-mechanical properties of the rock, with the exception of Cerchar abrasivity test, which is conducted using a special designed West apparatus at the Institute of Geology and Geophysics of Chinese Academy of Sciences.

3.1.1 Polarizing microscopy

Polarizing microscopy is a common method used in geology and mineralogy to investigate the petrological-mineralogical properties of the rock. Rock fabric (structure and texture), such as mineral composition and content, as well as grain size and shape can be identified in the thin section of a rock sample with a polarizing microscope.

Figure 3-1 Polarizing microscope - ZEISS Axioskop 40

3.1.2 X-Ray diffraction

When the constituent minerals within a rock are too small, especially when the grain size is finer than 0.01 mm, to observe under a polarizing microscope, a false identification of some important minerals may occur. Due to this, the X-Ray diffraction (XRD) method is recommended. This method is faster and simpler to measure the compositions and contents of constituent minerals than to perform a petrological analysis.

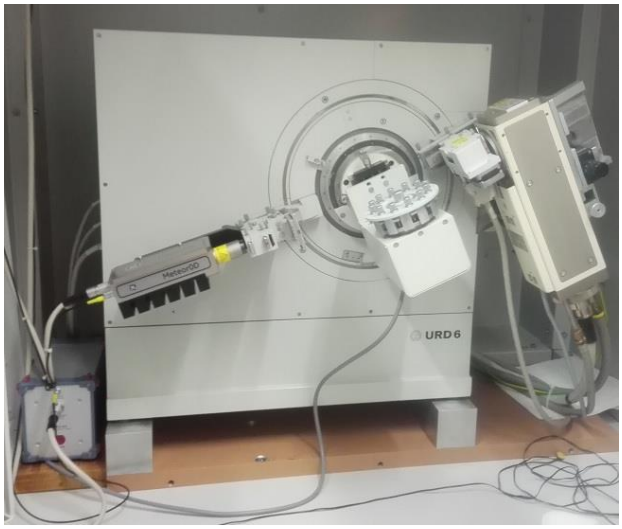

Figure 3-2 XRD apparatus - URD 6

3.1.3 Ultrasonic measurement

In rock mechanics, ultrasonic measurement is used to determine the velocity of different elastic waves in the rock, namely the longitudinal (also called primary or P-waves) and the transverse (also called secondary or S-waves). Dynamic elastic parameters including elastic modulus, Poisson's ratio and shear modulus can be derived based on the measured wave velocities. In addition, this method can be used to evaluate the quality (damage state) of the rock. By means of the P-wave velocity, the homogeneity of a rock can be examined without destruction of the sample.

Figure 3-3 Ultrasonic measurement equipment

3.1.4 Uniaxial compressive strength test

Uniaxial compressive strength (UCS) tests are carried out according to the ISRM-recommendation. The rock sample is cylinder-shaped with a diameter of 50 mm and a length of 100 mm. The loading rate on the cylindrical sample is set to 0.5 MPa/s. During the test, the stress-strain curve is recorded and displayed on the monitor. The peak compressive strength is obtained automatically from this curve. The Young's modulus is calculated at 50% peak load from deformation measurements.

Figure 3-4 Rock mechanics test system - TIRAtest 28500

3.1.5 Brazilian tensile strength test

Brazilian tensile strength (BTS) tests are carried out according to the ISRM-recommendation on disc-shaped rock samples with a diameter of 50 mm and a height of 25 mm. The sample is loaded with a constant loading rate of 200 N/s until failure occurs. The peak tensile strength is calculated in accordance with the analytical solution proposed by Hondros (1959).

Figure 3-5 Rock mechanics test system - MTS 20/M

3.1.6 Cerchar abrasivity test

Cerchar abrasivity tests are conducted by using a new designed Cerchar testing device named ATA-IGGI, as illustrated in Figure 3-6. Compared to the conventional testing apparatus, a horizontal loading-displacement sensor is mounted on the West apparatus and controlled by a servo system, by which the testing distance can be controlled and measured. The testing velocity can be specified with different values and kept constant during the test. The applied scratching force generated on the stylus can be measured and recorded during the scratching process. A program installed in a computer controls the device by specifying sliding distance and scratching velocity, respectively. It also records force-displacement data from the sensor and displays data on the monitor. The technical data of ATA-IGGI are listed in Table 3-1.

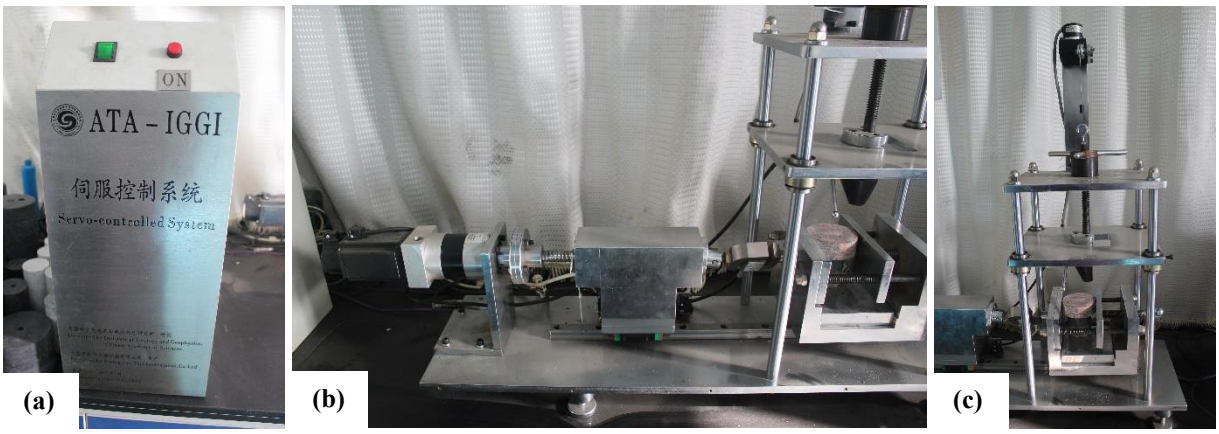

Figure 3-6 New Cerchar abrasivity testing device - ATA-IGGI: (a) servo-controlled system; (b) horizontal loading-displacement control unit; (c) West apparatus

Table 3-1 Technical data of ATA-IGGI

Parameter	**Value**
Applied normal force [N]	70
Measured horizontal force [N]	0.4 - 200
Specified scratching velocity [mm/min]	1 - 100
Data collection interval [ms]	1

After scratching, the wear flat on the stylus tip is determined using a digital binocular (see Figure 3-7). Compared to the conventional binocular, this binocular gives a more accurate measurement of tip wear. The correct angle of 90° is reproduced before the measurement of wear flat begins.

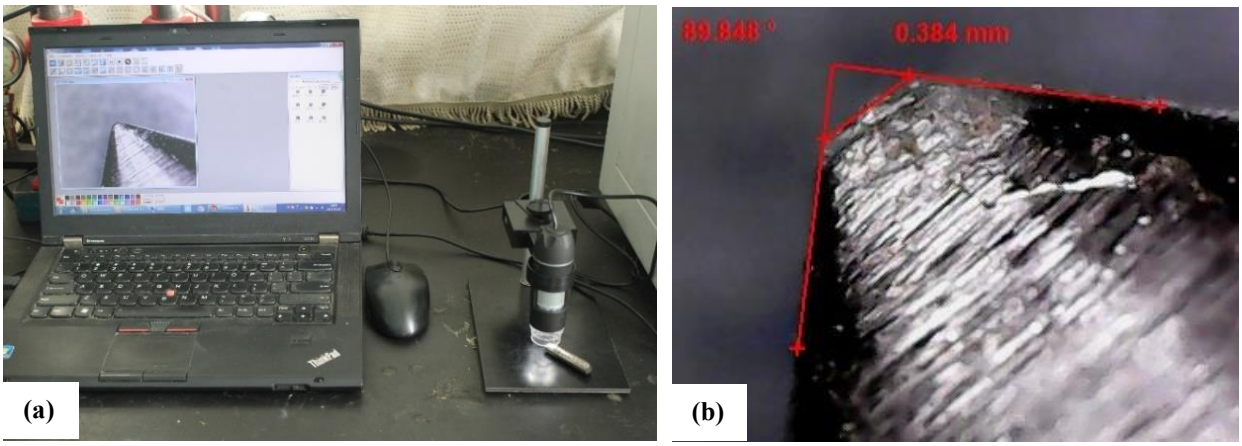

Figure 3-7 Digital binocular (a) and tip wear measurement (b)

3.1.7 Digital microscopy

Compared to the traditional optical microscope, the lenses, camera and graphics engine of a digital microscope are designed to optimize the relationship between depth of field, resolution and brightness. Due to the high frame rate of camera, this microscope can quickly scan through the focal range of a sample and recognize areas of focus to build a fully-focused image. Even when a target's surface has significant variation in height, a fully-focused image can be obtained instantly by compiling images at different focal planes. After creating the composite image, the focal position data can be used to construct a 3D model. Once a 3D image has been created, data can be collected to calculate the profile, height and volume for any area within the field of view. In this work, the depth profile of scratch groove produced on the sample surface as well as the volume of rock material removed in the scratch groove are observed and measured using a digital microscope.

Figure 3-8 Digital microscope - KEYENCE VHX 2000

3.1.8 Scanning electron microscopy

Scanning electron microscopy (SEM) is a microscope which uses electrons instead of light to form an image. This microscope has many advantages compared to a traditional optical microscope. The microscope has a large depth of field, which allows more of a sample to be in focus at one time. The microscope has much higher resolution so that closely spaced objects can be magnified at much higher levels. In this work, SEM is used to observe the figure of scratch groove formed by the stylus and produced on the rock surface.

Figure 3-9 SEM apparatus - QUANTA FEG 250

3.2 Rock mechanical property

3.2.1 Rock petrology and mineralogy

The petrological-mineralogical properties of rocks are investigated based on the observation of hand samples with naked eyes or on the analysis of thin sections under a polarizing microscope. Note that the thin sections are prepared for six of the eight tested rocks (limestone, sandstone, slate, gneiss, diorite and granite). The petrological property of dolomite and greywacke is depicted by means of the hand samples. Figure 3-10 illustrates the thin sections and hand samples of eight tested rocks with respect to their constituent minerals and microstructures.

The Mayen-Katzenberger slate taken from Rheinland-Pfalz of Germany is a fine-grained foliated metamorphic rock that can easily cleave into thin slabs. The cleavage structure is exhibited prominently by sheety minerals like mica and chlorite. The inter-foliation of mica-rich layers and quartz-rich layers can be identified in the thin section. This slate is a transverse-isotropic rock.

The Ostrauer (Saxony of Germany) dolomite is a well fine-grained rock with a color of yellowish to ocher. The grain sorting is well-sorted. The main constituent minerals are calcium and magnesium carbonates. The black flecks on the rock surface reflect a chemical reaction with acids. This dolomite is a homogeneous rock.

The milk-white limestone taken from the Erzgebirge of Germany is well fine-grained and well-sorted, and composed mainly of calcite. This limestone is a homogeneous rock.

The compact greywacke taken from Breitenau (Saxony of Germany) is fine- to medium-grained and therefore is a homogeneous rock. This rock consists mainly of quartz-, feldspar and mica-fragments. Due to its good-sorted structure, it can be termed as a lithic sandstone (rock fragment greywacke).

The Postaer sandstone from Pirna (Saxony of Germany) is fine- to medium-grained with grain size ranging from 0.1 mm to 0.2 mm. The grain sorting is between well- and moderately-sorted. The grain rounding varies from sub- to well-rounded. The grain bonding is exhibited predominantly by a direct grain-grain contact. The sandstone is porous and consists mainly of quartz. It is a quasi-homogeneous and isotropic rock.

The Leubsdorfer (Saxony of Germany) gneiss is termed as a biotite (10% - 20%) gneiss. Its main mineral constituents are feldspar (< 1.2 mm), quartz (< 1.0 mm), biotite (< 1.0 mm), muscovite (< 0.4 mm) and garnet (< 1.0 mm). It is medium-grained with regular, undulating foliation and occasional garnet porphyrblasts. This gneiss is an inhomogeneous and anisotropic rock.

The light-dark flecked diorite is a compact and medium- to coarse-grained rock. Plagioclase with twinning structure can be seen with the polarizing microscope. Dark-green pyroxene is another main mineral which can also be identified in the thin section. It is an inhomogeneous rock.

The compact granite from Mittweida (Saxony of Germany) is characterized by its medium- to coarse-grained structure with no grain size larger than 2.0 mm. Three typical minerals can be identified in the thin section: (1) the reddish feldspar that is colored by iron oxide Hematite, (2) the crystal clear, and (3) colorless quartz and the brown biotite that is evenly distributed in the rock. This granite is an inhomogeneous rock.

(a) Slate

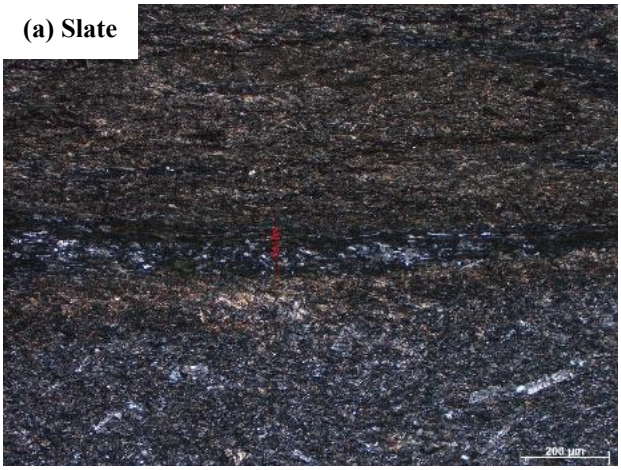

(b) Dolomite

(c) Limestone

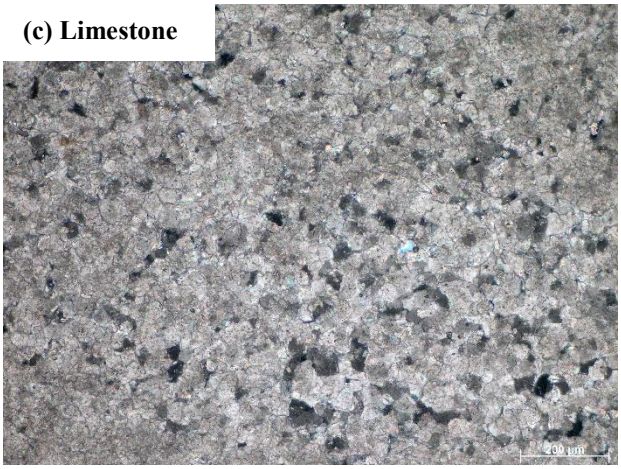

(d) Greywacke

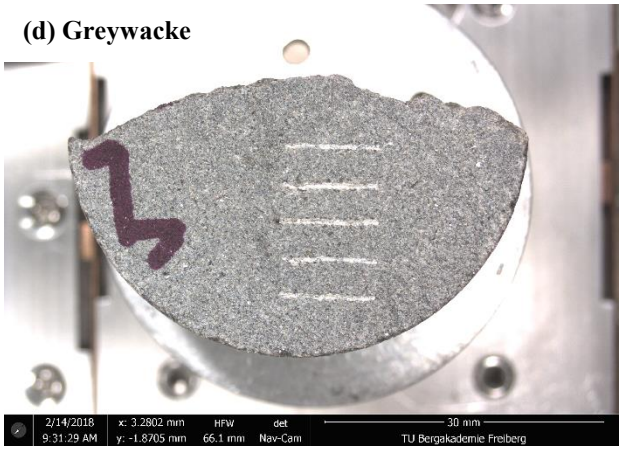

(e) Sandstone

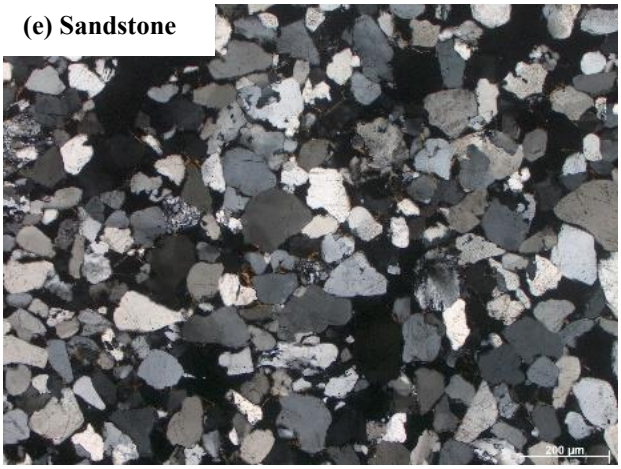

(f) Gneiss

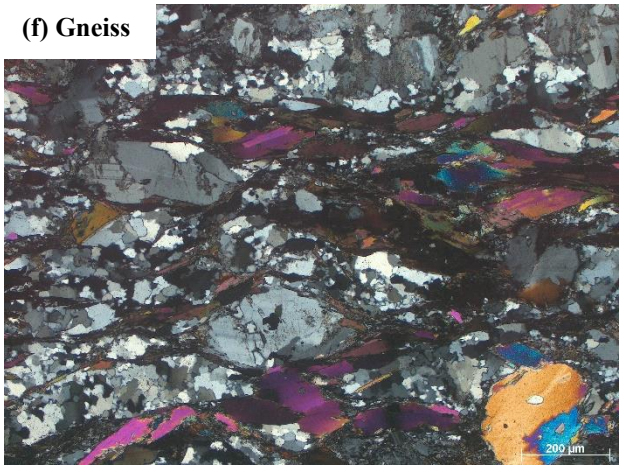

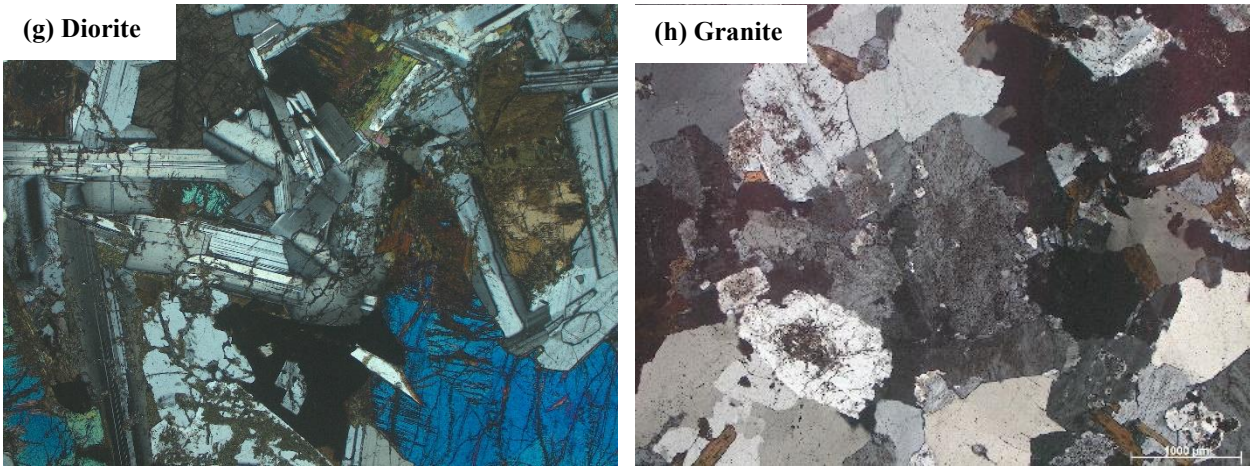

Figure 3-10 Thin sections and hand samples of
(a)-(h) slate-dolomite-limestone-greywacke-sandstone-gneiss-diorite-granite

The constituent minerals within the rock are determined under XRD-method for granite, sandstone, slate and gneiss, respectively. Based on the mineral compositions and contents, the abrasive mineral content (AMC) is calculated according to the equation (1-1) and the equivalent quartz content (EQC) is calculated according to the equation (1-2). Results are summarized in Table 3-2.

Table 3-2 Rock mineralogical properties (single value)

Rock type	**Mineral constituents [%]**		**Hardness number [-]**		**AMC [-]**	**EQC [%]**
			Mohs	**Rosiwal**		
Granite	Plagioclase	35.3	6	32	5.93	48.14
	Quartz	28.1	7	100		
	Potassium feldspar	26.4	6	32		
	Biotite	4.3	2.5	3.7		
	Chlorite	4.0	2.5	2		
	Kaolinite	1.3	2.5	2		
	Calcite	0.4	3	2.9		
	Apatite	0.2	5	10		
Sandstone	Quartz	99.1	7	100	6.96	99.12
	Kaolinite	0.9	2.5	2		
Slate	Muscovite	38.3	2.5	3.8	4.18	35.27
	Quartz	30.0	7	100		
	Chlorite	21.3	2.5	2		
	Plagioclase (Albite)	7.4	6	32		
	Rutile	1.3	6	55		
	Ankerite	1.2	3.5	2.9		
	Pyrite	0.5	6	55		
Gneiss	Feldspar	50	6	32	5.6	46.74
	Quartz	25	7	100		
	Biotite	15	2.5	3.7		
	Muscovite	5	2.5	3.7		
	Garnet	5	7	100		

3.2.2 Rock strength

Rock porosity (Ø) is determined for three typical rocks of granite, sandstone and slate. Note that, for both, UCS and BTS tests, the loading direction is perpendicular (90°) to the foliated surface of metamorphic rocks (slate and gneiss). Results of rock mechanical properties are summarized in Table 3-3.

Table 3-3 Rock mechanical properties (mean value ± standard deviation)

Rock type	**ρ [kg/m^3]**	**Ø [%]**	**v_p [m/s]**	**UCS [MPa]**	**E-modulus [GPa]**	**BTS [MPa]**
Slate	2751.3	6.1	2628.3	164.6±8.3 *)	26.9±0.8 *)	11.7±5.2 *)
Dolomite	2561.2	-	4013.7	113.4±25.7	19.9±3.1	6.1±1.4
Limestone	2568.3	-	5462.7	188.5±20.1	45.1±1.5	10.1±1.4
Greywacke	2818.2	-	6031.8	119.3±16.7	51.0±14.6	10.4±3.5
Sandstone	2060.8	20.8	3145.0	54.4±2.3	19.0±1.3	3.7±0.4
Gneiss	2714.4	-	5089.3	146.7±7.2 *)	24.7±15.8 *)	15.2±1.2 *)
Diorite	2935.4	-	5453.7	179.4±9.9	54.7±2.1	12.6±1.3
Granite	2612.7	4.1	5226.0	211.9±40.2	31.6±5.9	12.8±0.8

*): Loading is perpendicular (90°) to the foliated surface of metamorphic rocks (slate and gneiss)

3.3 Determination of Cerchar abrasive parameters

Cerchar abrasivity is measured under both, rough and sawn surface conditions for the eight tested rocks. The applied stylus is made of 115CrV3 tool steel and heat-treated to the hardness number of HRC 54 - 56. The testing setup and procedure are in accordance with Alber et al. (2014). The wear flat (Wt) on the stylus tip is determined using the digital binocular. The abraded tip is measured four times at each 90° rotation to obtain one wear value from one scratch. Depending on the homogeneity of rocks, five to ten scratches with new or reshaped styli are repeated to obtain a mean wear value for one rock sample.

Besides the abrasivity index, some parameters can also be derived from the Cerchar test. Figure 3-11 illustrates the flowchart for the determination of such parameters, which can be measured based on the applied stylus and the tested rock, as well as by means of the testing device.

According to the wear flat, the volume of steel material (Vs) abraded from the stylus tip is calculated as the volume of a cone by multiplying the wear area with the corresponding height reduction. The depth of scratch groove (Ds) formed on the sample surface and the volume of rock material (Vm) removed in the scratch groove are measured using the digital microscope. Since the applied scratching forces (F_S) are monitored during the scratching process, the mean scratching force (MSF) and the mean peak scratching force (MPSF) can be derived from the smoothed force-displacement curve. Note that, for the determination of scratching force, Cerchar measurements are only performed under sawn surface condition in order to exclude the influence of surface condition on the test result. The scratching energy (SE) is calculated by integrating the scratching force with the corresponding sliding distance of 10 mm. The scratching specific energy (SSE) is calculated by dividing the scratching energy by the material removal volume. The Cerchar abrasion ratio (CAR) is defined as the ratio of material removal volume to the tip wear volume.

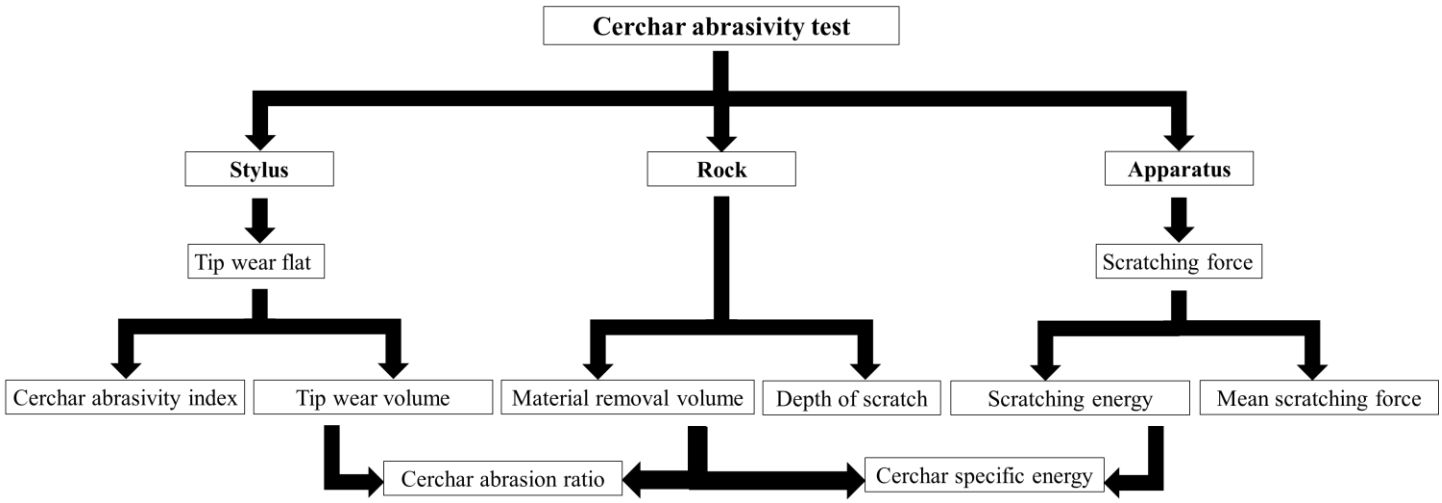

Figure 3-11 Flowchart for the determination of Cerchar abrasivity correlated parameters

3.3.1 Cerchar abrasivity index

The CAI values of tested rocks and their abrasive classifications are summarized in Table 3-4. The classification is in accordance with Alber et al. (2014) based on the CAI value measured on rough rock surface. Note that the large deviation of CAI values in diorite and granite, respectively, can be attributed to the heterogeneity of the rock. In sandstone, rock porosity plays an additional role affecting the CAI result and its deviation.

Table 3-4 Cerchar abrasivity index (mean value ± standard deviation) and abrasive classification

Rock type	**CAI [-]**		**Abrasive classification**
	Sawn surface	**Rough surface**	
Slate	0.79 ± 0.44 **)	0.81 ± 0.30 ***)	Very low
Dolomite	1.54 ± 0.20	1.63 ± 0.13	Low
Limestone	1.65 ± 0.38	2.04 ± 0.21	Medium
Greywacke	2.70 ± 1.14	3.19 ± 0.80	High
Sandstone	2.50 ± 0.66	3.30 ± 1.38	High
Gneiss	3.84 ± 0.41 **)	3.64 ± 0.11 ***)	High
Diorite	3.58 ± 0.71	3.76 ± 0.94	High
Granite	4.10 ± 0.45	4.39 ± 1.00	Very high

**): Scratching direction is orthogonal (90°) to the foliated surface of metamorphic rocks;

***): Scratching on the foliation surface of metamorphic rocks

3.3.2 Tip wear volume

Similar to the CAI, the tip wear volume (Vs) can be calculated by multiplying the one-third of wear area with the corresponding height reduction ($V_s = 1/3\pi r^2 h$). Results of tip wear volume for the tested rocks with sawn surfaces are summarized in Table 3-5.

Table 3-5 Tip wear volume (mean value)

Rock type	**Vs [10^{-5} mm^3]**
Slate **)	6.45
Dolomite	47.81
Limestone	58.80
Greywacke	257.65
Sandstone	204.53
Gneiss **)	741.19
Diorite	600.60
Granite	902.17

**): Scratching direction is orthogonal (90°) to the foliated surface of metamorphic rocks

3.3.3 Depth of scratch

Figure 3-12 illustrates the depth profile formed on the sawn sample surface of each tested rock. A relatively smooth surface of scratch groove is identified on fine-grained rocks like slate, dolomite and limestone, while severe groove surface on medium- to coarse-grained rocks like greywacke, sandstone, diorite and granite. More interesting is gneiss: both, smooth and severe groove surfaces are observed due to its inter-foliation structure.

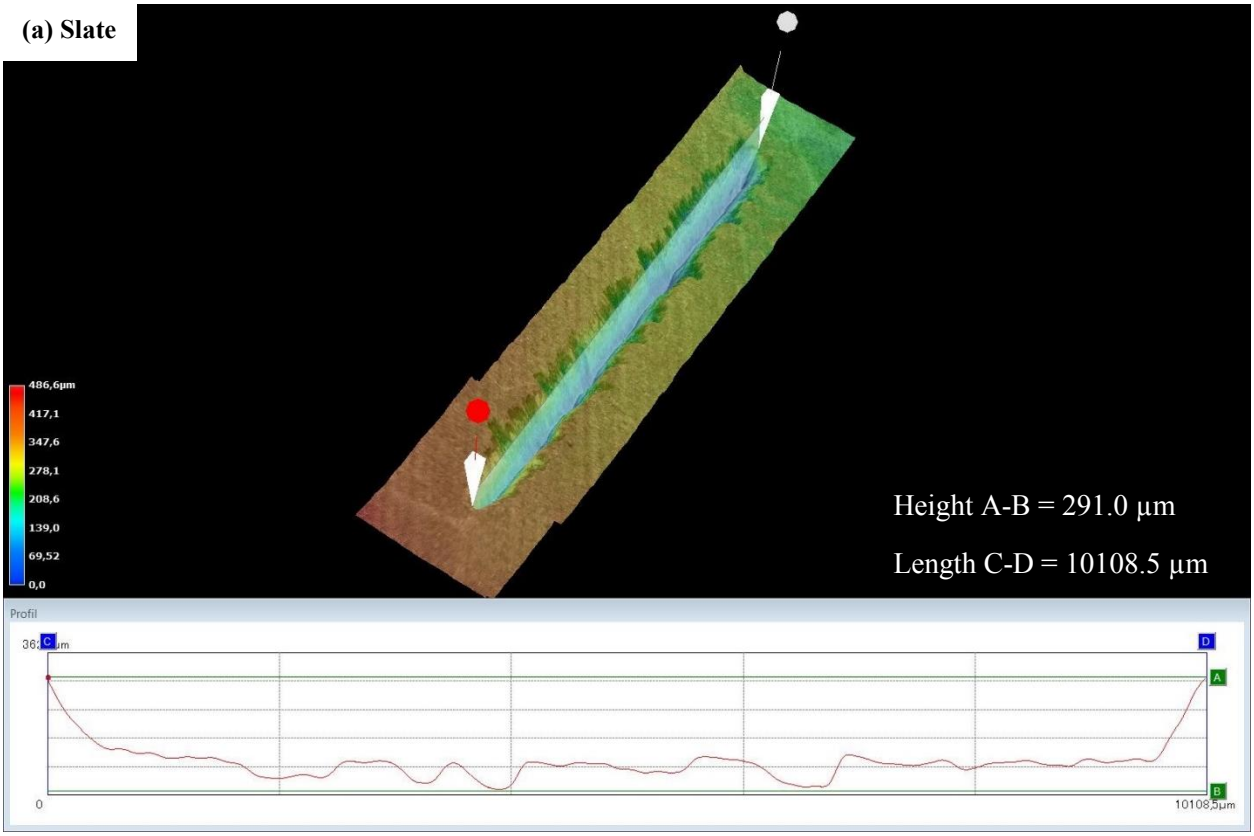

(b) Dolomite

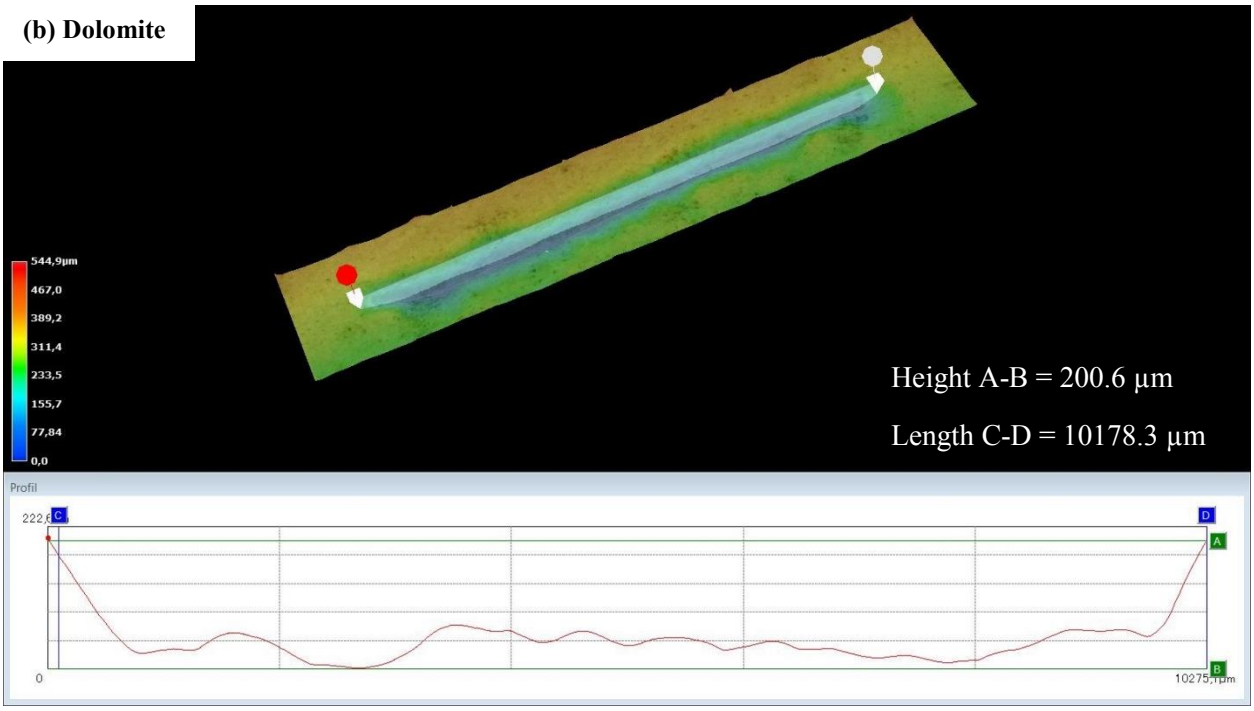

(c) Limestone

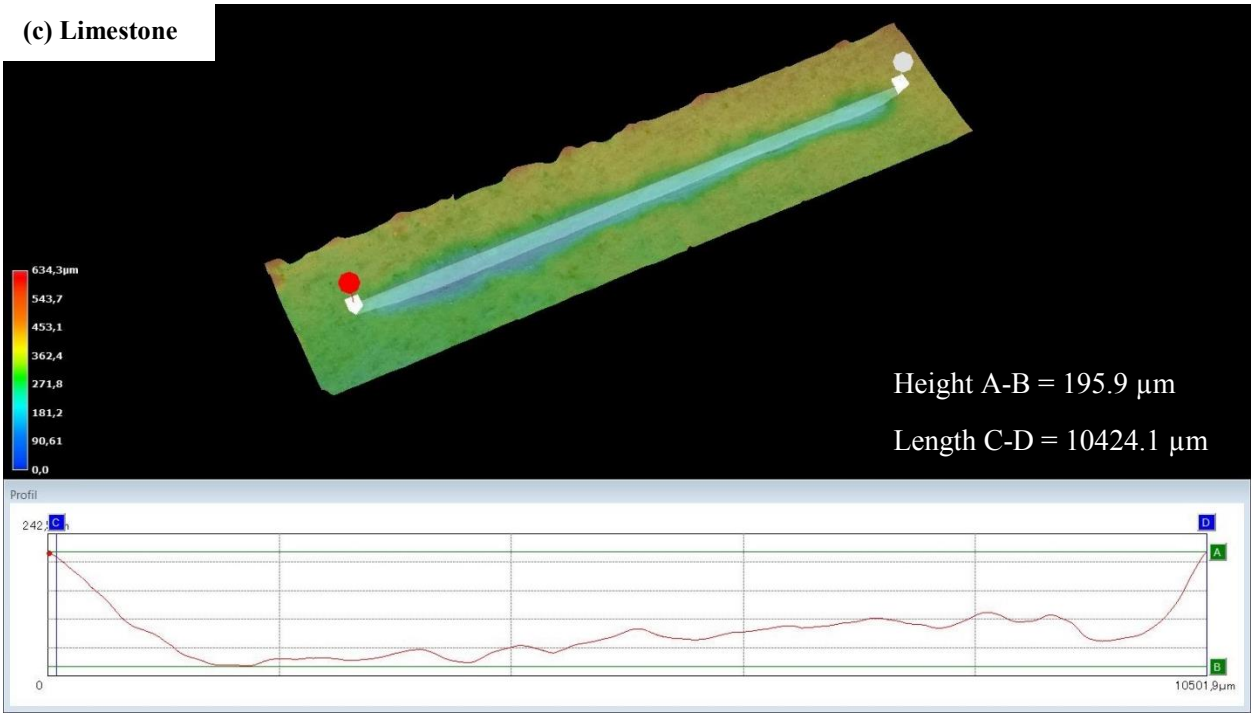

(d) Greywacke

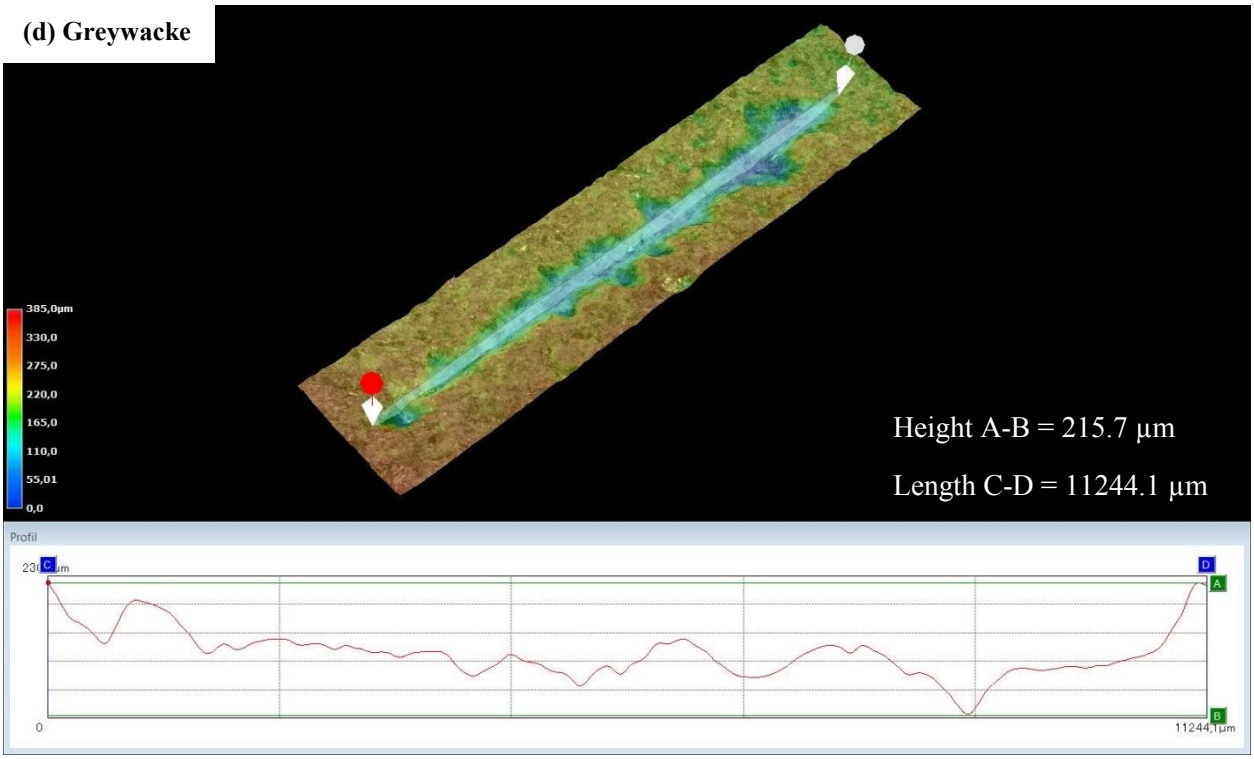

(e) Sandstone

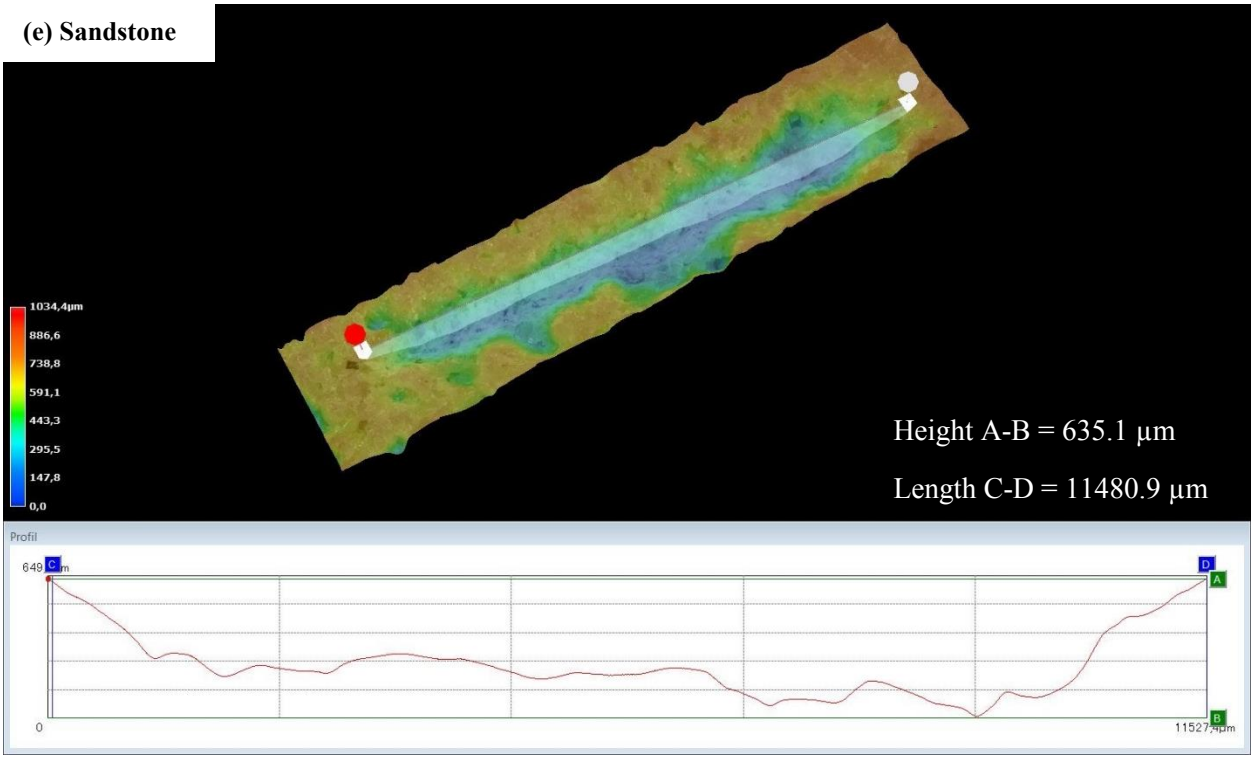

(f) Gneiss

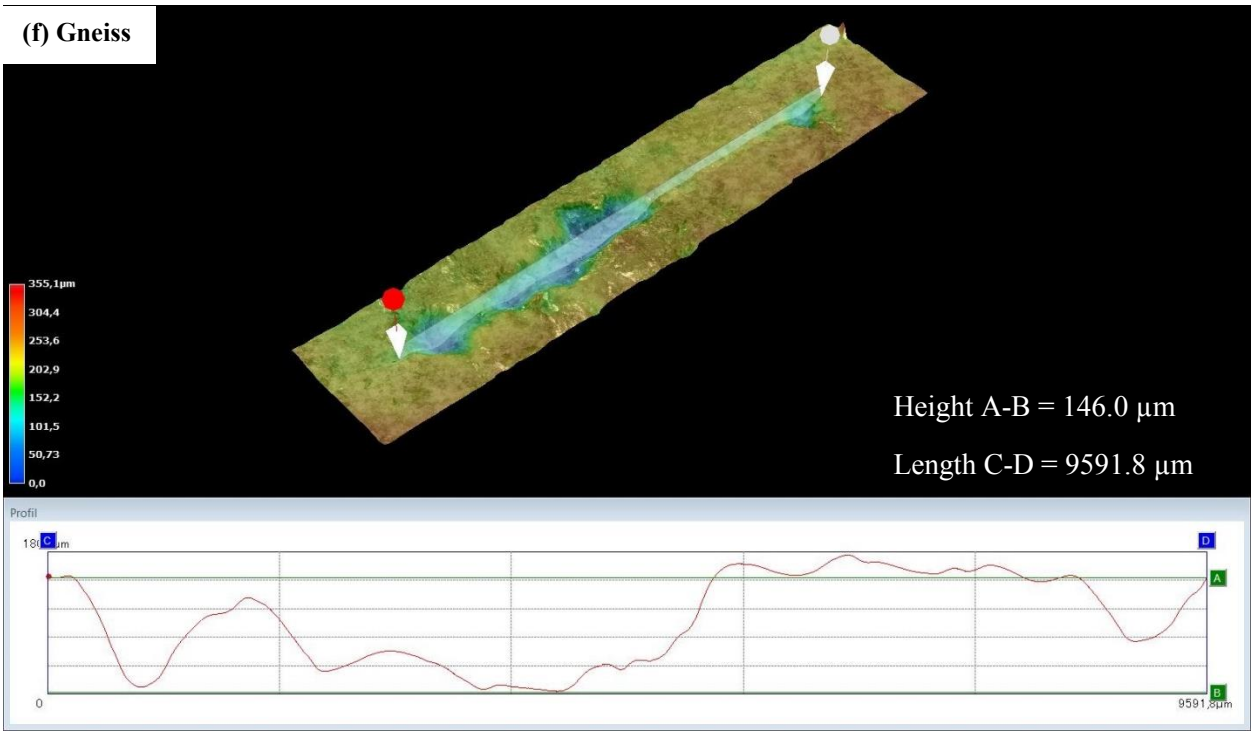

(g) Diorite

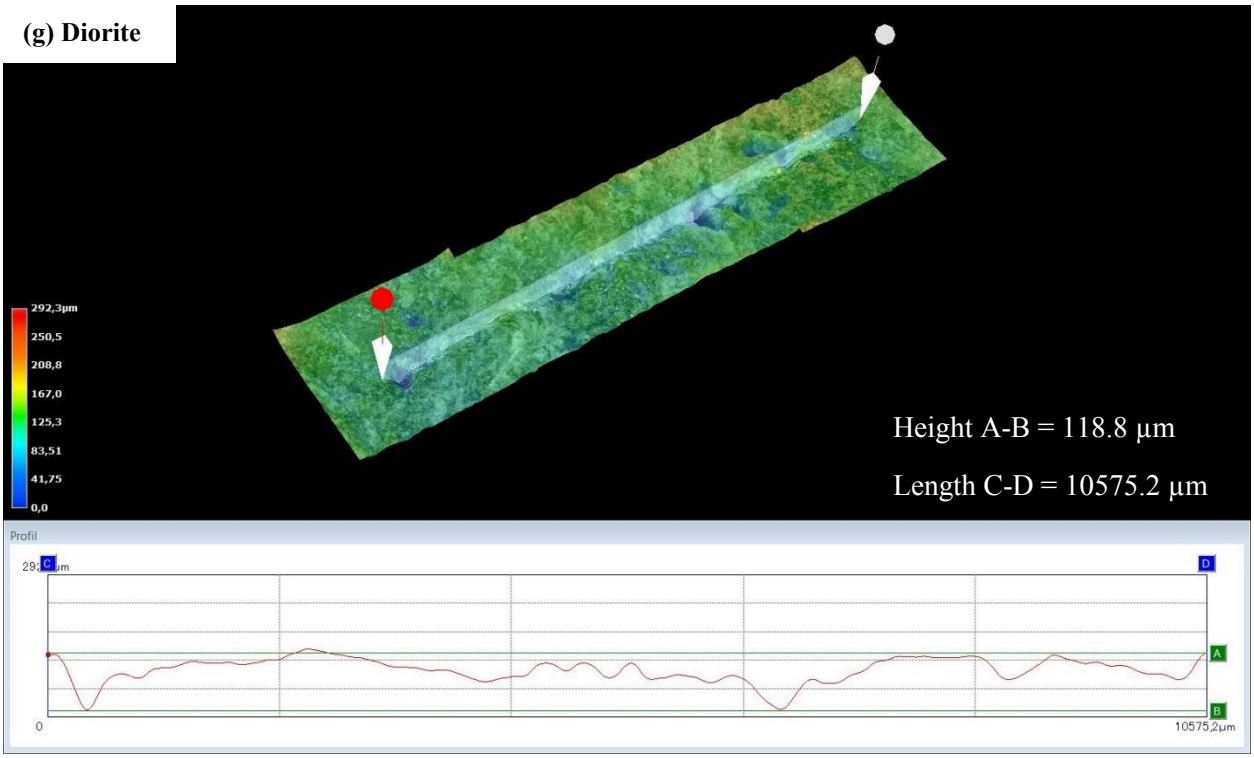

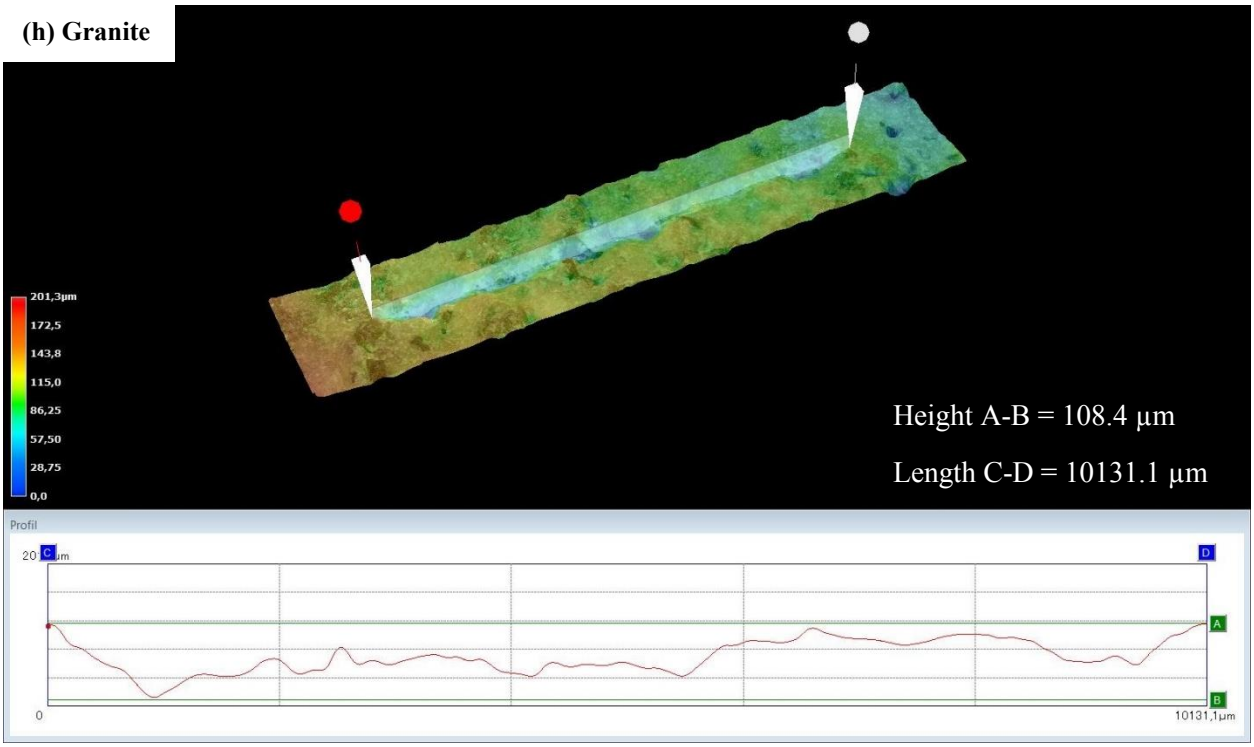

Figure 3-12 Exemplary: scratch groove profiles and measurements of maximum depths of scratches on (a)-(h) slate (90 degree to foliation)-dolomite-limestone-greywacke-sandstone-gneiss (on foliation surface)-diorite-granite

The maximum depth of scratch (Ds) in each tested rock can directly be derived from the depth profile. Results are summarized in Table 3-6. By comparing the two quartz-rich rocks of greywacke and sandstone, a great difference is found. This can be attributed to the constituent minerals with respect to their type, size and distribution within the rock, as well as rock strength and porosity. It is reasonable that the values of scratch depths are almost identical in both calcite-dominant rocks of dolomite and limestone. Similarly, a low and quasi-equal depth is identified in the two igneous rocks of diorite and granite due to their high strength and abrasive properties. Although slate has also a high strength, it is composed of many fine-grained and less abrasive minerals (muscovite and chlorite). Therefore, a relatively greater depth is generated. In gneiss, the highest depth occurs as the stylus slides on the soft mica minerals. Overall, results of scratch depths for the tested rock samples are reasonable and plausible.

Table 3-6 Maximum depth of scratch (single value)

Rock type	**Maximum Ds [mm]**
Slate **)	0.29
Dolomite	0.20
Limestone	0.20
Greywacke	0.22
Sandstone	0.64
Gneiss ***)	0.15
Diorite	0.12
Granite	0.11

**): Scratching direction is orthogonal (90°) to the foliated surface of the slate sample;

***): Scratching on the foliation surface of the gneiss sample

3.3.4 Material removal volume

During the rock cutting, the yield is defined as the volume of rock excavated per unit cutting distance (Bilgin et al. 2006). Different approaches can be used to determine the yield, for example, by means of theoretical models or manually by cleaning the removed rock materials. In this work, the material volume (Vm) removed from the rock surface is measured with a digital microscope. Taking slate as an example, the transparent shadow areas in Figure 3-13 indicate that, in total, about 0.81 mm^3 material are removed from the scratch groove of a slate sample.

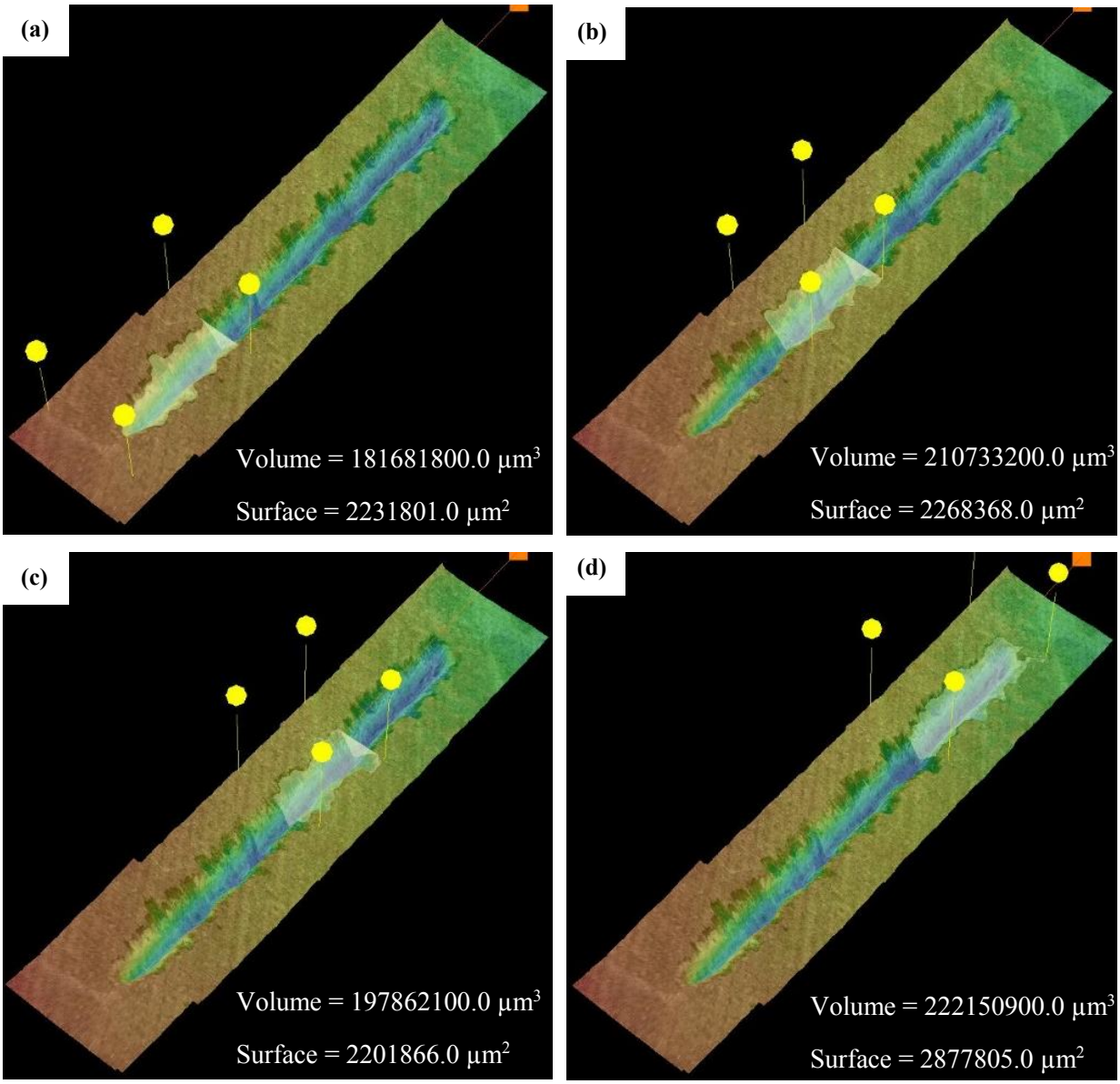

Figure 3-13 Exemplary: material removal volume in the scratch groove on a slate sample during the scratching of the stylus orthogonal (90°) to the foliated surface of the rock (The total removed volume is about 0.81 mm^3)

Note that, for each tested rock, at least two scratches are measured, and for each scratch, measurements are repeated two to three times to obtain a mean volume value. Results of material removal for the tested rocks are summarized in Table 3-7. The most material is removed on the sandstone sample due to its lowest strength and highest porosity. The removed volume is more or less identical to each other in both carbonate sedimentary rocks (dolomite and limestone), as well

as in the two ingenuous rocks (diorite and granite). In gneiss, a large deviation from the mean volume value is identified. This can be related to the constituent minerals within the rock, namely the hard quartz minerals and soft mica minerals, as well as the inter-foliation structure of the rock. During the scratching process, where more quartz minerals accumulate, less material is removed.

Table 3-7 Material removal volume (mean value ± standard deviation)

Rock type	**Vm [mm^3]**
Slate **)	0.88 ± 0.10
Dolomite	1.13 ± 0.30
Limestone	1.04 ± 0.33
Greywacke	0.56 ± 0.18
Sandstone	5.54 ± 1.42
Gneiss ***)	1.81 ± 1.27
Diorite	0.48 ± 0.19
Granite	0.69 ± 0.32

**): Scratching direction is orthogonal (90°) to the foliated surface of the slate sample;

***): Scratching on the foliation surface of the gneiss sample

Seen from Figure 3-14, by comparing the two volumetric parameters, Vm versus Vs, a low material removal volume with a high tip wear volume is determined in harder and more abrasive rocks like granite, diorite and gneiss, while a relation of high material removal to low tip wear is found in hard but less abrasive rocks like limestone, dolomite and slate. Although the tip wear volume in relatively soft and abrasive greywacke and sandstone is almost identical, the material removal is much larger in sandstone than in greywacke. This is most likely due to the fact that sandstone has a higher porosity than compact greywacke.

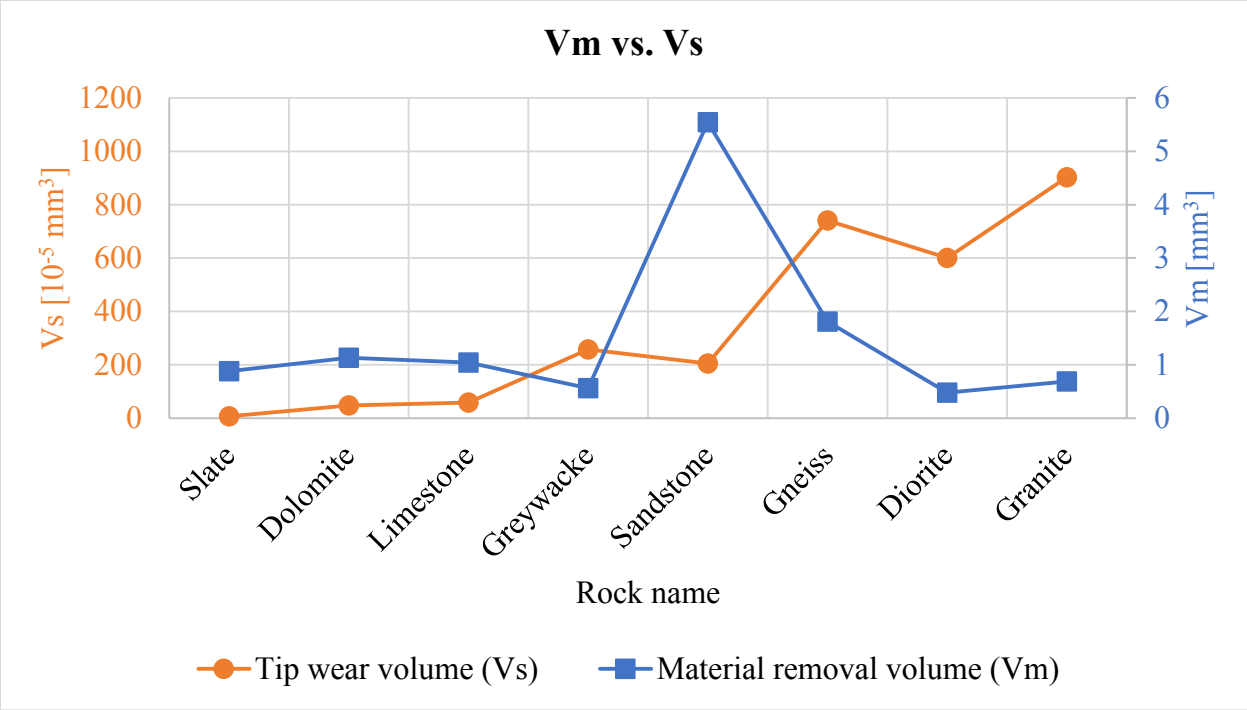

Figure 3-14 Material removal volume versus tip wear volume

3.3.5 Scratching force and mean scratching force

The scratching force generated on the stylus is monitored during the sliding distance of 10 mm. The red solid lines in Figure 3-15 show the force-displacement curves developed for the eight tested rocks. According to these curves, a cycle of scratching process can be interpreted as follows: (1) force increases as stylus contacts mineral grains until micro-cracks are formed due to cement breakage between grains. Slight decrement of force means occurrence of minor cracks, (2) coalescence of micro-cracks forms macro-cracks extending from stylus tip to rock surface, where force reaches its maximum within a cycle, (3) rapid release of stored energy in stylus leads to a drastic decrement of force, and (4) again increment of force until a major crack occurs and a new cycle begins.

The raw data of recorded scratching forces can be analyzed by a best-fit curve according to the following equation:

$$F_s = a + b \cdot \exp(-d_s) \quad (3\text{-}1)$$

where a and b are two best-fit parameters.

According to the best-fit curves (see blue dash lines the figures), the development of scratching force can be divided into two phases: (1) the 'indentation-dominant-phase' which occurs in the first 1 - 2 mm of the sliding distance indicating the penetration of the stylus into the rock due to a high pressure on the stylus tip, and (2) the 'scratching-dominant-phase' which occurs for the rest sliding distances reflecting more or less a not very discrete movement of the stylus within the rock due to tip abrasion. Then, the mean scratching force (MSF) can be referred to as the force value developed in the 'scratching-dominant-phase'. Moreover, the mean peak scratching force (MPSF) can be defined as the average of the highest forces in ten increments of force data developed in the 'scratching-dominant-phase' (green solid lines in the figures).

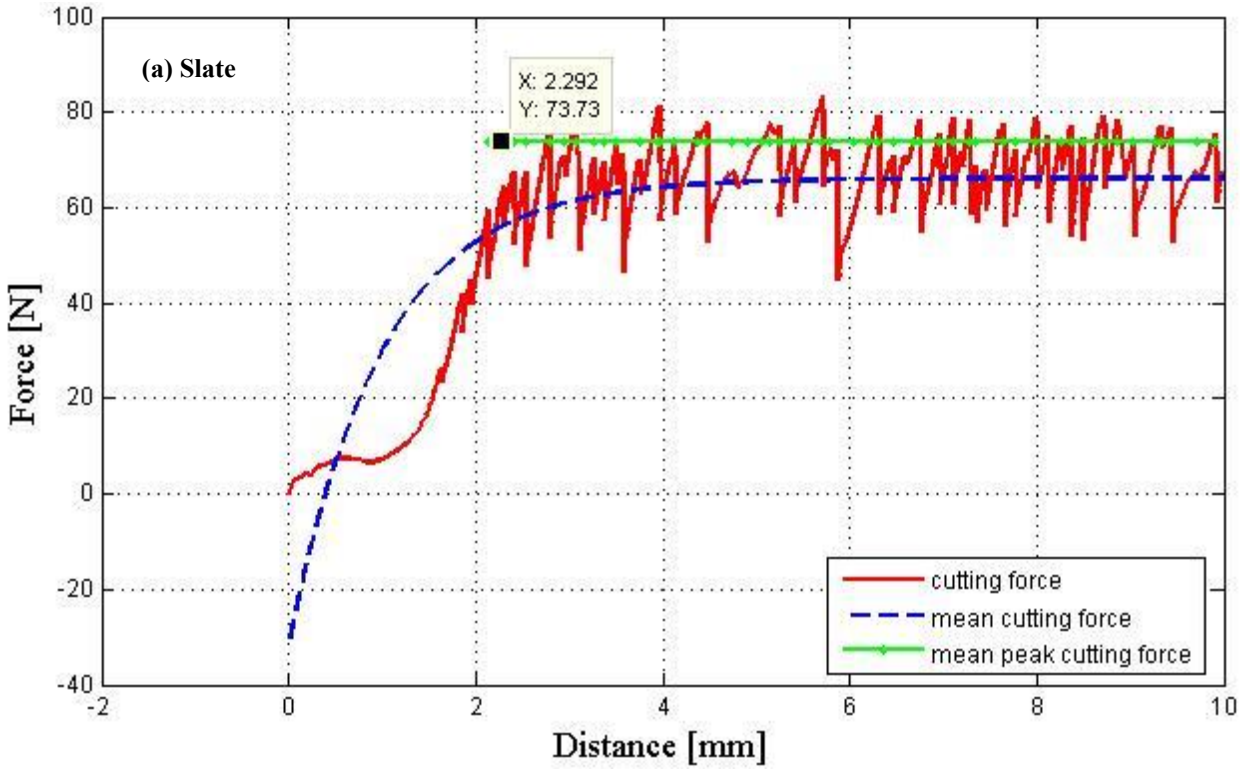

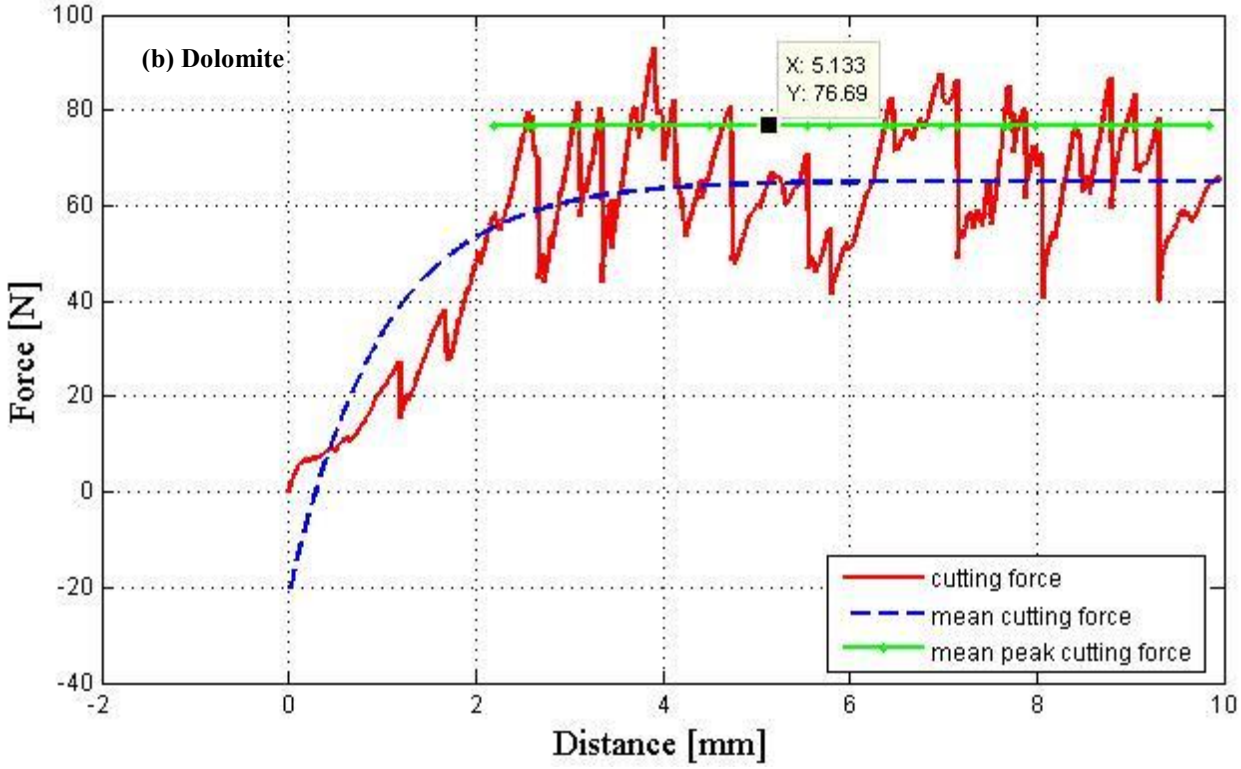
(b) Dolomite
X: 5.133
Y: 76.69
Force [N]
Distance [mm]
cutting force
mean cutting force
mean peak cutting force

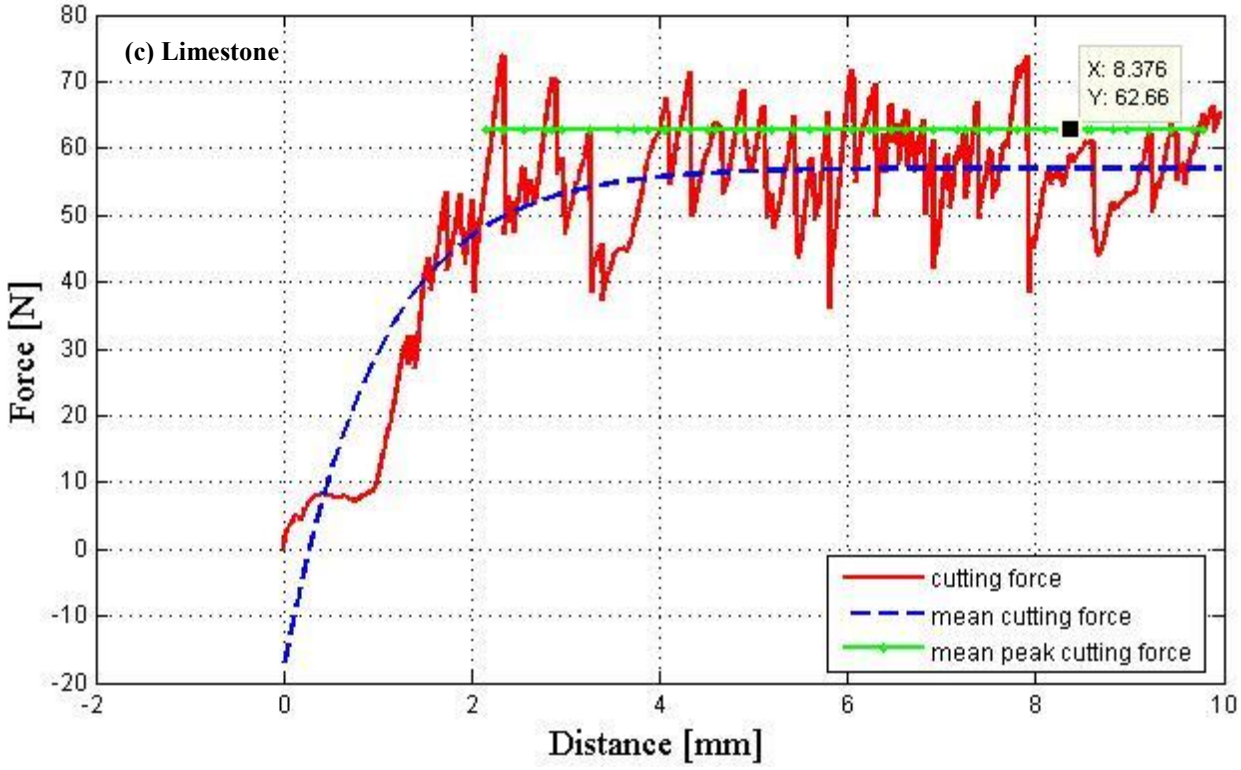
(c) Limestone
X: 8.376
Y: 62.66
Force [N]
Distance [mm]
cutting force
mean cutting force
mean peak cutting force

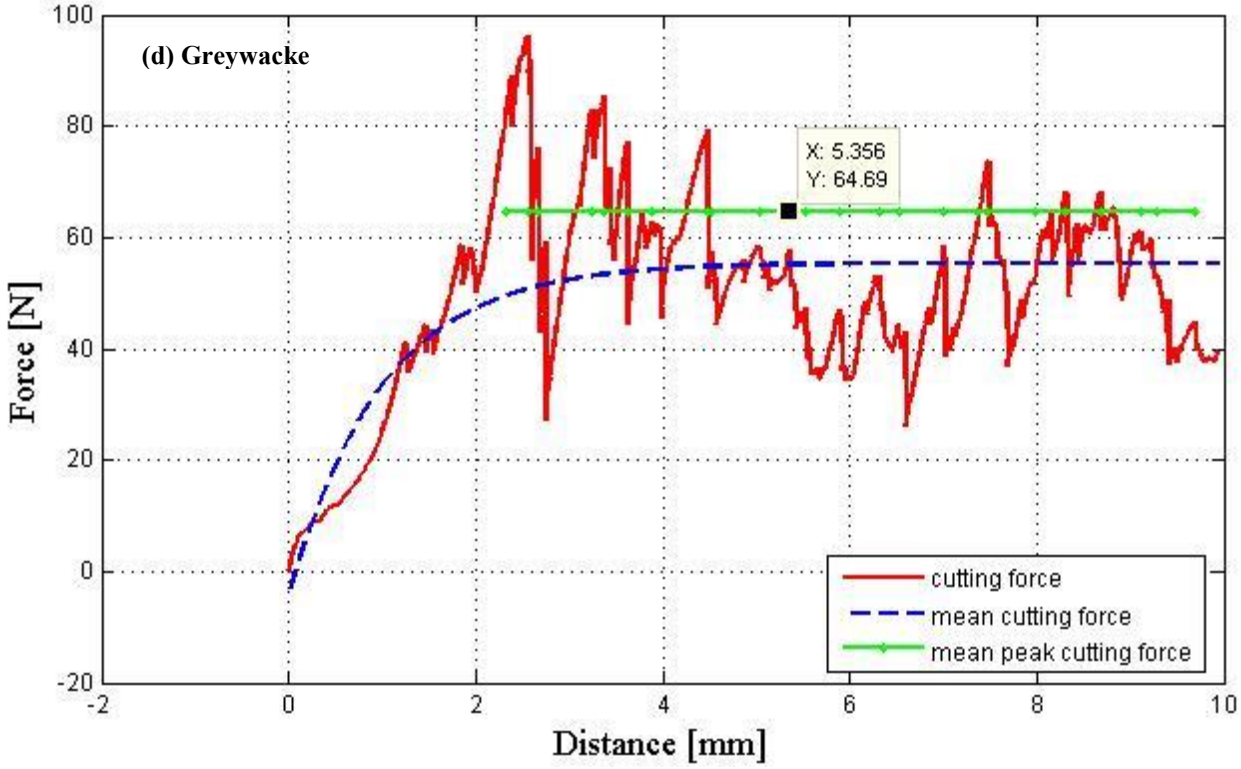
(d) Greywacke
X: 5.356
Y: 64.69
cutting force
mean cutting force
mean peak cutting force
Force [N]
Distance [mm]

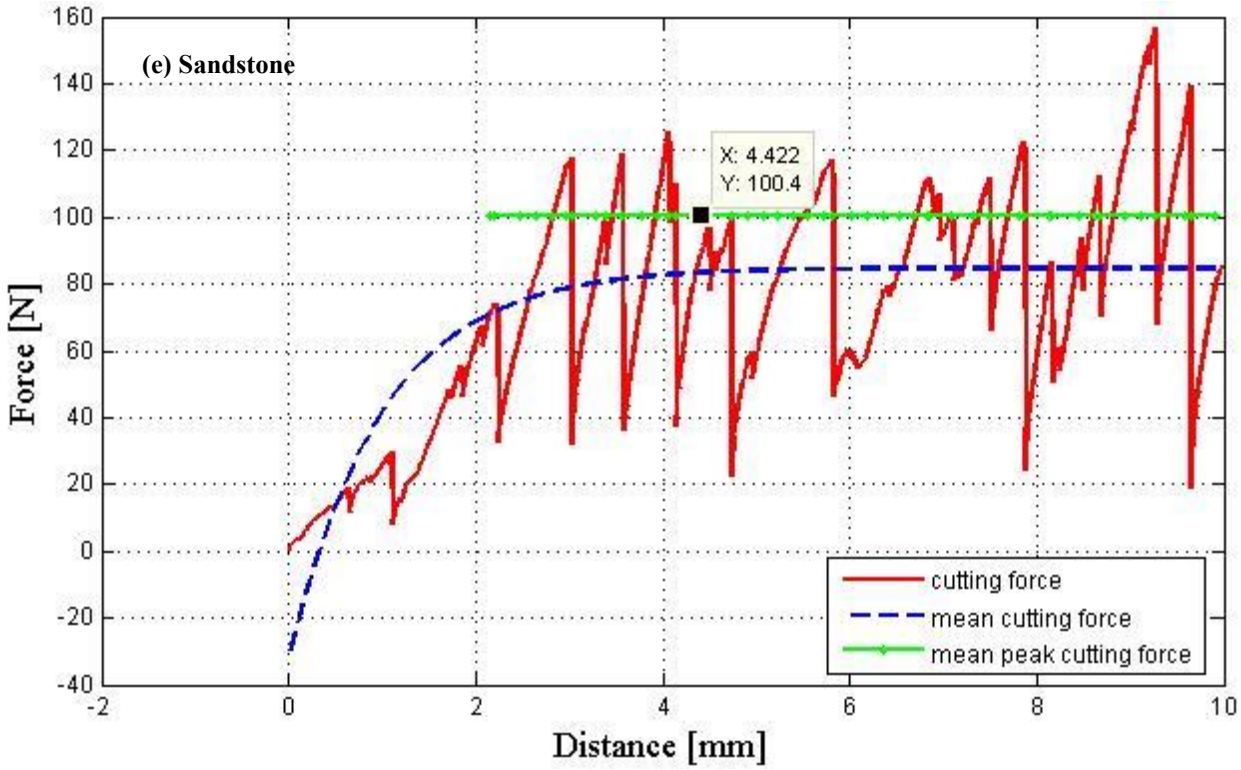
(e) Sandstone
X: 4.422
Y: 100.4
cutting force
mean cutting force
mean peak cutting force
Force [N]
Distance [mm]

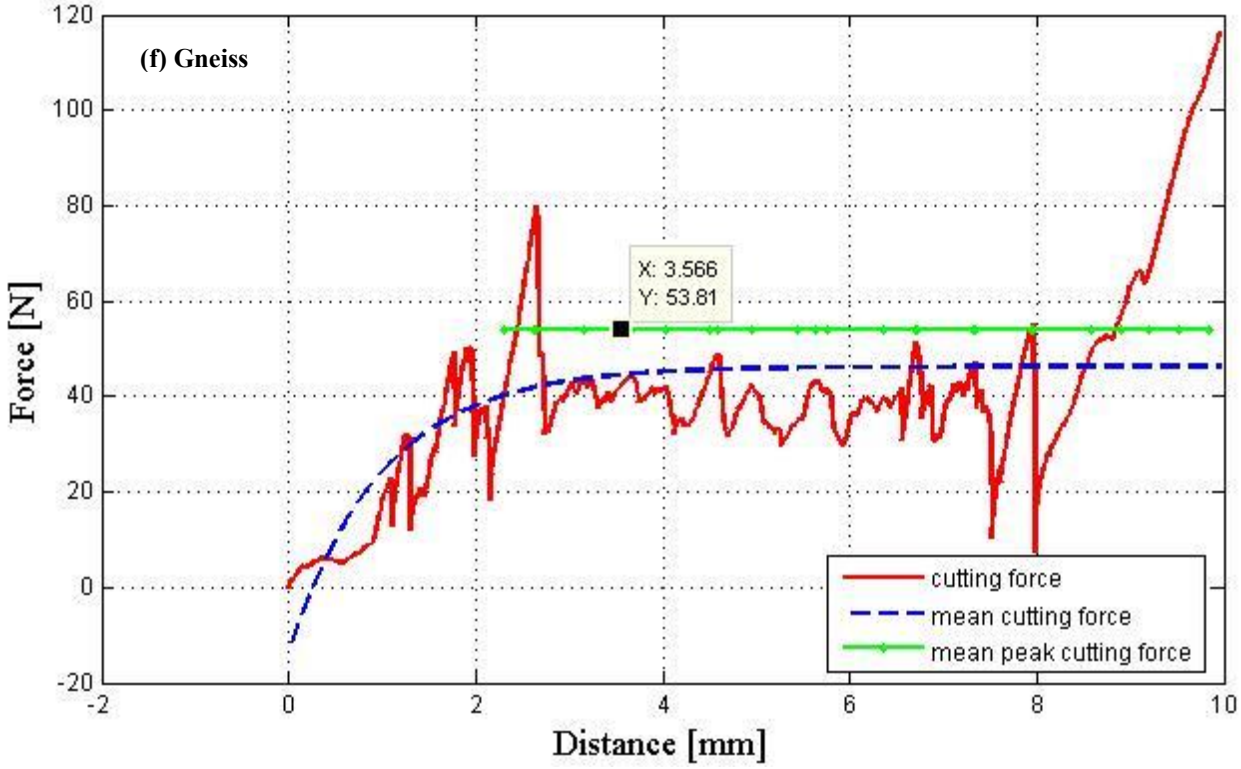
(f) Gneiss
X: 3.566
Y: 53.81
cutting force
mean cutting force
mean peak cutting force
Force [N]
Distance [mm]

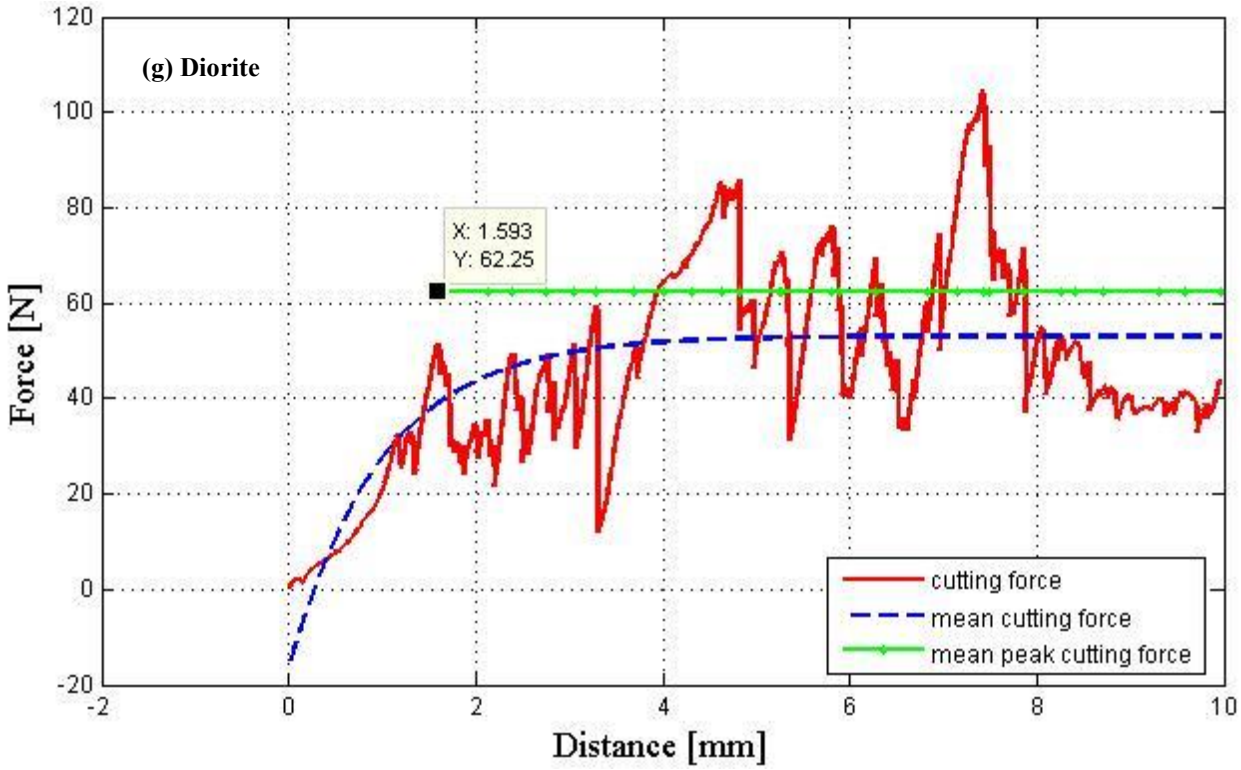
(g) Diorite
X: 1.593
Y: 62.25
cutting force
mean cutting force
mean peak cutting force
Force [N]
Distance [mm]

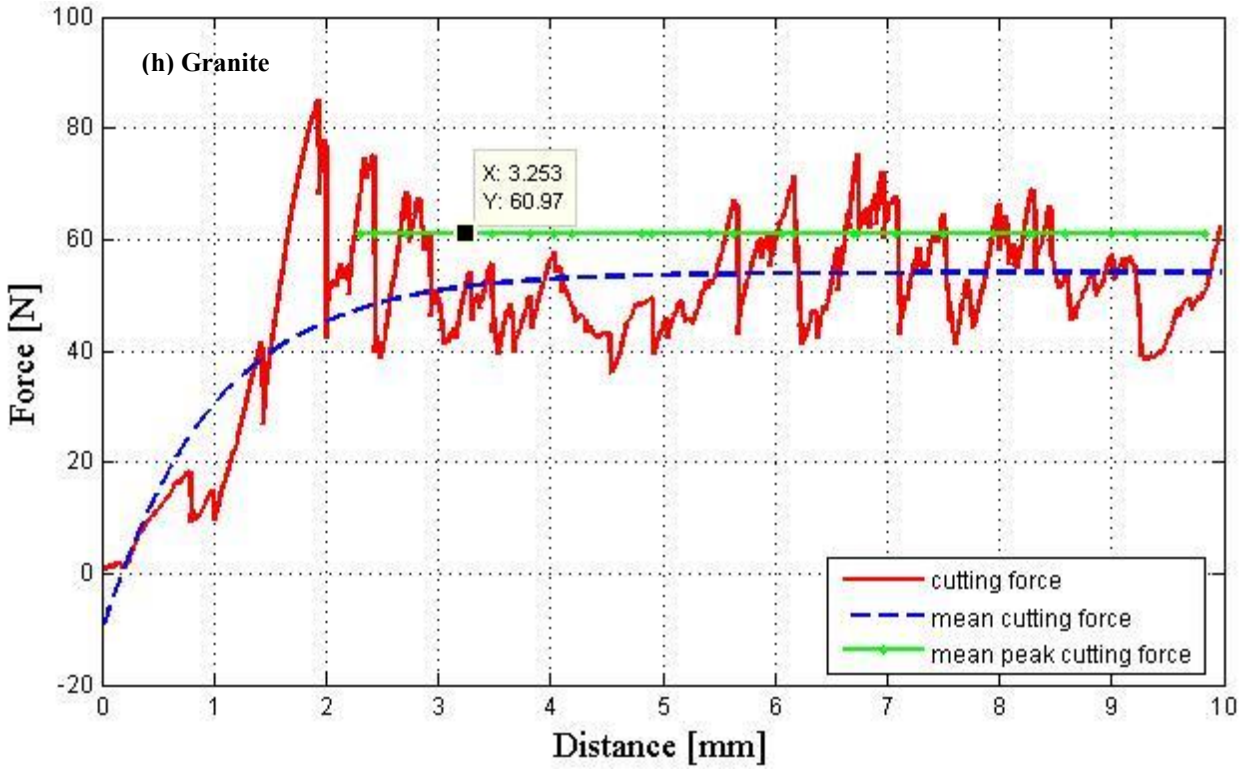

Figure 3-15 Exemplary: Development of scratching force, mean scratching force and mean peak scratching force for (a)-(h) slate (90 degree to foliation)-dolomite-limestone-greywacke-sandstone-gneiss (on foliation surface)-diorite-granite

Results of MSF and MPSF values are summarized in Table 3-8. The variation of mean or mean peak scratching force in different rocks can be attributed to the rock strength properties. In respect to the Cerchar test, it can be said that the higher the rock strength, the lower the resulting scratching force.

Table 3-8 Mean scratching force and mean peak scratching force (single value)

Rock type	**MSF [N]**	**MPSF [N]**
Slate **)	61.00	73.73
Dolomite	65.21	76.69
Limestone	57.11	62.66
Greywacke	55.44	64.69
Sandstone	84.83	100.40
Gneiss ***)	46.28	53.81
Diorite	53.13	62.25
Granite	54.06	60.97

**): Scratching direction is orthogonal (90°) to the foliated surface of the slate sample;

***): Scratching on the foliation surface of the gneiss sample

In Figure 3-16a, the MSF and MPSF values are plotted against the CAI values of tested rocks to see their correlation. In most cases, MSF or MPSF decreases as CAI increases. More interesting is sandstone. The value of MSF or MPSF in sandstone is much higher than that in other rocks. This is because the strength of sandstone (UCS = 54.4 MPa and BTS = 3.7 MPa) is quite low. It is also remarkable that, if the sandstone would be excluded from the test results, the correlation could be improved (see Figure 3-16b).

In addition, the MSF values are related to the corresponding CAI values under both, rough and sawn surface conditions. Seen from Figure 3-17a, no meaningful correlation is found. However, in Figure 3-17b, a weak linear relationship can be identified by ignoring the soft sandstone.

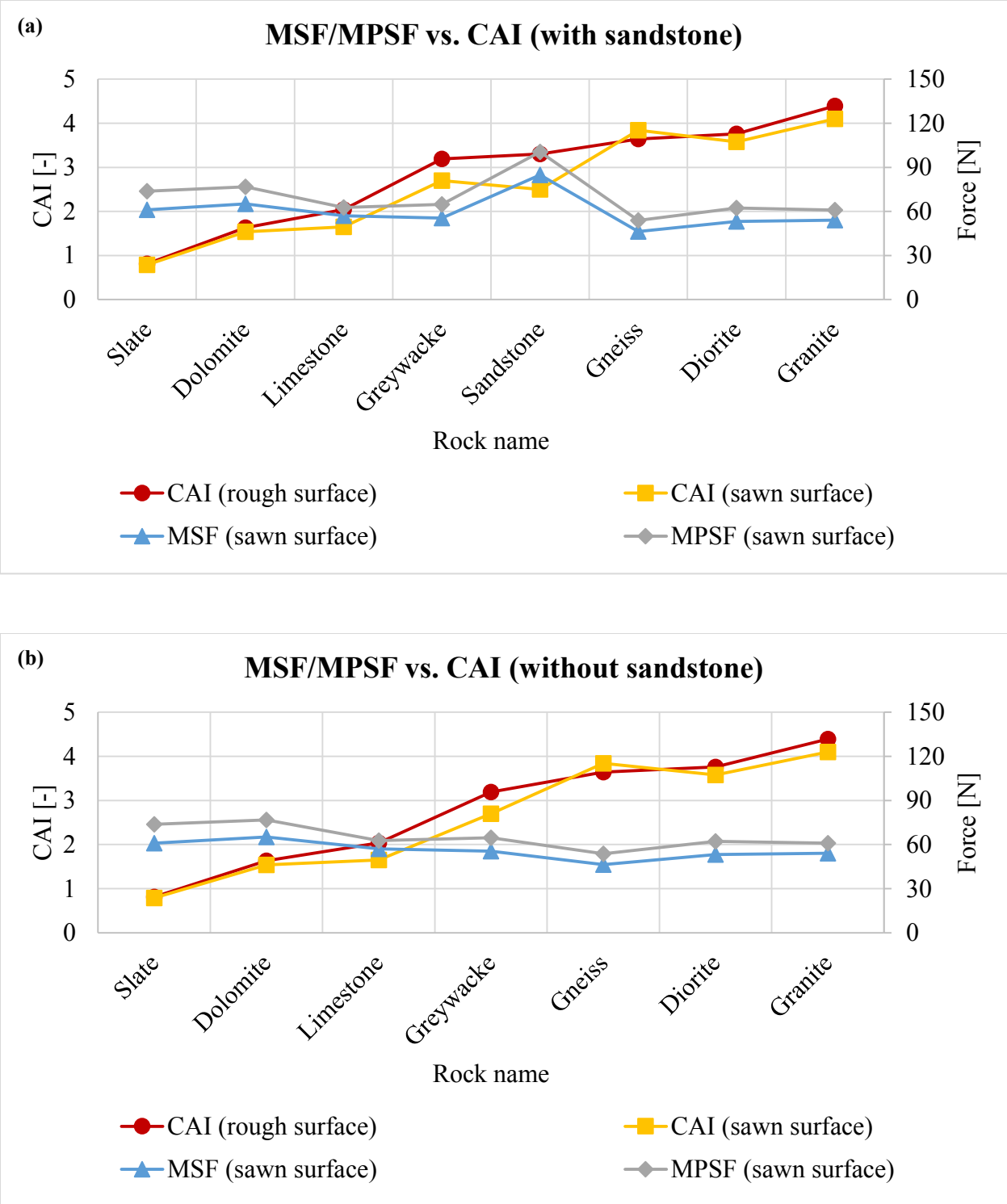

Figure 3-16 Mean and mean peak scratching force versus Cerchar abrasivity index (a) with sandstone; (b) without sandstone

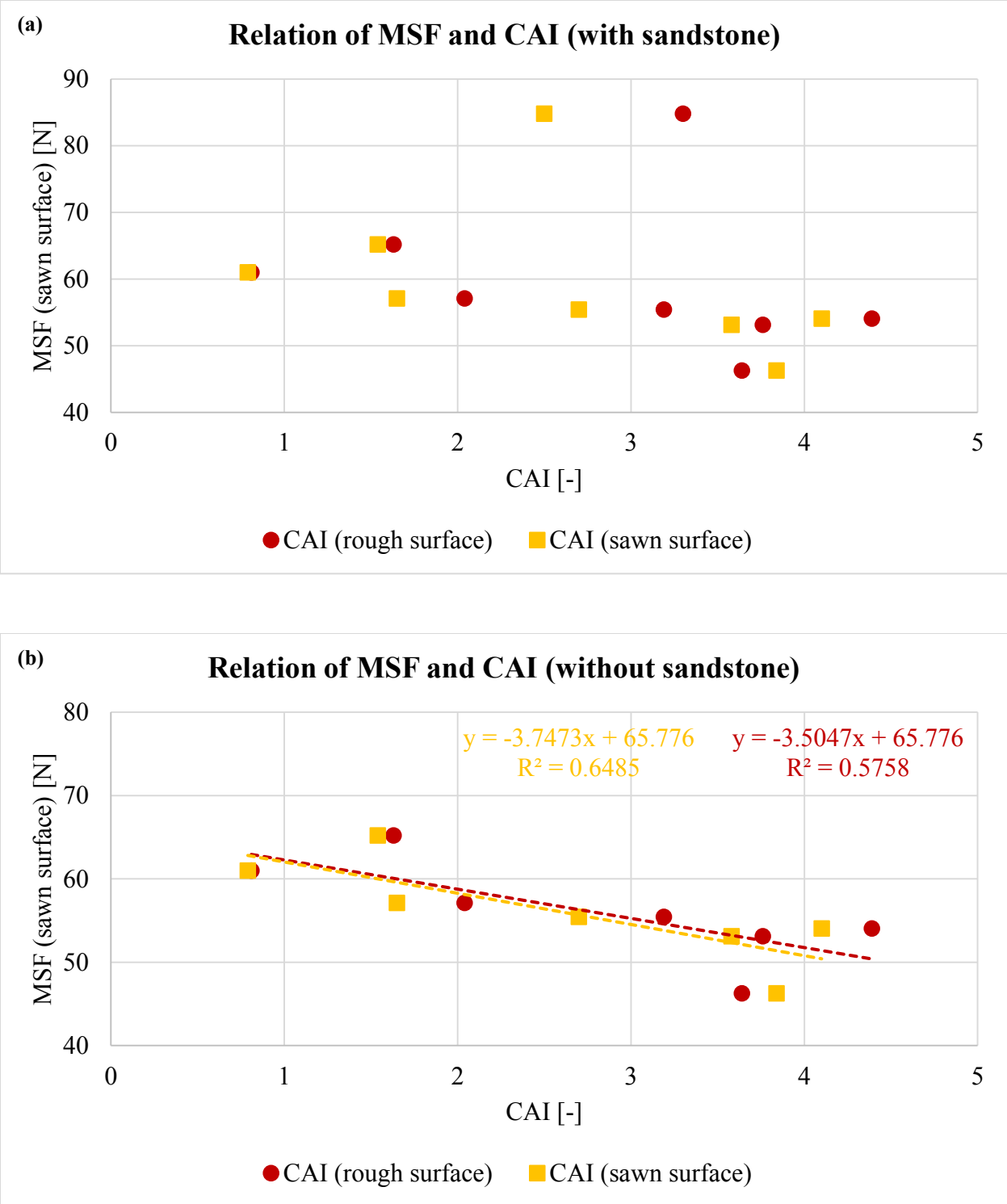

Figure 3-17 Relation of mean scratching force and Cerchar abrasivity index
(a) with sandstone; (b) without sandstone

3.3.6 Scratching energy and scratching specific energy

According to the physical definition, the applied work or consumed energy can be referred to as the area under the force-displacement curve. In respect to the Cerchar test, the scratching energy can be calculated by integrating the scratching force with the corresponding sliding distance of 10 mm. The equation is described as follows:

$$SE = \int_{0\ mm}^{10\ mm} F_s \cdot d(d_s) \tag{3-2}$$

where SE [mJ] is the scratching energy, and F_s [N] and d_s [mm] denote the scratching force and the sliding distance, respectively.

In the rock cutting process, the specific energy is defined as the work applied to cut a unit volume of rocks (Bilgin et al. 2006). The specific energy can be used to evaluate the cutting rate of a mechanical tool and it has an inverse relation to the efficiency of rock cutting. Similarly, the Cerchar scratching specific energy can be calculated by dividing the scratching energy with the material removal volume. The equation is described as follows:

$$SSE = \frac{SE}{Vm} \tag{3-3}$$

where SSE [mJ/mm^3] and SE [mJ] denote the scratching specific energy and the scratching energy, respectively, and V_m [mm^3] is the material volume removed on the rock surface. Results of SE and SSE values are summarized in Table 3-9.

Table 3-9 Scratching energy and scratching specific energy (single value)

Rock type	**SE [mJ]**	**SSE [mJ/mm^3]**
Slate **)	564.79	641.81
Dolomite	560.58	496.09
Limestone	493.92	474.92
Greywacke	490.78	876.39
Sandstone	727.41	131.23
Gneiss ***)	400.55	221.30
Diorite	458.86	955.96
Granite	474.40	687.54

**): Scratching direction is orthogonal (90°) to the foliated surface of the slate sample;

***): Scratching on the foliation surface of the gneiss sample

Similar to the MSF, the SE value is related to the CAI value of tested rocks. Seen from Figure 3-18 and Figure 3-19, no meaningful correlation is found between the SE and CAI with the soft sandstone sample, while the SE has a weak inverse linear relation to the CAI for hard rocks without sandstone.

It should be noticed that this finding does not coincide with the observation in the rock cutting test. In general, the higher the rock abrasivity, the higher the applied cutting force as well as the consumed energy. The reason may be due to that the Cerchar scratching process differs from the rock cutting process. In the rock cutting test, the depth of cut is specified with a certain value and this value is kept constant during the cutting process. In the Cerchar scratch test, however, the stylus starts from the rock surface and the depth of scratch varies in the course of the scratching process. The stylus penetrates into the rock sample due to high tip stress at the beginning of the scratching. With the abrasion of the stylus, hard rocks with high strengths forces the stylus to move to the sample surface and therefore the magnitude of applied scratching forces is reduced, as same as the consumed scratching energy. The Cerchar scratch can rather be regarded as a combined indenting-scratching process compared to the pure cutting (or scratching) process taking place in the rock cutting.

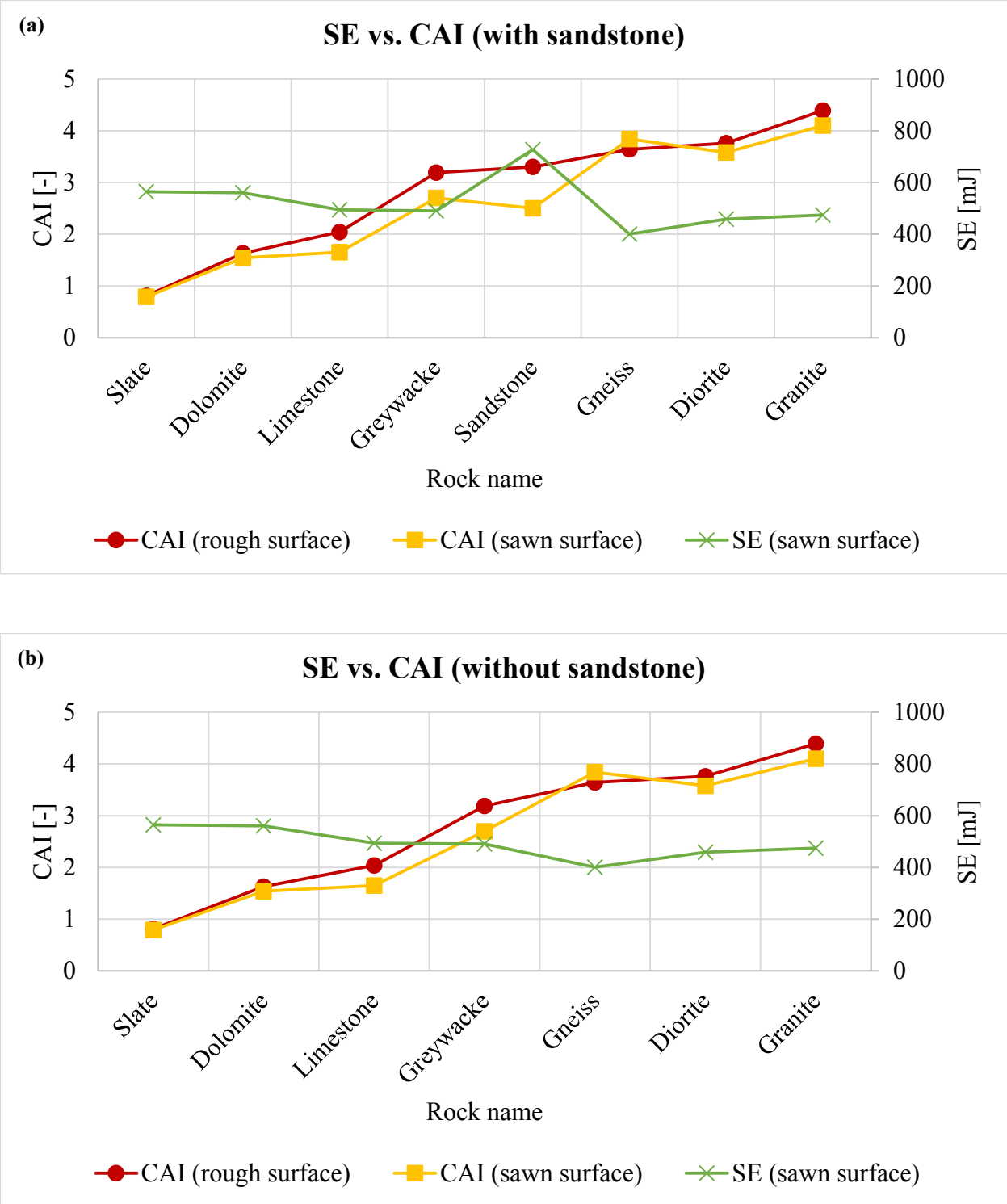

Figure 3-18 Scratching energy versus Cerchar abrasivity index
(a) with sandstone; (b) without sandstone

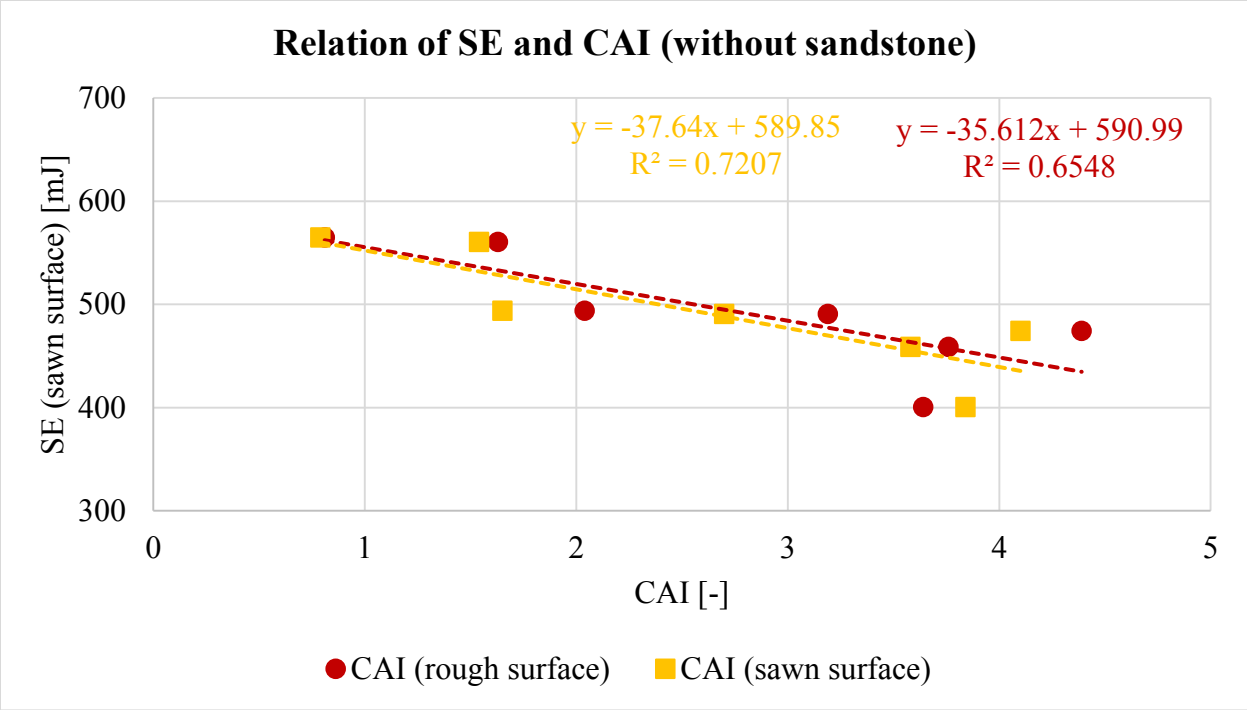

Figure 3-19 Relation of scratching energy and Cerchar abrasivity index (without sandstone)

Seen from Figure 3-20 and Figure 3-21, although it is also considered to relate the SSE to the CAI, no significant dependency is found. In addition, it should be noticed that the SSE value can be used to study the interaction of the stylus with the rock. It correlates the consumed energy, or more exactly, the applied scratching force on the stylus and the removed material on the rock surface. The efficiency of rock scratching can be evaluated according to the SSE value. Based on the available data, it can be said that the highest scratching efficiency occurs in cutting sandstone. This is reasonable because the efficiency of scratching can be linked to the ability of the stylus to damage the rock material, which is also highest in sandstone.

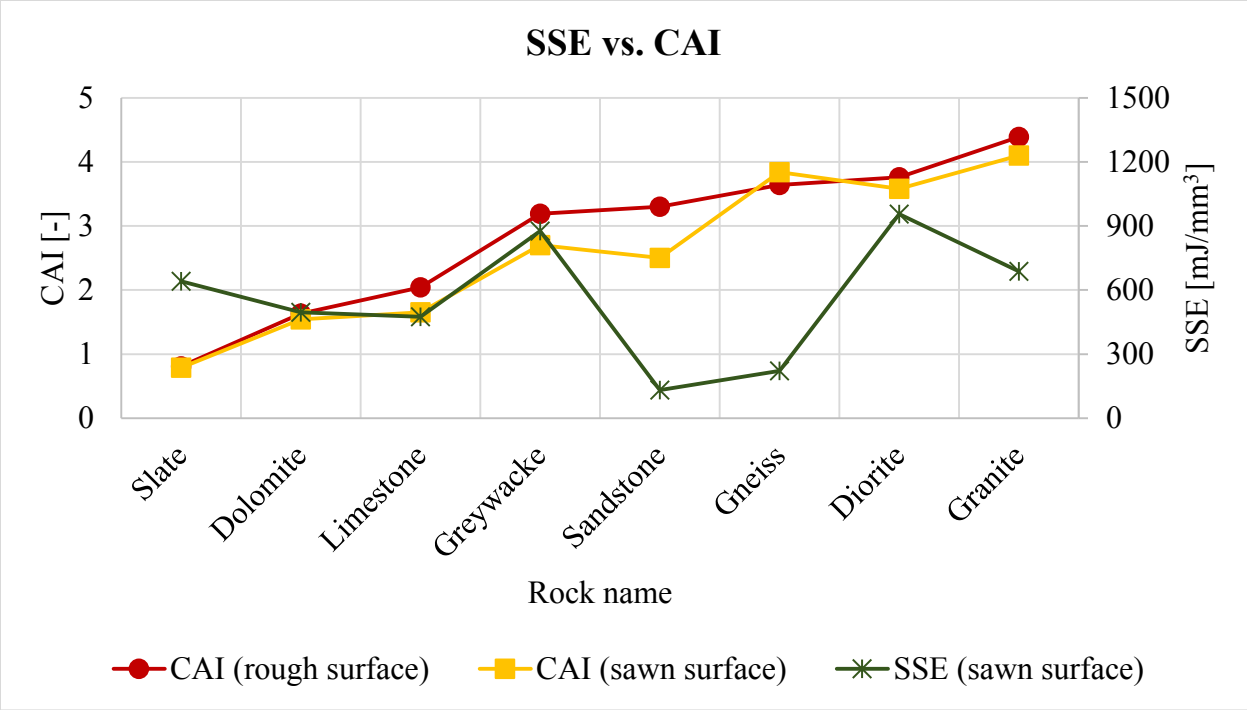

Figure 3-20 Specific scratching energy versus Cerchar abrasivity index

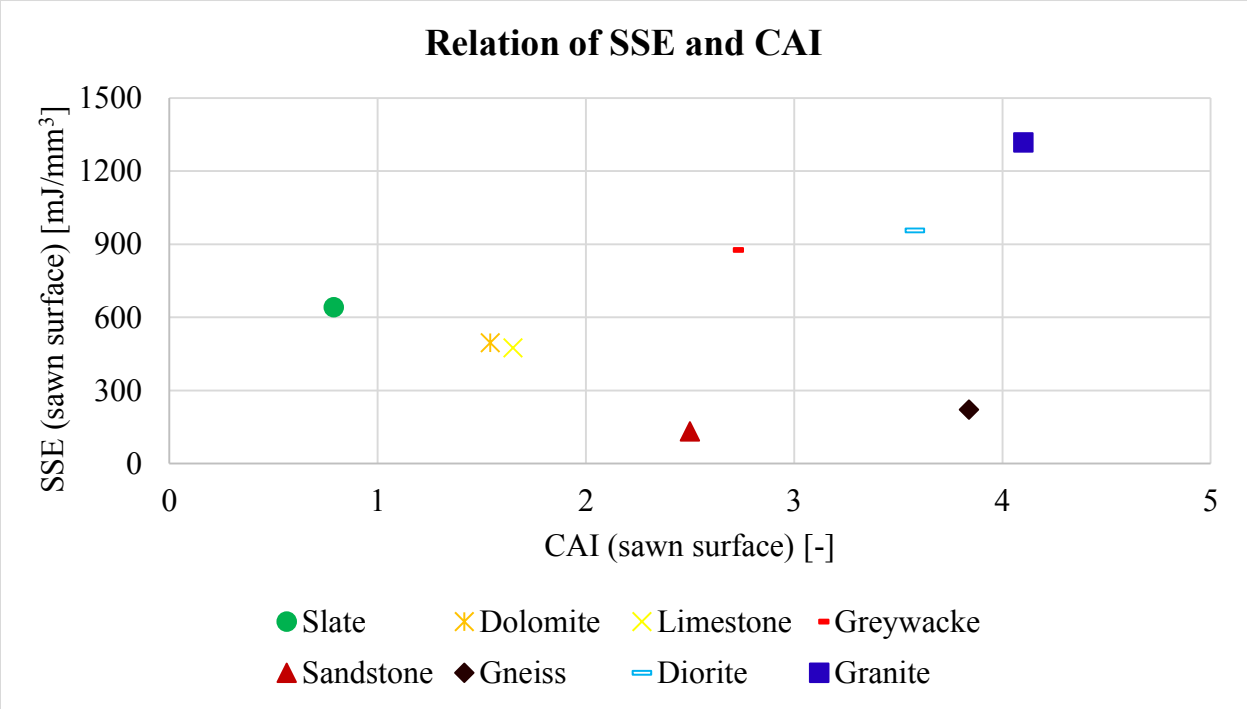

Figure 3-21 Relation of scratching specific energy and Cerchar abrasivity index

3.3.7 Cerchar abrasion ratio

In this work, a new parameter named Cerchar abrasion ratio is proposed to assess the rock abrasivity. It is defined as the volume of material removed on the rock surface divided by the volume of material abraded on the stylus tip. The equation is described as follows:

$$\mathrm{CAR} = \frac{\mathrm{Vm}}{\mathrm{Vs}} \tag{3-4}$$

where CAR [mm^3/mm^3] is the Cerchar abrasion ratio, and Vm [mm^3] and Vs [mm^3] denote the material removal volume and the tip wear volume, respectively. Results of CAR values are summarized in Table 3-10.

Table 3-10 Cerchar abrasion ratio (mean value)

Rock type	**CAR [mm^3/mm^3]**
Slate **)	13635.24
Dolomite	2363.62
Limestone	1768.65
Greywacke	217.35
Sandstone	2710.11
Gneiss ***)	244.20
Diorite	79.92
Granite	76.48

**): Scratching direction is orthogonal (90°) to the foliated surface of the slate sample;

***): Scratching on the foliation surface of the gneiss sample

Figure 3-22 shows the CAR values compared with the corresponding CAI values. In most cases CAR increases as CAI decreases. For high abrasive granite, diorite and gneiss, where the material removal volume is lower and the tip wear volume is higher, the CAR is lowest. In medium to low abrasive limestone and dolomite, since material removal volume and stylus wear volume increase or decrease simultaneously, a medium CAR value is obtained. For very low abrasive slate, where the material removal is more considerable than the tip wear, the highest CAR is derived. Most

interesting is sandstone. The CAI value for sandstone is very similar to that of greywacke and only slightly lower than that of gneiss, but the CAR value is about 1 order of magnitude higher than that of greywacke or gneiss.

Figure 3-23 shows the correlation of CAR values with the corresponding CAI values with and without soft sandstone. For both cases, CAR has an inverse exponential relation to the CAI and therefore can also be used to quantify the rock abrasivity. Since the CAR relates both, the material removal on the rock and the tip wear on the stylus, it quantifies the efficiency of a rock cutting process and might be a meaningful parameter for any design and decision making in respect to rock cutting processes in rock engineering.

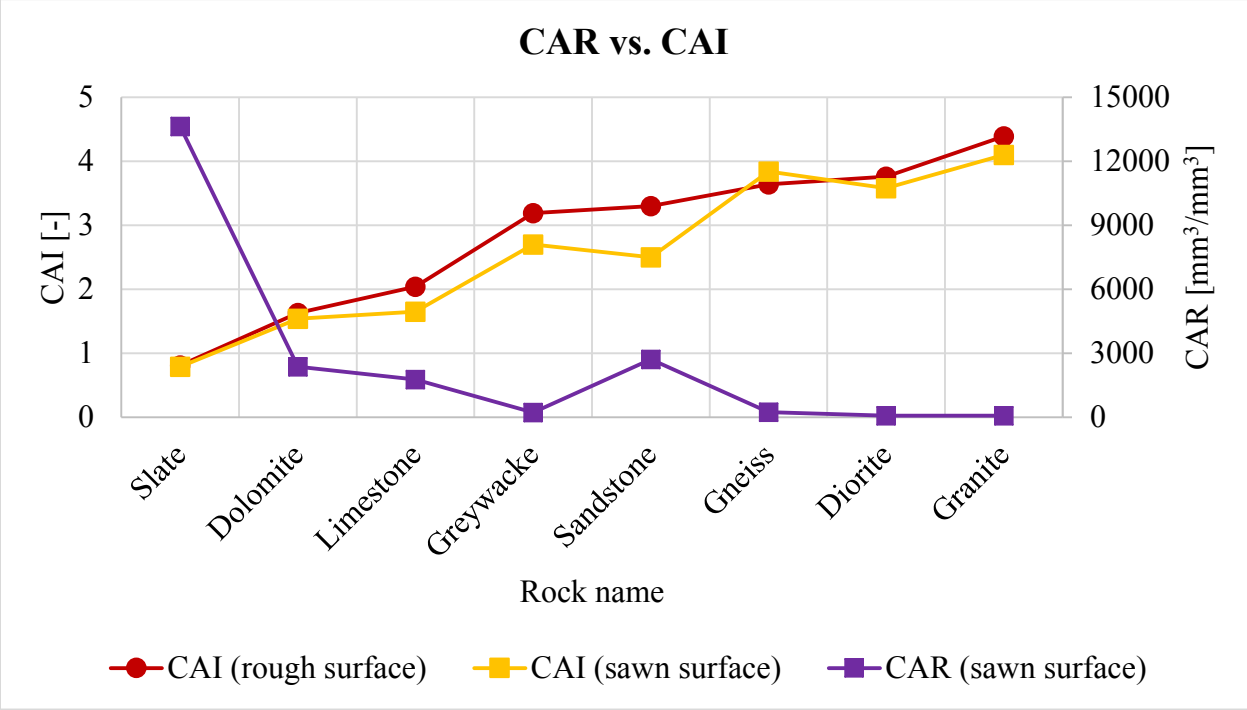

Figure 3-22 Cerchar abrasion ratio versus Cerchar abrasivity index

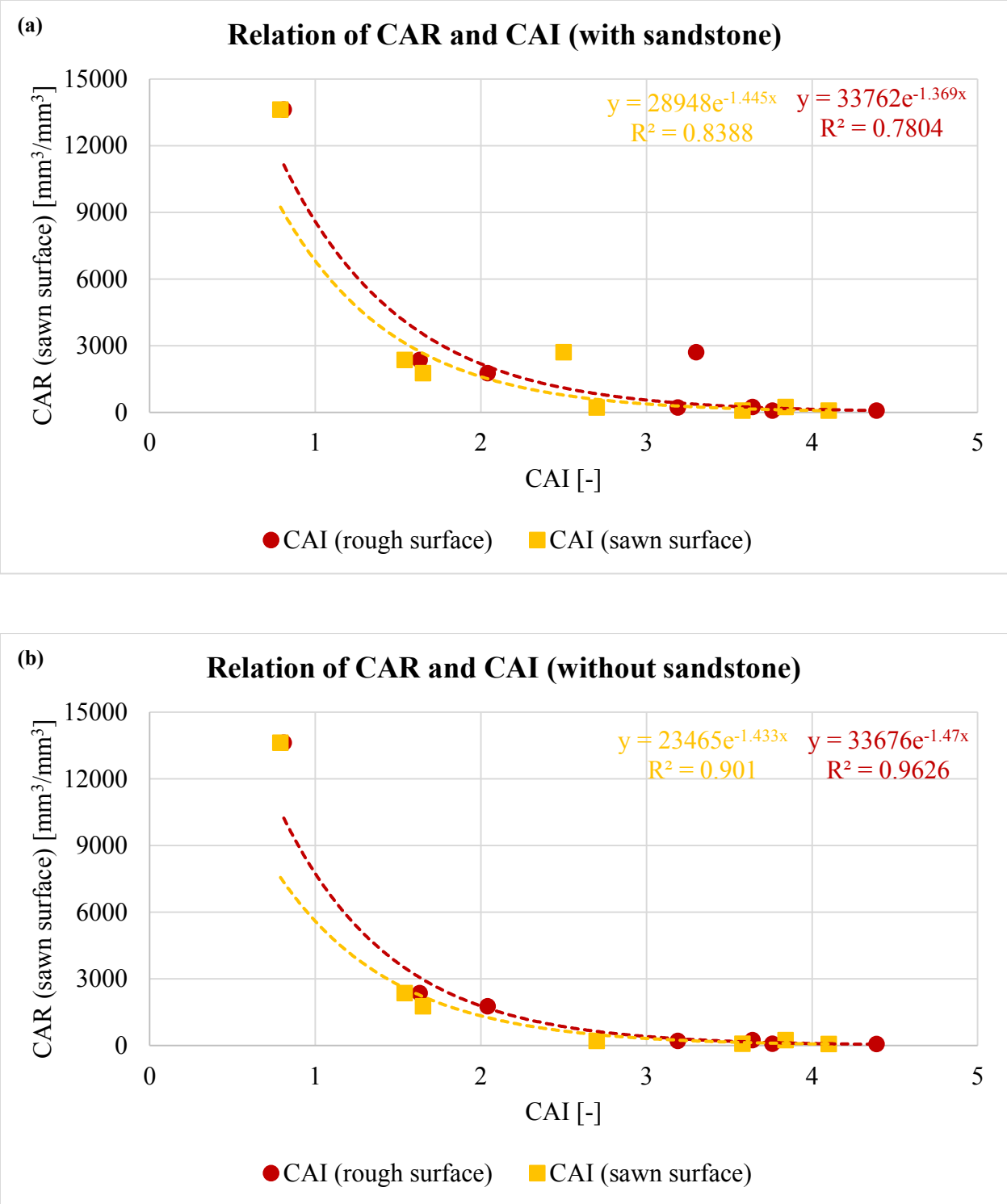

Figure 3-23 Relation of Cerchar abrasion ratio and Cerchar abrasivity index
(a) with sandstone; (b) without sandstone

3.4 Analysis of damaged surface

In this work, damaged surface formed by the stylus and produced on the sample surface is observed under a scanning electron microscope. The SEM micrographs provide a better insight into the damage mechanism and material removal process on the sample surface. Figure 3-24 and Figure 3-25 illustrate the scratch grooves on the eight tested rocks and their SEM pictures, respectively.

The surface damage on very low abrasive slate (Figures 3-24a and 3-25a) shows a clear V-shaped groove due to significant penetration of the stylus into the rock. The groove bottom is relatively smooth and the groove edges are straight. The groove interior is free of wear debris, which means that material was severed from the host rock and swept off by the stylus. The flattened debris remaining within the groove indicates that plastic deformation has occurred. Fracture by micro-cracking and lateral cracking is the major cause of material removal. Scale-like cracks can also be identified on the groove surface.

The scratch grooves on low abrasive dolomite (Figures 3-24b and 3-25b) and medium abrasive limestone (Figures 3-24c and 3-25c) have a similar shape. In comparison to slate, the groove width becomes larger, the groove depth becomes lower, and the groove edges lose their straightness in these two rocks. The soft calcite minerals are crushed into finer debris due to high stress and are removed by the stylus. Wear debris are forced to move to the sides of the groove bottom and accumulate there. Intra-granular cracking at grain size level is the dominant feature of abrasive wear.

The surface damage on high abrasive greywacke (Figures 3-24d and 3-25d) shows that the groove width is larger and the groove depth is lower. Fine-grained materials are squeezed and removed by the stylus as wear debris. It seems that plastic deformation-controlled wear is more prominent than the cracking-induced one. Grinding of material grains is dominant.

The formed groove on high abrasive sandstone (Figures 3-24e and 3-25e) is completely different from that in other rocks. The groove bottom is extremely rough and the groove edges vary, which can be related to the inherent porosity of the rock. This means that the rock porosity and especially the pore structure may affect the fracture formation. The groove interior contains a large volume

of crushed particles and ground materials, which are still bonded to the host rock. Fractured surface shows predominantly inter-granular fractures, trans-granular fractures and pull-out of grains.

Inter-foliation is a typical characteristic of metamorphic rocks. The surface damage on high abrasive gneiss (Figures 3-24f and 3-25f) shows various wear behaviors. As stylus slides on mica-rich layers, a chaotic groove is formed due to less resistance of soft mica minerals to high impressed stress. A deep groove is formed. The surface damage is predominantly induced by fractures. However, during scratching on quartz-rich layers, hard quartz minerals force the stylus to move to the sample surface. In this case, the groove depth is relatively low. The grooved surface exhibits rather a plastic deformation. This means that wear behavior is significantly affected by the rock microstructure.

The observations in high abrasive diorite (Figures 3-24g and 3-25g) show that the scratch groove depth is even lower compared to other rocks. Almost no material removal can be identified on the sample surface. The grooved surface exhibits a plastic deformation at macroscopic scale due to hard and abrasive quartz and feldspar minerals resisting against the stylus penetration. It is found that the wear induced by fracture produces larger material removal volume than that induced by plastic deformation.

In very high abrasive granite (Figures 3-24h and 3-25h), the scratch groove indicates a cracking-induced surface damage. The groove depth is low and the groove bottom is rough. It can be imagined that plastic deformation has occurred before fracture. The groove edges are sharp due to severe chipping of material along the edge. Fracture is predominately caused by trans-granular cracking and flaking. Cracks extending beneath the damage surface can be expected.

(a) Slate

(b) Dolomite

(c) Limestone

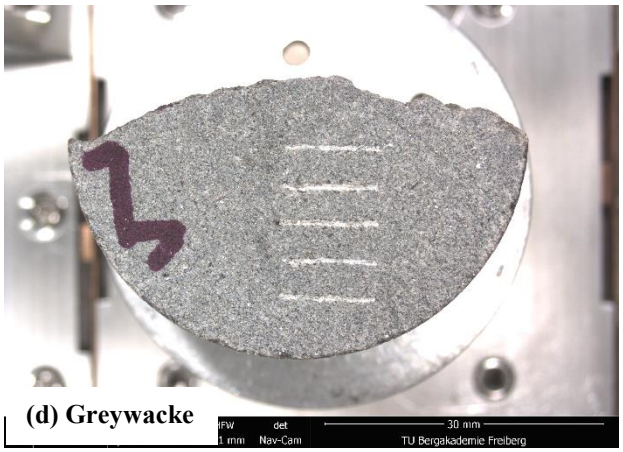

(d) Greywacke

(e) Sandstone

(f) Gneiss

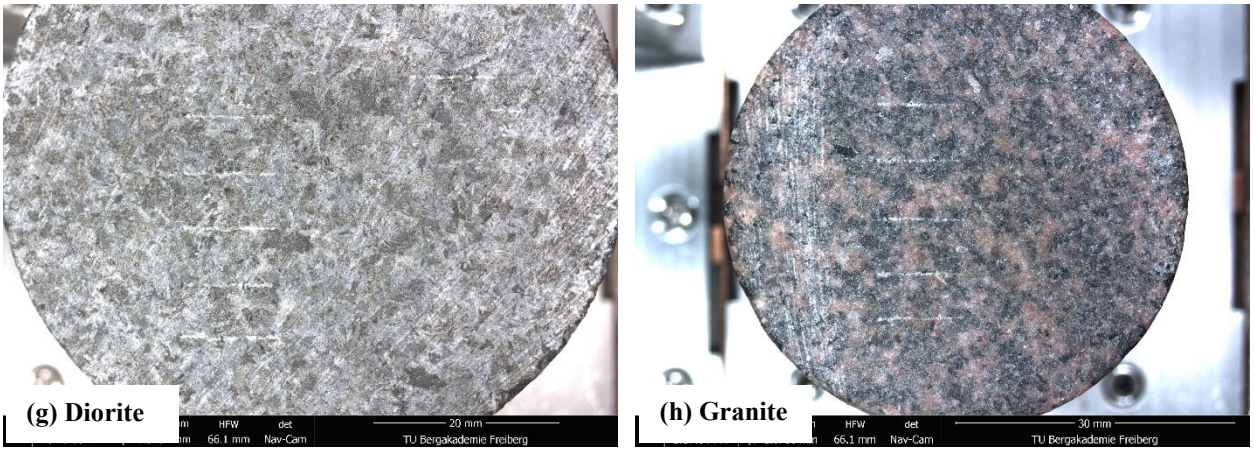

Figure 3-24 Scratches produced on (a)-(h) slate (90 degree to foliation)-dolomite-limestone-greywacke-sandstone-gneiss (on foliation surface)-diorite-granite

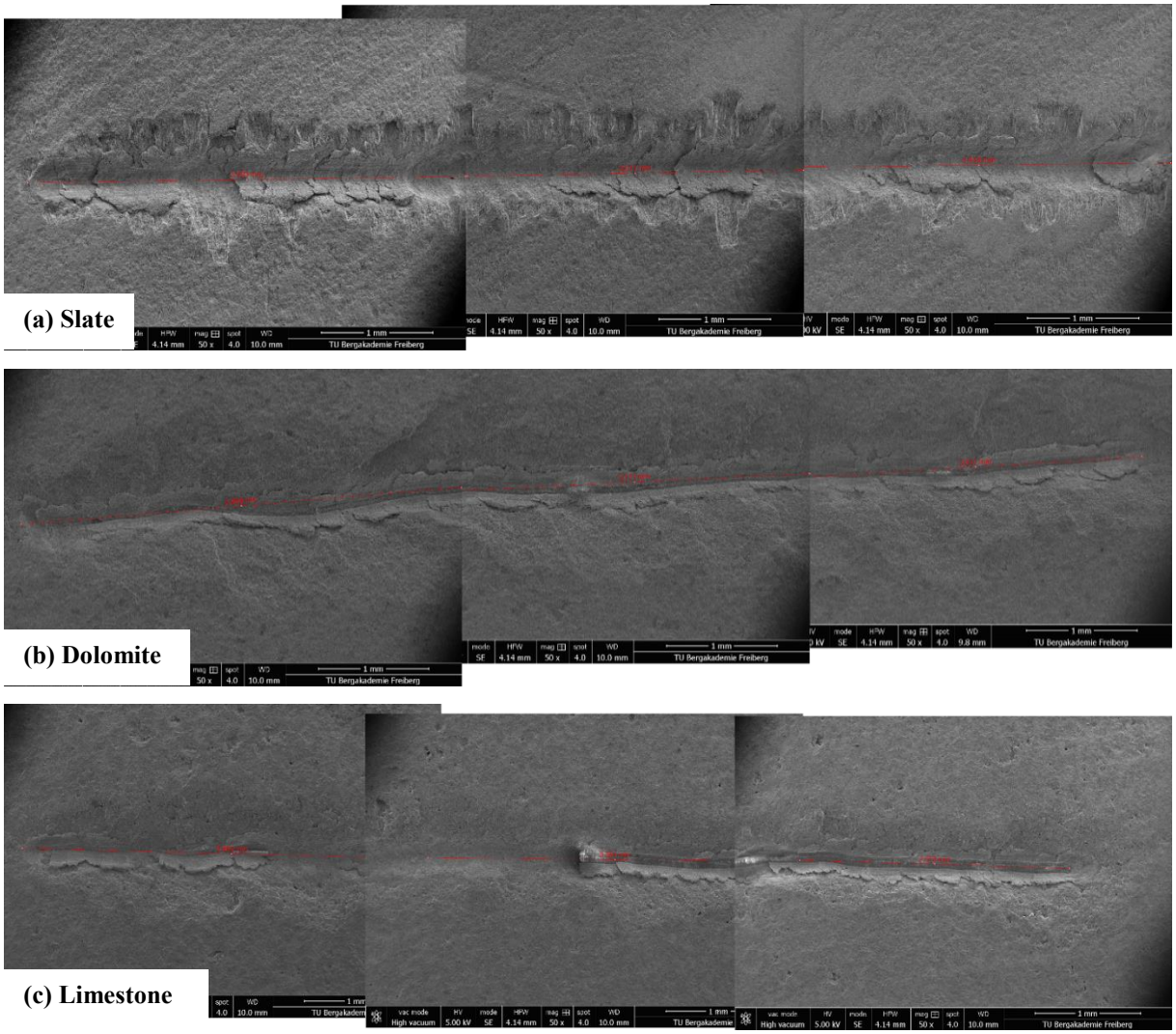

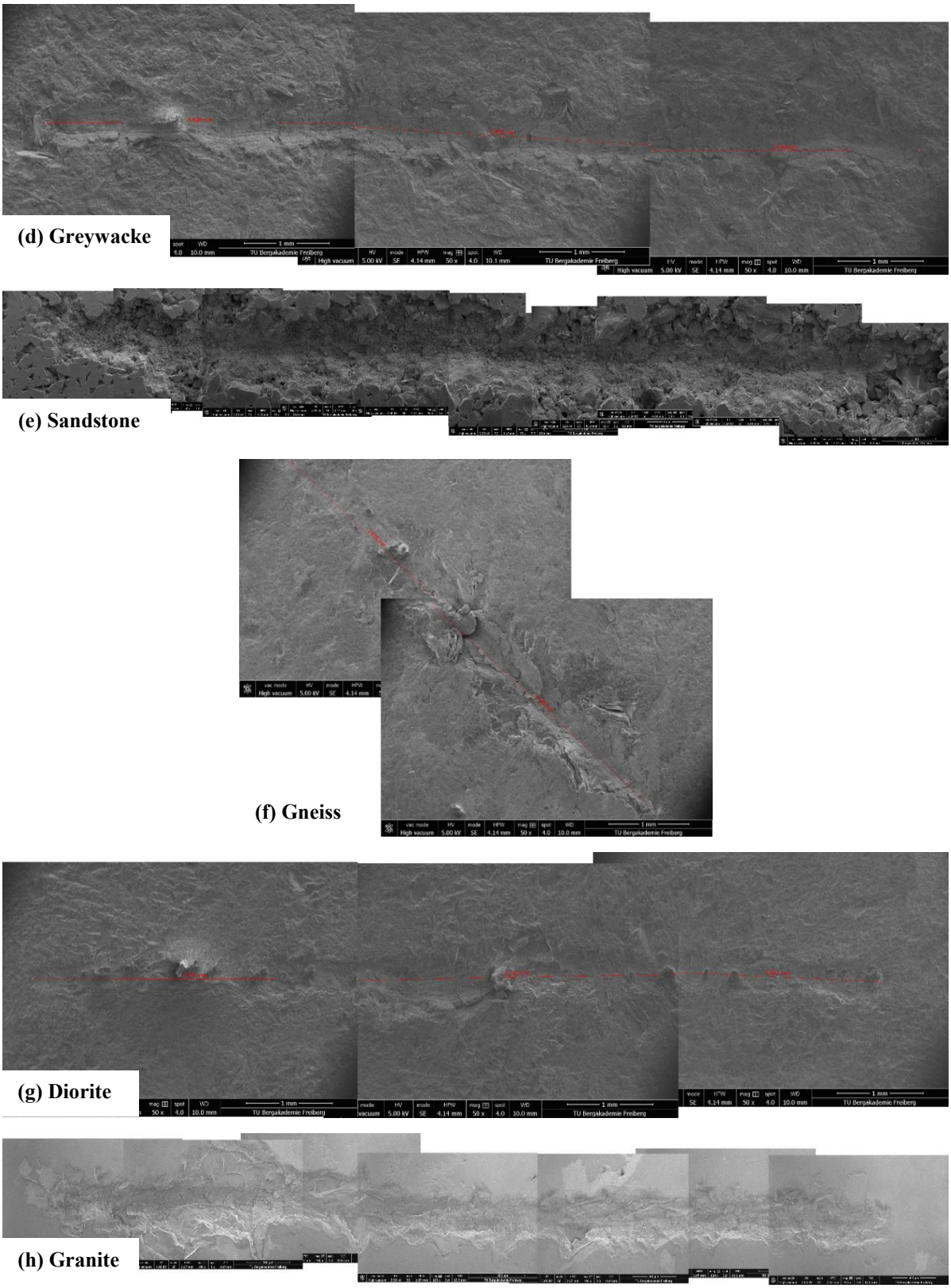

Figure 3-25 SEM micrographs of scratches on (a)-(h) slate (90 degree to foliation)-dolomite-limestone-greywacke-sandstone-gneiss (on foliation surface)-diorite-granite

3.5 Correlation of Cerchar abrasive parameters with rock intrinsic properties

In this section, three typical rocks (granite, sandstone and slate) are chosen to study the correlation of Cerchar abrasive parameters with rock intrinsic properties. Under sawn testing conditions, Cerchar tests are carried out with different testing distances (1 - 2 - 3 - 5 - 7 - 10 mm). Results of abrasive parameters for each rock sample at each testing distance are summarized in Table 3-11.

Table 3-11 Cerchar abrasive parameters (mean value) obtained at different testing distances

Rock type	**d_s [mm]**	**Wt [mm]**	**CAI [-]**	**Vs [$10^{-5}mm^3$]**	**Ds [mm]**	**Vm [mm^3]**	**SE [mJ]**	**SSE [mJ/mm^3]**	**CAR [mm^3/mm^3]**
Granite	1	0.292	2.92	325.90	0.18	0.022	9.19	417.73	6.68
	2	0.293	2.93	329.26	0.15	0.093	55.60	597.85	28.24
	3	0.373	3.72	679.31	0.13	0.437	112.51	257.46	64.33
	5	0.372	3.73	673.86	0.07	0.543	205.36	378.20	80.58
	7	0.400	4.00	837.76	0.06	0.596	316.74	531.44	71.14
	10	0.410	4.10	902.17	0.04	0.686	475.89	693.72	76.04
Sandstone	1	0.149	1.49	43.43	0.28	0.226	13.65	60.40	520.43
	2	0.167	1.67	60.94	0.4	0.483	48.63	100.68	792.53
	3	0.198	1.98	100.56	0.41	0.907	124.79	137.59	902.00
	5	0.203	2.03	108.19	0.52	1.716	282.82	164.81	1566.10
	7	0.216	2.16	132.29	0.52	3.638	451.34	124.06	2750.06
	10	0.250	2.50	204.92	0.54	5.541	729.46	131.65	2704.01
Slate **)	1	0.056	0.56	2.28	0.18	0.020	37.13	1856.5	875.99
	2	0.060	0.60	2.89	0.19	0.070	97.34	1390.57	2425.98
	3	0.061	0.61	3.04	0.21	0.239	160.33	670.84	7867.57
	5	0.064	0.64	3.50	0.24	0.347	280.76	809.11	9926.22
	7	0.065	0.65	3.65	0.21	0.568	399.16	702.75	15581.90
	10	0.079	0.79	6.42	0.29	0.882	566.08	641.81	13733.92

**): Scratching direction is orthogonal (90°) to the foliated surface of the slate sample

3.5.1 Cerchar abrasivity index and tip wear volume

Figure 3-26 shows the CAI values plotted against the corresponding testing distances for granite, sandstone and slate, respectively. It is reasonable that CAI increases with increasing sliding distance. The Cerchar abrasivity is mainly dependent on two factors: (1) the rock strength property including UCS, BTS and Young's modulus, and (2) the hard and abrasive minerals, especially the quartz mineral, within the rock. It has been proven that the quartz content and its equivalence can be referred to as an important indicator to represent the predicted abrasivity of the rock compared to the CAI that is defined as measured abrasivity. Since hard minerals like feldspar and quartz are randomly distributed within the granite sample, the stylus is abraded continuously over the entire sliding distance. A high CAI value is determined in granite due to its high strength (UCS = 212 MPa, BTS = 12.8 MPa). Although sandstone has the highest EQC value of 99% among the three tested rocks, the CAI value is lower than that in granite (EQC = 48%). This is because sandstone has a lower strength (UCS = 54 MPa, BTS = 3.7 MPa), the stylus keeps penetrating into the rock progressively in the course of the scratching process. The occurrence of abrasion is not on the tip but on the conical side of the stylus and therefore a relatively low CAI result is obtained. In slate (UCS = 165 MPa, BTS = 11.7 MPa, EQC = 35%), the inter-foliated structure with hard and abrasive quartz and soft and less abrasive mica and clay minerals can reduce the resistance of the rock against the action of the stylus. Therefore, a lower CAI value is measured.

Summarized, rock abrasivity can be considered as a combined action of rock strength, mineralogy and microstructure. Overall, the higher the rock strength and the more the abrasive minerals within the rock, the more abrasive the rock.

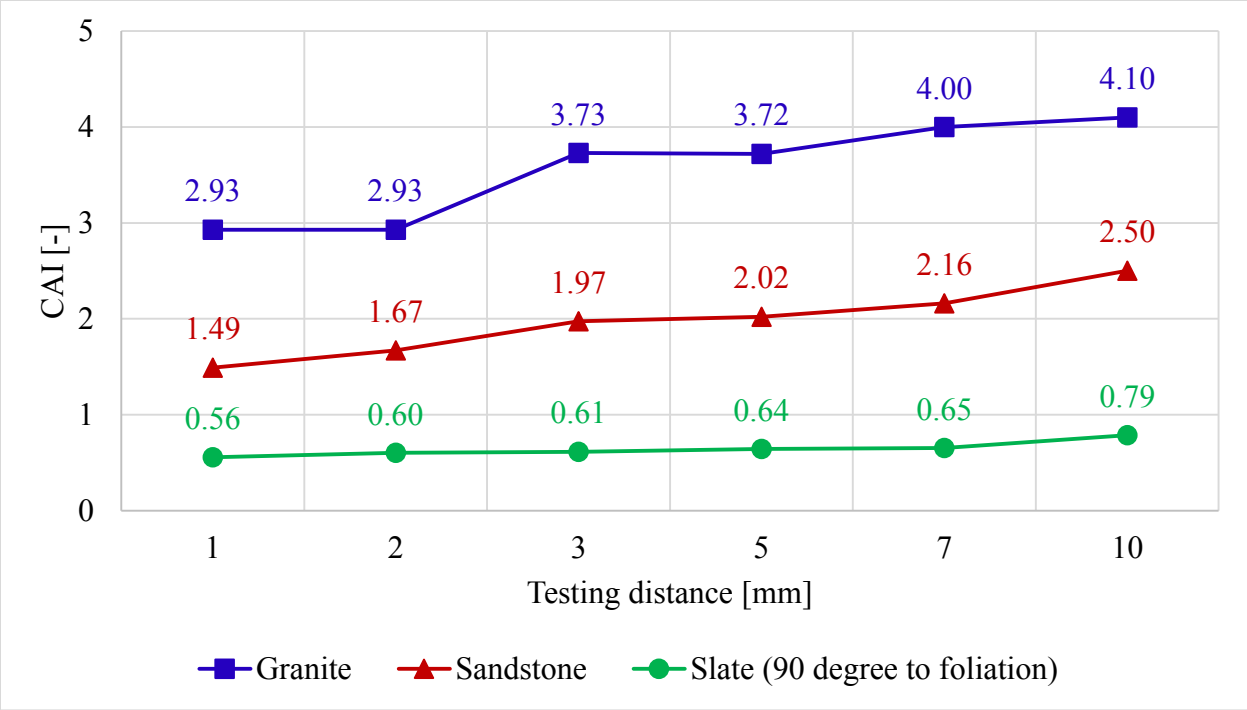

Figure 3-26 Development of Cerchar abrasivity index versus testing distance

Figure 3-27 shows the Vs values plotted against the corresponding testing distances. Similar to the CAI, the Vs is high in granite, medium in sandstone and low in slate. The reason is the same as explained for the CAI.

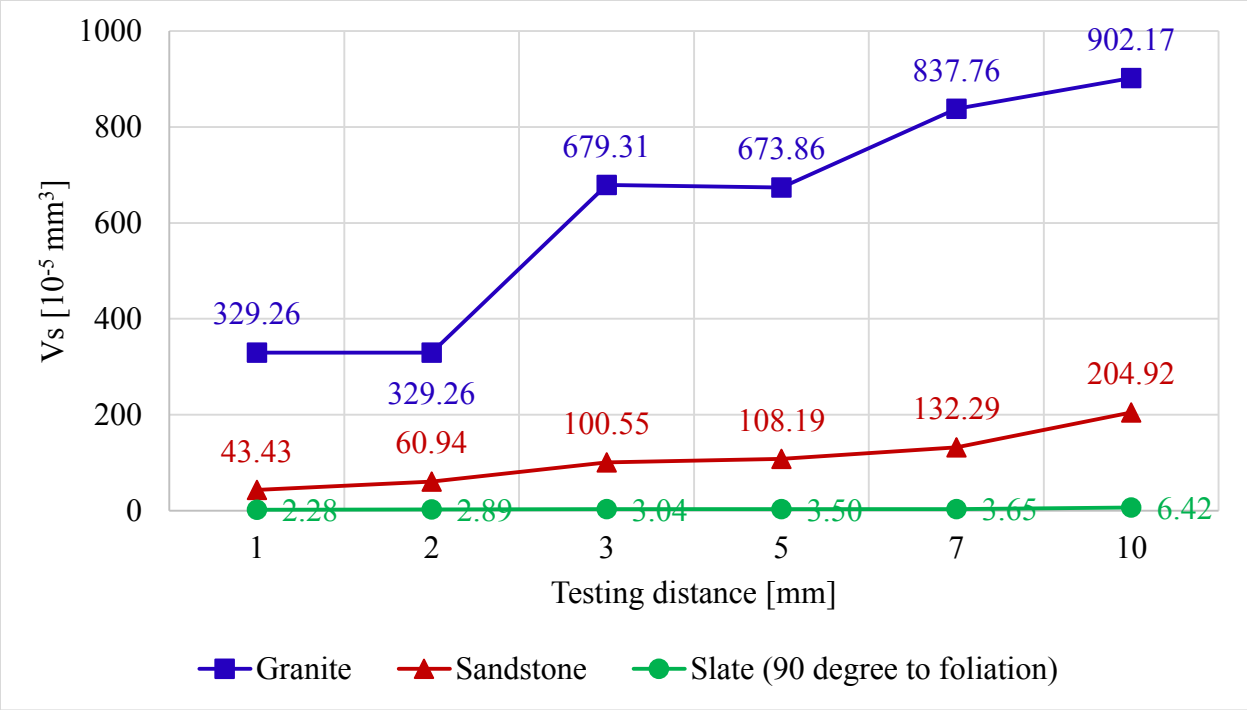

Figure 3-27 Development of tip wear volume versus testing distance

3.5.2 Depth of scratch

Figure 3-28 shows the Ds values measured at different points along the entire sliding distance in granite, sandstone and slate, respectively. It is not difficult to see that the depth curves of the three tested rocks are quite different in shape. This phenomenon can be related to the rock strength and abrasive properties. In hard and abrasive granite (UCS = 212 MPa, CAI = 4.1), the stylus penetration decreases rapidly with increased wear on the tip. When the produced stress is no longer greater than the rock strength, the stylus is forced to move to the sample surface. The penetration depth decreases progressively for the remaining sliding distance. In softer but abrasive sandstone (UCS = 54 MPa, CAI = 2.5), the stylus penetrates deeper into the rock at the beginning of the test and keeps indenting the rock during the scratching due to low strength of the rock. The penetration depth increases drastically over the entire sliding distance due to high abrasion of the stylus. In hard but lower abrasive slate (UCS = 165 MPa, CAI = 0.8), the increment of the tip wear is slower due to less abrasive minerals in slate (AMC = 4) than in granite (AMC = 6) and sandstone (AMC = 7). A slower decrement of the stress on the stylus is caused in the course of the scratching process. The stylus keeps moving within the rock and the penetration rate is relatively slow.

It should be noticed that the drastic fluctuation of scratch depths from about 5 mm to 9 mm in sandstone sample might not be due to the errors of measurement, it could be related to the pore structure of the rock. The greater depth values indicate that the stylus is encountered with holes or pores between compact mineral grains in scratching sandstone. In addition, a literature review shows that the depth of cut (or scratch) is the most significant factor affecting the cutting (or scratching) force. This phenomenon is also confirmed by the fact that a higher scratching force is required on sandstone (MSF = 84 N) due to a deeper cutting compared to slate (MSF = 61 N) and granite (MSF = 54 N).

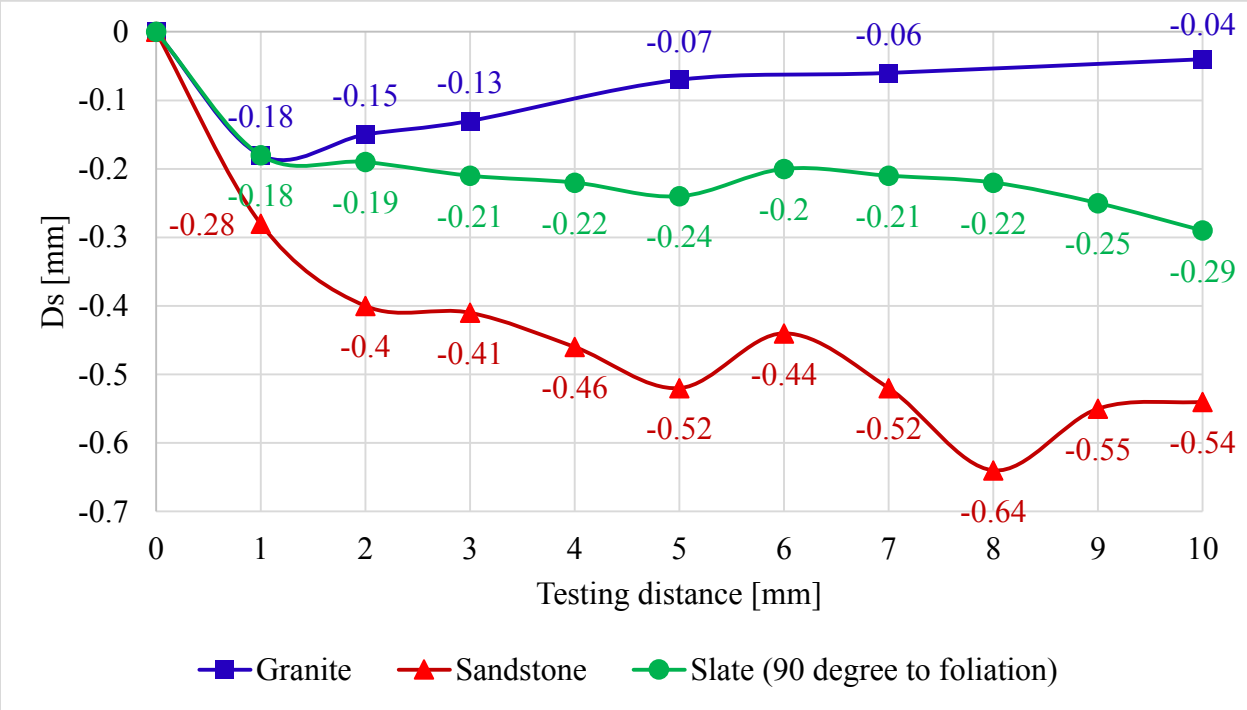

Figure 3-28 Development of depth of scratch versus testing distance

3.5.3 Material removal volume

Figure 3-29 shows the Vm values related to the testing distances for the three tested rocks. It is obvious that the most material is removed in cutting sandstone. The material removal is more or less the same in granite and slate. By observing the damaged surface on the tested rocks, it is found that the grain size and shape within the rock may affect the fracture behavior and therefore the material removal. In addition, pore structure in the rock and rock strength are further factors affecting the severity of the sample surface as well as the material removal. The porosity in sandstone (Ø = 20.8%) is greater than that in slate (Ø = 6.1%) and granite (Ø = 4.1%). It can be said that less material is removed in compact and hard rocks like slate and granite than that in porous and relatively soft rocks like sandstone.

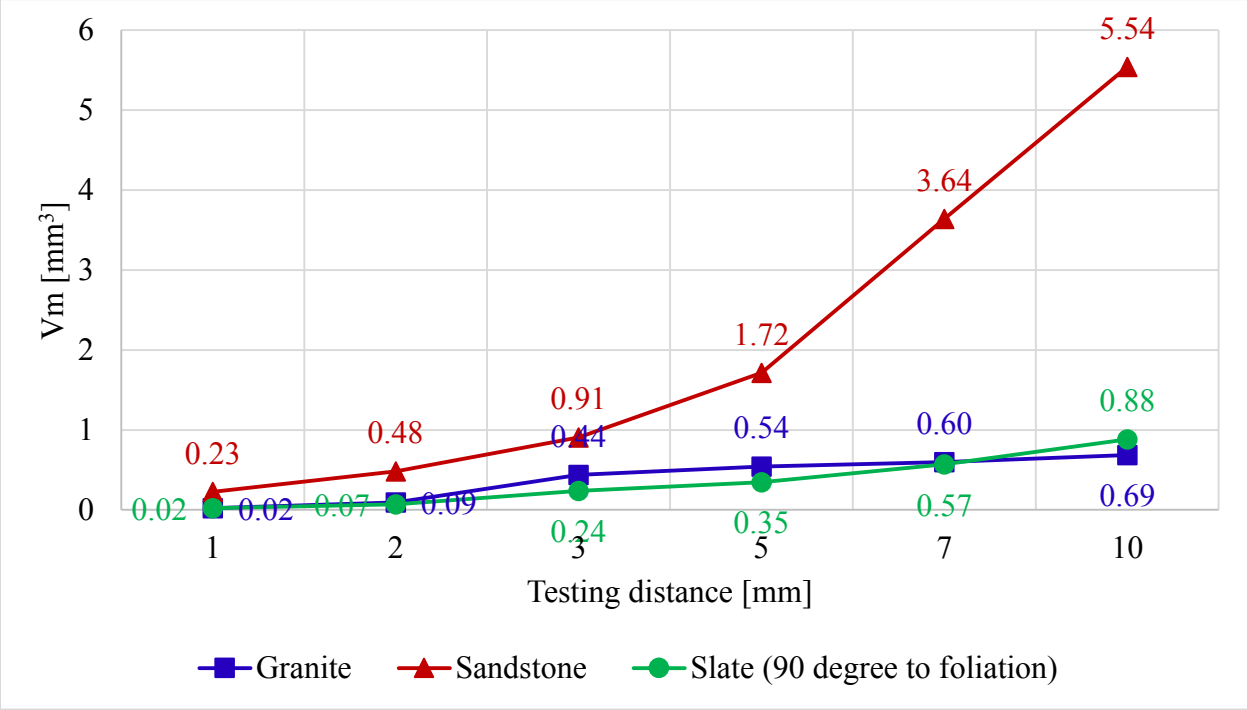

Figure 3-29 Development of material removal volume versus testing distance

3.5.4 Scratching energy

Figure 3-30 shows the SE values correlated with the corresponding sliding distances. Although sandstone has the lowest strength among the three tested rocks, the consumed scratching energy is the highest in it. This can be related to the constituent minerals within the rock, especially the quartz mineral and its size, shape and content. In general, quartz needs a higher energy to be fractured compared to other minerals. Moreover, the larger the quartz grain, the lower sphericity of an individual quartz grain and the higher the quartz content, the more energy is required to scratch over it or to cut it off. Obviously, sandstone has the largest amount of quartz minerals (QC = 99%), followed by slate (QC = 31%) and granite (QC = 28%). This in fact means that, besides the rock strength, the consumed scratching energy in rock cutting is also dependent on the rock abrasivity.

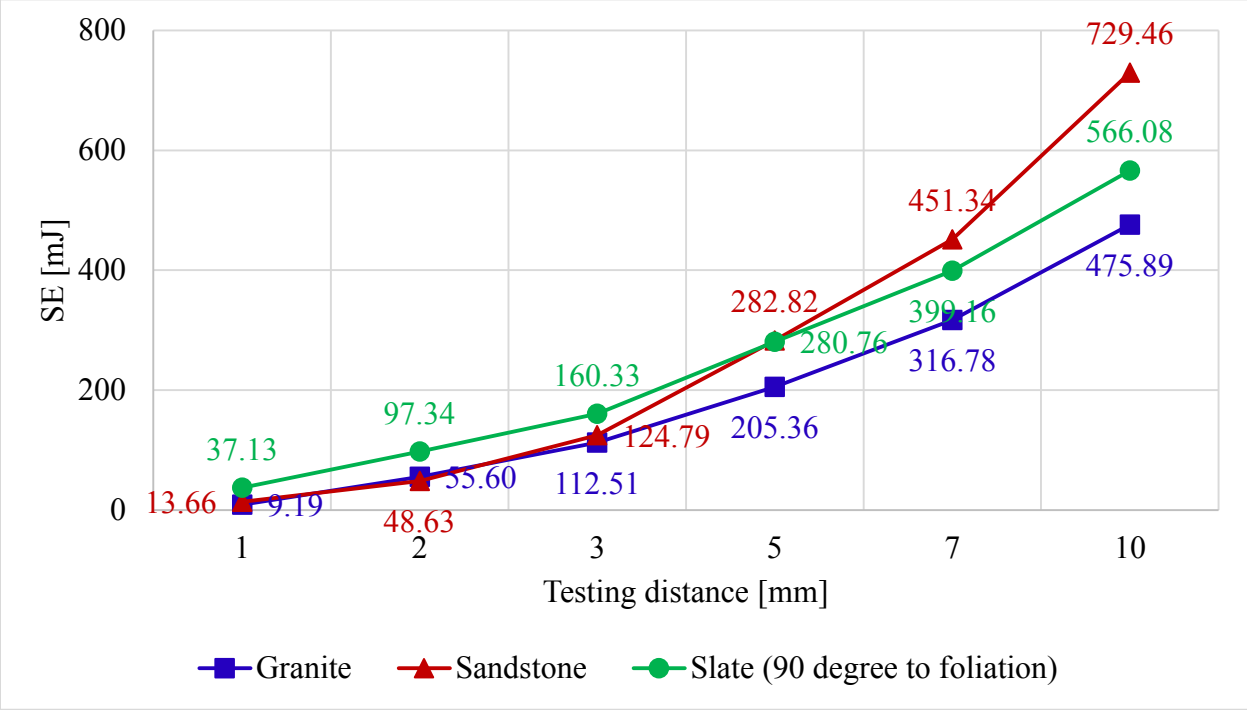

Figure 3-30 Development of scratching energy versus testing distance

3.5.5 Scratching specific energy

In Figure 3-31, the SSE values are plotted against the sliding distances. Result shows that the SSE value is the lowest in sandstone, followed by granite and slate. This is reasonable because the deepest penetration is reached and therefore the largest amount of materials is removed in sandstone due to its low strength and high porosity.

It is found that the development of SSE for the three tested rocks is quite different. The SSE in sandstone shows a more or less stable development with the sliding distance. This is due to the progressive and simultaneous increase in energy consumption and material removal. The SSE in slate indicates a decreasing trend with increasing sliding distance, because the increment of removed material volume is relatively stronger than that of consumed scratching energy. In granite, the SSE value seems to be increasing when the sliding distance increases. This phenomenon can be attributed to the fact that the penetration depth is extremely low due to high strength of the granite sample. In this case, the increment of the material removal is much slower than that of the consumed energy.

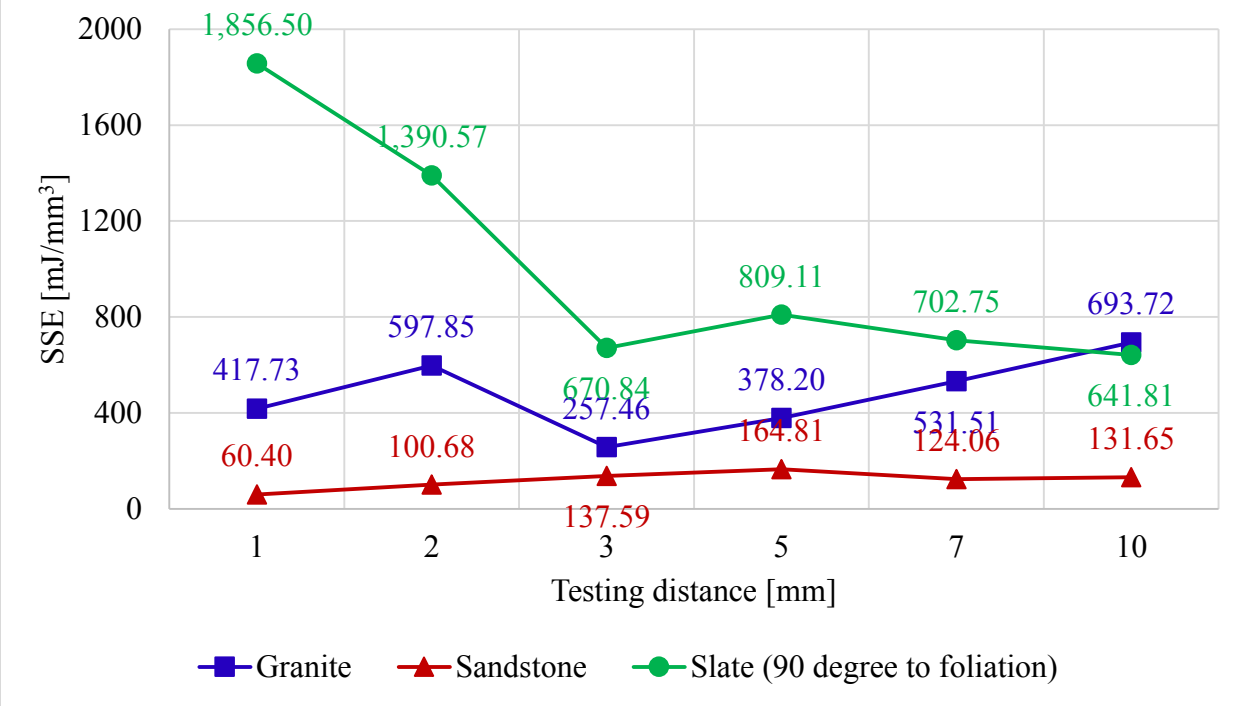

Figure 3-31 Development of scratching specific energy versus testing distance

3.5.6 Cerchar abrasion ratio

Figure 3-32 shows the CAR values related to the sliding distances. For all three rock samples, power relationships between the CAR and sliding distance are found. However, the growth rates of the CAR are different: (1) the CAR rises very slowly in the high abrasive granite, (2) the ratio experiences a moderate growth in the medium abrasive sandstone, and (3) a high growth rate is obtained for the low abrasive slate.

It has been found that the CAI value must be associated with other rock mechanical parameters to predict the tool consumption and effectivity of rock cutting or drilling. The CAR (defined as m^3 materials removed per m^3 abraded tip on a pick) can offer a possibility to estimate the wear rate (defined as amounts of bit, pick or disc worn per m^3 removed materials) or lifetime (defined as m^3 material removed per bit, pick or disc) for cutting or drilling heads. By comparing the three tested rocks, it can be concluded that the stylus has a less wear rate or a longer lifetime in scratching or cutting slate than that in sandstone and granite. Obviously, a formula, which relates the CAR to the lifetime, should be derived by testing more rocks in further studies.

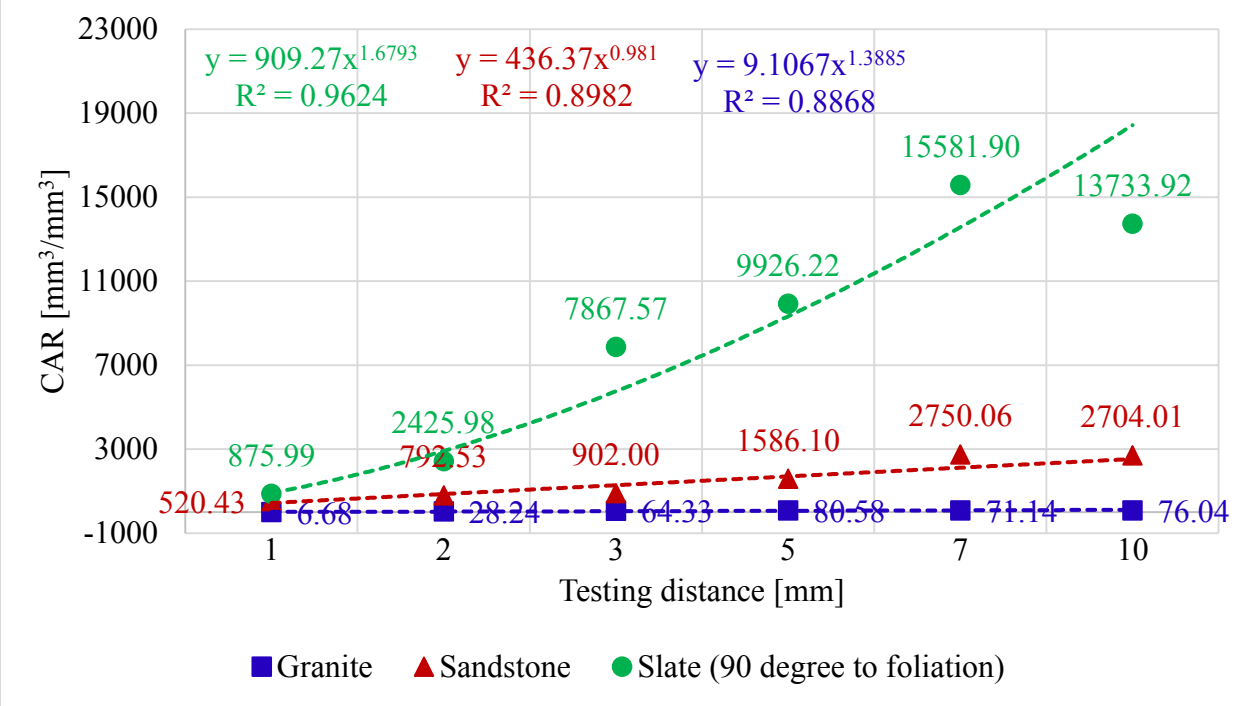

Figure 3-32 Development of Cerchar abrasion ratio versus testing distance

3.6 Influence of test conditions on Cerchar abrasivity index

In this section, three typical rocks (granite, sandstone and slate) are tested to investigate the influence of some dominant testing condition-based factors, such as surface condition, sliding distance and scratching velocity, on the CAI due to their sensitive impact on the test result. In addition, the influence of rock anisotropy on the Cerchar index is studied based on the two intact foliated metamorphic rocks of slate and gneiss.

3.6.1 Surface condition

Experiences have shown that no flat surface can be produced using a hammer to split hard and/or inhomogeneous rocks. A diamond saw is usually used to split such rocks. To investigate the influence of surface condition on the CAI value, Cerchar tests are carried out on granite, sandstone and slate with rough, sawn and polished surfaces, respectively. The testing procedure is in accordance with Alber et al. (2014). Figure 3-33 illustrates the scratches produced on the three tested rock samples with different surface conditions. Results are summarized in Table 3-12.

By comparing the three surface conditions with one another (see Figure 3-34), it is found that the surface roughness can affect the CAI result. Especially in hard rocks like granite, the surface roughness plays a key role. This can be attributed to the strength property of the rock. By scratching a granite with high strength, the stylus is forced to move on the rock surface rather than penetrating into it. In this case, when the sample surface is rough, the stylus needs to follow an irregular-shaped track and therefore a higher CAI value is caused. The effect of surface condition in hard slate is not obvious due to low abrasive constituent minerals and their homogeneous distributions within the rock. Soft rocks like sandstone with low strength cannot resist the penetration of the stylus. As the stylus is moving into the rock, the abrasion occurs not on the tip but mainly on the conical sides of the stylus. In this case, amount of abrasive minerals or quartz equivalences within the rocks has a stronger influence on rock abrasivity.


(a-1)
Mittweidaer Granite
(a-2)
Mittweidaer Granite
(b-1)
Postaer Sandstone
(b-2)
Postaer Sandstone

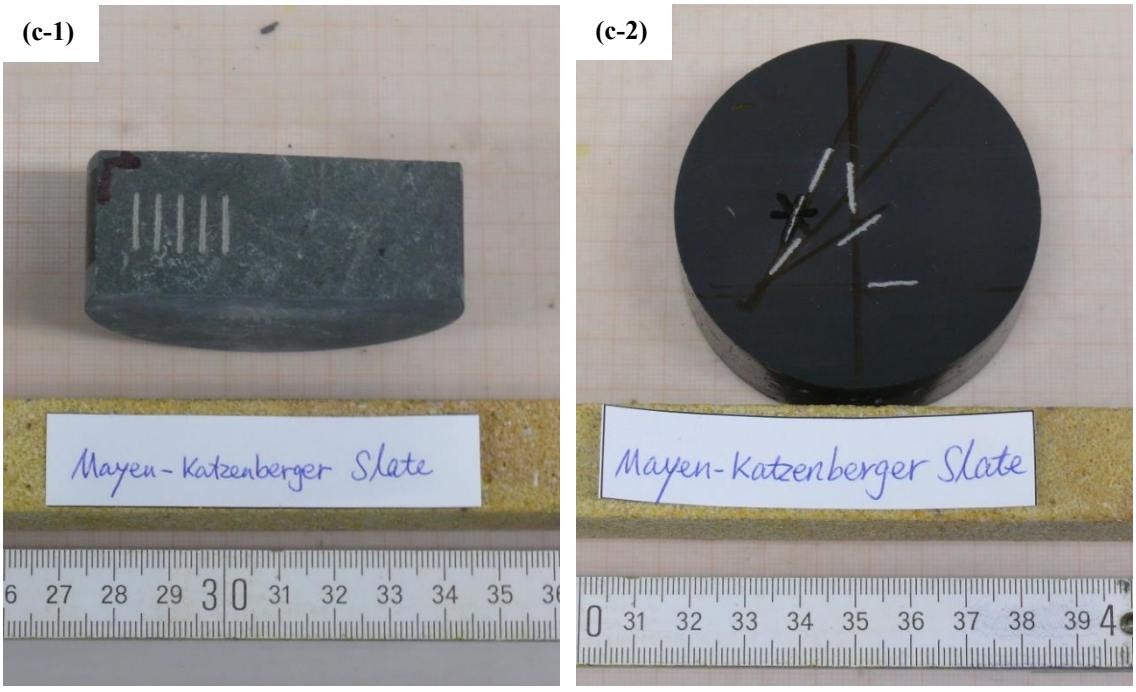

Figure 3-33 Exemplary: scratches produced on (a) granite; (b) sandstone; (c) slate with different surface conditions (for example: (a-1) granite sample with sawn and rough surfaces; (a-2) granite sample with polished surface; (b-1) sandstone sample with rough surface; (b-2) sandstone sample with polished surface; (c-1) slate sample with rough surface and scratching of the stylus on the foliation surface of the sample; (c-2) slate sample with polished surface and scratching direction with different angles to the foliated surface of the sample)

Table 3-12 Cerchar abrasivity index measured under different surface conditions (mean value ± standard deviation)

Rock type	**Surface conditions**		
	Rough surface	**Sawn surface**	**Polished surface**
Granite	4.39 ± 1.00	4.10 ± 0.45	2.71 ± 0.44
Sandstone	3.30 ± 1.38	2.50 ± 0.66	2.26 ± 0.30
Slate **)	0.81 ± 0.30	0.79 ± 0.44	0.91 ± 0.16

**): Scratching direction is orthogonal (90°) to the foliated surface of the slate sample

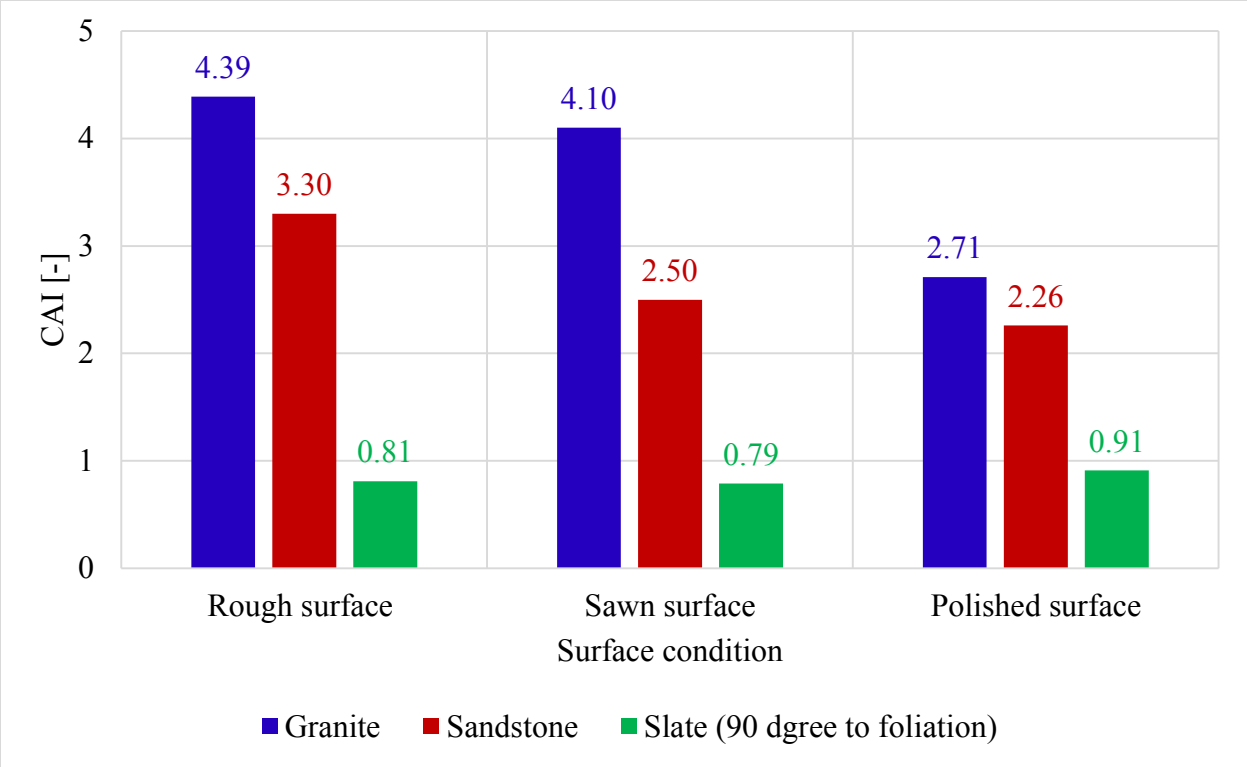

Figure 3-34 Variation of Cerchar abrasivity index for different surface conditions

In Figure 3-35, by monitoring the applied scratching forces on the granite sample with three different surface conditions, it is remarkable that the force value falls down suddenly and strongly within the last few millimeters of sliding in the polished granite. The so-called 'skating effect' occurs due to high strength of granite and low friction on the smooth surface. This phenomenon can also be observed in scratching some crystalline rocks like quartzite and marble. This indicates that the CAI value measured on hard rocks with polished surfaces is inaccurate and therefore unsuitable for determining the Cerchar abrasivity.

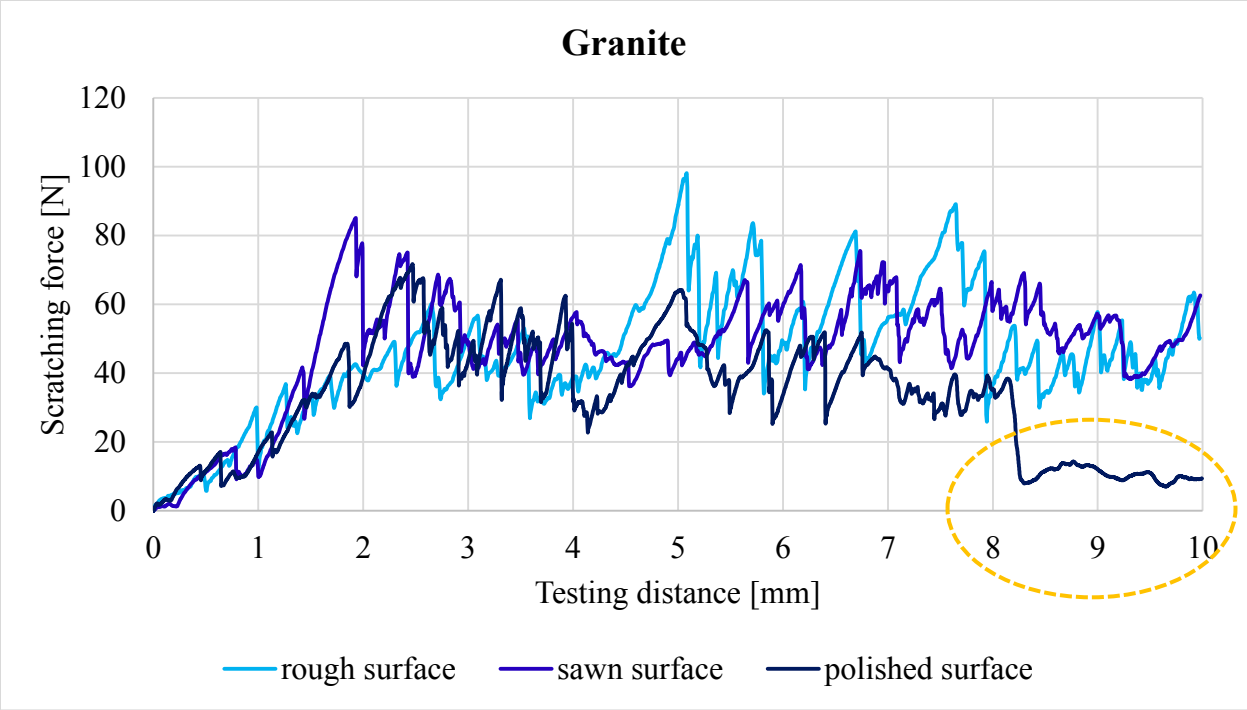

Figure 3-35 Development of scratching force for granite under different surface conditions

In addition, the CAI values measured on the eight tested rocks with both, rough and sawn surfaces are compared in Figure 3-36. Regression analysis is conducted to relate the two surface conditions. Based on the available data, a linear relationship is derived:

$$\mathrm{CAI}_{\mathrm{rough}} = 0.99 \cdot \mathrm{CAI}_{\mathrm{sawn}} + 0.3 \qquad (3\text{-}5)$$

where $\mathrm{CAI}_{\mathrm{rough}}$ [-] and $\mathrm{CAI}_{\mathrm{sawn}}$ [-] denote the Cerchar abrasivity index measured on rough and sawn rock surfaces, respectively. The CAI of rough rock surfaces is about 0.3 times higher than that of sawn rock surfaces.

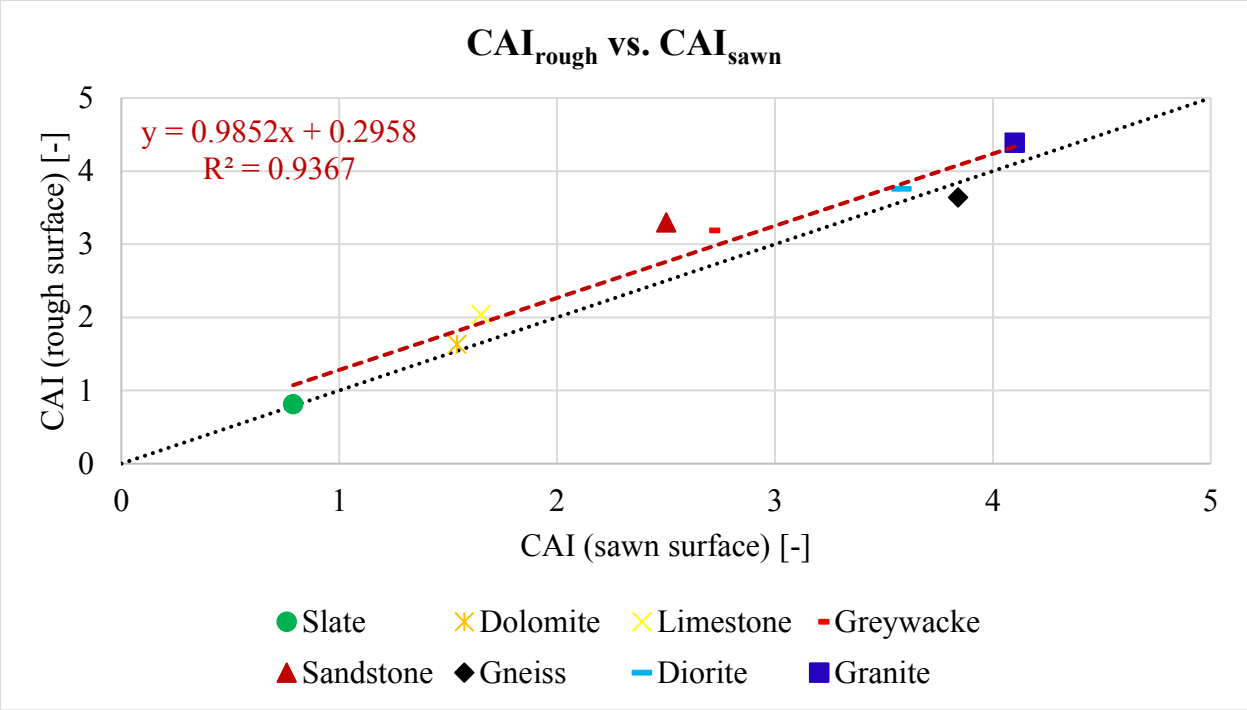

Figure 3-36 Relation of Cerchar abrasivity index under rough and sawn surface conditions

The CAI values are related to the rock strengths (i.e. UCS and BTS) to investigate their dependency. Seen from Figure 3-37a, no meaningful correlation is found between the CAI and UCS for all tested rock samples, while a linear relationship can be identified for abrasive rocks. This indicates that the CAI may be correlated to the UCS for abrasive rocks, but not for less abrasive rocks. In Figure 3-37b, a similar result is found between the CAI and BTS for abrasive rocks with sawn surface conditions. Although there are less available data, rock strength has an influence on the rock abrasivity. Overall, the higher the rock strength, the higher the rock abrasivity.

Similarly, Figure 3-38 shows the correlation of the CAI with the EQC and AMC of four tested rocks (granite, sandstone, slate and gneiss). The dependency is also not significant due to less available data. Despite that, it can be said that the more the amount of quartz equivalences or abrasive minerals within the rock, the more abrasive the rock.

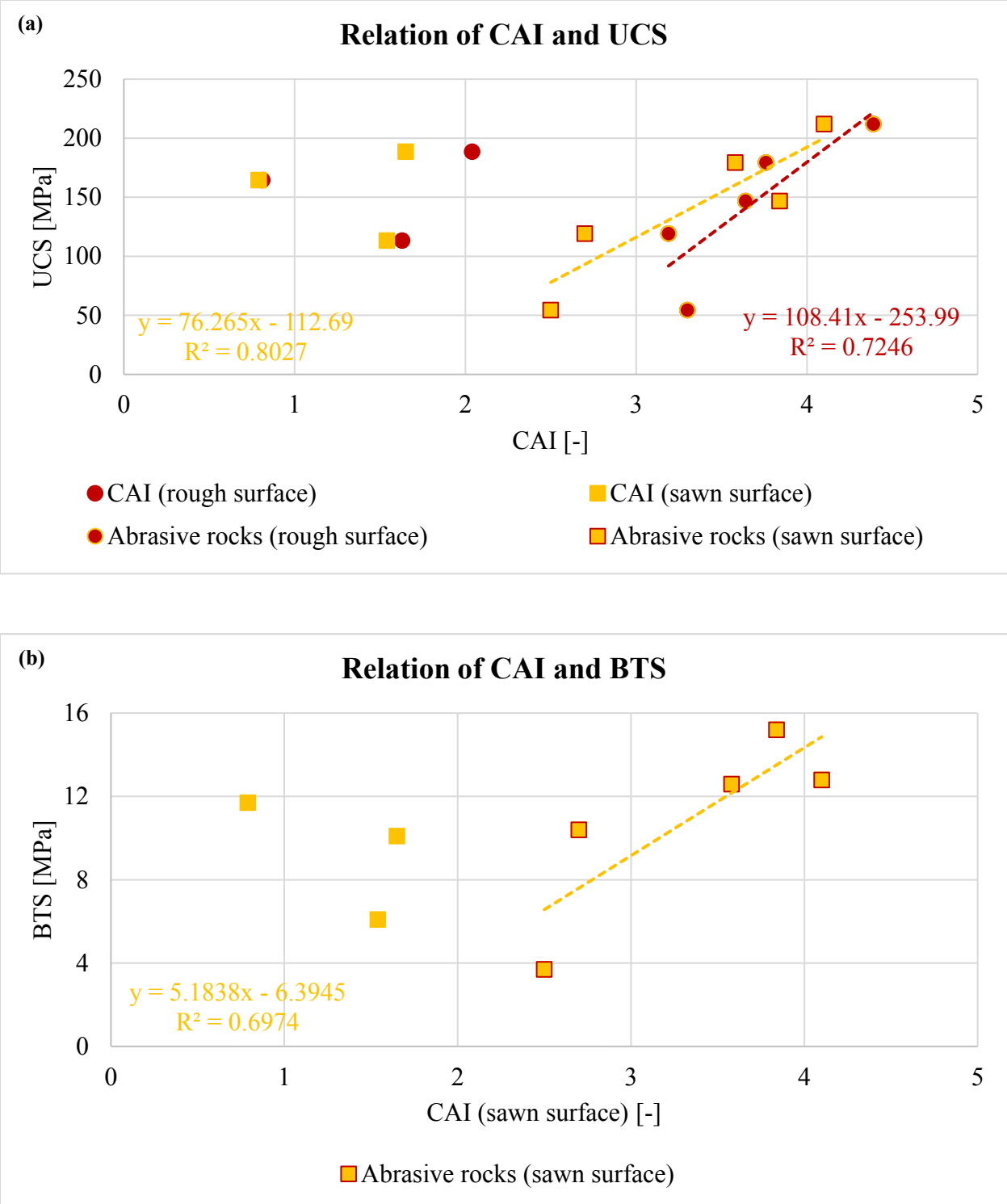

Figure 3-37 Relation of Cerchar abrasivity index and (a) uniaxial compressive strength; (b) Brazilian tensile strength

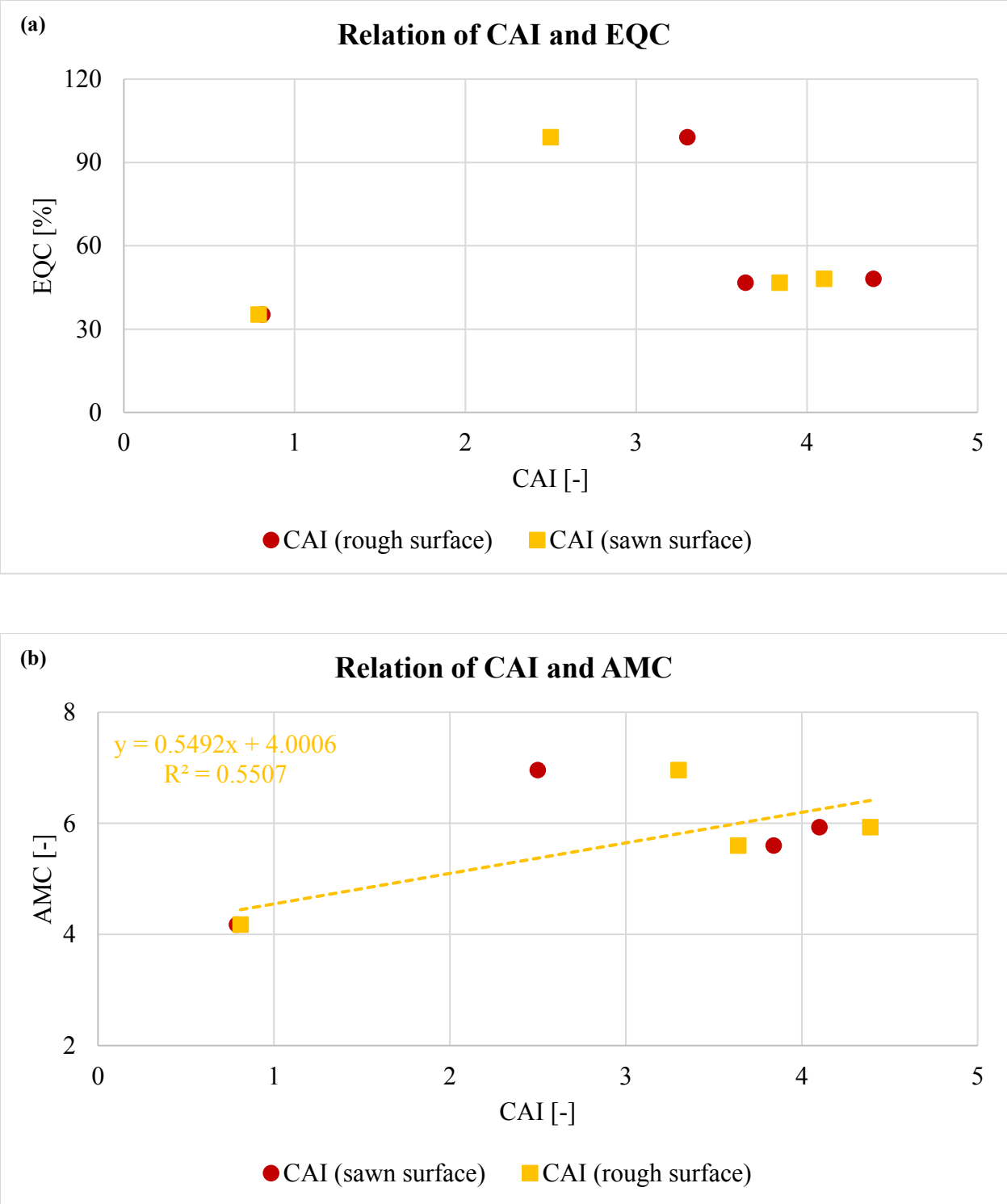

Figure 3-38 Relation of Cerchar abrasivity index and (a) equivalent quartz content; (b) abrasive mineral content

3.6.2 Sliding distance

The testing distance is defined to be 10 mm in Cerchar (1986). Based on granite, sandstone and slate samples, this effecting factor is studied by performing tests with different sliding distances (1 - 3 - 5 - 7 - 10 - 12 - 15 - 20 mm) applying the same scratching velocity of 1 mm/s. All tested samples are sawn in order to avoid additional effects in respect to different surface roughness. Note that the stylus is scratching orthogonal to the foliated surface of slate sample in order to cross the entire foliation (see Figure 3-39c). Results are summarized in Table 3-13.

Figure 3-40 shows the CAI values plotted against the corresponding testing distances. For each rock sample, a power trend is identified. Regression curves indicate that the growth rate of the CAI value slightly reduces with increasing testing distance. In Figure 3-41, each CAI value is referred to the standard testing distance of 10 mm. For all three tested rocks hold: about 60% of the CAI is reached after the first 1 mm and over 80% of the CAI is achieved after the first 3 mm. It is also found that the CAI value has an increment of about 20 - 40% after the testing distance of 20 mm related to the standard distance of 10 mm. Based on the available data, it can be said that a lengthening of the testing distance is not necessary, which confirms the statement of Plinninger et al. (2003).

It should be noticed that the predefined distance should be carefully watched in soft but abrasive rocks like sandstone. The stylus penetrates into the rock progressively during the entire sliding distance due to the low strength of the sandstone. The abrasion occurs not on the tip but on the conical sides of the stylus. This may lead to an underestimation of the CAI value. Therefore, it is necessary to vary the hardness of the stylus based on the rock strength, for example, to use a lower hardness stylus for testing softer rocks and a higher hardness stylus for testing harder rocks. It has been suggested to measure the CAI value in soft rocks by using a relatively soft stylus with HRC of 40 - 43.

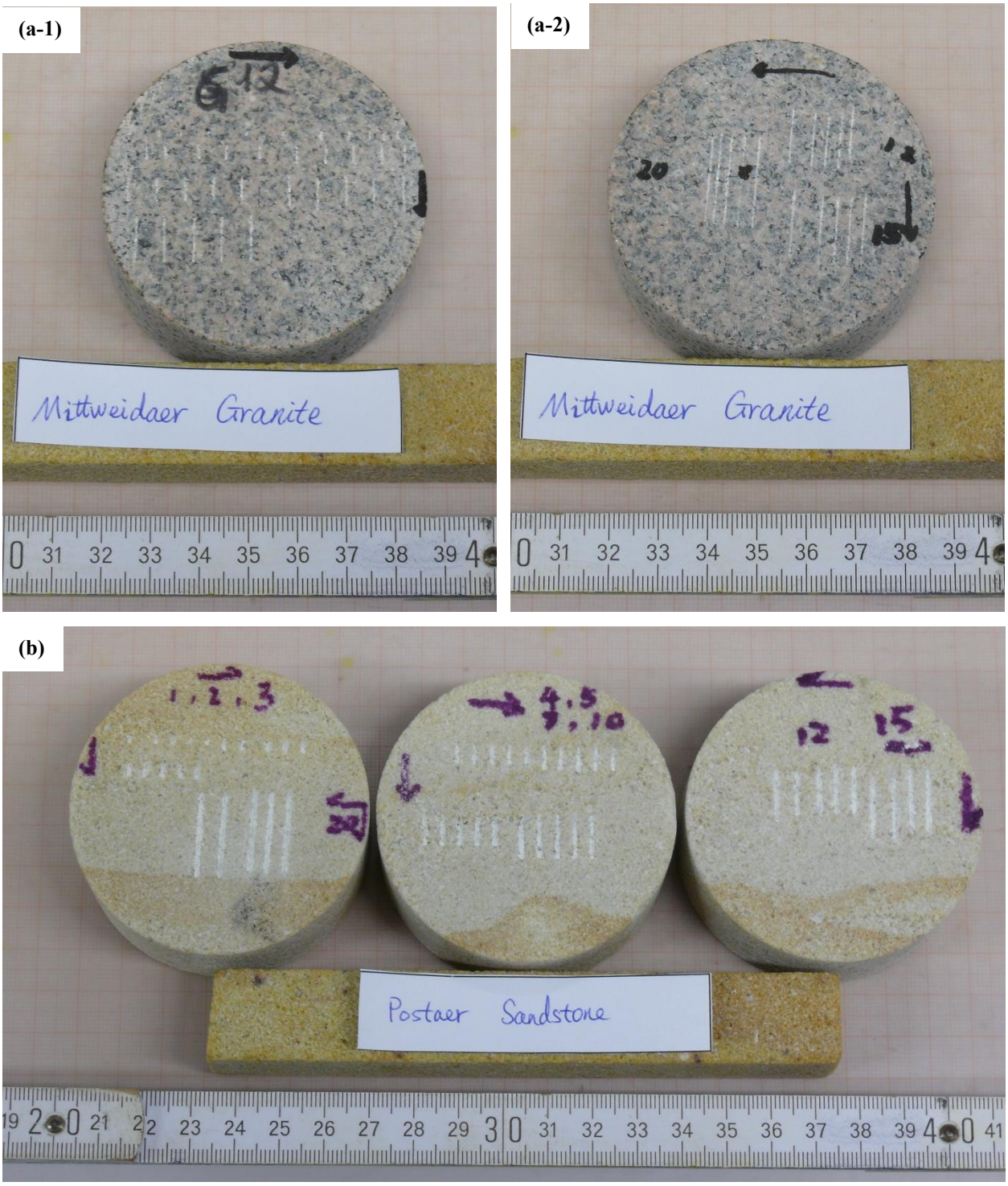
(a-1)
Mittweidaer Granite
(a-2)
Mittweidaer Granite
(b)
Postaer Sandstone

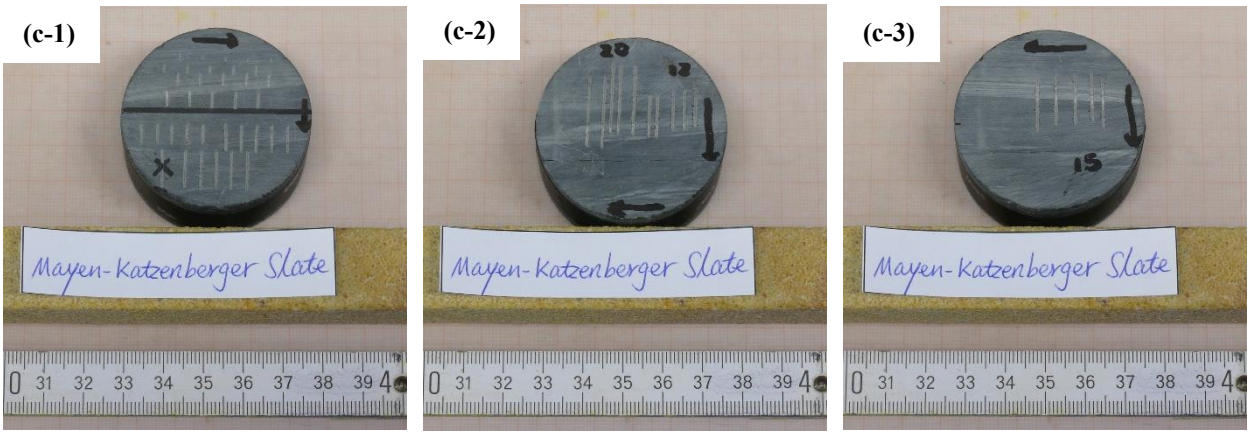

Figure 3-39 Exemplary: scratches produced on (a) granite; (b) sandstone; (c) slate (90 degree to foliation) with different testing distances (for example: number 15 marked on the sample surface means a testing distance of 15 mm)

Table 3-13 Cerchar abrasivity index measured with different testing distances (mean value ± standard deviation)

Rock type	**Testing distance [mm]**							
	1	**3**	**5**	**7**	**10**	**12**	**15**	**20**
Granite	2.93 ± 0.75	3.73 ± 0.67	3.72 ± 0.28	4.00 ± 0.48	4.10 ± 0.45	4.19 ± 0.35	4.25 ± 0.06	4.79 ± 0.66
Sandstone	1.49 ± 0.32	1.97 ± 0.50	2.02 ± 0.94	2.16 ± 1.10	2.50 ± 0.66	2.89 ± 0.60	3.06 ± 0.62	3.27 ± 0.55
Slate **)	0.56 ± 0.24	0.61 ± 0.20	0.64 ± 0.24	0.65 ± 0.25	0.79 ± 0.44	0.84 ± 0.16	0.92 ± 0.43	1.13 ± 0.77

**): Scratching direction is orthogonal (90°) to the foliated surface of the slate sample

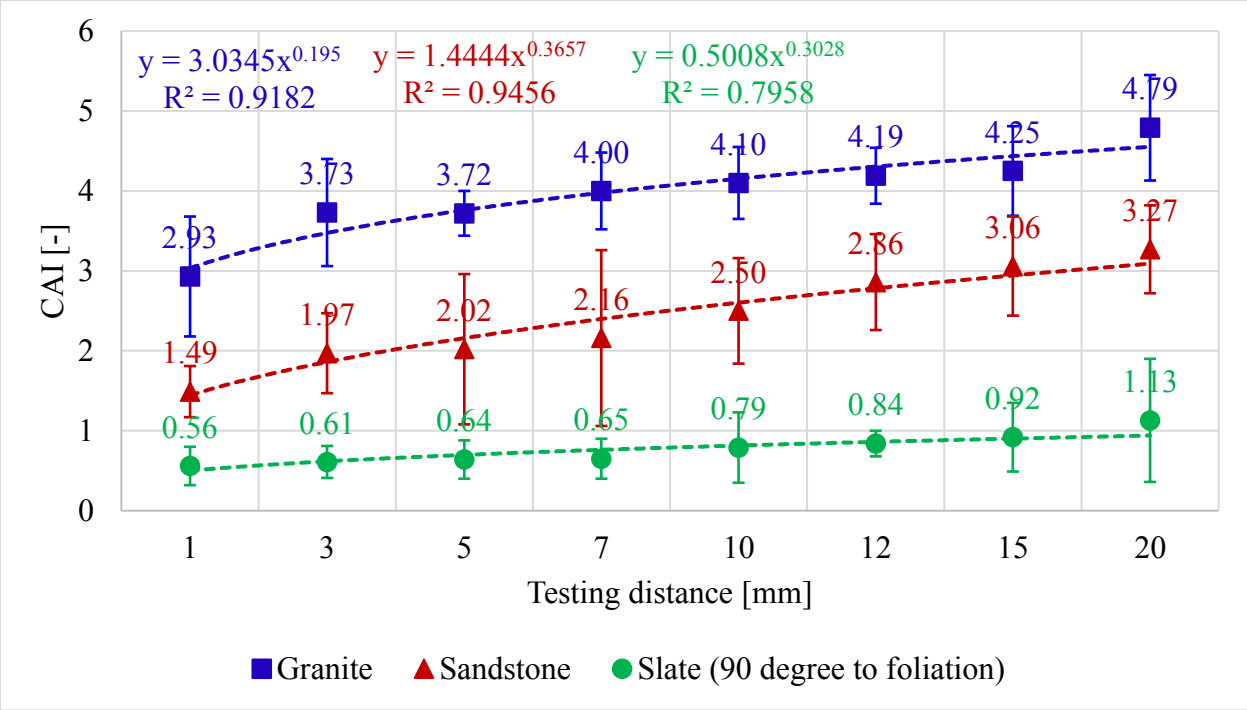

Figure 3-40 Variation of Cerchar abrasivity index with testing distances

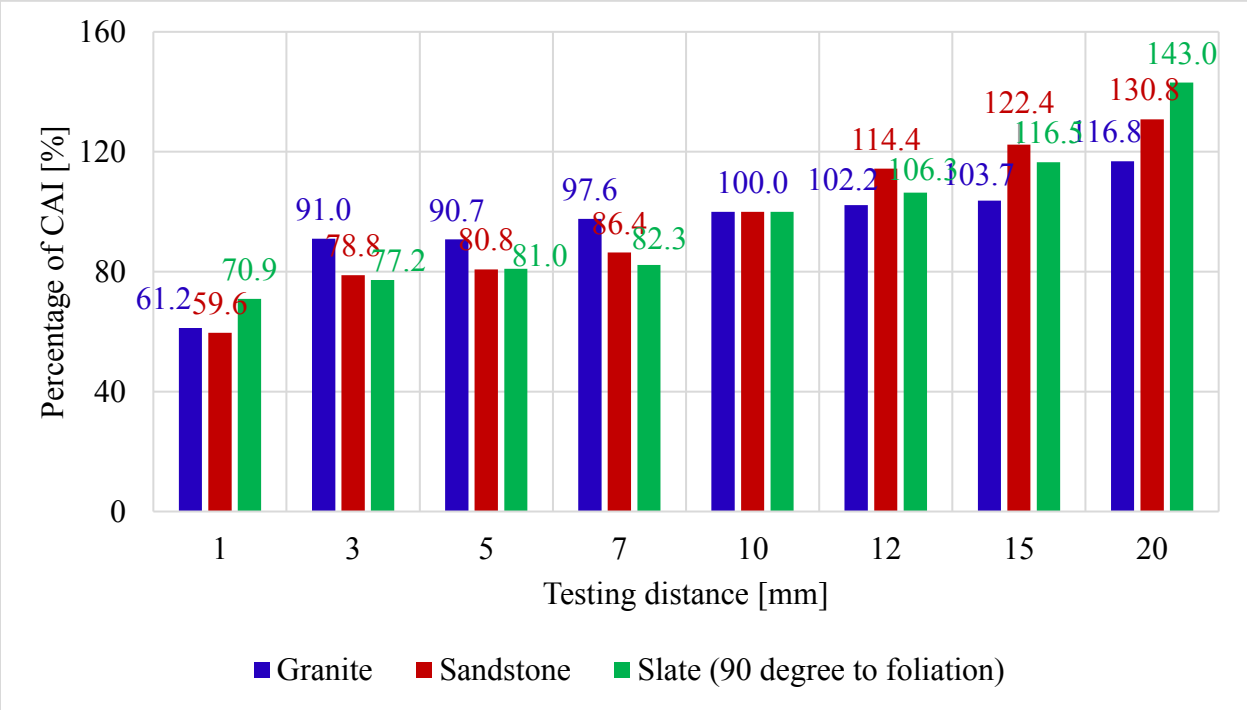

Figure 3-41 Percentage of Cerchar abrasivity index in relation to the standard distance of 10 mm

3.6.3 Scratching velocity

Plinninger et al. (2004) stated that, although there is a great difference in testing velocity between these two apparatuses (Cerchar versus West), the CAI results seem to be equal. Rostami et al. (2014) also concluded that CAI does not vary by changing the scratching velocity. However, experiences showed that the testing velocity may be a major factor affecting the CAI value. For example, in case the rock surface is extremely rough, coarse grains may force the stylus to jump from the sample surface and then the testing velocity should be reduced. Also time-dependent damage may affect the test result.

The influence of scratching velocity on the CAI is investigated using granite, sandstone and slate samples, respectively. Under sawn testing conditions, rock samples are moved under the stylus over a testing distance of 10 mm within different testing durations (60 - 30 - 20 - 10 - 6 s). The stylus is scratching orthogonal to the foliated surface of the slate sample (see Figure 3-42c). Results are summarized in Table 3-14.

Figure 3-43 shows the CAI values related to the testing durations for the three tested rocks. As can be seen, for each rock sample, no clear correlation is found for the CAI results with different testing velocities. This means that the testing velocity does not affect the CAI. This observation coincides with the conclusion of Plinninger et al. (2004) and Rostami et al. (2014).

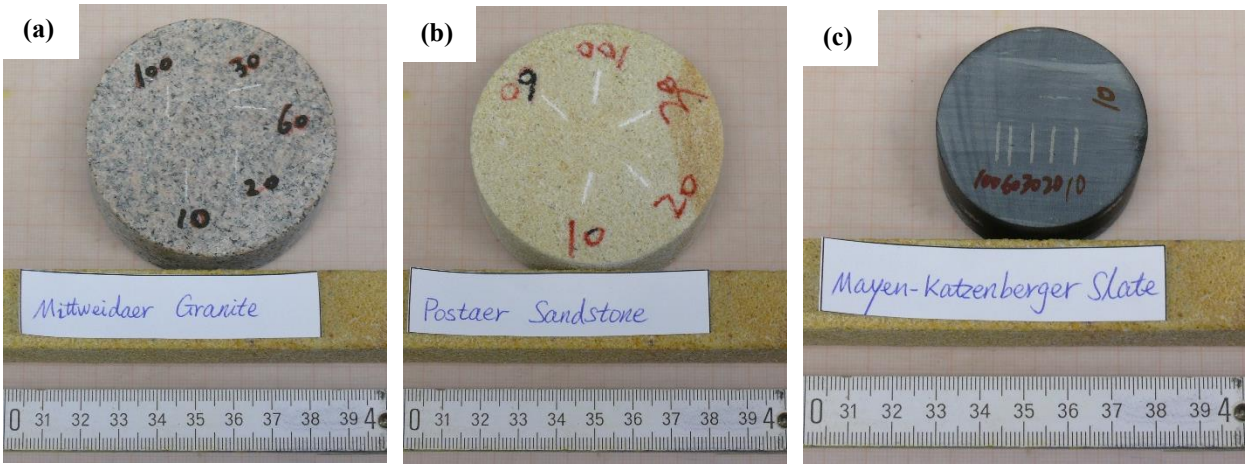

Figure 3-42 Exemplary: scratches produced on (a) granite; (b) sandstone; (c) slate (90 degree to foliation) with standard testing distance of 10 mm finished within different testing durations

(for example: number 100 marked on the sample surface means a testing velocity of 100 mm/60 s (= 1.67 mm/s); 60 means 60 mm/60 s (= 1 mm/s); 30 means 30 mm/60 s (= 0.5 mm/s); 20 means 20 mm/60 s (= 0.33 mm/s); 10 means 10 mm/60 s (= 0.167 mm/s))

Table 3-14 Cerchar abrasivity index measured at different testing velocities (mean value ± standard deviation)

Rock type	**Testing duration [s]**				
	60	**30**	**20**	**10**	**6**
Granite	3.75 ± 0.06	5.31 ± 0.26	3.60 ± 0.16	4.10 ± 0.45	4.22 ± 0.14
Sandstone	1.51 ± 0.04	2.58 ± 0.06	2.32 ± 0.51	2.50 ± 0.66	3.59 ± 0.12
Slate **)	1.20 ± 0.13	1.29 ± 0.18	2.12 ± 0.28	0.79 ± 0.44	1.83 ± 0.53

**): Scratching direction is orthogonal (90°) to the foliated surface of the slate sample

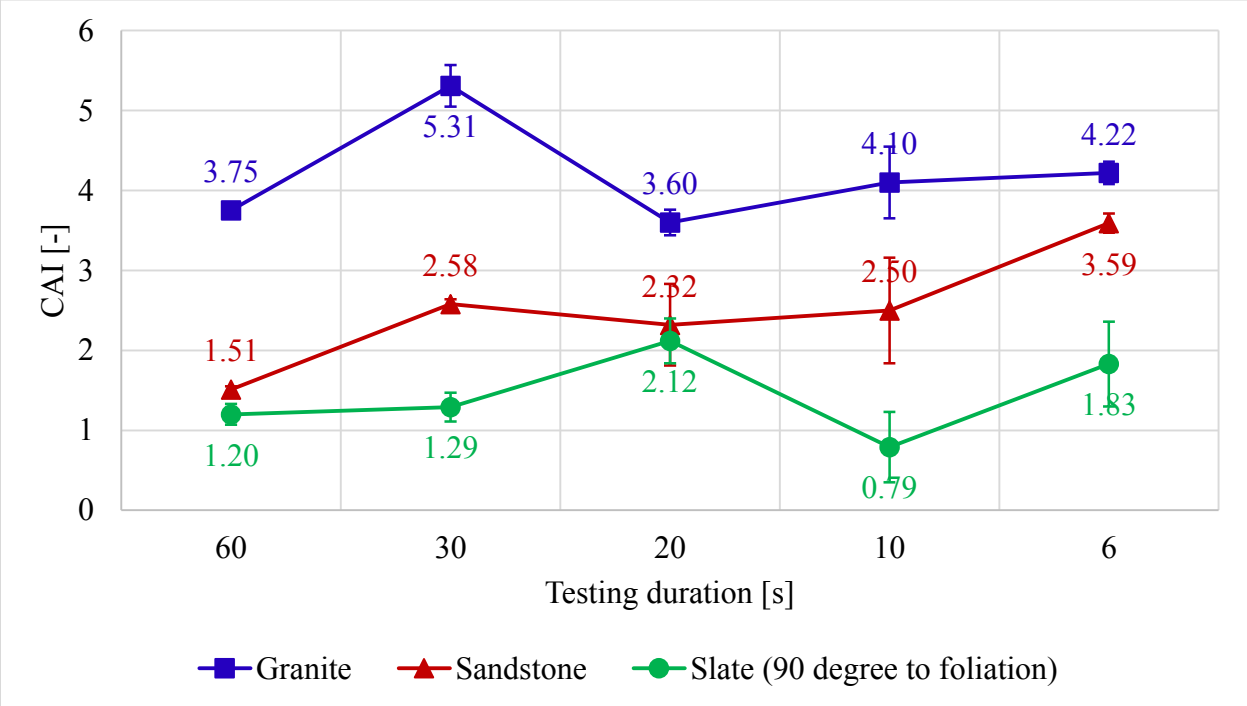

Figure 3-43 Variation of Cerchar abrasivity index with testing durations

3.6.4 Rock anisotropy

In Cerchar (1986), testing procedure for stratified or foliated rocks is not discussed. Käsling et al. (2007) stated: Cerchar measurements in layered rock samples should be conducted three times to obtain the final CAI value, namely sliding direction of the stylus parallel and orthogonal to the foliated surface, and sliding on the foliation surface. Alber et al. (2014) suggested to scratch orthogonal to as well as on the anisotropic surface of layered rocks. Moradizadeh et al. (2016) performed their tests parallel and orthogonal to schistosity direction using metamorphic rocks.

To investigate this topic in more detail, two metamorphic transversely isotropic rocks, slate and gneiss, are tested. A series of Cerchar tests are carried out at different angles of scratching direction to foliated surface (0° - 30° - 45° - 60° - 90°), as well as on the foliation surface. The tested samples are sawn. Testing distance, velocity and duration are set to 10 mm, 1 mm/s and 1 s, respectively. The mean CAI value is obtained from one single test with five scratches for one single angle. Figure 3-44 illustrates the scratches produced on the slate and gneiss samples, respectively, at different testing angles. Results are summarized in Table 3-15.

The CAI values measured on the slate and gneiss samples at different testing angles are compared in Figure 3-45. Results indicate that the influence of scratching angles on the CAI is not obvious. It can be said that the CAI is more affected by rock mineralogy and microstructure rather than by rock anisotropy. This confirms the statement that rock abrasivity is a function of many intrinsic properties, for example, mineral composition and content, grain size, shape and hardness and rock strength.

Note that, by comparing the mean CAI value calculated from one single test with that calculated from all single tests, a better CAI result on anisotropic rocks could be derived from three testing angles: scratching parallel or orthogonal to the foliated surface, scratching inclined to the foliated surface, as well as scratching on the foliation surface of the rock sample.

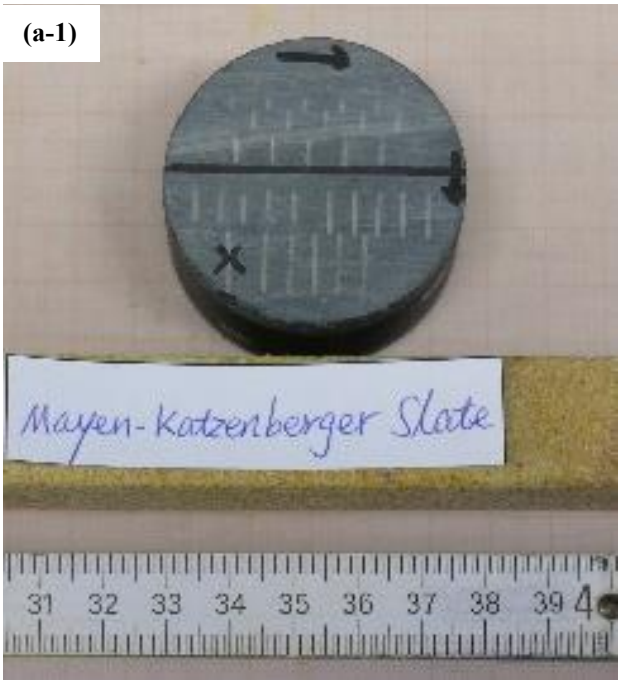
(a-1)
Mayen-Katzenberger Slate


(a-2)
Mayen-Katzenberger Slate


(a-3)
Mayen-Katzenberger Slate


(a-4)
Mayen-Katzenberger Slate

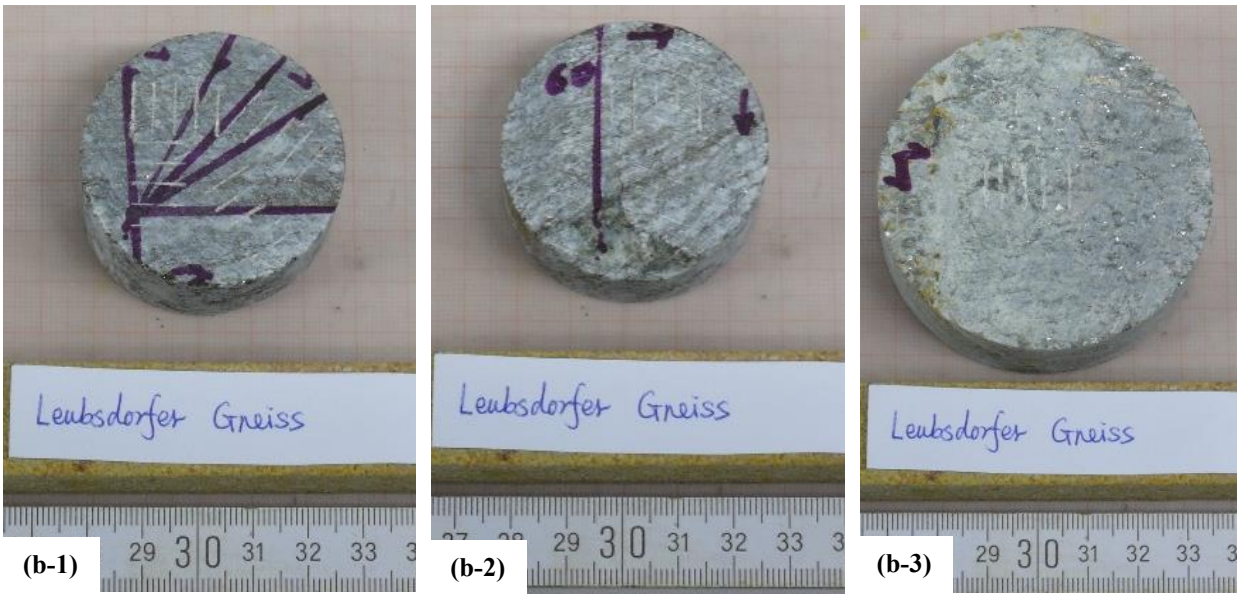

Figure 3-44 Exemplary: scratches produced on (a) foliated slate samples; (b) schistose gneiss samples at different testing angles (for example: number 60 marked on the sample surface means that the angle of scratching direction-to foliated surface is 60 degree)

Table 3-15 Cerchar abrasivity index measured at different testing angles
(mean value ± standard deviation)

Rock type	**Testing angles**						**Mean value (from all tests)**
	Scratching direction to foliated surface					**Scratching on foliation surface**	
	0°	**30°**	**45°**	**60°**	**90°**		
Slate	0.68 ± 0.15	0.68 ± 0.14	0.86 ± 0.11	0.70 ± 0.03	0.79 ± 0.43	0.81 ± 0.30	0.74 ± 0.28
Gneiss	3.74 ± 0.27	4.18 ± 1.16	4.04 ± 0.34	4.03 ± 0.33	3.84 ± 0.41	3.64 ± 0.11	3.91 ± 0.53

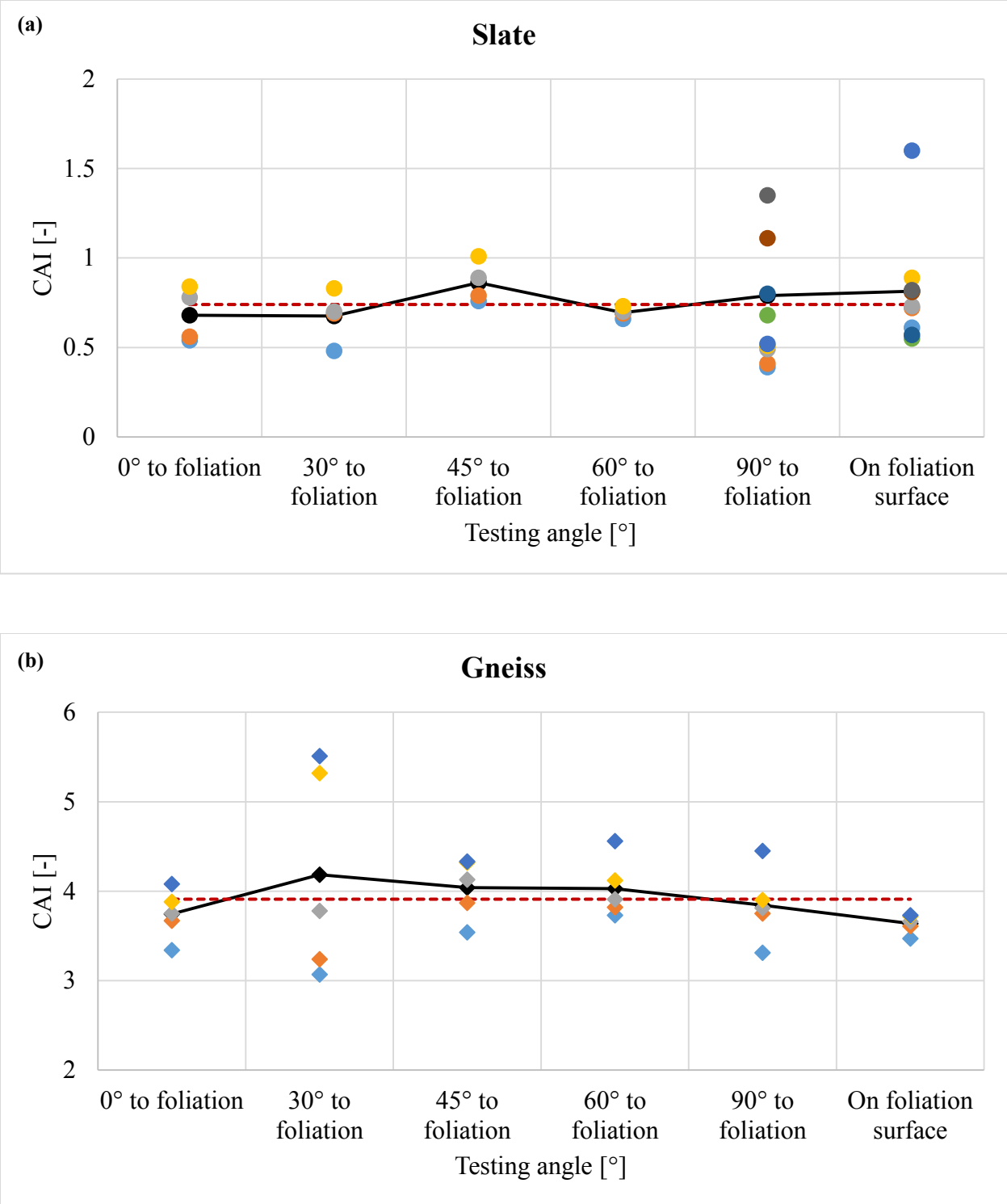

Figure 3-45 Variation of Cerchar abrasivity index with testing angles for (a) slate; (b) gneiss (for example: black solid line indicates mean CAI calculated from one single test; red dash line indicates mean CAI value calculated from all single tests)

4. Numerical simulation of Cerchar scratch test

4.1 Discrete element method and particle flow code

The discrete element method (DEM) was firstly proposed to model the mechanical behavior of rocks by Cundall (1971) and then applied to analyze the mechanical behavior of granular materials (i.e. soils) by Cundall and Strack (1979). A detailed description of this method is given by Cundall (1988) and Hart et al. (1988). According to the original definition (Cundall and Hart 1992), DEM is a modeling technique that allows finite displacements and rotations of discrete bodies including complete detachment and automatic recognition of new contacts during the simulation progress.

A particular instance of DEM is a particle based model, which can model the mechanical behavior of a system composed of an assembly of discrete spherical particles. The particles can move independently of one another and interact at pair-wise contacts. The particles are assumed to be rigid. The mechanical behavior of such a system is described in terms of movement of each particle and the inter-particle forces acting at each contact point.

4.1.1 Assumptions in PFC

PFC is based on the following assumptions: (1) the fundamental particle shape, referred to as ball, is a circular disc with unit thickness in 2D or a sphere in 3D. (2) Particles are treated as rigid bodies that can move independently of one another. (3) Particles interact at pair-wise contacts by means of internal forces and moments. Contact mechanics are embodied in particle-interaction laws that update the internal forces and moments. (4) Behavior at contacts uses a soft-contact approach where the rigid particles are allowed to overlap at contact points. The contacts occur over a vanishingly small area (i.e. at a point). The magnitude of the overlap or the relative displacement at the contact point are related to the contact force via the force-displacement law. (5) Particles can be bonded together by specifying shear and tensile bond strengths. When specified bond strengths are exceeded by applied local stresses (i.e. tension, shear or moment by particle rotation), bonds break and form a rupture surface (i.e. a crack). Bonds exist at contacts between particles, but do not exist between particles and walls.

4.1.2 Calculation cycles in PFC

Figure 4-1 shows the calculation cycles in PFC. The calculations alternate between the application of the force-displacement law at contacts and the Newton's law of motion for particles. The force-displacement law is used to update the contact forces arising from the relative motion at each contact. The Newton's law of motion, or in other word, Newton's second law, provides the fundamental relationship between particle motion and the forces causing that motion. It is used to determine the motion of each particle arising from contact forces acting on it.

At the beginning of each timestep, the set of contacts is updated from the known particle and wall positions. First, the force-displacement law is applied to each contact to update the contact forces based on the relative motion between the two particles at the contact and the contact constitutive model. Second, the law of motion is applied to each particle to update its velocity and position based on the resultant force and moment arising from the contact forces and any body forces acting on the particle.

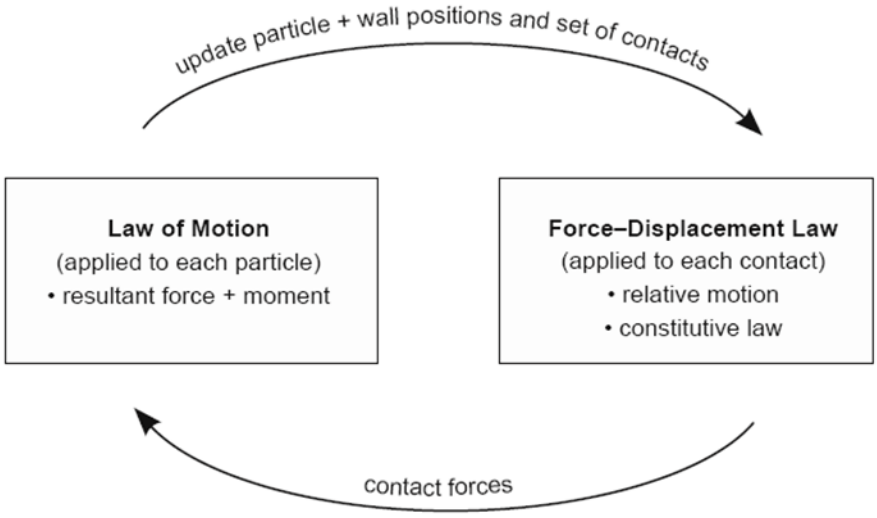

Figure 4-1 Calculation cycle in PFC (Itasca 2016)

Force-displacement law

The force-displacement law is described for both, particle-particle contact and particle-wall contact, as illustrated in Figure 4-2.

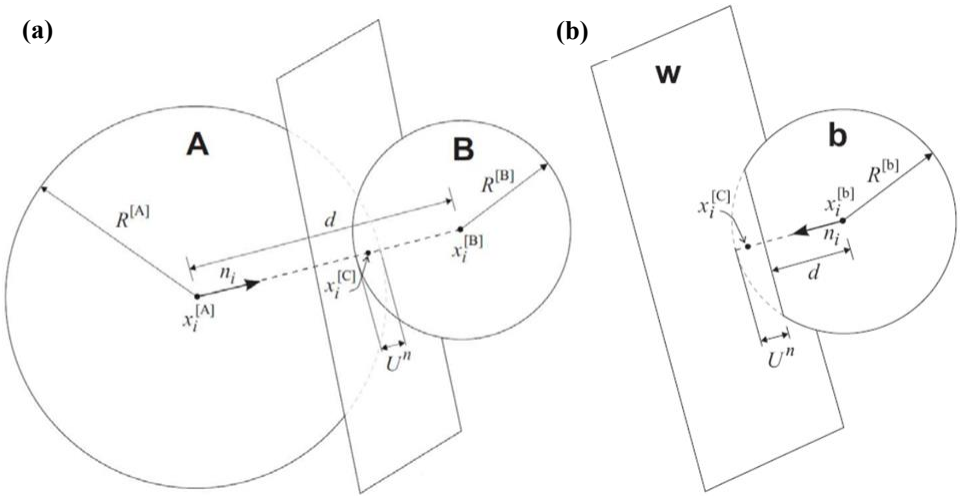

Figure 4-2 Contact between two particles (a) and between a particle and a wall (b) (Itasca 2016)

where,

A, B, b = Particles

d = Distance between two particles or between a particle and a wall

n_i = Normal unity vector

$R^{[A]}$, $R^{[B]}$, $R^{[b]}$ = Radius of particles

U^n = Overlap of two particles or between a particle and a wall in the normal direction

w = Wall

$x_i^{[A]}$, $x_i^{[B]}$, $x_i^{[b]}$ = Position vectors of the particle center

$x_i^{[c]}$ = Position vector of the contact point

The contact force vector can be resolved into normal and shear components with respect to the contact plane as:

$$F_i = F_i^n + F_i^S \quad (4\text{-}1)$$

F_i = Contact force vector

F_i^n = Normal component vector

F_i^S = Shear component vector

The magnitude of the normal contact force is calculated by:

$$F_n = K_n \cdot U_n \quad (4\text{-}2)$$

F_n = Normal contact force

U_n = Overlap of two particles in the normal direction

K_n = Normal contact stiffness

$$F_s^{new} = F_s^{old} + \Delta F_s \quad (4\text{-}3)$$

$$\Delta F_s = -k_s \cdot \Delta u_s \quad (4\text{-}4)$$

$$\Delta u_s = v_s \cdot \Delta t \quad (4\text{-}5)$$

F_s^{new} = Updated shear contact force

F_s^{old} = Shear contact force of the previous timestep

ΔF_s = Shear contact force increment

k_s = Shear contact stiffness

Δu_s= Contact displacement increment in the shear direction

v_s = Velocity in the shear direction

Δt = Timestep

Law of motion

The equations of motion relate the translational motion to the resultant force, and the rotational motion to the resultant moment:

$$F_i = m \cdot (\ddot{x}_i - g_i) \text{ (translational motion)} \quad (4\text{-}6)$$

$$M_i = I \cdot \dot{\omega}_i \text{ (rotational motion)} \quad (4\text{-}7)$$

Integration of law of motion

The equations of motion are integrated using a centered finite difference procedure involving a timestep of Δt. The translational and rotational accelerations at time t can be written in terms of velocities at the mid-intervals:

$$\ddot{x}_i^{(t)} = \frac{1}{\Delta t} \cdot (\dot{x}_i^{(t+\Delta t/2)} - \dot{x}_i^{(t-\Delta t/2)}) \quad (4\text{-}8)$$

$$\dot{\omega}_i^{(t)} = \frac{1}{\Delta t} \cdot (\dot{\omega}_i^{(t+\Delta t/2)} - \dot{\omega}_i^{(t-\Delta t/2)}) \quad (4\text{-}9)$$

Inserting equation (4-8) into equation (4-6) and solving for the translational velocity at time $(t + \Delta t/2)$:

$$\dot{x}_i^{(t+\Delta t/2)} = \dot{x}_i^{(t-\Delta t/2)} + (\frac{F_i^{(t)}}{m} + g_i) \cdot \Delta t \quad (4\text{-}10)$$

Inserting equation (4-9) into equation (4-7) and solving for the rotational velocity at time $(t + \Delta t/2)$:

$$\omega_i^{(t+\Delta t/2)} = \omega_i^{(t-\Delta t/2)} + (\frac{M_i^{(t)}}{I}) \cdot \Delta t \quad (4\text{-}11)$$

Updating of particle coordinates

After the determination of the translational and rotational velocities of particles, the position of particles is updated by:

$$x_i^{(t+\Delta t)} = x_i^{(t)} + \dot{x}_i^{(t+\Delta t/2)} \cdot \Delta t \quad (4\text{-}12)$$

F_i = Resultant force acting on the particle

g_i = Body force acceleration vector (i.e. gravitational acceleration)

I = Moment of inertia of the particle

m = Total mass of the particle

M_i = Resultant moment acting on the particle

$x_i, \dot{x}_i, \ddot{x}_i$ = Position, translational velocity, translational acceleration

$\omega_i, \dot{\omega}_i$ = Angular velocity, angular acceleration

The calculation cycle for the law of motion can be summarized as follows: given the values of $\dot{x}_i^{(t-\Delta t/2)}$, $\omega_i^{(t-\Delta t/2)}$, $x_i^{(t)}$, $F_i^{(t)}$ and $M_i^{(t)}$, equitions (4-10) and (4-11) are used to obtain $\dot{x}_i^{(t+\Delta t/2)}$ and $\omega_i^{(t+\Delta t/2)}$. Then, Euqation (4-12) is used to obtain $x_i^{(t+\Delta t)}$. The values of $F_i^{(t+\Delta t)}$ and $M_i^{(t+\Delta t)}$, to be used in the next cycle, are obtained by application of the force-displacement law.

4.1.3 Constitutive models in PFC

The constitutive model in PFC consists of three parts: a contact stiffness model, a slip model and a bonding model, which control deformation, detachment and movement of particle assemblies. The contact stiffness model provides an elastic relation between contact force and relative displacement. The slip model enforces a relation between shear and normal contact forces such that the two contacting particles may slip relative to each other. The bonding model serves to limit the total normal and shear forces that the contact can carry by enforcing bond-strength limits (Cho et al. 2007).

Contact model

The linear elastic contact model is defined by the normal contact stiffness (K_n) and the shear contact stiffness (k_s) of two contacting entities (i.e. particle-wall and particle-particle). For particle-wall contact, since the wall is treated as rigid, the normal and shear stiffness of the particle are inherited. For particle-particle contact, the normal and shear contact stiffness are calculated as the average of the normal and shear stiffness of two particles A and B:

$$K_n = \frac{(K_n^{[A]} \cdot K_n^{[B]})}{(K_n^{[A]} + K_n^{[B]})} \tag{4-13}$$

$$k_s = \frac{(k_s^{[A]} \cdot k_s^{[B]})}{(k_s^{[A]} + k_s^{[B]})} \tag{4-14}$$

Slip model

The slip model is described by the friction coefficient, which is taken as the minimum value of the two particles forming the contact. The friction coefficient gives the value of shear force, at which slip occurs at the contact. When the maximum shear contact force is exceeded by the applied shear force, the slip model is activated. The friction coefficient (μ) is defined as the ratio of maximum shear contact force (F_s^{max}) to normal contact force (F_n):

$$F_s^{max} = \mu \cdot |F_n| \tag{4-15}$$

F_s^{max} = Maximum shear contact force [force]

F_n = Normal contact force [force]

μ = Friction coefficient [-]

Parallel bond model

The bonded particle model (BPM) is defined as an assembly of non-uniform-sized circular or spherical particles that can be bonded together at their contact points (Potyondy and Cundall 2004). The particles can be bonded together by specifying shear and tensile bond strength. When specified bond strengths are exceeded by applied local stresses (i.e. tension, shear or moment by particle rotation), bonds break to form cracks. In PFC, various bonding models are provided, such as contact bond model, parallel bond model, flat joint model, etc. Among the bonding models, the parallel bond model (PBM) can be considered as a set of elastic springs which are uniformly distributed over a rectangular cross section with constant normal bond stiffness and shear bond stiffness lying on the contact plane and centered at the contact point. Since the bonding is activated over a finite area, it can resist moments. The stiffness is contributed by both, contact stiffness and bond stiffness. Bond breakage immediately results in stiffness reduction, which not only affects the stiffness of adjacent particles, but also affects the macro stiffness of the particle assembly. The PBM is more realistic to model the mechanical behavior of rock or rock-like materials, whereby the bonds may break in either tension or shear with an associated reduction in stiffness (Cho et al. 2007).

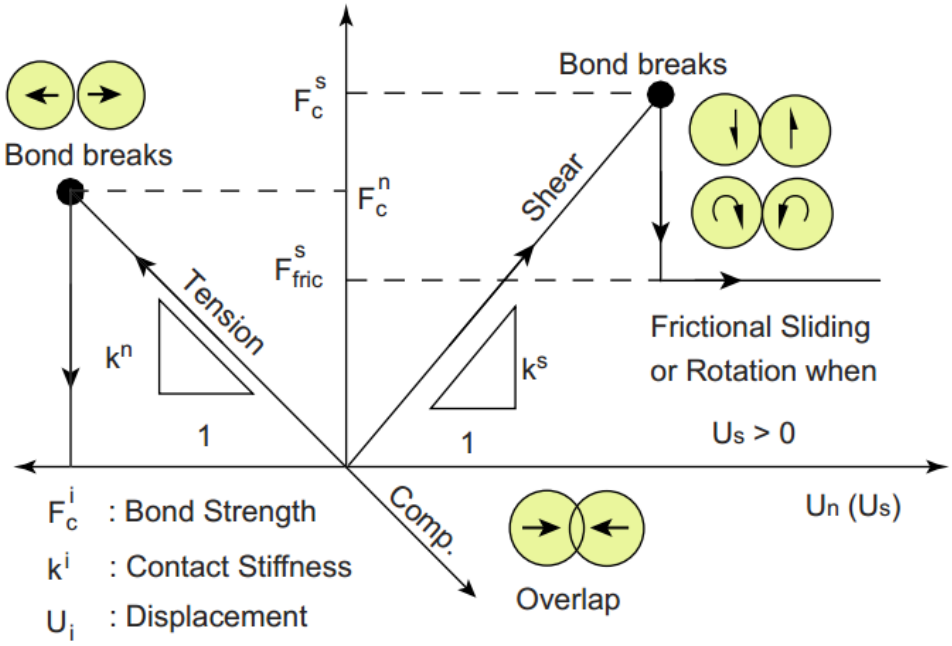

Figure 4-3 Yielding process of micro-bonding in PFC (Cho et al. 2007)

4.2 Three dimensional simulation of rock scratching

4.2.1 Mechanical properties of sandstone

In this work, the particle flow code of PFC^{3D} (Itasca 2016) is used to simulate the Cerchar scratch test on the Postaer sandstone with respect to its mineralogical and mechanical properties. According to the thin-section observation and XRD analysis, this sandstone is a quasi-homogeneous rock with the grain size ranging from 0.1 mm to 0.2 mm. It is composed of 99% of quartz mineral. Table 4-1 summarizes the rock mechanical properties of tested sandstone samples. Figure 4-4 illustrates the rock sample fragmentation after UCS and BTS tests, respectively.

Table 4-1 Rock mechanical properties of sandstone sample

Sandstone sample	**ρ [kg/m³]**	**v_p [km/s]**	**UCS [MPa]**	**E-modulus [GPa]**	**ν [-]**	**BTS [MPa]**	**Ø [%]**	**φ [°]**	**c [MPa]**
UCS-S1	2080	3.24	57.01	19.40	0.21	-	20.8	-	-
UCS-S2	2090	3.18	53.54	20.10	0.14	-	-	-	-
UCS-S3	2060	3.01	52.60	17.53	0.16	-	-	-	-
BTS-1	2050	-	-	-	-	4.02	-	-	-
BTS-2	2050	-	-	-	-	4.58	-	-	-
BTS-3	2060	-	-	-	-	3.42	-	-	-
BTS-4	2050	-	-	-	-	3.80	-	-	-
BTS-5	2070	-	-	-	-	3.70	-	-	-
BTS-6	2070	-	-	-	-	3.83	-	-	-
BTS-7	2060	-	-	-	-	3.65	-	-	-
BTS-8	2070	-	-	-	-	3.08	-	-	-
mv(±sd)	2060.8±15.0	3.1±0.1	54.4±2.3	19.0±1.3	0.17±0.04	3.7±0.4	20.8	23[*)]	36[*)]

mv: mean value; sd: standard deviation; [*)]: according to Baumgarten (2015)

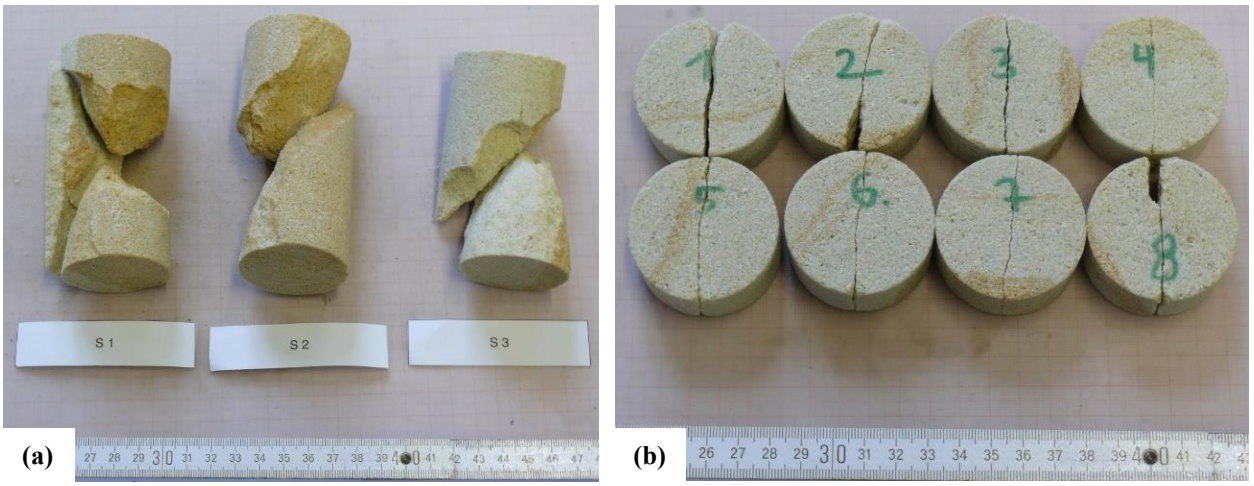

Figure 4-4 Failed sandstone samples after (a) UCS test and (b) BTS test

4.2.2 Calibration of micro-parameters

A problem by using DEM is that the input micro-parameters cannot be derived from laboratory tests directly. The macro-parameters must be calibrated by simulating rock mechanical experiments, such as UCS and BTS tests.

Figure 4-5a illustrates a cylindrical model with 50 mm in diameter and 100 mm in height constructed for the simulation of UCS test, while Figure 4-5b illustrates the disc model (50 mm in diameter and 25 mm in thickness) for the BTS simulation. Since sandstone can be referred to as a mono-mineral and homogeneous rock, the ball radii are set to 0.4 - 0.6 mm. The resulting sample piece for the UCS test is composed of 357,982 balls. The UCS simulation is progressed by moving the top and bottom loading-walls compressing the particle assembly. The velocity of the loading-walls is set to 0.05 m/s to reduce the calculation time. The particle assembly is made of 91,525 balls for the BTS test and the compressing velocities of loading-walls on the particle assembly are set to 0.02 m/s.

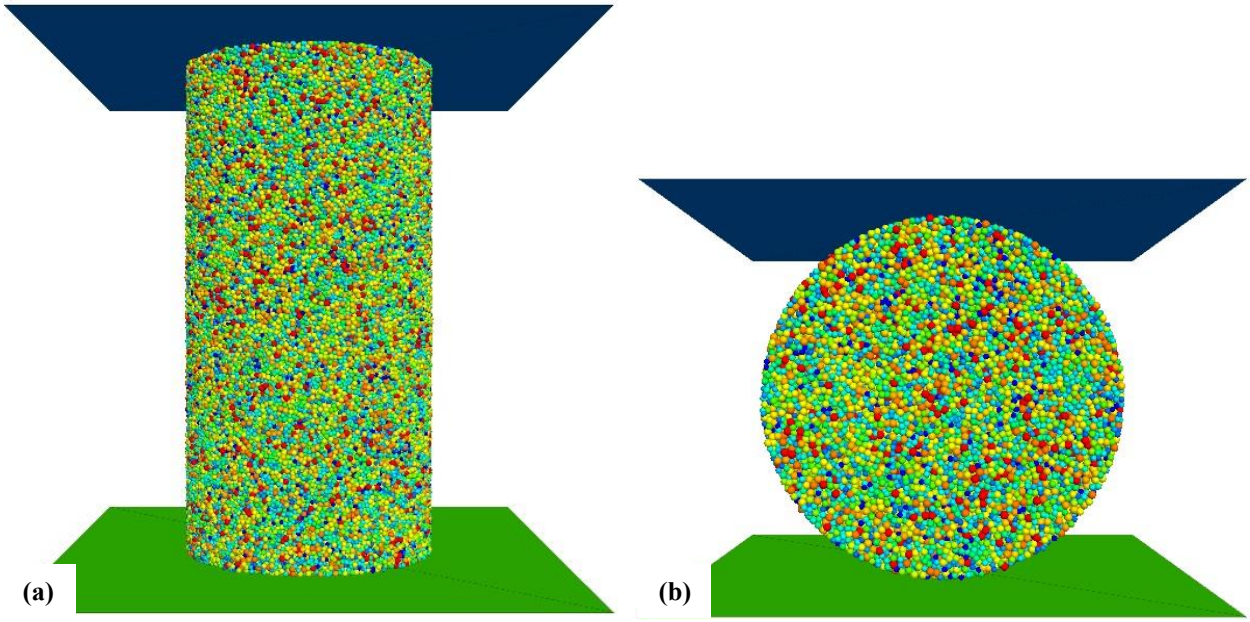

Figure 4-5 PFC model for the simulation of (a) UCS test and (b) BTS test

In PFC, the UCS is matched by varying the tensile strength (σ_c) and the shear strength (τ_c) of the contacts, where τ_c is related to the cohesion (c) and friction angle (φ). Note that the UCS increases with increasing tensile and shear strength. The Young's modulus is matched by varying the effective modulus (E and E^*) of the particles and contacts. The Poisson's ratio is matched by varying the ratio of normal to shear stiffness of the particles and contacts (k_n/k_s and k_n^*/k_s^*). Note that, in the present simulation, the effective moduli and the ratio of normal to shear stiffness of the particles and contacts are chosen to be equal. A friction coefficient (μ) of 0.5 is specified as a reasonable non-zero value. A mechanical (or local) damping factor (damp) is supposed as 0.1. The micro-parameters calibrated for the sandstone for both, UCS and BTS tests are listed in Table 4-2.

Table 4-2 Micro-parameters calibrated for sandstone

Component	**Micro-parameter**	**Value**
Particle (Grain)	Density (ρ) [kg/m^3]	2060
	Minimum radius (r_{min}) [mm]	0.4
	Maximum radius (r_{max}) [mm]	0.6
	Effective modulus (E) [GPa]	8.2
	Normal-to-shear stiffness ratio (k_n/k_s) [-]	2.5
	Friction coefficient (μ) [-]	0.5
	Mechanical damping coefficient (damp) [-]	0.1
Parallel-bond (Cement)	Effective modulus (E^*) [GPa]	8.2
	Normal-to-shear stiffness ratio (k_n^*/k_s^*) [-]	2.5
	Tensile strength (σ_t) [MPa]	13
	Cohesion (c) [MPa]	13
	Friction angle (φ) [°]	0

Figure 4-6a compares the stress-strain curves derived from the experiments and simulation of the UCS test. According to the simulated curve, the UCS is about 53.4 MPa and the Young's modulus becomes to 15.6 GPa. Figure 4-6b shows the Poisson's ratio evolved during the UCS simulation and a constant Poisson's value of about 0.2 is determined from the curve before the yielding of the rock sample. Figure 4-6c shows the force-time curve monitored during the BTS simulation. The peak loading force with a value of about 0.01 MN can be obtained from the curve. According to the analytical solution of Hondros (1959), the BTS can be calculated as follows:

$$\mathrm{BTS} = \frac{2F_P}{\pi DT} = \frac{2 \cdot 0.01 \cdot 10^6}{3.142 \cdot 0.05 \cdot 0.025} = 5.1 \text{ MPa} \quad (4\text{-}16)$$

where F_p [N] is the peak loading force, D [m] is the diameter and T [m] is the thickness of the disc. As a result, the BTS is calculated to 5.1 MPa.

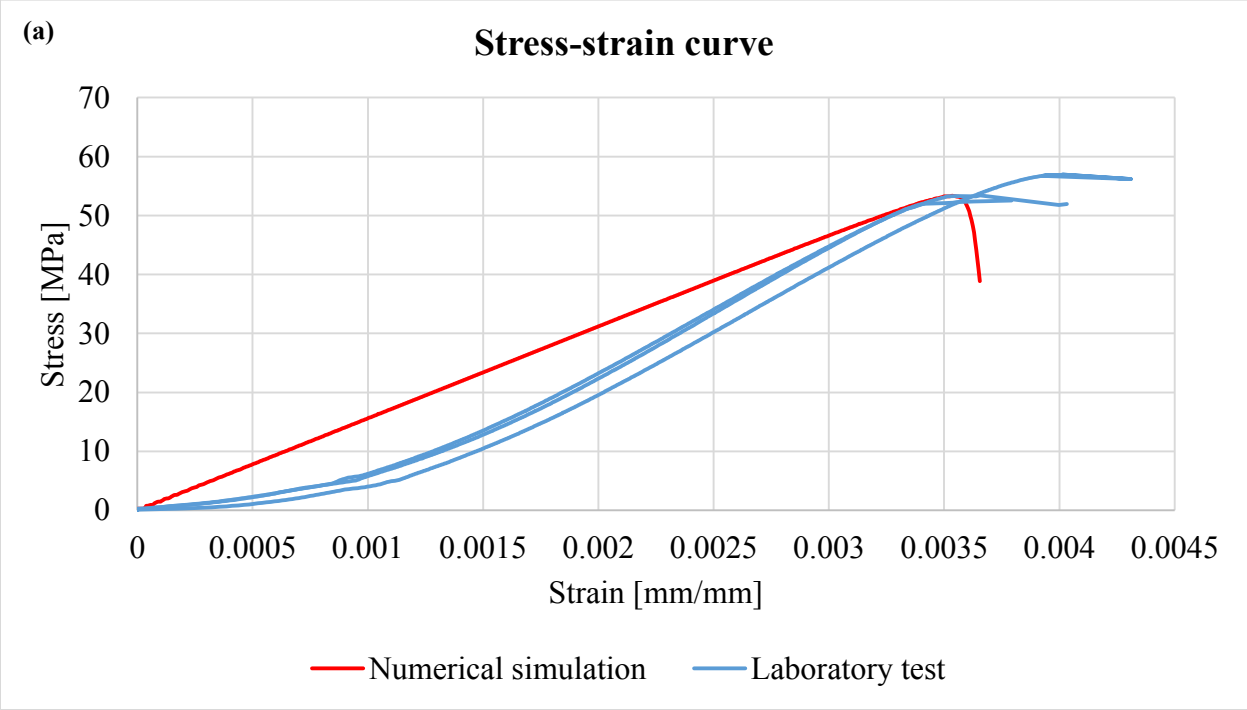

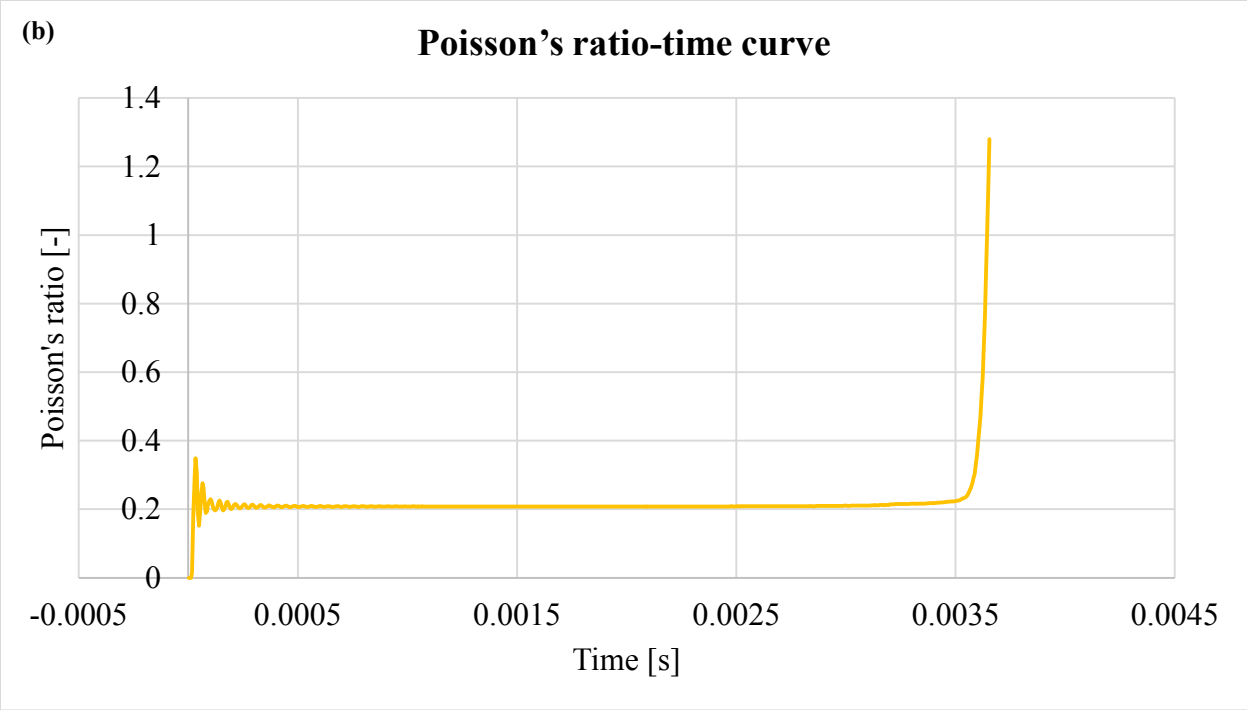

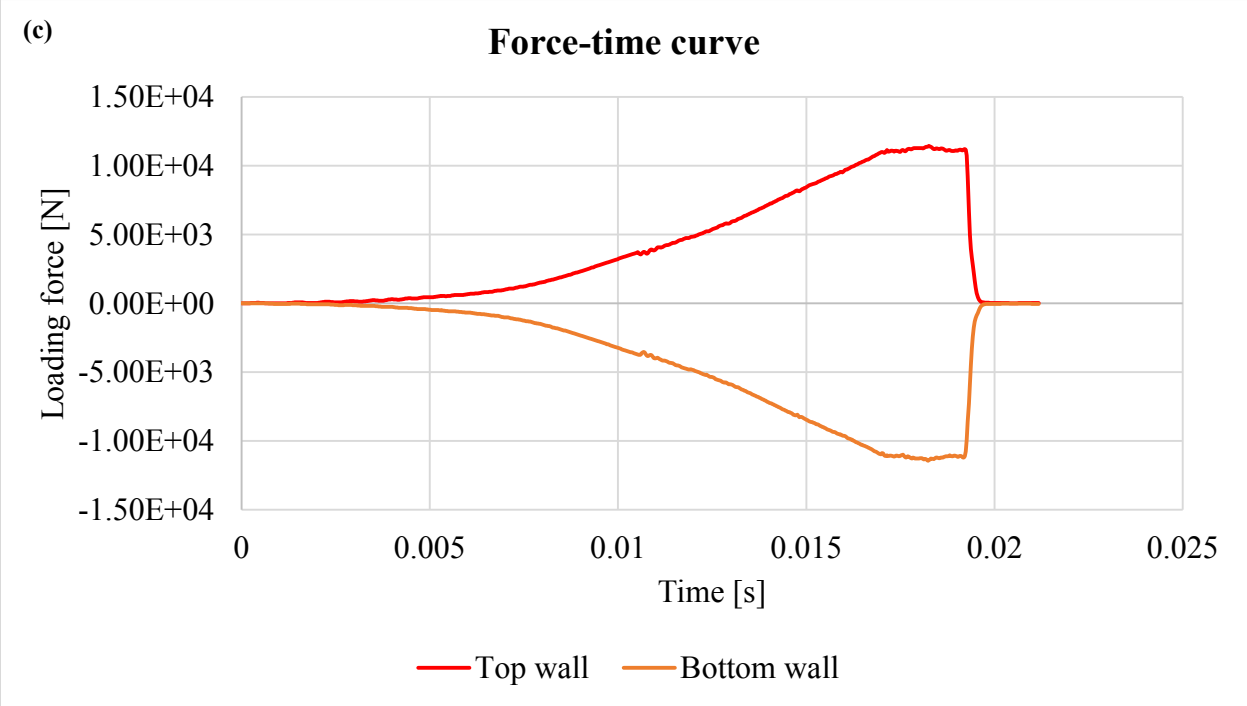

Figure 4-6 (a) Stress-strain curves derived from laboratory tests and numerical simulation of the UCS test; (b) Poisson's ratio curve evolved during the UCS simulation; (c) Force-time curve derived from numerical simulation of BTS test

The macro-properties of sandstone obtained from experiments and simulations are compared in Table 4-3. It can be seen that UCS and Poisson's ratio obtained from numerical simulations match well with the experimental results. Note that a better match could be obtained, but does not make much sense, because we have to take into account the scatter in properties also observed in the laboratory, if we compare several samples.

Table 4-3 Comparison of macro-properties between laboratory test and numerical simulation

Macro-property	**Experiment**	**Simulation**	**Deviation**
UCS [MPa]	52.6 (UCS-S3)	53.4	1.5%
Young's modulus [GPa]	17.5 (UCS-S3)	15.6	10.9%
Poisson's ratio [-]	0.21 (UCS-S1)	0.2	4.8%
BTS [MPa]	4.6 (BTS-2)	5.1	10.9%

4.2.3 Model construction and scratching scenarios

Figure 4-7 illustrates a DEM model constructed for the simulation of Cerchar scratching process. The rectangular parallelepiped model is generated with a dimension of 50 mm in length, 50 mm in width and 30 mm in height. The particle assembly consists of 134,872 particles with ball radii between 0.4 mm and 0.6 mm. A conical stylus with 90° tip angle is created to act as the stylus. This solid tool is made by SOLIDWORK (Solidwork 2010), meshed with RHINO (Rhinoceros 2014), and then implemented in PFC^{3D}. The tool is located at the left side of the sample piece with a given scratch depth of 0.5 mm. Then, the scratching process is progressed by moving the stylus from left to right over the top surface of the sample piece. For the simulation of rock scratching, the mechanical damping is set to 0.1.

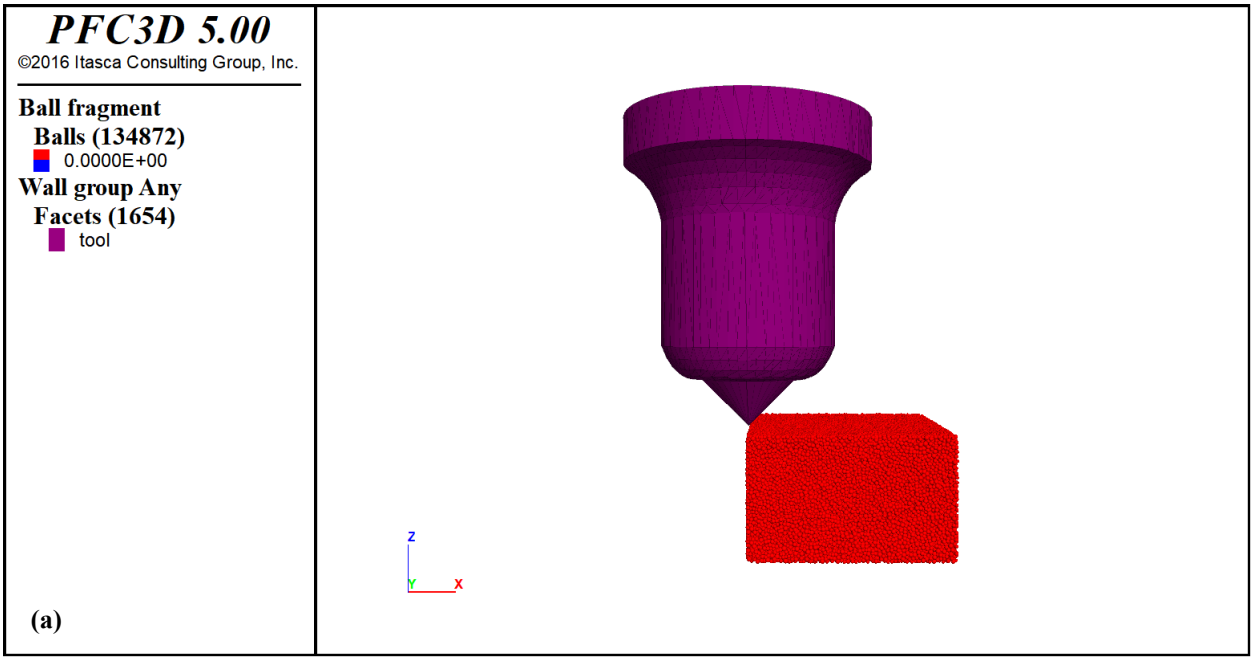

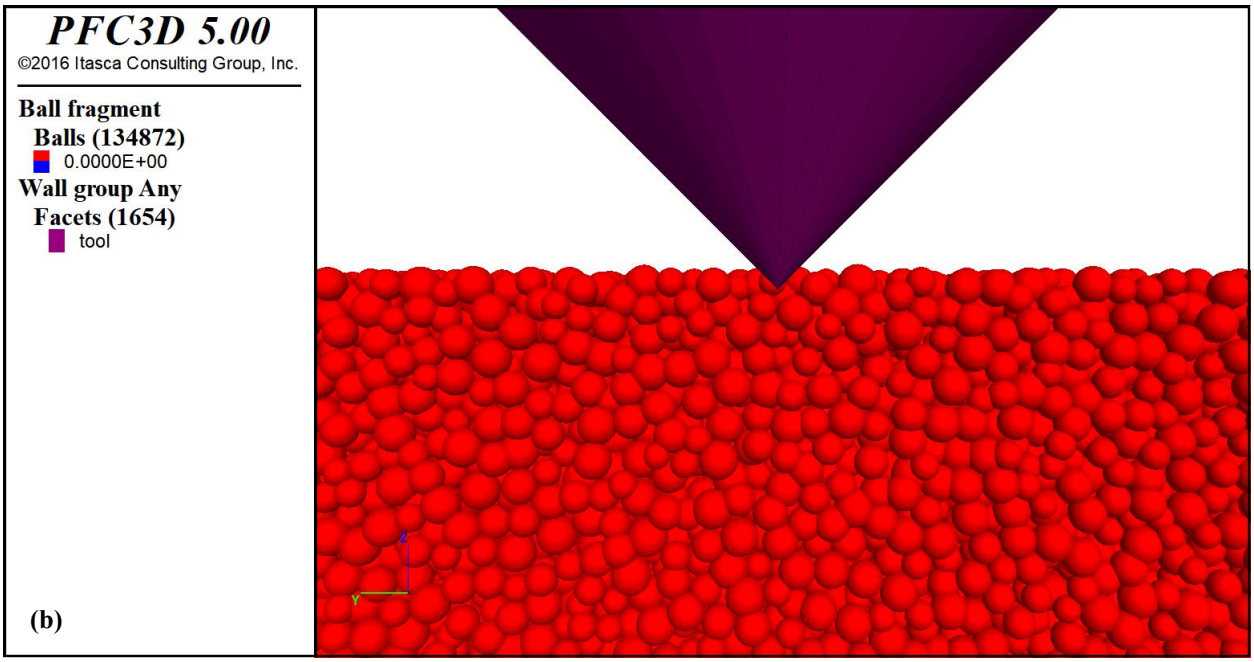

Figure 4-7 Model setup for the simulation of the Cerchar scratching process in (a) side view; (b) front view (50 mm x 50 mm x 30 mm, 134,872 particles with radius of 0.4 - 0.6 mm, depth of scratch = 0.5 mm)

According to the Cerchar testing procedure, a constant loading force of 70 N is applied on the stylus in the normal direction and a stable scratching velocity of 1 mm/s has to be applied in the horizontal direction for a sliding distance of 10 mm. In addition, experimental observation of Cerchar scratching process shows that the scratching of the stylus on the sandstone sample is accomplished with its penetration into the rock. However, in PFC, force and velocity vectors cannot be simultaneously assigned to a wall or the facets. Due to this, two scratching scenarios are considered to simulate the Cerchar scratch test. A list of test schemes for the numerical simulations of Cerchar tests is given in Table 4-4.

For scenario 1 (cases 1-1, 1-2 and 1-3), the stylus is moved only with a horizontal scratching velocity and at a given scratch depth. Normal and sideway velocities are set to zero. After many tentative simulations, the scratching velocity on the stylus is assigned to 2 m/s or 2.5 m/s. Since the depth of scratch measured on the sandstone sample is about 0.64 mm, two different depths (0.5 mm and 0.7 mm) are used at the beginning of each simulation to see how experimentally obtained scratching force varies within a range of simulation results. The sliding distance of the stylus over the model surface is lengthened to 25 mm in order to have a better understanding of evolution of scratching forces and identification of rock fragmentation as well as fracture formation. The corresponding calculation time is 0.0125 s or 0.01 s depending on the specified scratching velocity. The micro-parameters for the model are taken from Table 4-2.

For scenario 2 (cases 2-1, 2-2 and 2-3), besides the horizontal velocity, a small velocity in the vertical direction is applied on the stylus during the rock scratching. In this scenario, the stylus is located on the top surface of the sample piece, which means that the scratch depth starts at 0 mm before a simulation begins. Similarly, two scratching velocities (2.5 m/s and 3 m/s) and two indentation velocities (0.05 m/s and 0.07 m/s) are used in order to coincide with the final scratch depth of 0.64 mm, as well as to see the variation of simulation results.

Compared to scenario 1, which can be regarded as a pure scratching (or cutting) process, scenario 2 represents rather the rock breakage under an indenting-scratching process, which can be attributed to the fracture theory of brittle material indentation.

Table 4-4 Test scheme for the simulation of Cerchar test

Parameter	**Scratching scenario 1**			**Scratching scenario 2**		
	Case 1-1	**Case 1-2**	**Case 1-3**	**Case 2-1**	**Case 2-2**	**Case 2-3**
Scratching velocity (v_s) [m/s]	2	2.5	2.5	2.5	2.5	3
Indentation velocity (v_i) [m/s]	0	0	0	0.05	0.07	0.07
Initial depth of scratch [mm]	0.5	0.5	0.7	0	0	0
Final depth of scratch [mm]	0.5	0.5	0.7	0.5	0.7	0.588
Testing distance (d_s) [mm]	25	25	25	25	25	25
Computational time (t) [s]	0.0125	0.01	0.01	0.01	0.01	0.0084

4.2.4 Comparison of tool forces between numerical and experimental studies

In the rock cutting process, the applied tool forces can be decomposed into three orthogonal components: normal force, cutting force and sideway force. Normal force is perpendicular to the cutting direction, cutting force is in line with the cutting direction, and sideway force is lateral to the cutting direction. In this work, these definitions are adopted to determine the resultant tool forces derived from the scratching simulations.

Figure 4-9 shows the normal, scratching and sideway force, respectively, evolved for case 1-1. It is obvious that the scratching force-displacement curve derived from the simulation develops in the same way as the experimental result (Figure 4-9b versus Figure 4-8). However, in the simulation, there are a few moments, where the corresponding cutting force is close to zero. This phenomenon can be attributed to the fact that the balls cannot be crushed or ground in PFC instead of that they are removed completely as a whole when bond is broken. Then, the tool needs a while to interact with the next balls again. Different from the experimental calculation method, the mean tool forces are calculated as the average of the force data over the sliding distance of 25 mm. As a result, the mean normal, scratching and sideway force are found to be 140.4 N, 89.2 N and 10.0 N, respectively. Since the sideway force is less important than the other two forces, the analysis is only focused on the normal force and scratching force. By comparing the mean normal and scratching forces between the numerical and experimental studies, it is found that the numerically obtained normal force is two times higher than the experimentally defined normal force (140.4 N

versus 70 N), while the simulated scratching force shows a good agreement with the experimental result (89.2 N versus 84.8 N).

Figure 4-10 shows the evolution of applied tool forces for case 2-3. Similarly, the evolution of scratching force during the simulation matches more or less with the experimental result (Figure 4-10b versus Figure 4-8). The mean normal force obtained from the simulation is also about two times higher compared to the experiment (154.9 N versus 70 N), but the scratching force results coincide with each other (86.4 N versus 84.8 N).

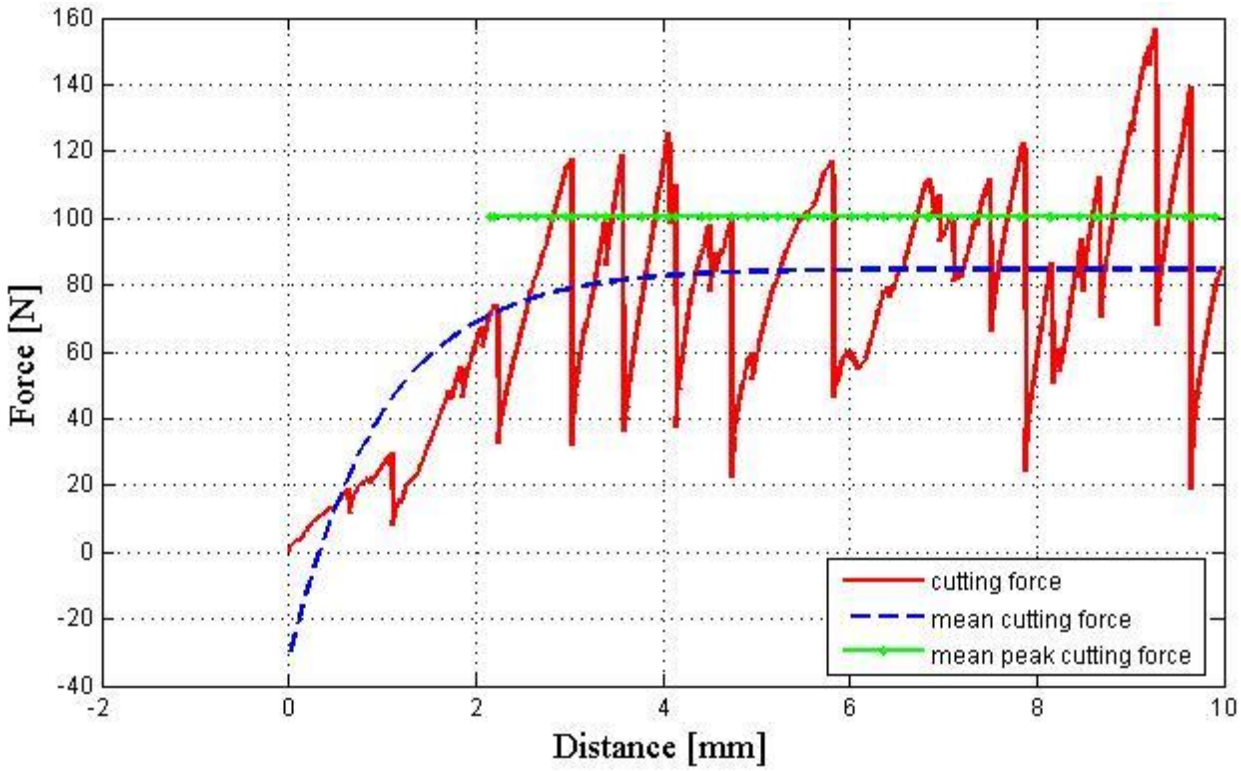

Figure 4-8 Evolution of scratching force for sandstone (from experiment: scratching velocity = 1 mm/s, initial depth of scratch = 0 mm, maximum depth of scratch = 0.64 mm, mean scratching force = 84.8 N, mean peak scratching force = 100.4 N)

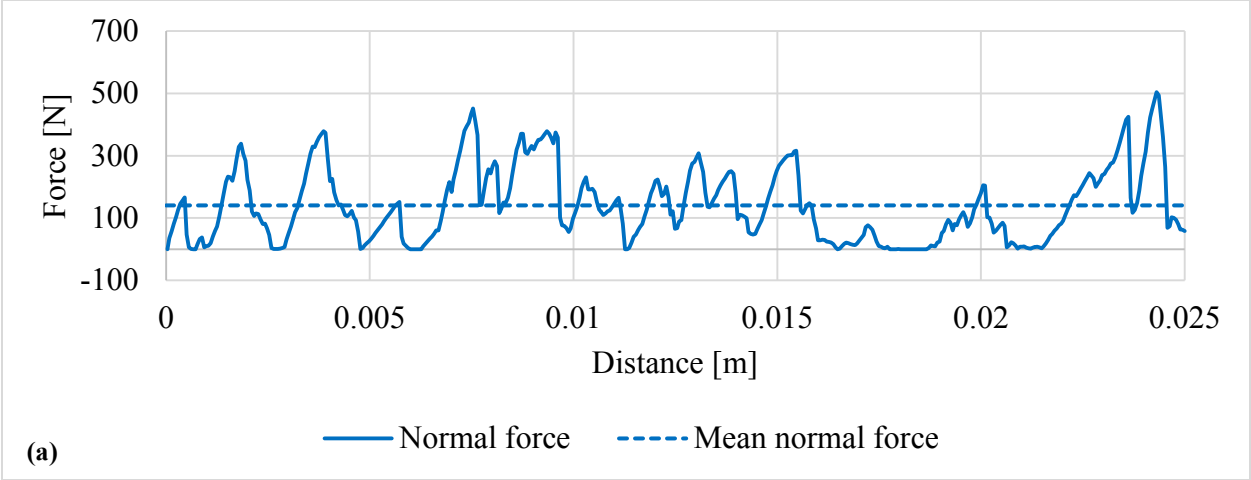

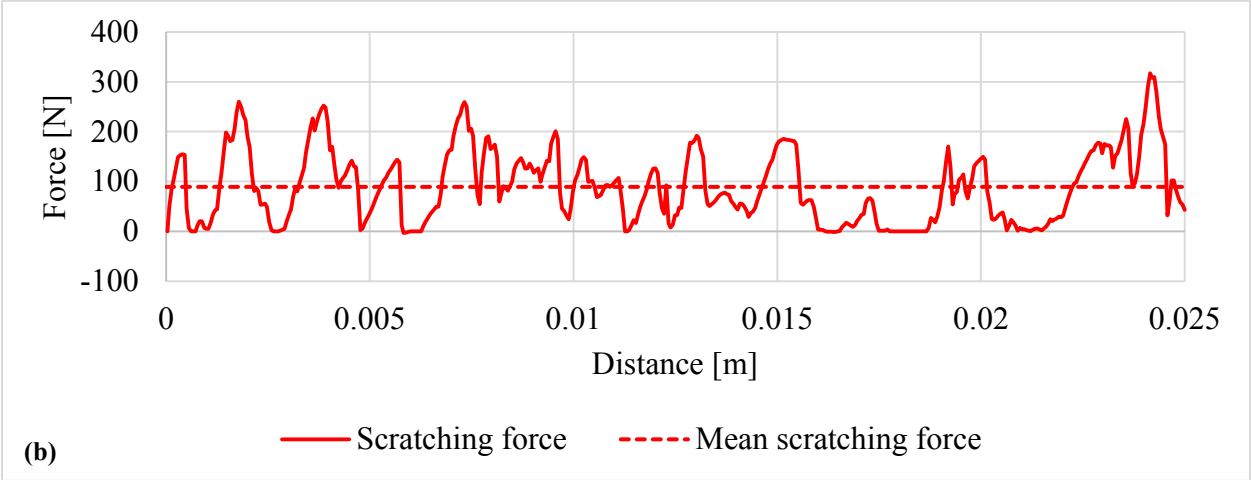

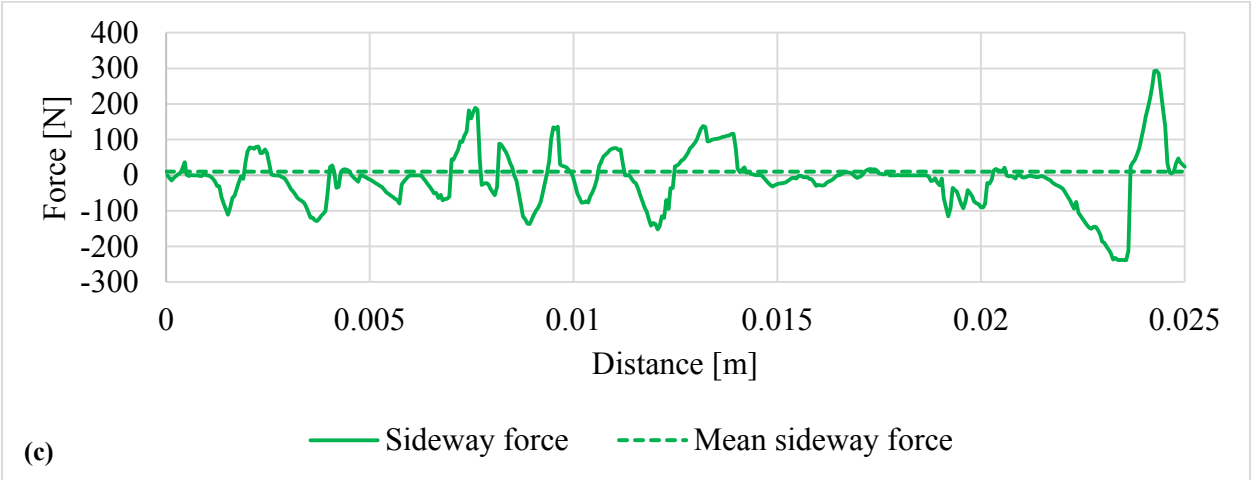

Figure 4-9 Evolution of (a) normal force; (b) scratching force; (c) sideway force (case 1-1: scratching velocity = 2 m/s, indentation velocity = 0 m/s, initial/final depth of scratch = 0.5/0.5 mm)

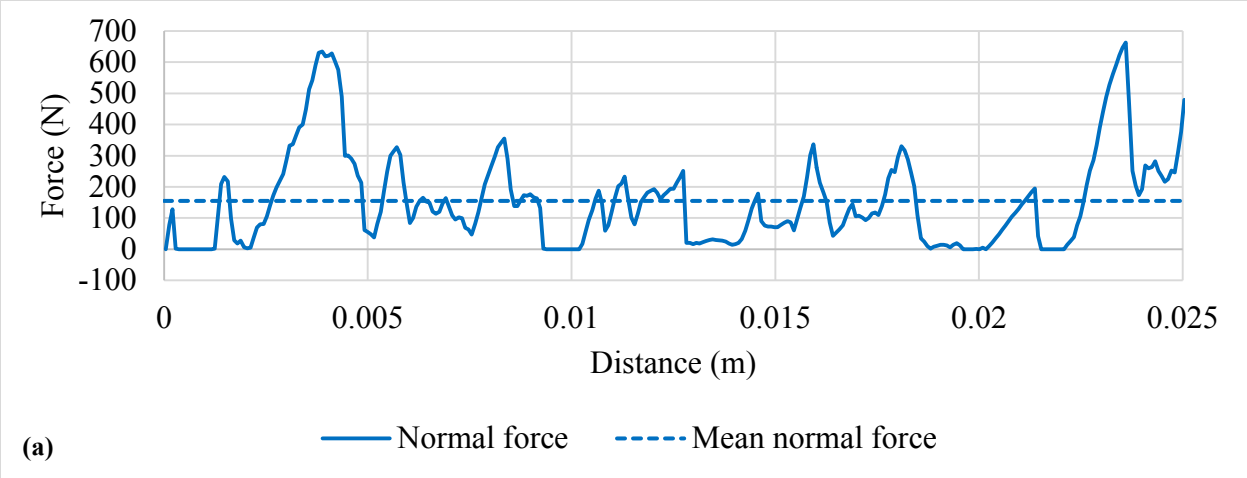

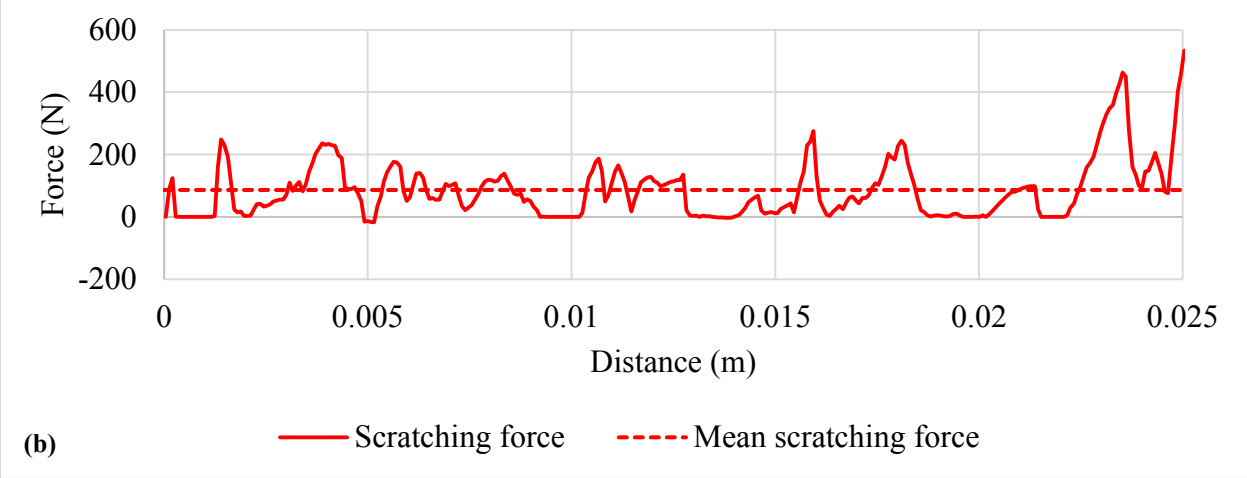

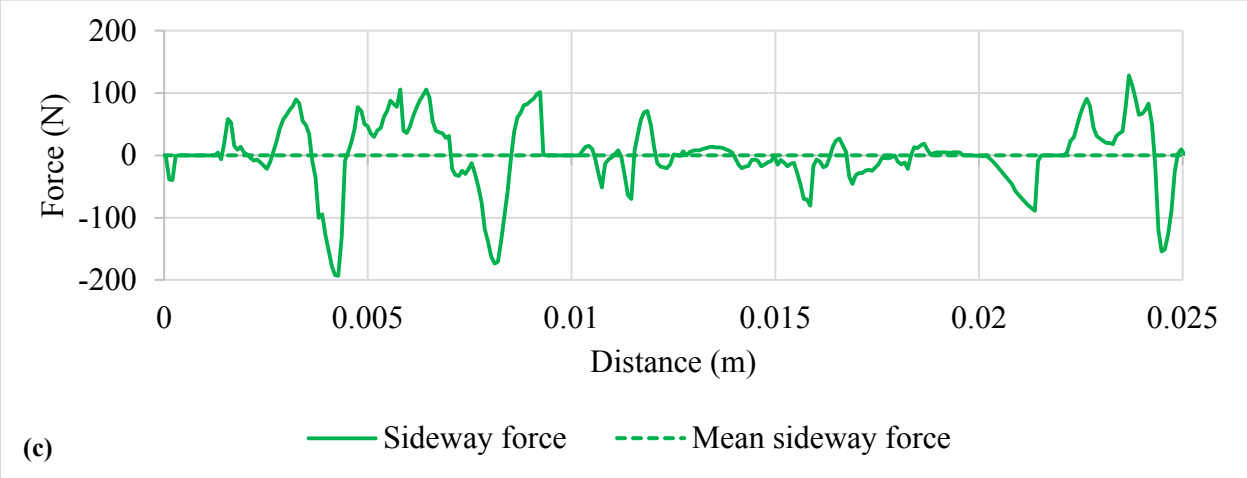

Figure 4-10 Evolution of (a) normal force; (b) cutting force; (c) sideway force (case 2-3: scratching velocity = 3 m/s, indentation velocity = 0.07 m/s, initial/final depth of scratch = 0/0.7 mm)

Table 4-5 compares the applied tool forces obtained numerically under different scratching scenarios. According to the simulation result, it can be said that both, normal and scratching forces, increase when (1) the scratching velocity is increased from 2 m/s to 2.5 m/s, (2) the scratch depth is increased from 0.5 mm to 0.7 mm and (3) the indentation velocity is increased from 0.05 m/s to 0.07 m/s.

Table 4-5 Comparison of applied tool forces between experimental and numerical studies

Scenario	**Testing condition**	**Mean normal force [N]**	**Mean scratching force [N]**	**Mean sideway force [N]**
Experiment	v_s = 1 mm/s FN = 70 N Ds = 0.64 mm	70	84.8	-
Case 1-1	v_s = 2 m/s v_i = 0 m/s Ds = 0.5 mm	140.4	89.2	10.0
Case 1-2	v_s = 2.5 m/s v_i = 0 m/s Ds = 0.5 mm	173.1	96.7	5.1
Case 1-3	v_s = 2.5 m/s v_i = 0 m/s Ds = 0.7 mm	189.0	127.2	5.6
Case 2-1	v_s = 2.5 m/s v_i = 0.05 m/s Ds = 0.5 mm	121.5	69.8	18.8
Case 2-2	v_s = 2.5 m/s v_i = 0.07 m/s Ds = 0.7 mm	124.9	68.8	11.8
Case 2-3	v_s = 3 m/s v_i = 0.07 m/s Ds = 0.7 mm	154.9	86.4	0.2

4.2.5 Investigation of rock fragmentation and fracture formation

The crack initiation and propagation beneath the sample surface cannot be observed in the Cerchar measurement, but this can be analyzed by means of the numerical simulation. Figure 4-11 and Figure 4-12 illustrate the rock fragmentation and crack initiation and propagation during the rock scratching for case 1-1. Seen from Figure 4-11, as the stylus peels off the particles, micro-cracks are initiated and propagate from the stylus tip, and then lead to the chip formation. The green and blue circles, which are visible in Figure 4-12, indicate the cracks induced by tensile or shear failure. After the stylus tip interacts with the particles, tension and shear micro-cracks are initiated and propagate from the tool tip, which results in fractures. With ongoing stylus movement, more and more bonded particles are detached and removed by the stylus and forward propagation of cracks leads to the removal of the front particles. Moreover, the fracture geometry formed beneath the rock surface can be determined based on the induced tension or shear cracks. Seen from Figure 4-12, it is found that the maximum damage depth reaches about 4.5 mm and the damage length and width are about 29.1 mm and 13.2 mm, respectively. Results of damage geometry (length, width and depth) under different scratching scenarios are summarized in Table 4-6.

During the rock scratching, both tensile and shear failures are considered co-responsible for the rock breakage. Figure 4-13 shows the accumulated number of cracks induced by tensile and shear failure, respectively, as well as in total. It is found that the number of tensile cracks is approximately three times higher than the number of shear cracks (2,748 versus 902), which indicates that the failure mode in the rock scratching simulation model is dominant a tensile one. This finding shows a good agreement with Nishimatsu's rock cutting theory (Nishimatsu 1972).

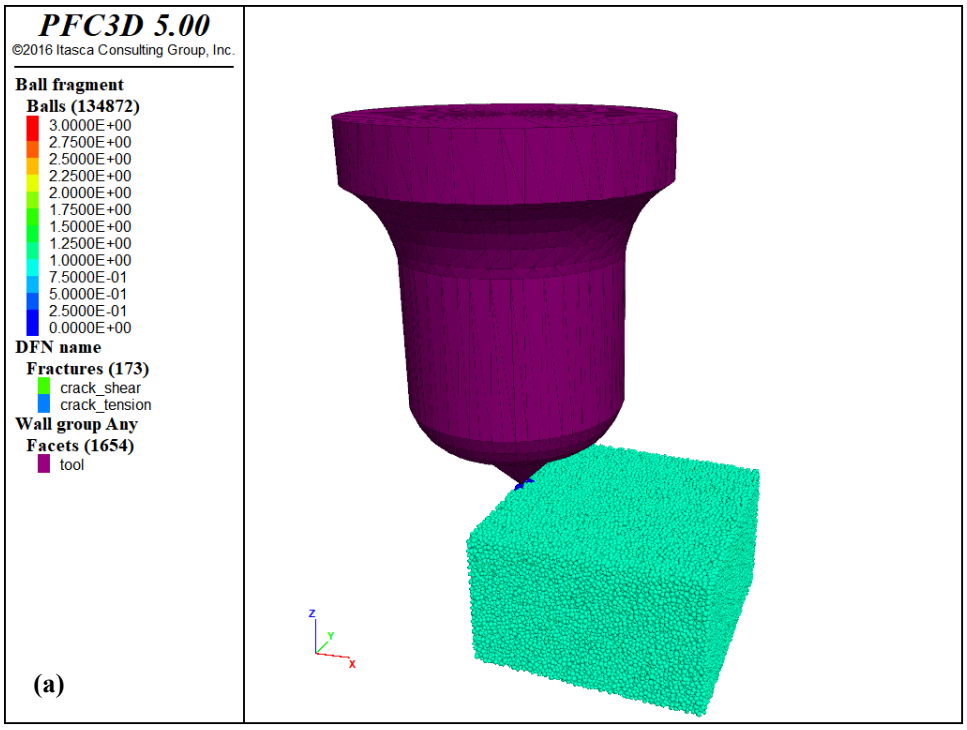
PFC3D 5.00
©2016 Itasca Consulting Group, Inc.
Ball fragment
Balls (134872)
3.0000E+00
2.7500E+00
2.5000E+00
2.2500E+00
2.0000E+00
1.7500E+00
1.5000E+00
1.2500E+00
1.0000E+00
7.5000E-01
5.0000E-01
2.5000E-01
0.0000E+00
DFN name
Fractures (173)
crack_shear
crack_tension
Wall group Any
Facets (1654)
tool
(a)

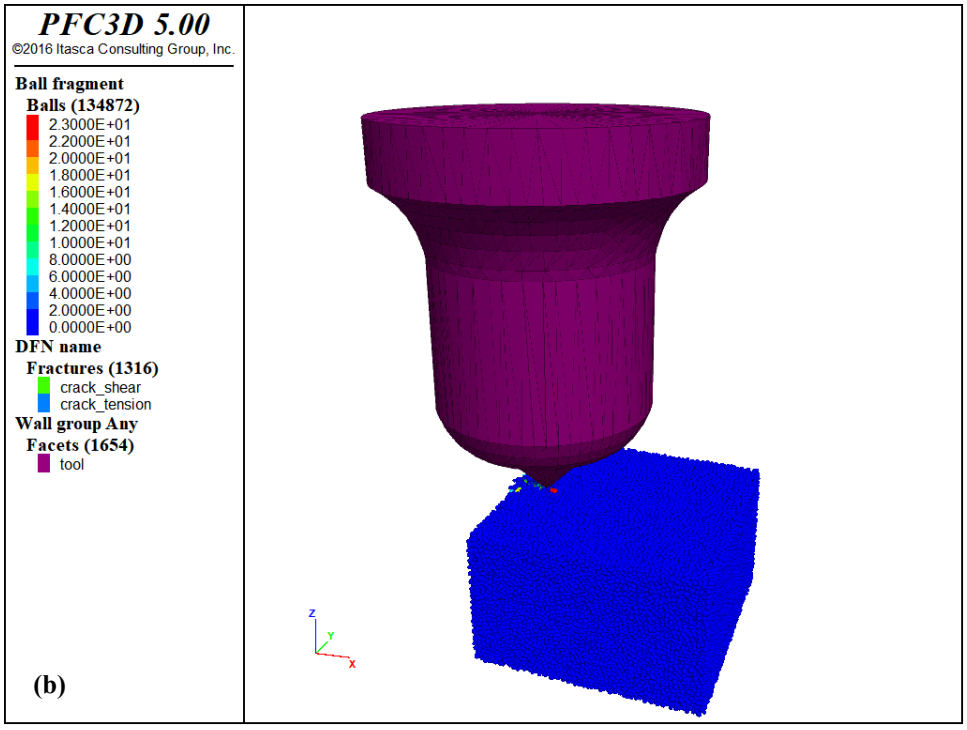
PFC3D 5.00
©2016 Itasca Consulting Group, Inc.
Ball fragment
Balls (134872)
2.3000E+01
2.2000E+01
2.0000E+01
1.8000E+01
1.6000E+01
1.4000E+01
1.2000E+01
1.0000E+01
8.0000E+00
6.0000E+00
4.0000E+00
2.0000E+00
0.0000E+00
DFN name
Fractures (1316)
crack_shear
crack_tension
Wall group Any
Facets (1654)
tool
(b)

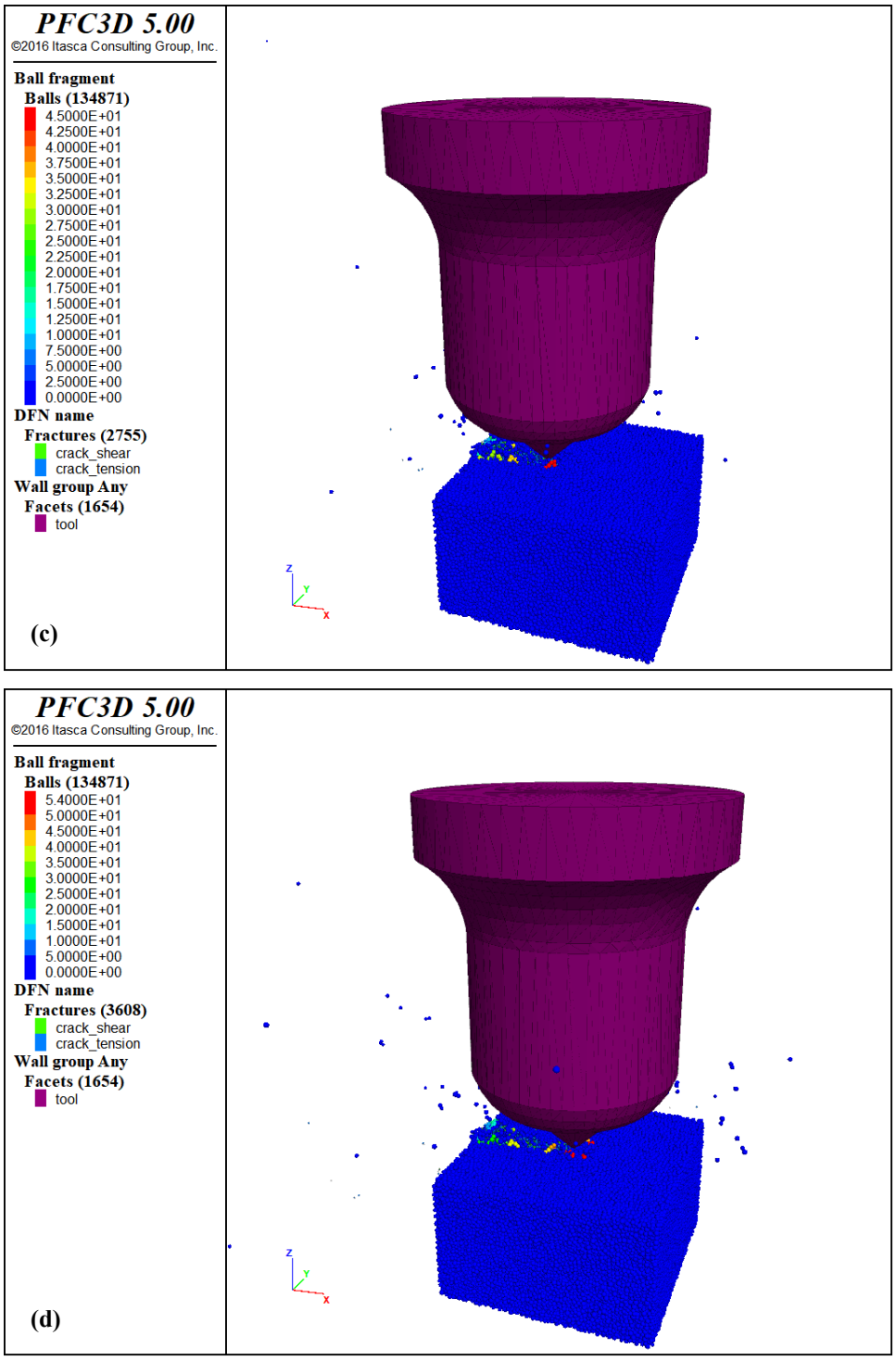

Figure 4-11 Rock fragmentation after (a) 0.0005 s; (b) 0.0035 s; (c) 0.0085 s; (d) 0.0125 s (case 1-1: scratching velocity = 2 m/s, indentation velocity = 0 m/s, initial/final depth of scratch = 0.5/0.5 mm)

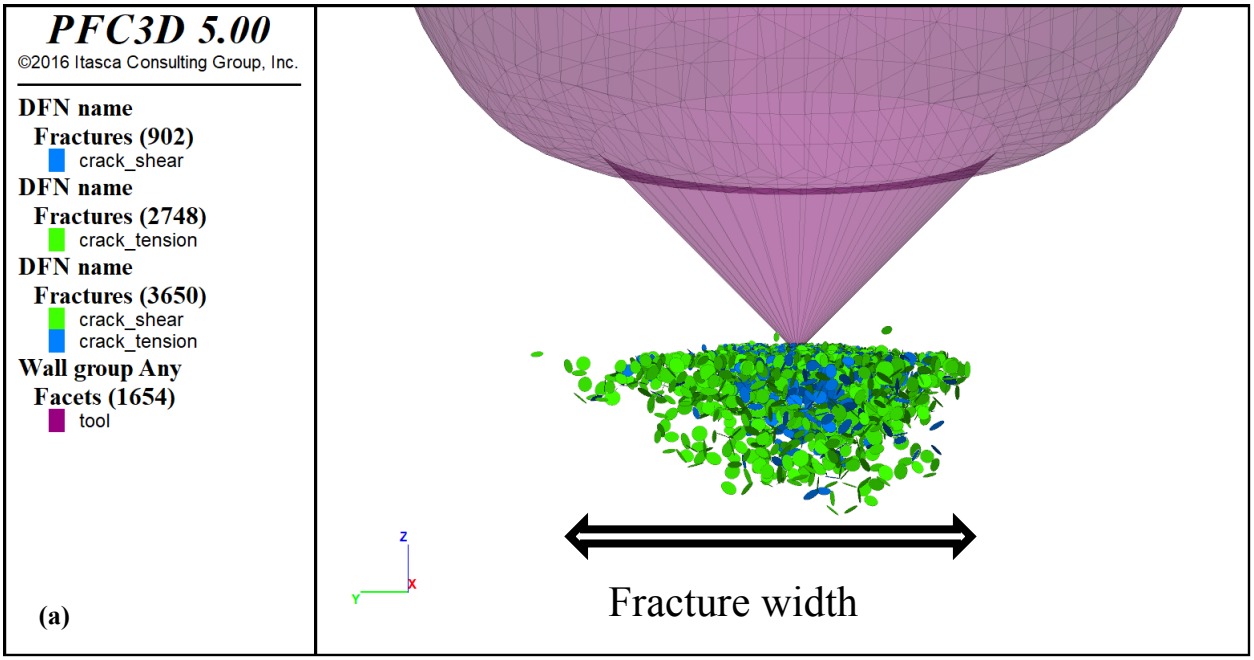
PFC3D 5.00
©2016 Itasca Consulting Group, Inc.
DFN name
Fractures (902)
crack_shear
DFN name
Fractures (2748)
crack_tension
DFN name
Fractures (3650)
crack_shear
crack_tension
Wall group Any
Facets (1654)
tool
(a)
Fracture width

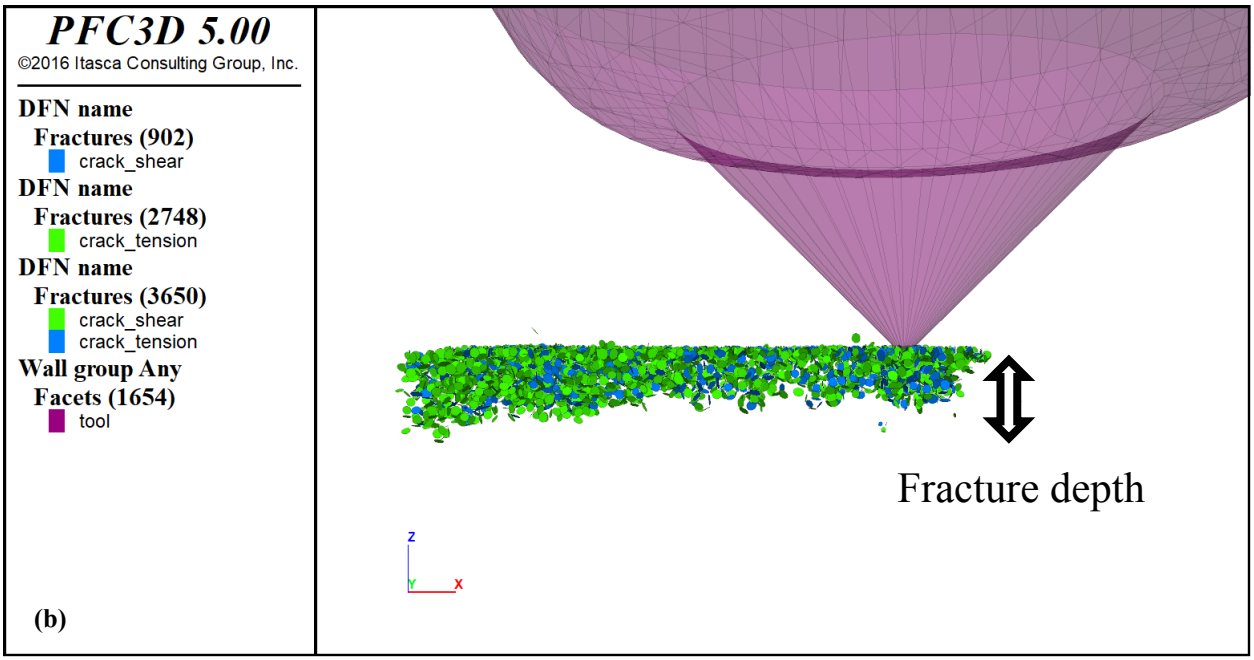
PFC3D 5.00
©2016 Itasca Consulting Group, Inc.
DFN name
Fractures (902)
crack_shear
DFN name
Fractures (2748)
crack_tension
DFN name
Fractures (3650)
crack_shear
crack_tension
Wall group Any
Facets (1654)
tool
(b)
Fracture depth

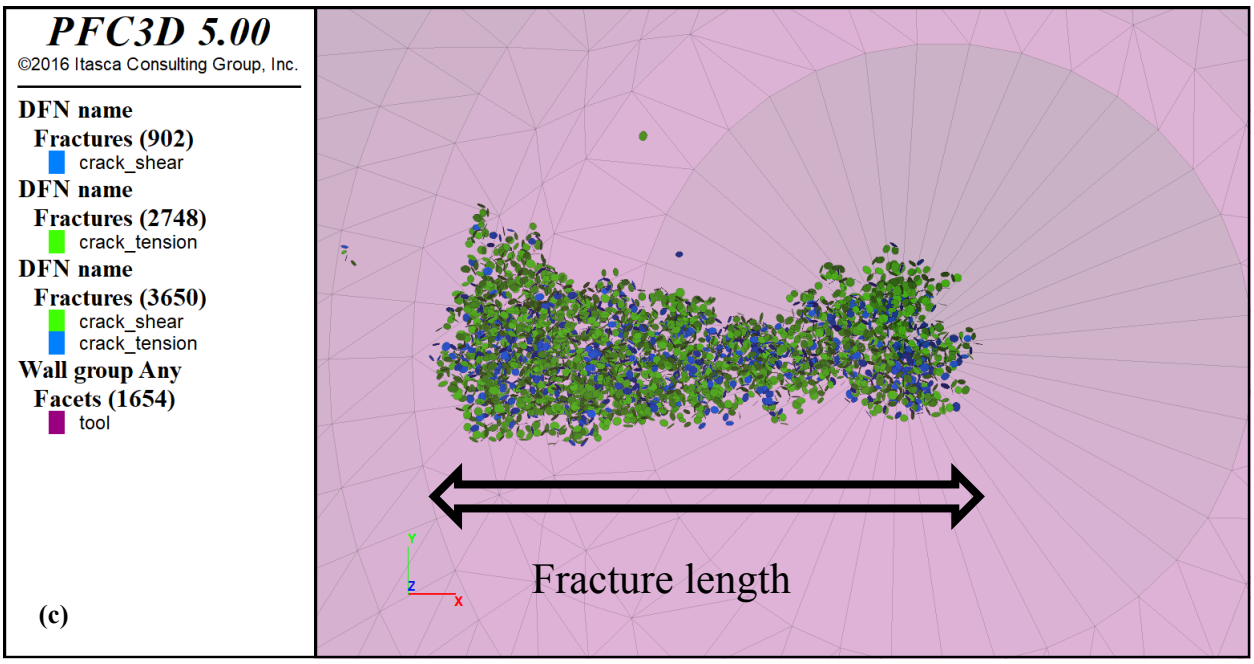

Figure 4-12 Measurement of damage geometry in (a) front view; (b) side view; (c) top view (case 1-1: scratching velocity = 2 m/s, indentation velocity = 0 m/s, initial/final depth of scratch = 0.5/0.5 mm)

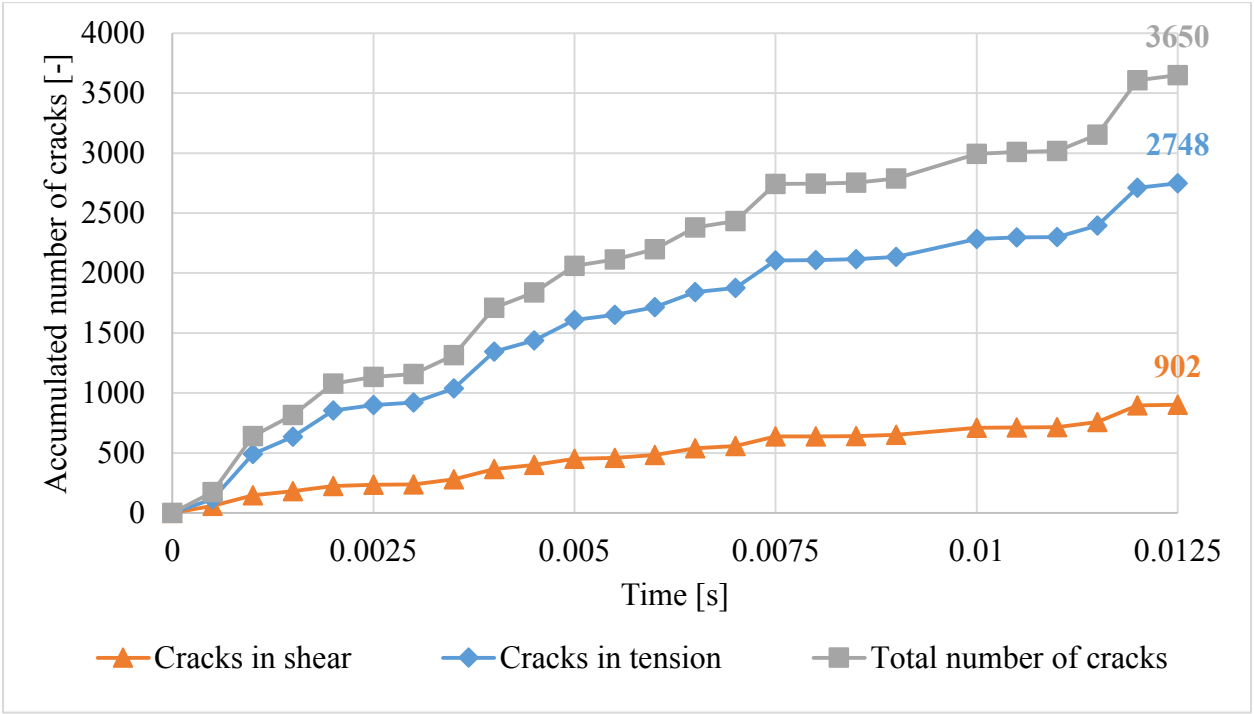

Figure 4-13 Evolution of accumulated number of cracks versus time (case 1-1: scratching velocity = 2 m/s, indentation velocity = 0 m/s, initial/final depth of scratch = 0.5/0.5 mm)

Table 4-6 compares the results of induced number of cracks and provides fracture geometry under different scratching scenarios. According to the simulation result, the following findings can be drawn: more and larger fractures are formed when (1) the scratching velocity is increased from 2 m/s to 2.5 m/s, (2) the scratch depth is increased from 0.5 mm to 0.7 mm and (3) the indentation velocity is increased from 0.05 m/s to 0.07 m/s.

Table 4-6 Accumulated number of cracks and damage geometry obtained from numerical study

Scenario	**Testing condition**	**Cracks in shear [-]**	**Cracks in tension [-]**	**Total number of cracks [-]**	**Damage geometry [mm]**
Case 1-1	v_s = 2 m/s v_i = 0 m/s Ds = 0.5 mm	902	2748	3650	Length: 29.10 Width: 13.15 Depth: 4.50
Case 1-2	v_s = 2.5 m/s v_i = 0 m/s Ds = 0.5 mm	1022	3362	4384	Length: 31.66 Width: 14.34 Depth: 4.94
Case 1-3	v_s = 2.5 m/s v_i = 0 m/s Ds = 0.7 mm	1091	3412	4503	Length: 29.27 Width: 13.97 Depth: 5.97
Case 2-1	v_s = 2.5 m/s v_i = 0.05 m/s Ds = 0.5 mm	757	2207	2964	Length: 28.35 Width: 10.69 Depth: 4.96
Case 2-2	v_s = 2.5 m/s v_i = 0.07 m/s Ds = 0.7 mm	700	2280	2980	Length: 30.43 Width: 11.02 Depth: 4.87
Case 2-3	v_s = 3 m/s v_i = 0.07 m/s Ds = 0.7 mm	995	3001	3996	Length: 36.23 Width: 11.70 Depth: 5.03

4.3 Discussions

In this work, as discussed above, two scratching scenarios are used to simulate the Cerchar scratch test. First, a pure scratching process is conducted by specifying a horizontal velocity on the stylus with a given scratch depth. Second, a combined scratching and indenting process is simulated by applying both, vertical and horizontal velocities on the stylus. For both cases, the resultant scratching force obtained numerically is more or less the same as that measured in the laboratory, while the normal force is greater by a factor of about 2 compared to the laboratory result.

Hence, to reduce the magnitude of the normal force, we can consider another scratching scenario by using the wall-servo mechanism, which provides an ability to control the velocity of the wall using a servo-mechanism to maintain a desired force. In other words, if the recorded normal force exceeds or is becoming smaller than the desired normal force, for example, of 70 N, the normal velocity on the wall is adjusted (automatically de- or increased) so that the desired force is reached.

The major task of the numerical simulations of Cerchar scratch test is to study the interaction between the stylus and the rock, namely to see how the tool force evolves in the course of the scratching process as well as how fractures are initiated and propagate beneath the sample surface under the action of a cutting tool. Therefore, the two simplified simulation approaches are sufficient, especially if the major aim is to investigate the influence of different factors on the scratching process in a qualitative manner.

Note that the difference of scratching forces between experimental and numerical studies can be attributed to several factors, such as rock mineralogy and microstructure, scratching (or cutting) velocity and depth of scratch (or cut), abrasion of tools, and temperature.

The difference is due to the petrological-mineralogical property of the rocks, particularly important are grain size within the rock. It has been found in the rock cutting simulation that the cutting force increases with increasing particle size. This is reasonable because the larger the particles created in the DEM model, the more forces are required to cut them off. Therefore, if the ball radius is considerably reduced in the simulation, the cutting force could be decreased significantly. However, when the model dimension is kept constant, the number of balls will be dramatically

increased, as same as the computational time. Moreover, the grain shape effect cannot be neglected. In general, more forces are required for cutting the irregular grains. The shape of mineral grains varies in the real rock material due to the geological process, as same as their hardness and abrasive property, but only spherical balls with the identical attributes are defined and used in PFC. In addition, rocks are natural materials and fractures, cracks and fissures may exist within the rock, which could reduce the ability of rock resisting against the action of mechanical tools, but these features are not considered in the DEM model. Therefore, the experimental cutting forces may not be identical with the numerical results.

The difference can also be attributed to the testing parameters used for the simulation which does not coincide with the actual experimental testing condition. In the numerical simulation of rock cutting, cutting velocity and depth of cut are two important factors affecting the applied tool forces. Experimental and numerical studies have proven that a faster cutting velocity associated with a larger cutting depth can cause a higher cutting force (Verhoef 1997, Menezes et al. 2014). A challenge in the rock cutting simulation lies in rendering the cutting velocity on the mechanical tool. Because the balls cannot be crushed and they are moved away as a whole one from the sample piece, if the specified cutting velocity is defined as too slow, the cutting tool needs a longer time until it interacts with the new balls again. Then, the calculated mean cutting force is reduced.

Another reason for the difference between experimental and numerical results is due to the tool wear and its impact on the pressure and stress distribution generated on the cutting tool. Su and Akcin (2011) stated: when a worn or rounded pick is used to cut the rock, the resultant force will inevitably be increased. Van Wyk et al. (2014) emphasized that only a small amount of wear on the cutter can influence a cutting process to a great extent and make the cutting more difficult. In the present simulation, a sharp stylus is used and does not become blunt, while the abrasion occurs on the stylus tip during the Cerchar measurement. Therefore, a deviation between the numerical and experimental results can be expected.

It has also been found during the rock cutting process that heating (or temperature) combined with rock abrasivity can affect the applied cutting force. Overall, the more abrasive the rock, the greater the heating impact and the lower the critical cutting velocity (Hurt and MacAndrew 1985). Under

the cooperation of diverse cutting conditions, the pick tip might be suffered to an excessive thermal stress on itself and more forces might be required for cutting rocks. The heating effect is not taken into account in the numerical simulation.

5. Application of numerical model for rock cutting

In rock and mining engineering, conical (or point-attack) picks assembled on roadheaders, continuous miners, longwall ploughs and shearers are the essential cutting tools used to excavate hard rocks or coal. Hence, it is important to understand the cutting behavior in rock fragmentation and to estimate the cutting performance of a mechanical machine. For this propose, rock cutting experiments including in-situ, full-scale and small-scale tests have been conducted by many researchers (Fowell and McFeat-Smith 1976, Fowell et al. 1994, Bilgin et al. 2006, Balci and Bilgin 2007). Nevertheless, laboratory rock cutting tests are usually costly and time consumption and sometimes it is difficult to gain a large rock sample for a scale-one rock cutting experiment. Moreover, it is impossible to detect the fracture formation in detail during the rock cutting process. Due to this, numerical simulation of rock cutting can be used to investigate the interaction between the rock and the applied tools.

With the development of computer technology, numerical investigations of rock cutting have been performed by using various modeling techniques, such as finite element method (FEM), finite difference method (FDM), discrete element method (DEM) and boundary element method (BEM). Among these, the DEM is the most capable and suitable tool to provide a better understanding of rock-tool interactions. It has also been proven as an efficient and economical approach to give a useful insight into rock fragmentation under different cutting scenarios.

During the past few years, numerical simulations of rock cutting using DEM have been conducted by many researchers. Just to name a few, Huang et al. (1999, 2013) discussed ductile and brittle failure modes during rock cutting, which is dependent on the depth of cut, using 2D models. Lei and Kaitkay (2003, 2004) developed a methodology to apply hydrostatic pressure on a sample surface for the rock cutting simulation using a 2D approach, and studied the influence of simulation condition-based parameters on the resulting cutting force. Su and Akcin (2011) extended 2D simulations of rock cutting tests towards 3D, and established a relationship of cutting forces between numerical, experimental and theoretical results. Rojek et al. (2011) conducted the DEM simulation of rock cutting subjected to a conical pick to study the rock fragmentation and its relation to applied cutting force in both, 2D and 3D. Lunow and Konietzky (2012) used two

different DEM-based codes to simulate the rock indenting and cutting by specifying different cutting parameters, such as indentation depth, shape and tip angle of cutter and rake angle. Van Wyk et al. (2014) performed simulations of the rock cutting process with two different cutting tools (chisel- and button-shaped), and investigated the influence of particle size on the resultant tool forces using 3D models.

In this work, numerical simulations of rock cutting are conducted based on the calibrated sandstone model to see how cutting force varies under a wide range of cutting conditions. The effecting factors can be divided into two parts: tool geometry like pick type, tip angle and tip wear, and cutting parameters including cutting velocity, depth of cut and rake angle. Figure 5-1 illustrates the two dimensional definition of cutting parameters for rock cutting with a conical pick. The sideway force is neglected. A list of test schemes for the numerical investigations of rock cutting under different cutting conditions is given in Table 5-1.

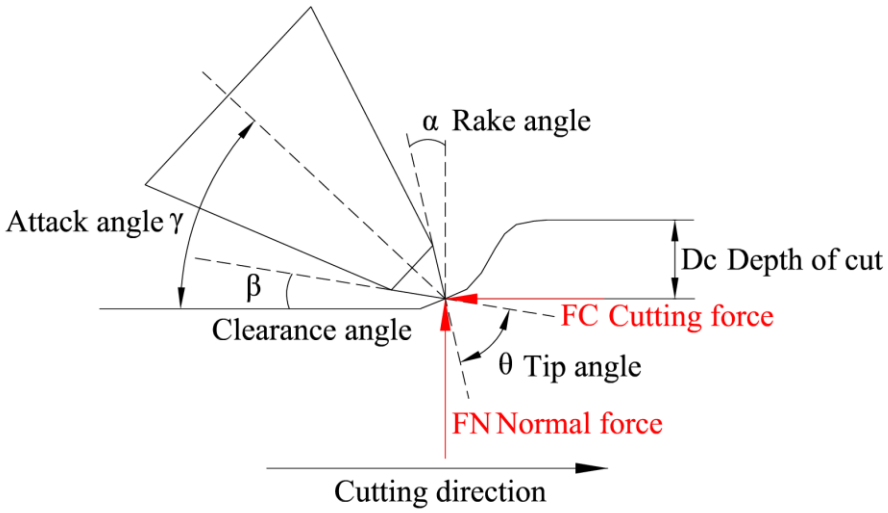

Figure 5-1 Definition of cutting parameters for conical pick

Table 5-1 Test scheme for the simulation of rock cutting

Tool geometry	
Pick type	Conical / Ballistic / Rounded
Tip angle (θ) [°]	60 / 75 / 90 / 105
Tip wear (or top bluntness) (W_t) [mm]	0 / 0.1·$Ø_B$ / 0.2·$Ø_B$ / 0.5·$Ø_B$
Cutting parameter	
Cutting velocity (v_c) [m/s]	1 / 2.5 / 5 / 10
Depth of cut (D_c) [mm]	1 / 3 / 5 / 7
Rake angle (α) [°]	-52.5 / -45 / -37.5 / -30 / -15 / 0 / 7.5 / 12.5 / 20

5.1 Model setup and simulation results of rock cutting

Figure 5-2 illustrates the model setup for the numerical simulation of rock cutting. The generation of particle assembly is the same as constructed for the sandstone model. However, compared to the Cerchar test, a conical pick with 75° tip angle is created to cut the sample piece and a negative rake angle of -15° is set between the tool and the rock during the cutting process. The cutting velocity is fixed at 5 m/s in order to reduce the calculation time. Normal and sideway velocities are zero. The depth of cut is assigned to 3 mm to ensure that the pick can interact with at least three particles in the assembly. The cutting distance is 25 mm and the corresponding calculation time is 0.005 s. The micro-parameters are inherited from those calibrated for the sandstone. The coefficient of mechanical damping is set to 0.1.

Figure 5-3 shows the evolution of applied tool forces during the rock cutting simulation. After the calculation, the mean normal, cutting and sideway force are found to be 319.8 N, 391.3 N and 2.6 N, respectively. Figure 5-4 and Figure 5-5 illustrate the rock fragmentation and crack propagation, respectively, in the final state of the simulation. The rock fragmentation is represented by the separation of bonded particles (or balls). The number of tensile-induced cracks is much higher than the number of shear-induced cracks (10,178 versus 2,736). This indicates that the failure mode in the rock cutting simulation model is dominant a tensile one. The total accumulated number of cracks is 12,914.

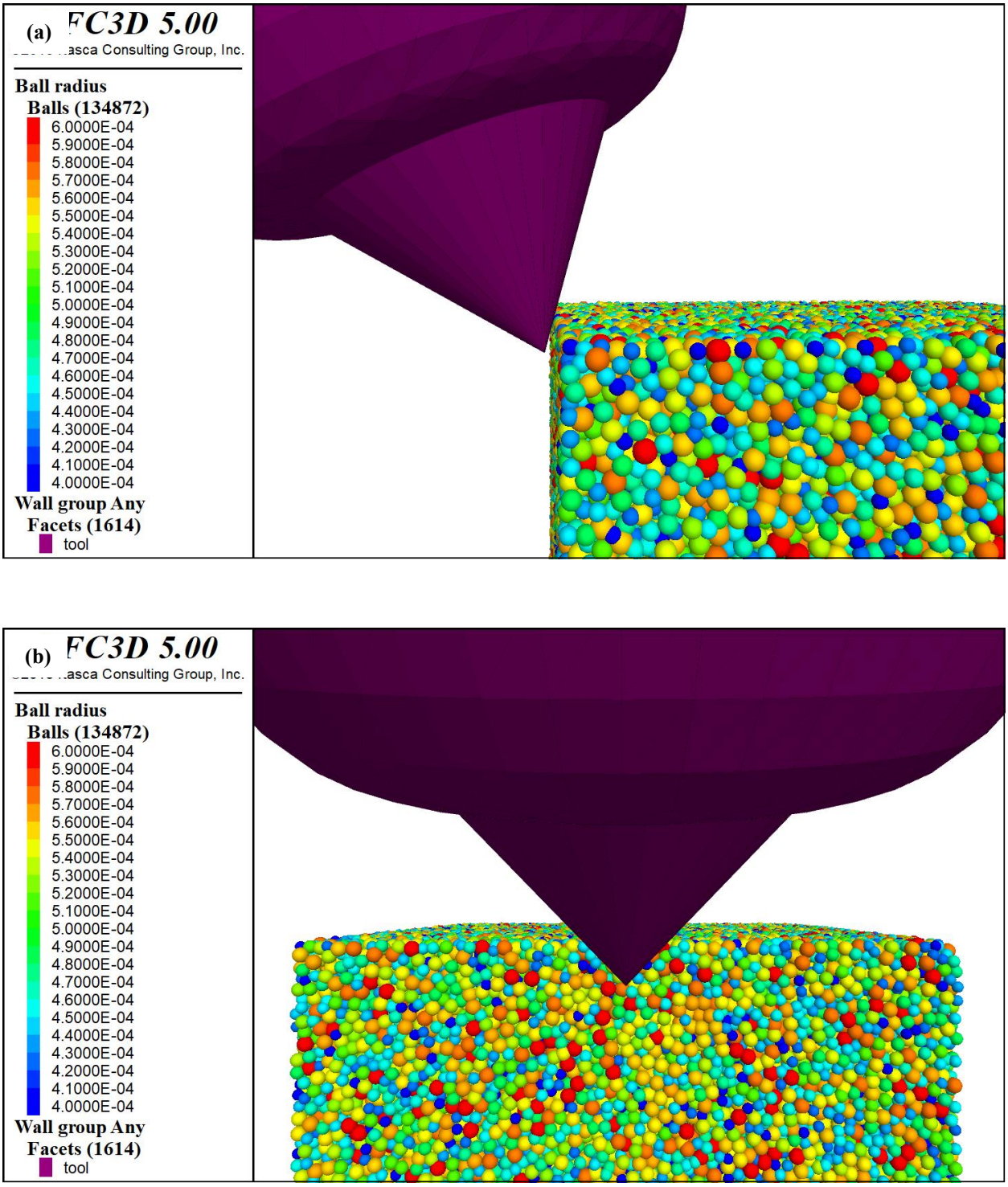

Figure 5-2 Model setup for the simulation of rock cutting in (a) side view; (b) front view (134,872 particles with radius of 0.4 - 0.6 mm, tip angle = 75°, cutting velocity = 5 m/s, depth of cut = 3 mm, rake angle = -15°)

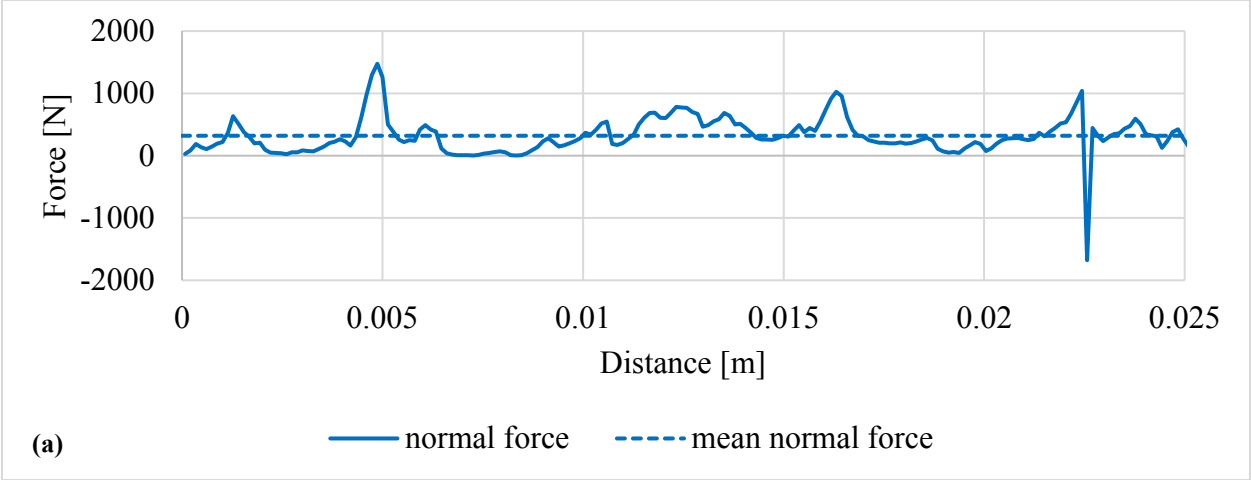

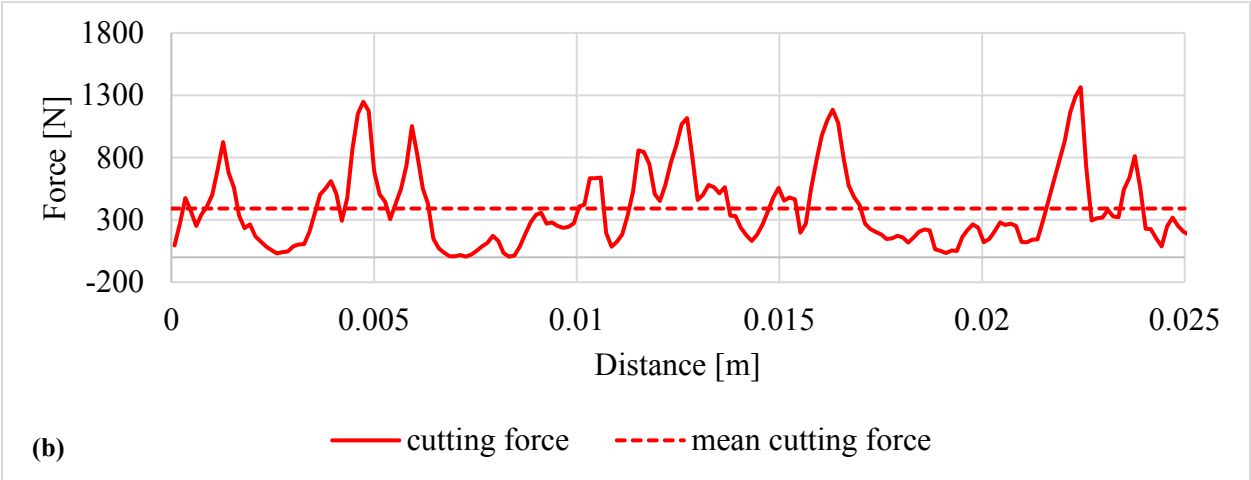

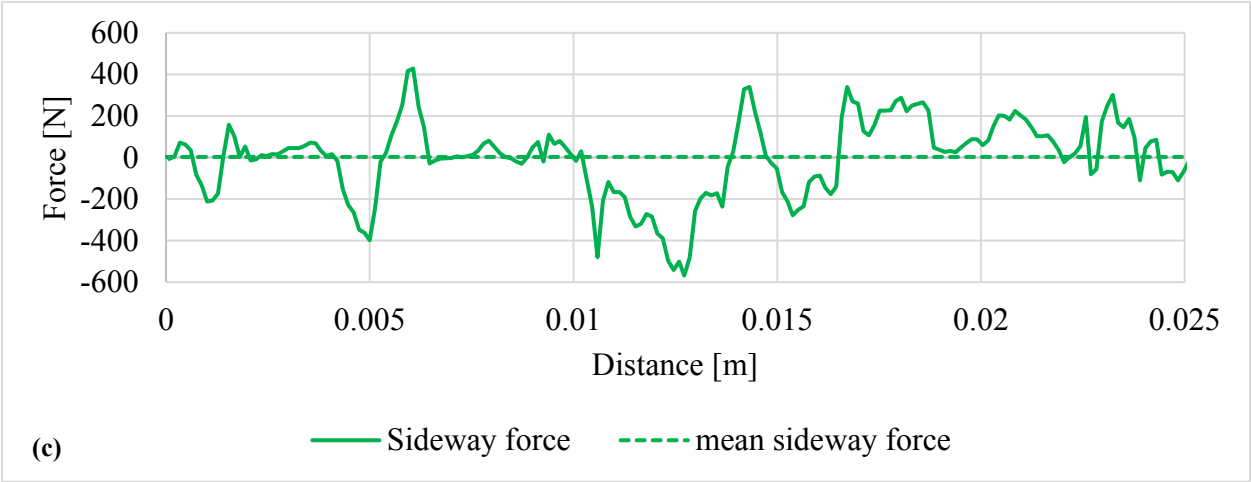

Figure 5-3 Evolution of (a) normal fore; (b) cutting force; (c) sideway force (cutting scenario: tip angle = 75°, cutting velocity = 5 m/s, depth of cut = 3 mm, rake angle = -15°)

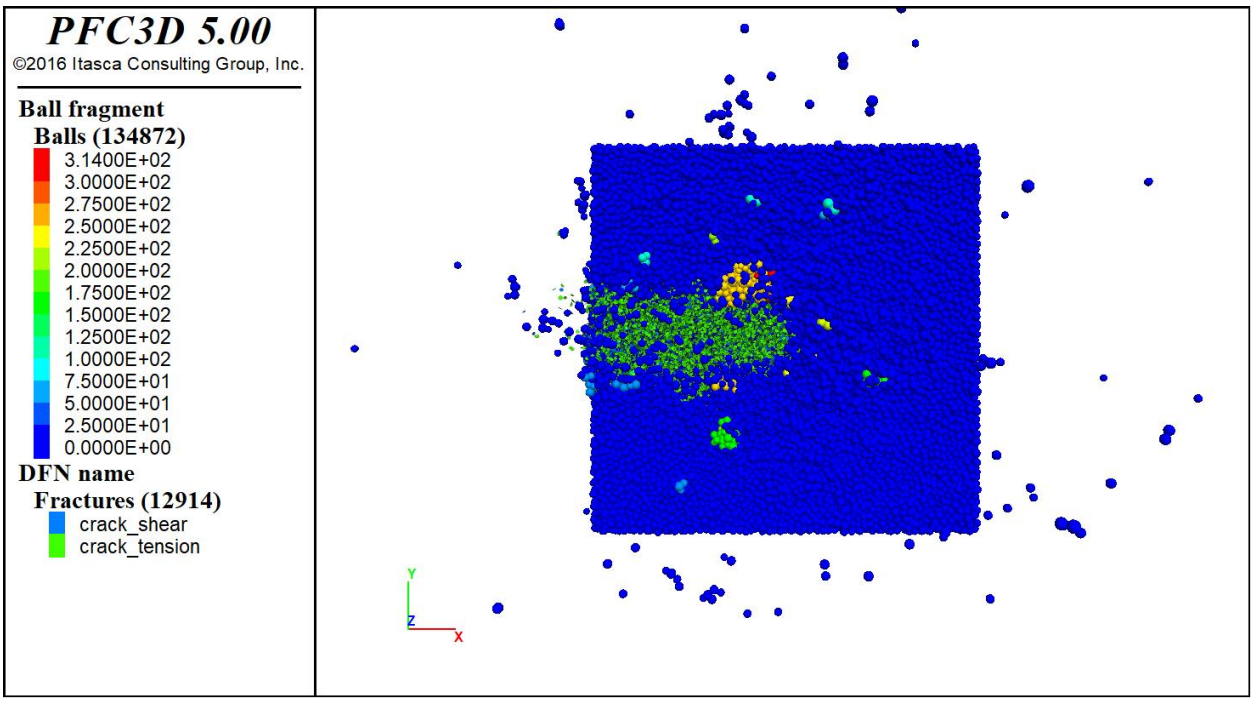

Figure 5-4 Rock fragmentation in top view (cutting scenario: tip angle = 75°, cutting velocity = 5 m/s, depth of cut = 3 mm, rake angle = -15°)

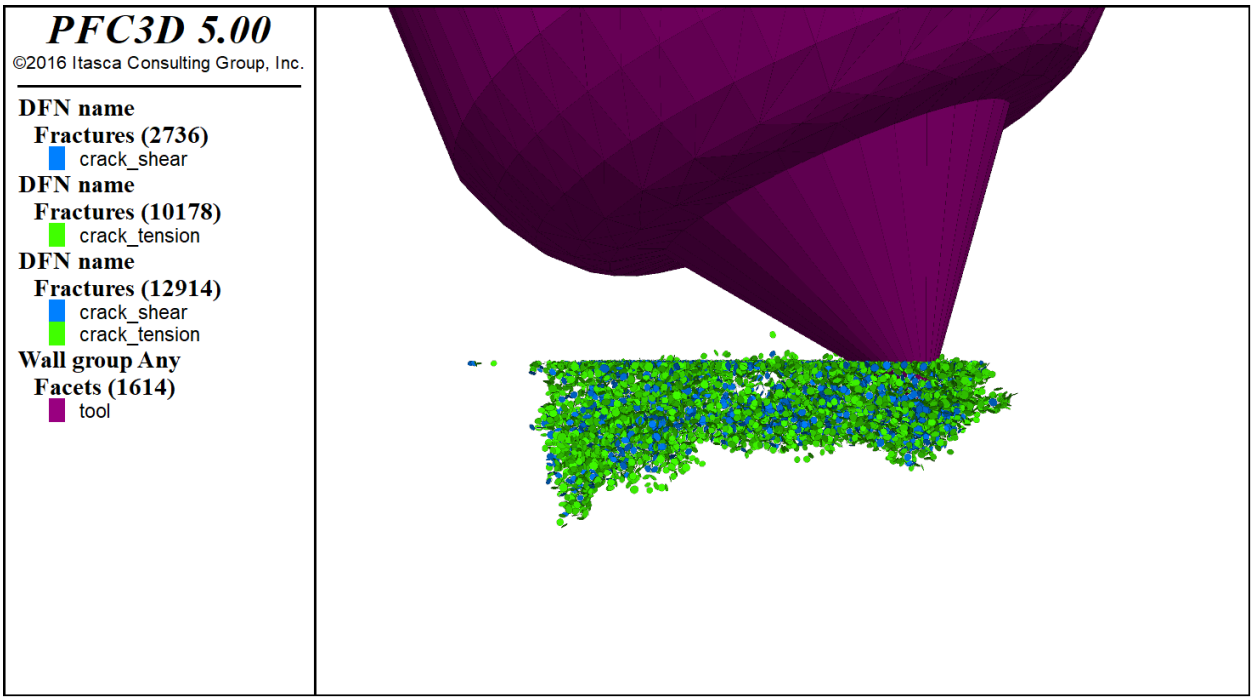

Figure 5-5 Crack initiation and propagation beneath the sample surface in side view (cutting scenario: tip angle = 75°, cutting velocity = 5 m/s, depth of cut = 3 mm, rake angle = -15°)

5.2 Influence of simulation parameters on cutting force and crack pattern

In PFC, several simulation parameters have significant influence on the numerical results. Such parameters are particle size, damping coefficient, coefficient of friction and contact deformability. Hence, it is necessary to investigate these factors and their influence on the simulation result of rock cutting. In this section, the parameter study is based on the rock cutting simulation. The chosen values for the parameter study are given in Table 5-2. For each simulation, only one parameter is changed, while the other parameters are kept constant.

Table 5-2 Parameter study of simulation condition-based factors (cutting scenario: tip angle = 75°, cutting velocity = 5 m/s, depth of cut = 3 mm, rake angle = -15°)

Simulation condition-based factor	
Minimum ball radius (r_{min}) [mm]	0.4 / 0.5 / 0.6 / 1
Mechanical damping coefficient (damp) [-]	0.05 / 0.1 / 0.2 / 0.5 / 0.7
Friction coefficient (μ) [-]	0 / 0.2 / 0.5 / 0.8
Contact deformability (E^*) [GPa]	0.5 / 1 / 5 / 10

5.2.1 Particle size

By simulating the rock mechanical behavior using DEM, it has been found that the particle size is a major factor affecting the macro-properties of rock including UCS, BTS and Young's modulus (Lei et al. 2004, Van Wyk et al. 2014). To understand the particle size effect on the cutting force, different minimum ball radii (0.4 - 0.5 - 0.6 - 1 mm) with the same ratio to the maximum ball radius of 1.5 are used for the simulation.

Figure 5-6 shows the mean cutting forces and total number of cracks related to the minimum ball radii. It is obvious that the cutting force increases with increasing particle size. This is reasonable because the larger the particle, the more force is required to move over it or to cut it off. It should be noticed that, if the particle size is reduced considerably, the force can be decreased significantly. Despite that, when the model dimension is kept constant, the number of particles will be dramatically increased, as same as the computational time. In addition, an inverse phenomenon is observed: the amount of cracks is reduced when larger particles are used.

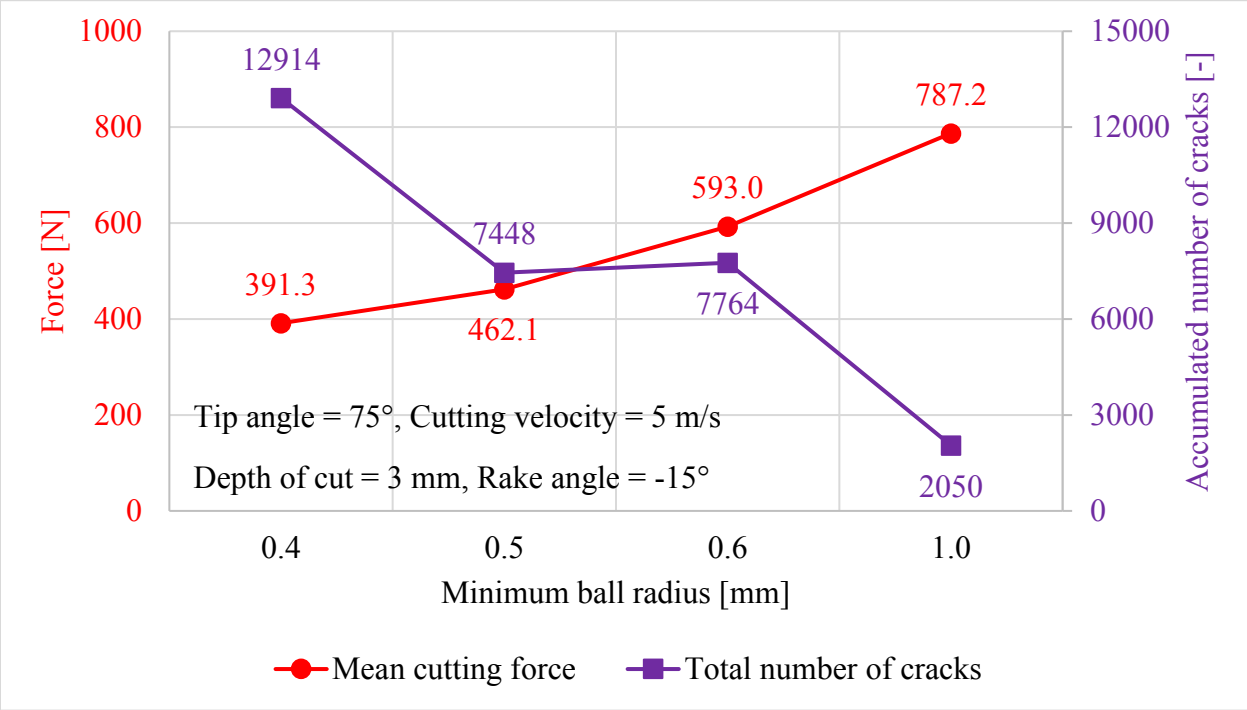

Figure 5-6 Variation of mean cutting forces and total number of cracks versus minimum ball radius

5.2.2 Mechanical damping

In PFC, a particle-based damping scheme termed mechanical (or local) damping acting on each particle is mainly used to remove the kinetic energy (Itasca 2016). For rock mechanical simulations, it is not easy to assign the damping coefficient to a rock sample, especially when it suffers a dynamic process of rock cutting or ploughing. A literature review shows that the mechanical damping can affect the simulation result significantly (Lei et al. 2014). Therefore, five damping coefficients (0.05 - 0.1 - 0.2 - 0.5 - 0.7) are used to see how the mechanical damping affecting the results of cutting forces and cracks.

Figure 5-7 shows the variation of cutting forces and accumulated number of cracks using different damping coefficients. It is not difficult to see that the cutting force is dependent on the mechanical damping: more force is needed when the damping coefficient is increased and this influence is more significant for greater damping values. Looking at the evolution of cracks, a more or less similar result is obtained: more cracks are induced with an increase in mechanical damping.

However, it should be noticed that the mechanical damping should be set to zero or to a small value for realistic dissipation of energy in dynamic simulations, which means that the damping coefficient of 0.7 is not appropriate for the rock cutting simulation. If this value would be excluded from the numerical results, no meaningful correlation could be found for the cracks.

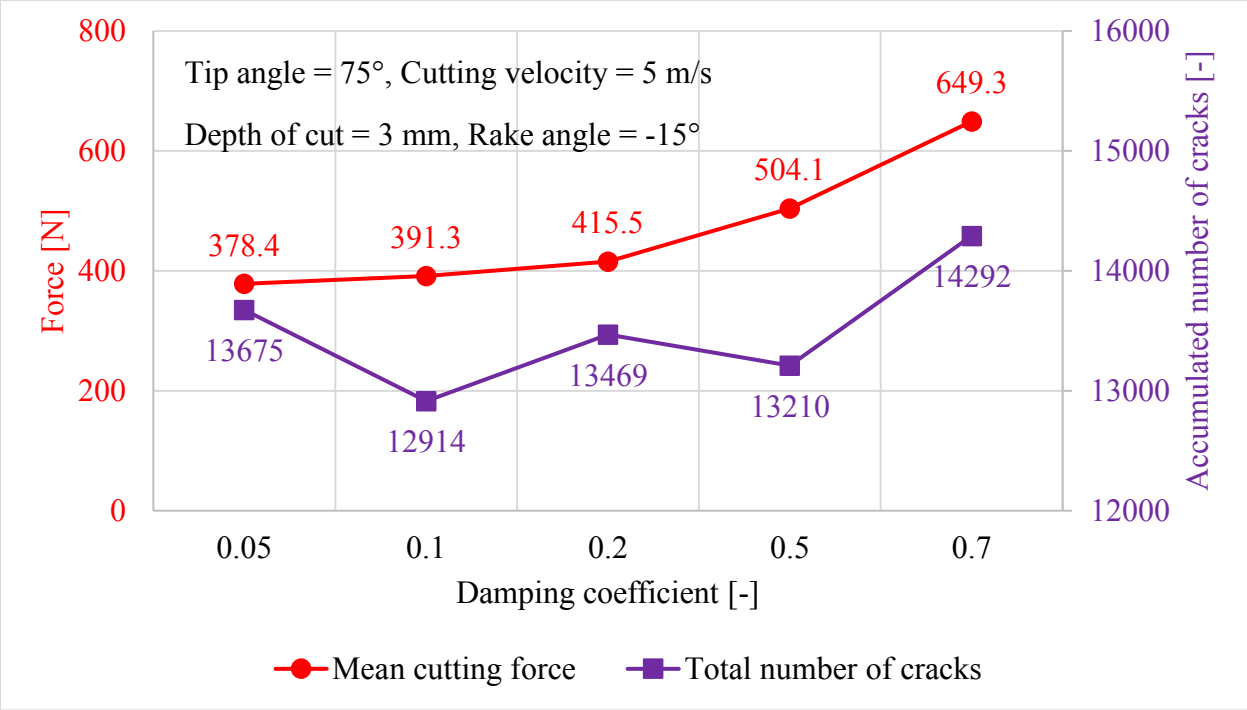

Figure 5-7 Variation of mean cutting forces and total number of cracks versus damping coefficient

5.2.3 Coefficient of friction

During the numerical simulation - after the particles are detached due to bond breakage - the coefficient of friction between particles and wall and other particles plays an important role impacting the movement magnitude of balls and their interaction with the tool. The influence of friction coefficient on the mechanical behavior of rocks and cutting force is studied by applying different friction coefficients (0.2 - 0.5 - 0.8) in the simulations. First, the values for both, ball-wall and ball-ball, are changed separately, namely keep one of them constant and vary the other one gradually, and second vary both of them simultaneously and gradually.

In Figure 5-8, the cutting forces and numbers of cracks are plotted against the corresponding friction coefficients with separately de- or increased ball friction coefficient, separately de- or increased wall friction coefficient and simultaneously de- or increased friction coefficient. Simulation results show that, in all three cases, the higher the friction coefficient, the more the required force used for the cutting, and the more the amount of induced cracks within the rock.

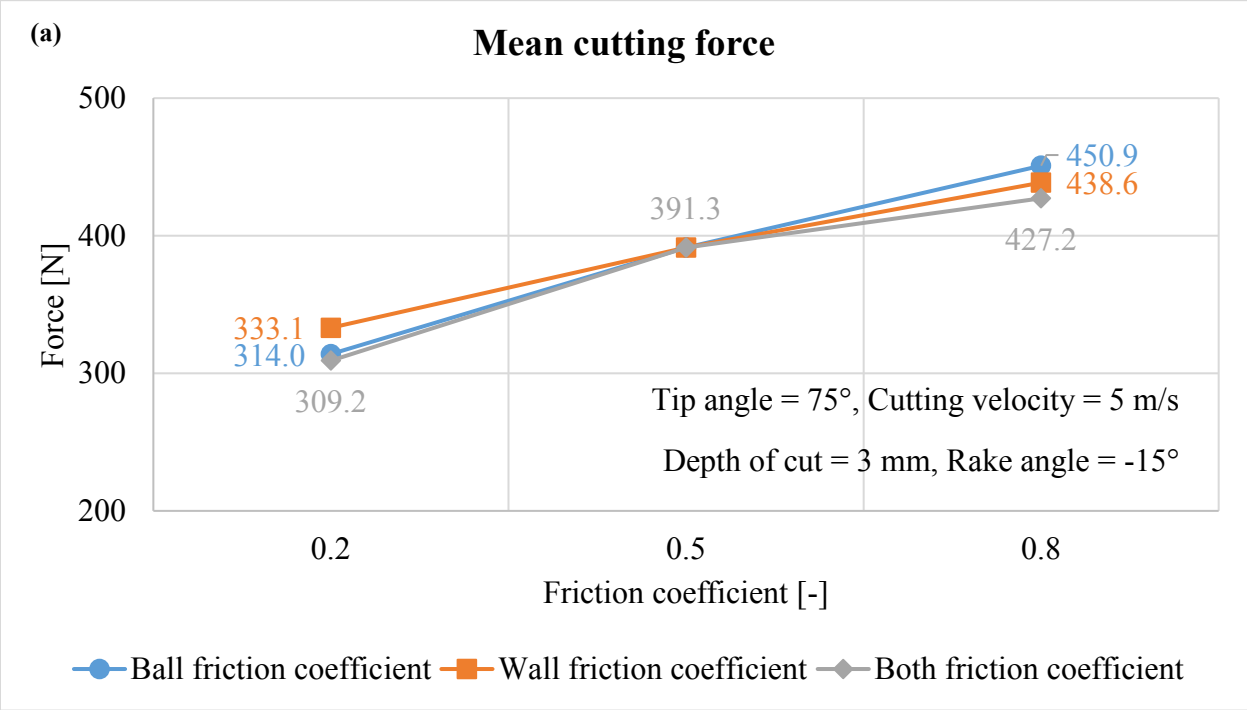

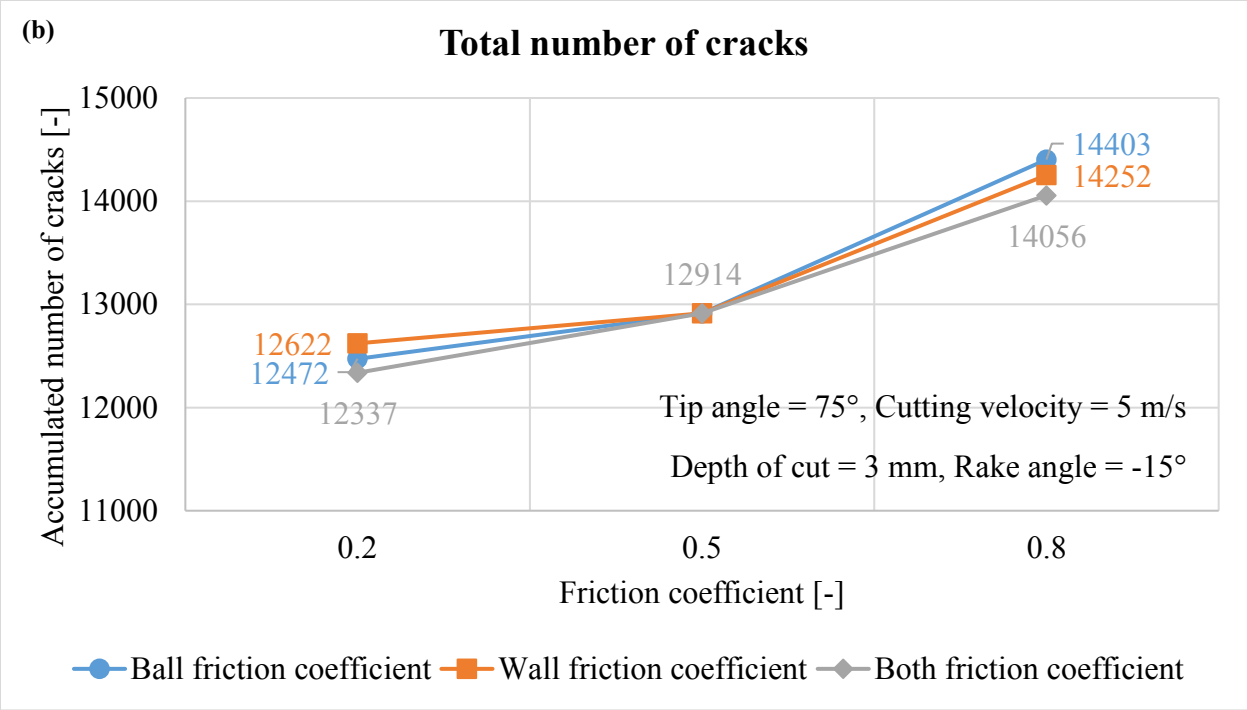

Figure 5-8 Variation of (a) mean cutting forces and (b) total number of cracks versus friction coefficient

5.2.4 Contact stiffness or deformability

According to the constitutive model, a force is produced by linear springs with constant normal and shear stiffnesses (K_n and k_s). The deformability of a homogeneous and isotropic particle assembly can be fitted by an isotropic material model, which is described by the elastic constants of Young's modulus and Poisson's ratio. These two parameters can further be related to the effective modulus (E) and the normal-to-shear stiffness ratio (k) at the contact. In PFC, the surface properties can be specified with two methods, either the K_n and k_s or the E and k.

In actual rock cutting or ploughing, the cutter heads are usually made of tungsten carbide or polycrystalline diamond with different hardnesses and stiffnesses. To study how wall stiffness influences the applied cutting force and the reaction of particles to the tool action, different values of deformability (0.5 - 1 - 5 - 10 GPa) are assigned to the contact between the cutting tool (or wall) and mineral grains (or balls).

Figure 5-9 shows the variation of cutting forces and induced cracks with different contact deformabilities. Results show that the magnitude of cutting force is reduced when deformability value becomes greater. This reflects that the wall stiffness also has an influence on the cutting force. The higher the wall stiffness, the lower the resulting force. However, the influence of wall stiffness on the induced cracks is not significant.

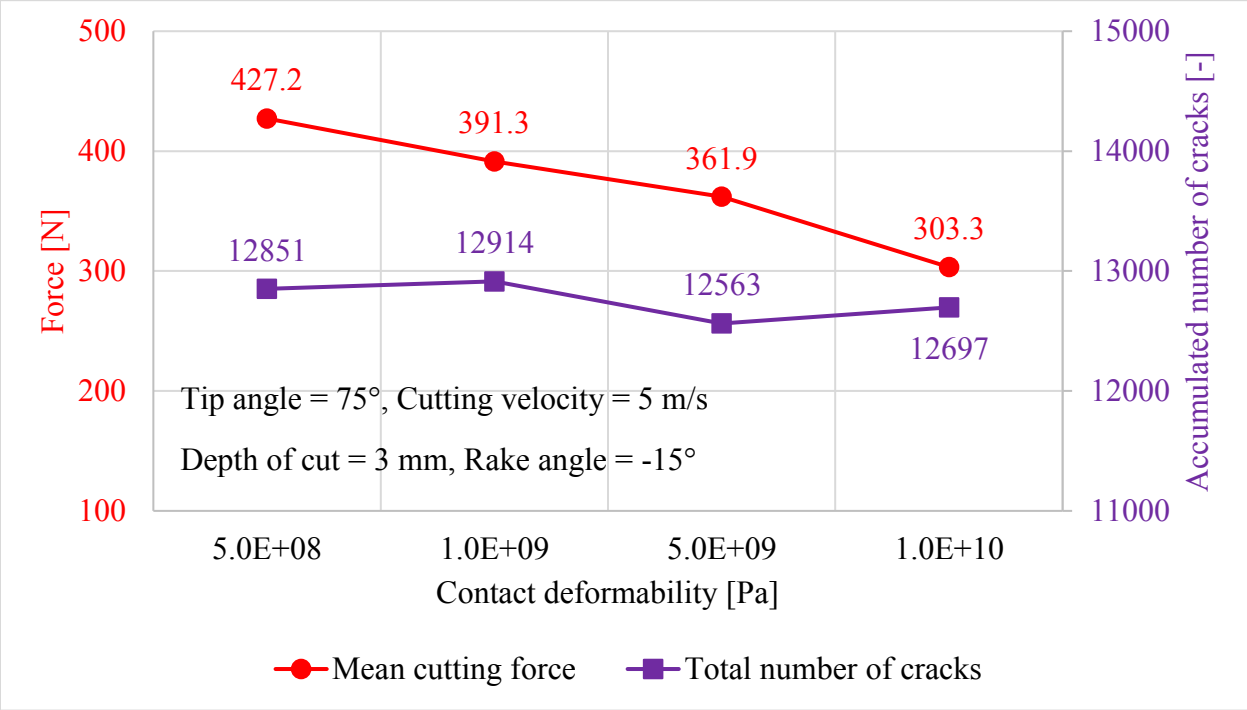

Figure 5-9 Variation of mean cutting forces and total number of cracks versus contact deformability

5.3 Influence of tool geometry on cutting force and crack pattern

5.3.1 Pick type

In mining engineering during rock cutting and ploughing, a large variety of picks has been designed to excavate rocks with different strength and abrasivity properties. As summarized in Table 5-3, conical picks are often used to excavate softer and lower abrasive rocks, but the wear on it is also higher. Ballistic picks are used for hard rocks with low abrasivity and its abrasion is moderate. Rounded picks can be used to excavate rocks with higher strength and greater abrasive potential due to lower abrasion (Thuro 1996).

To investigate the dependency of cutting forces and crack patterns on the tool geometry, a series of rock cutting simulations are conducted with three different pick types, namely conical, ballistic and rounded, as illustrated in Figure 5-10. Note that, for the simulation, each pick is set orthogonal (90°) to the rock sample in order to exclude the influence of rake angle on the numerical result.

In Figure 5-11, the mean cutting forces and total number of cracks are related to the three pick types. It is obvious that the greatest cutting force is required for the rounded pick, followed by the ballistic pick, and then by the conical pick. It can also be seen that the rounded pick causes the highest amount of cracks, while the conical pick causes the lowest amount of cracks. This finding confirms the statement of Thuro (1996).

Table 5-3 Pick types and their properties and applications (Thuro 1996)

Pick type	**Property**	**Application**
Conical	Very aggressive, maximum excavation rate, high wear	Rocks with low UCS and abrasivity, e.g. phyllite
Ballistic	Aggressive, high excavation rate, moderate wear	Rocks with high UCS and abrasivity, e.g. sandstone
Rounded	Non-aggressive, minimum excavation rate, low wear	Rocks with high UCS and abrasivity, e.g. gneiss and quartzite

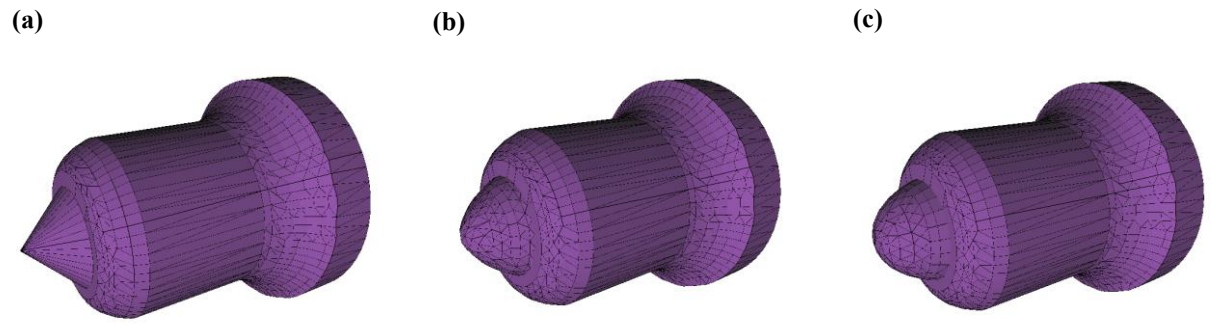

Figure 5-10 Types of (a) conical (90° tip angle); (b) ballistic; (c) rounded picks

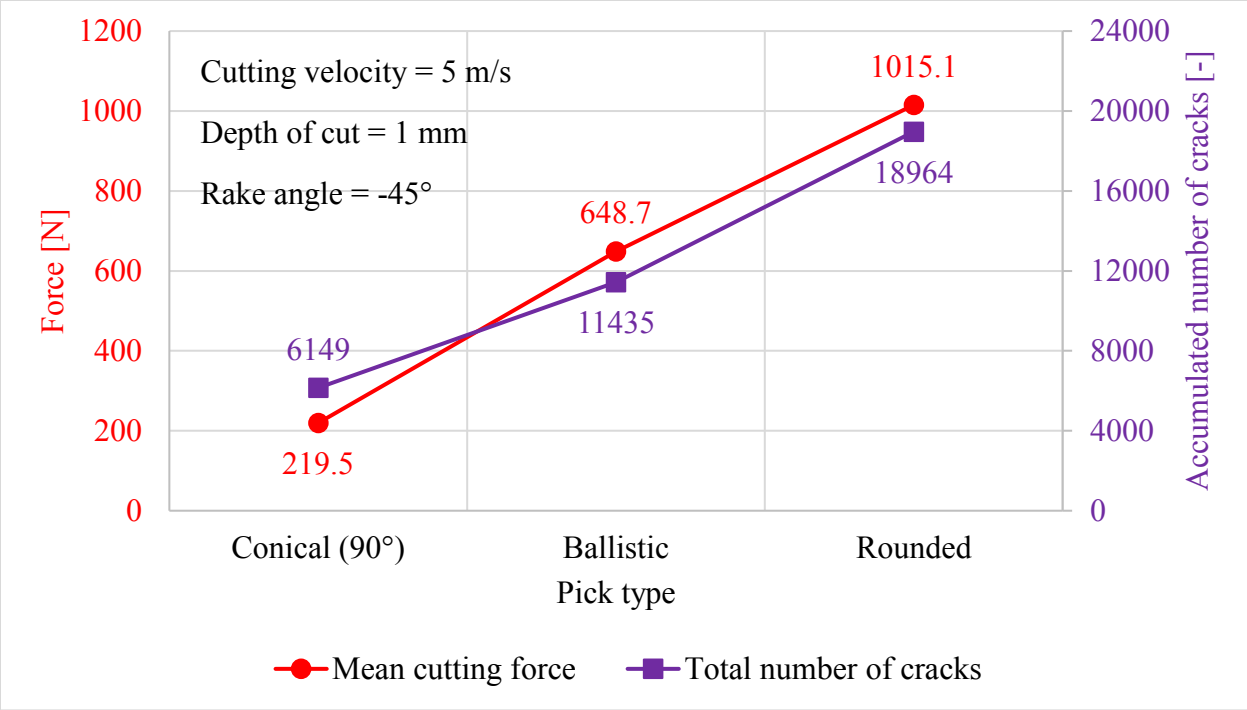

Figure 5-11 Variation of mean cutting forces and total number of cracks for different pick types

5.3.2 Tip angle

In the mining industry, tip angles of conical picks are usually designed between 60° and 90°, namely 60° for cutting soft rocks and 90° for cutting hard rocks, and 75° - 80° are the most commonly manufactured tip angles (Bilgin et al. 2006). Experimental investigations of tip angles affecting the cutting forces have been conducted by Sarwary and Hagan (2016), in which four tip angles (70°, 90°, 100° and 110°) were tested on two rock types (sandstone and limestone). They found that the cutting force increases with the increase in tip angle. However, it should be noticed that the rake angles for the corresponding tip angles used for their experiments are quite different from each another, namely with the value of 10° rake angle for 70° tip angle, 0° rake angle for 90° tip angle, -5° rake angle for 100° tip angle and -10° rake angle for 110° tip angle.

To evaluate the efficiency of different cutters and to design an optimal cutting head, it is necessary to examine the dependency of cutting forces and fracture formations on the tip angles. Besides the 90° tip angle, three additional tip angles of 60°, 75° and 105° are used for the numerical investigation, as illustrated in Figure 5-12. Two cutting scenarios are taken into account during the simulation. First, each pick is set orthogonal (90°) to the rock sample according to its tip angle,

which means that the rake angle between the pick and rock is different. Second, three picks of 60°, 75° and 90° are located on the sample surface with an equal rake angle of -15°.

Figure 5-13 shows the mean cutting forces and total number of cracks, respectively, related to the corresponding tip angles, but with regard to different rake angles. It is obvious that a higher cutting force is required by enlarging the tip angle. A linear increase of cutting force with the increase of tip angles ranging from 60° to 105° is found. Moreover, it can be seen that the amount of cracks also increases with increased tip angles.

Figure 5-14 shows the variation of cutting forces and cracks with the tip angles in the case of an equal rake angle. Results indicate that both of them increase with increased tip angle, but the growth rate is reduced as the tip angle becomes larger. This means that, for a given rake angle, the tip angle effect shows a weakened trend affecting tool force and rock fragmentation.

Summarized, it can be concluded that the tip angle has an influence on the resultant cutting force and crack evolution. A larger tip angle generates more cracks, but the applied cutting force is also higher on it, and vice versa.

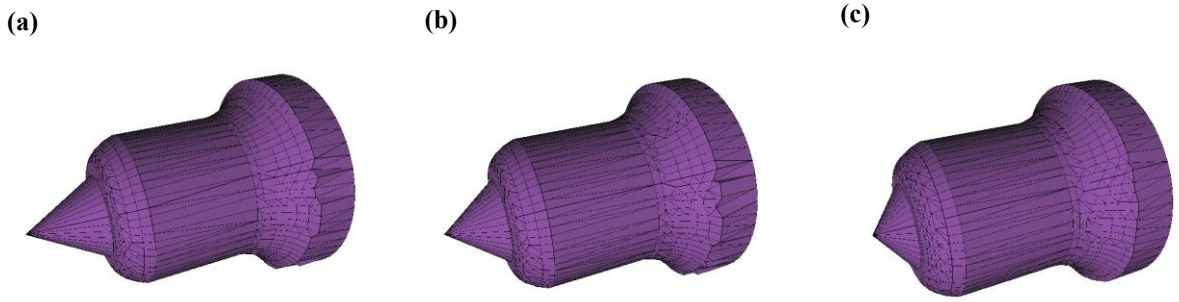

Figure 5-12 Conical pick with tip angle of (a) 60°; (b) 75°; (c) 105°

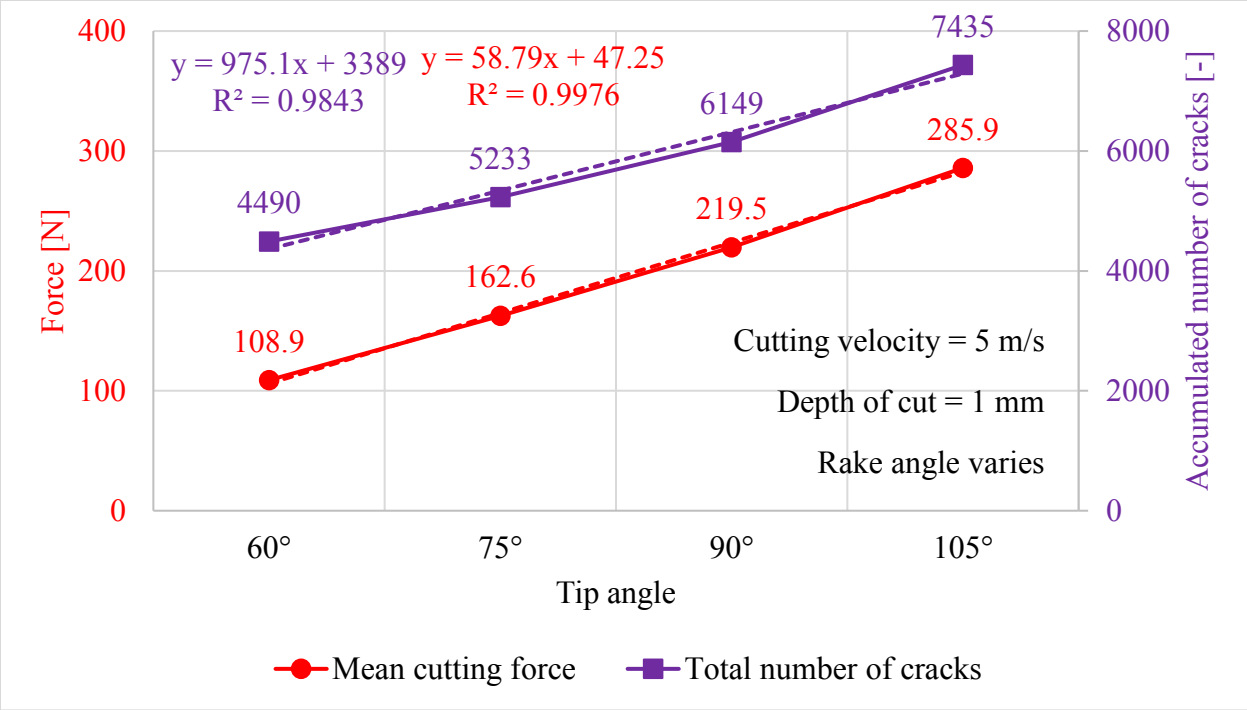

Figure 5-13 Variation of mean cutting forces and total number of cracks for different tip angles (rake angle varies)

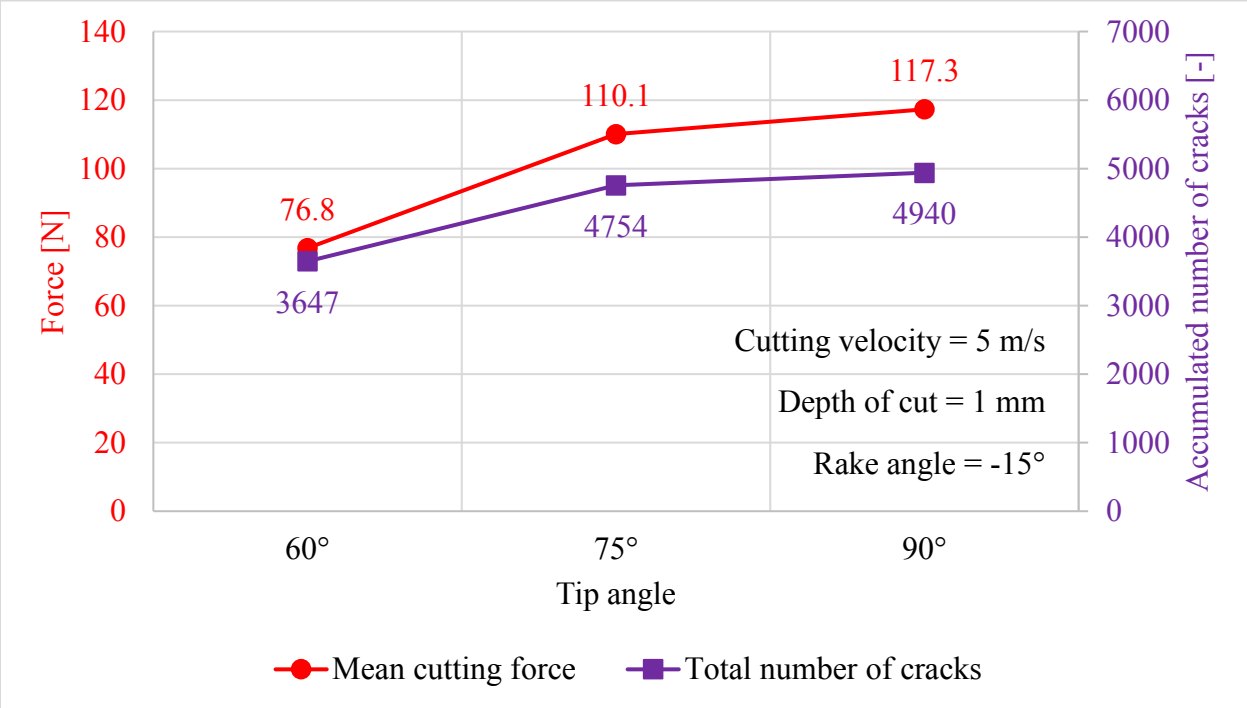

Figure 5-14 Variation of mean cutting forces and total number of cracks for different tip angles (rake angle constant)

5.3.3 Tip wear

A clear difference between the actual experiments and numerical simulations of rock cutting is that the wear on the cutting tool is not considered in the simulation. Therefore, a deviation between the numerical and experimental results can be expected. Study of Guo (1990) showed that the required force increases as the bluntness of cutting tool increases and then a low cutting efficiency occurs. Su and Akcin (2011) stated: when a worn pick is used for the simulation, the applied force will inevitably be increased. Van Wyk et al. (2014) emphasized that only a small amount of wear on the cutters can affect a cutting process to a great extent and make the cutting more difficult.

The influence of tool wear on cutting forces and crack patterns is investigated by blunting a 90° conical pick artificially with three different wear areas on the tip top. The ratio of the blunted tip top to the bottom diameter ($Ø_B$) of the conical pick are 0.1, 0.2 and 0.5, respectively, as illustrated in Figure 5-15. For the simulation, each pick is set orthogonal (90°) to the rock sample to avoid the influence of rake angle on the numerical result.

Figure 5-16 shows the variation of cutting forces and accumulated numbers of cracks, respectively, with diverse wear areas. It is not difficult to see that the cutting force increases when the pick abrasion increases. This is caused by the friction coefficient at the interface between worn tip and sample surface, which cannot be neglected in altering the rake angles between the tool and rock in the course of the cutting process and therefore the stress distribution on the cutting tool as well as the cutting force during the rock cutting. It is concluded that rock cutting with sharp tips obviously needs less force than with blunt tips. In addition, it is found that the increase of cutting force is not linear with the tip wear. An exponential relationship can better describe this relation. This in fact means an increased demand in power and makes the cutting process inefficient. Looking at the rock fracturing during the simulated cutting process, it is concluded that the abraded pick can induce more cracks than that without abrasion. Similarly, exponential relationship is established.

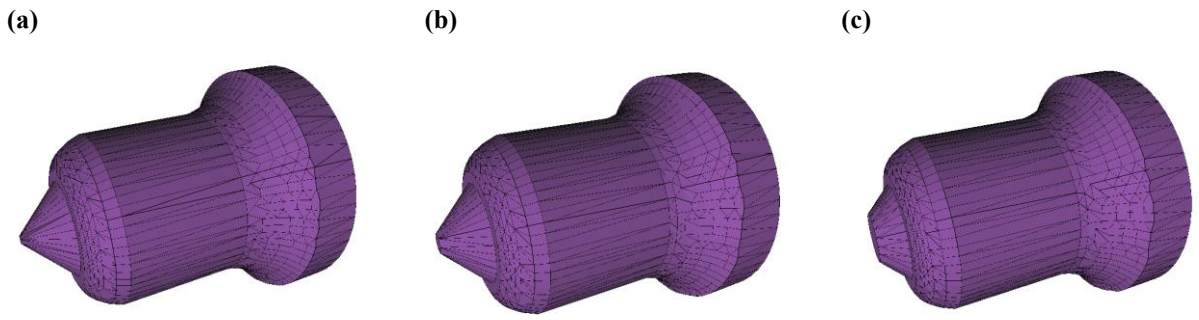

Figure 5-15 Conical pick (90° tip angle) with bluntness of (a) $0.1 \cdot Ø_B$; (b) $0.2 \cdot Ø_B$; (c) $0.5 \cdot Ø_B$ on the tip top

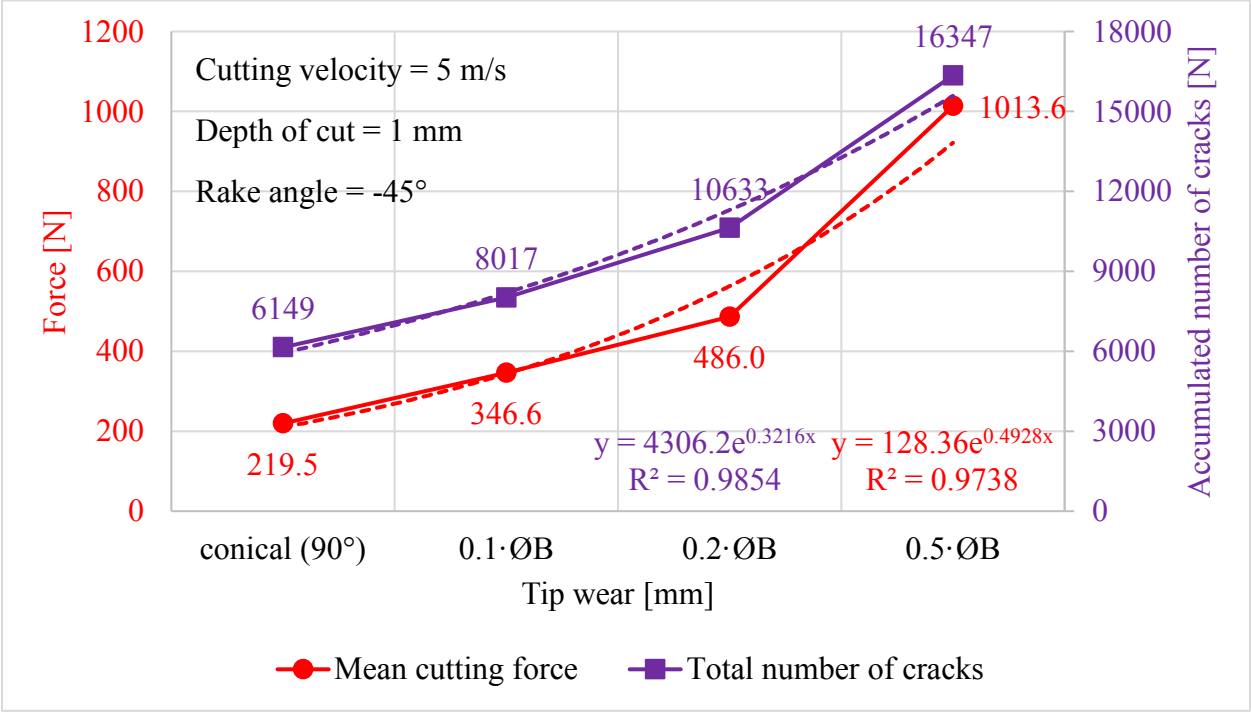

Figure 5-16 Variation of mean cutting forces and total number of cracks for different tip abrasions

5.4 Influence of cutting parameters on cutting force and crack pattern

5.4.1 Cutting velocity

Verhoef (1997) found that the cutting force does not vary much with cutter velocity at lower speeds, while the influence of cutter velocity on cutting forces is substantial only at higher speeds. He concluded also that the cutting velocity has a significant influence on the cutting force at a greater depth of cut. This conclusion is confirmed by Menezes et al. (2014) by simulating rock cutting using a FEM-based code. In addition, numerical study of Tan et al. (2009) shows that a higher cutting velocity combined with a smaller cutting depth can reduce the surface damage of brittle material, as same as the accumulated number of cracks.

The influence of cutting velocity on cutting forces and crack patterns is investigated by specifying different cutting velocities (1 m/s, 2.5 m/s, 5 m/s and 10 m/s) on a 75° conical pick and at different depths of cut (1 mm, 3 mm, 5 mm and 7 mm) for a given rake angle of -15°. The mechanical (or local) damping coefficient is set to 0.1 in each simulation.

The mean cutting forces are plotted against the corresponding cutting velocities with different cutting depths in Figure 5-17a. Results show that the cutting force increases with increasing cutter velocity. More specifically, the cutting velocity affecting the cutting force is more significant when the depth of cut is increased. The induced cracks show a similar result, as can be seen in Figure 5-17b: more cracks occur in cutting rocks with higher cutter velocity and at greater depth of cut. According to the simulation results, linear relationships of cutting forces and numbers of cracks to the cutting velocities for a given depth of cut are found, respectively.

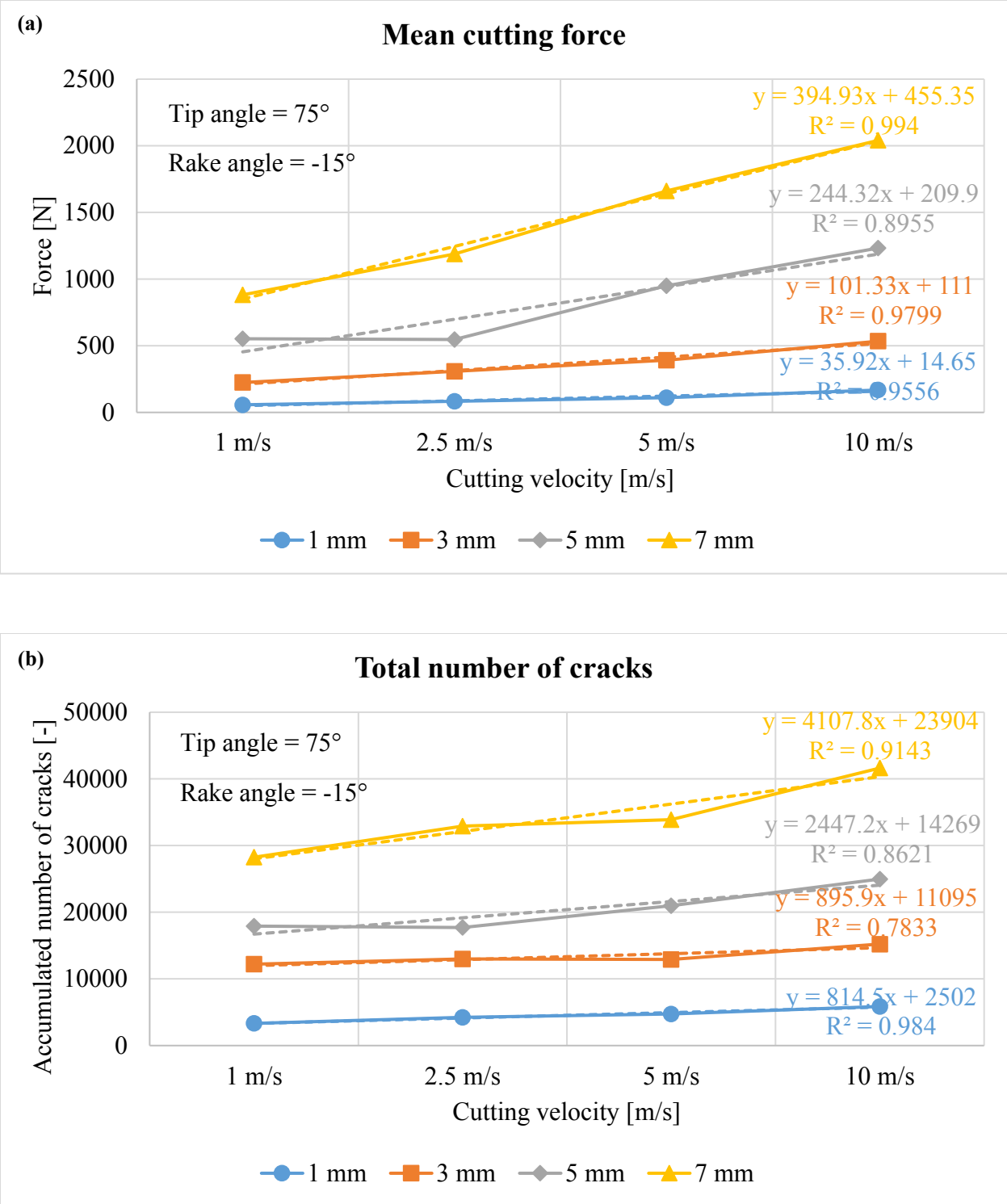

Figure 5-17 Variation of (a) mean cutting forces and (b) total number of cracks for different cutting velocities (depth of cut varies)

5.4.2 Depth of cut

The depth of cut is a key factor affecting the applied tool forces and the modes of failure in the rock cutting process. Experimental studies have shown that ductile failure takes place at a small depth of cut, while brittle failure occurs at a large depth of cut (Huang 1999). It has also been found that the cutting force and chip size increases with increasing depth of cut (Gray et al. 1962, Lei et al. 2004, Menezes et al. 2014).

This effecting factor is studied by assigning different depths of cut (1 mm, 3 mm, 5 mm and 7 mm) at the beginning of the simulation and applying different cutting velocities (1 m/s, 2.5 m/s, 5 m/s and 10 m/s). In the simulations, the rake angle between the rock and tool is fixed at -15°.

Figure 5-18a shows the variation of mean cutting forces with the corresponding depths of cut for different cutting velocities. It is not difficult to see that the cutting depth has a significant influence on the cutting force. For a given cutting velocity, the greater the cutting depth, the higher the required cutting force. This is reasonable because, in this case, more particles are accumulated in front of the cutting head and then need to be removed by it. This leads to an enhancement of force values. Moreover, a power relationship between cutting force and depth of cut is found based on the available data. Seen from Figure 5-18b, a similar result is obtained between induced cracks and cutting depth: more cracks are induced with the increase in cutting depth.

Summarized, it is concluded that the cutting velocity associated with the depth of cut can affect the cutting force as well as rock fragmentation and crack formation significantly. A higher cutter velocity with greater depth of cut enhances the cutting force and increases the number of cracks compared to a lower velocity with a smaller depth. For shallow cutting, the cutting velocity effect on the cutting force is not very obvious, but the influence becomes more and more significant as the cutting depth is increased. According to the simulation results, power relationships of the cutting forces and cracks in relation to the cutting velocities and depths are established.

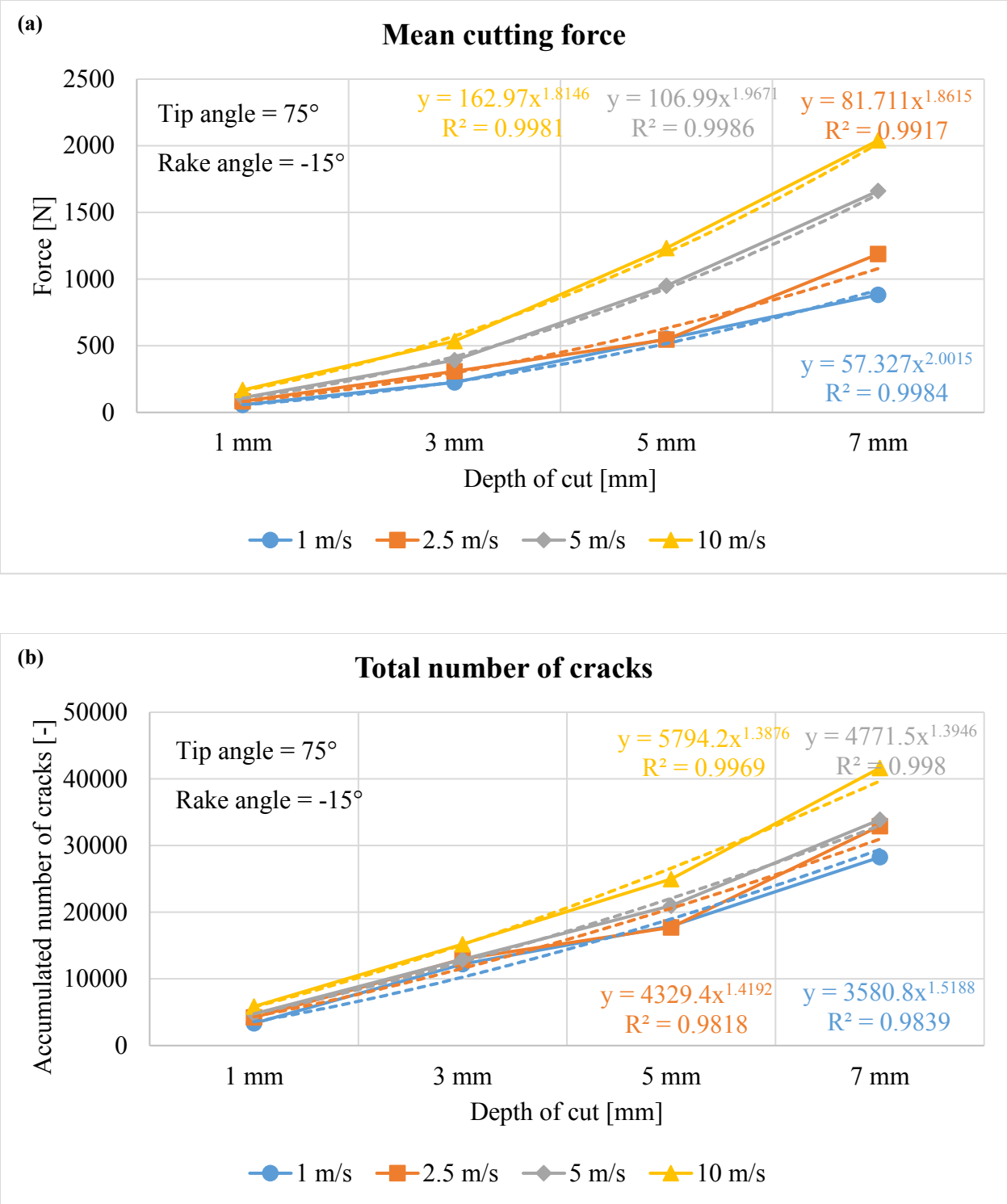

Figure 5-18 Variation of (a) mean cutting forces and (b) total number of cracks for different depths of cut (cutting velocity varies)

5.4.3 Rake angle

A literature review shows that rake angle is another main factor affecting the cutting force and rock fragmentation results significantly. Gray et al. (1962) performed a series of cutting tests on limestone with a drag pick at different rake angles ranging from positive to negative values (30°, 15°, 0°, -15° and -30°) and gained two important conclusions: (1) tool forces including normal and cutting force increase as rake angle decreases, especially for rake angles smaller than 0°, and (2) small increase of vertical loading leads to a large depth of cut for rake angles greater than 0°. Based on the rock cutting theory of Evans (1984) and Nishimatsu (1972), as well as on the basis of rock cutting tests conducted on limestone and granite at different negative rake angles (0°, -5°, -10°, -15° and -20°), Goektan (1990) concluded that the cutting force decreases with increased negative rake angles. By performing rock cutting experiments on sandstone and concrete with a drag pick, Guo (1990) found that the cutting force increases with the increase of positive rake angle (0°, 7.5° and 15°). Moreover, he concluded that crack propagation along a curved path becomes larger when the rake angle is greater. Lei et al. (2004) conducted two dimensional numerical simulations of rock cutting based on marble with two different rake angles (15° and 25°). Simulation results showed that the resultant cutting force with a rake angle of 25° is also higher than that with 15°.

The rake angle effect on cutting forces and crack patterns is studied for two tip angles of 75° and 60° by applying different rake angles ranging from negative to positive values (-37.5°, -30°, -15°, 0°, 7.5°, 12.5° and 20°), and with different cutting velocities (1 m/s, 2.5 m/s, 5 m/s and 10 m/s) and depths of cut (1 mm, 3 mm, 5 mm and 7 mm), respectively. Note that, for each simulation, only one parameter is changed, while the other parameters are kept constant.

Figure 5-19 shows the mean cutting forces and total number of cracks correlated with the corresponding rake angles, respectively, in the case of two tip angles. Seen from Figure 5-19a, for both, 60° and 75° tip angles, the cutting force decreases with increased negative rake angles and then increases with increased positive rake angles. The lowest force value is obtained for a rake angle of 0°. In Figure 5-19b, a similar result for the induced cracks is identified for the 75° tip angle, while the amount of accumulated cracks decreases with increasing negative rake angle and then stays more or less constant with the increase in positive rake angle with respect to the 60° tip angle. This phenomenon is due to the depth of cut with a relatively low value of 1 mm.

In Figure 5-20, the mean cutting forces and total number of cracks, respectively, are related to the rake angles with different depths of cut for a given tip angle of 75° and with a constant cutting velocity of 5 m/s. It is not difficult to see that, for a given depth of cut, forces and cracking are decreased as the negative rake angles are increased and then increased with increased positive rake angles. For both, negative and positive rake angles, the cutting force becomes more and more sensitive to the increased cutting depth, as same as the cracks.

Figure 5-21 shows the mean cutting forces and total number of cracks plotted against the rake angles, respectively, by specifying two cutting velocities of 2.5 m/s and 5 m/s on a 75° tip angle at a 3 mm cutting depth. In the case of two cutting velocities, both the cutting forces and numbers of cracks decrease firstly and increase subsequently as the rake angles alter from negative to positive values. Although only two velocities are studied, it can be envisaged that a higher cutting velocity has a more obvious influence on force and crack results.

Summarized, three conclusions can be drawn: (1) the requirement of cutting forces is firstly reduced and then enhanced as the rake angle increases from negative to positive, (2) the rake angle effect on cutting forces is more sensitive for larger tip angles, greater depths of cut and higher cutting velocities. This finding is also valid for the induced cracks, and (3) based on the available data, a polynomial relationship is found between force, crack values and rake angles.

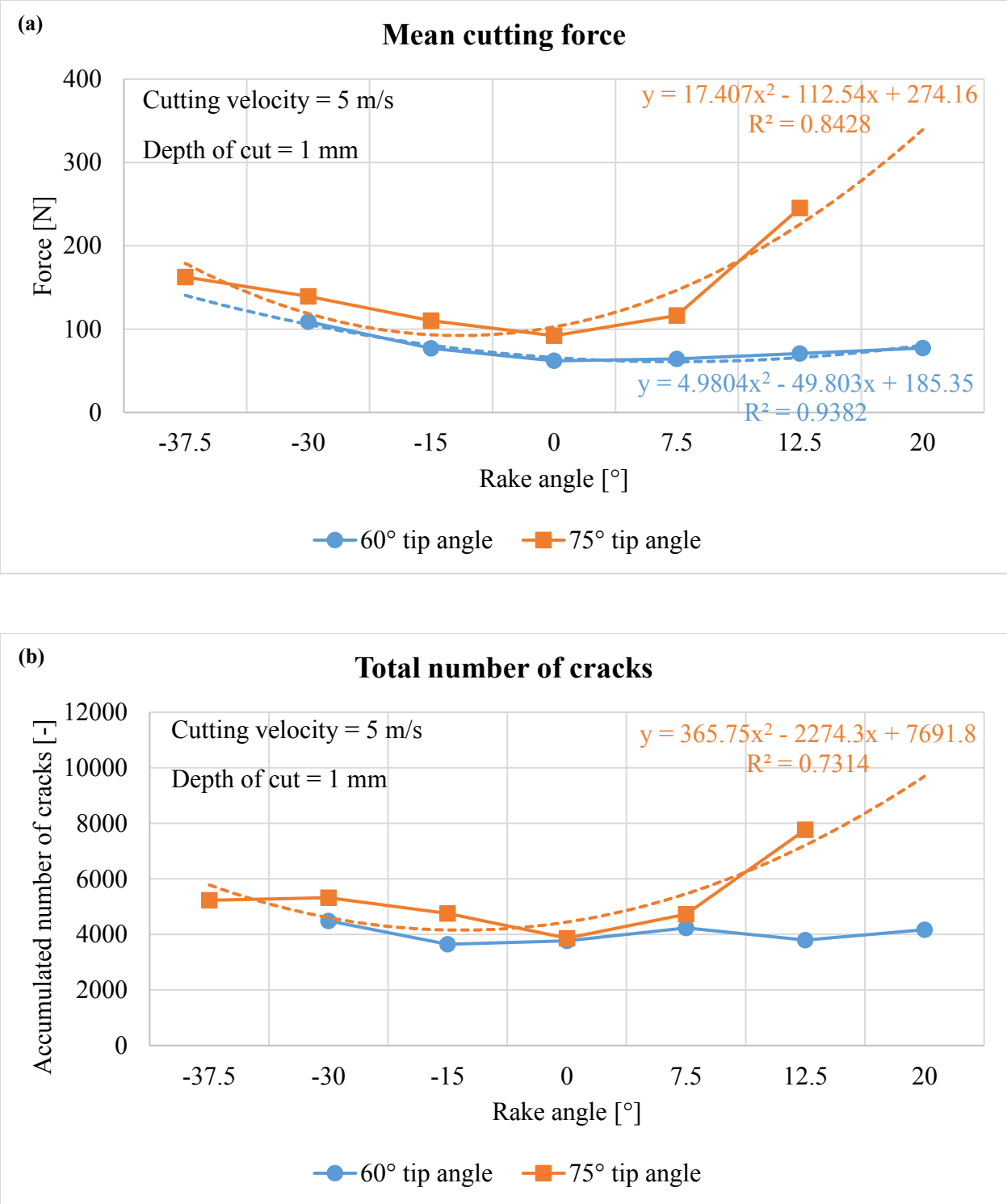

Figure 5-19 Variation of (a) mean cutting forces and (b) total number of cracks for different rake angles (cutting velocity and depth of cut constant, tip angle varies)

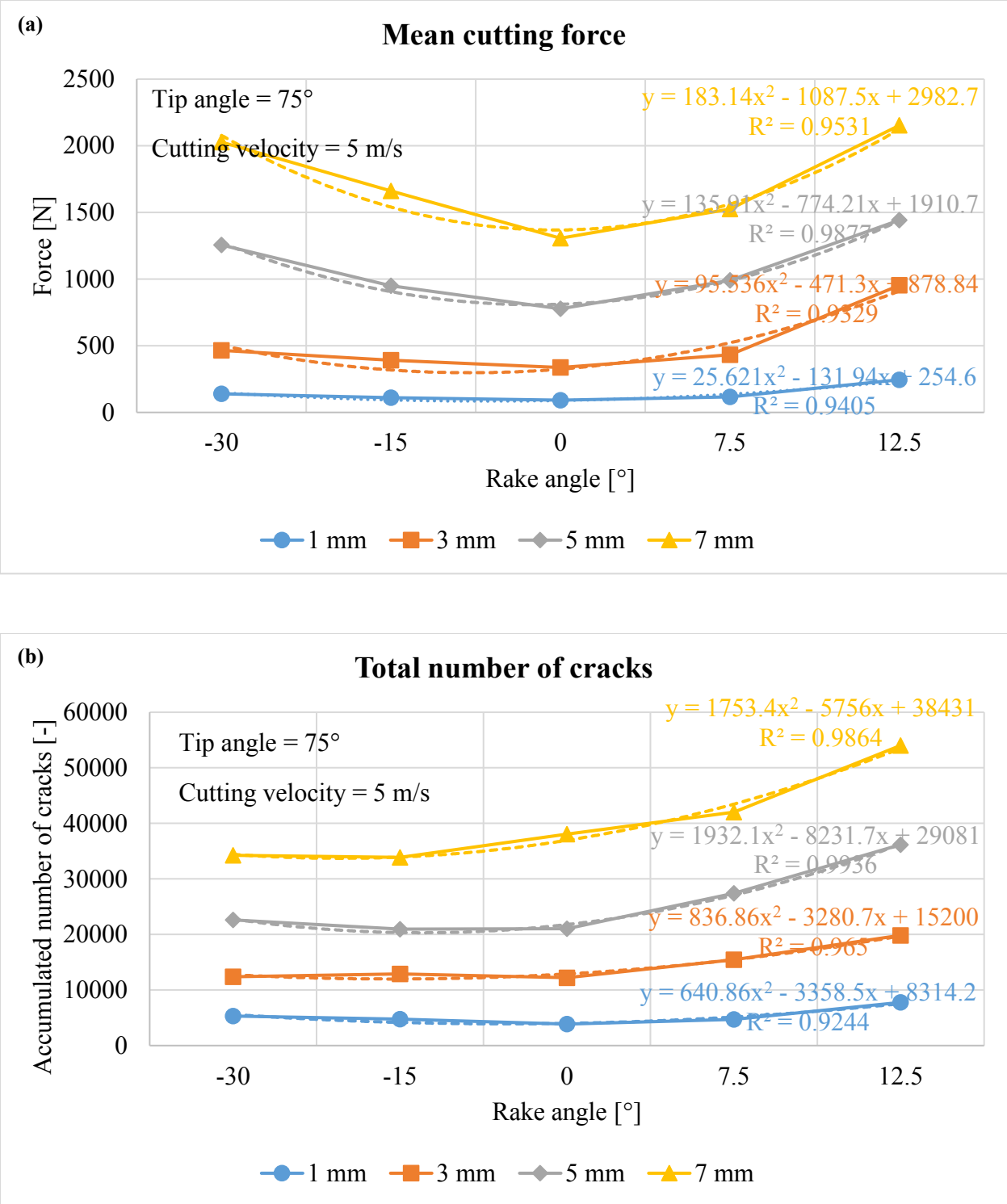

Figure 5-20 Variation of (a) mean cutting force and (b) total number of cracks for different rake angles (tip angle and cutting velocity constant, depth of cut varies)

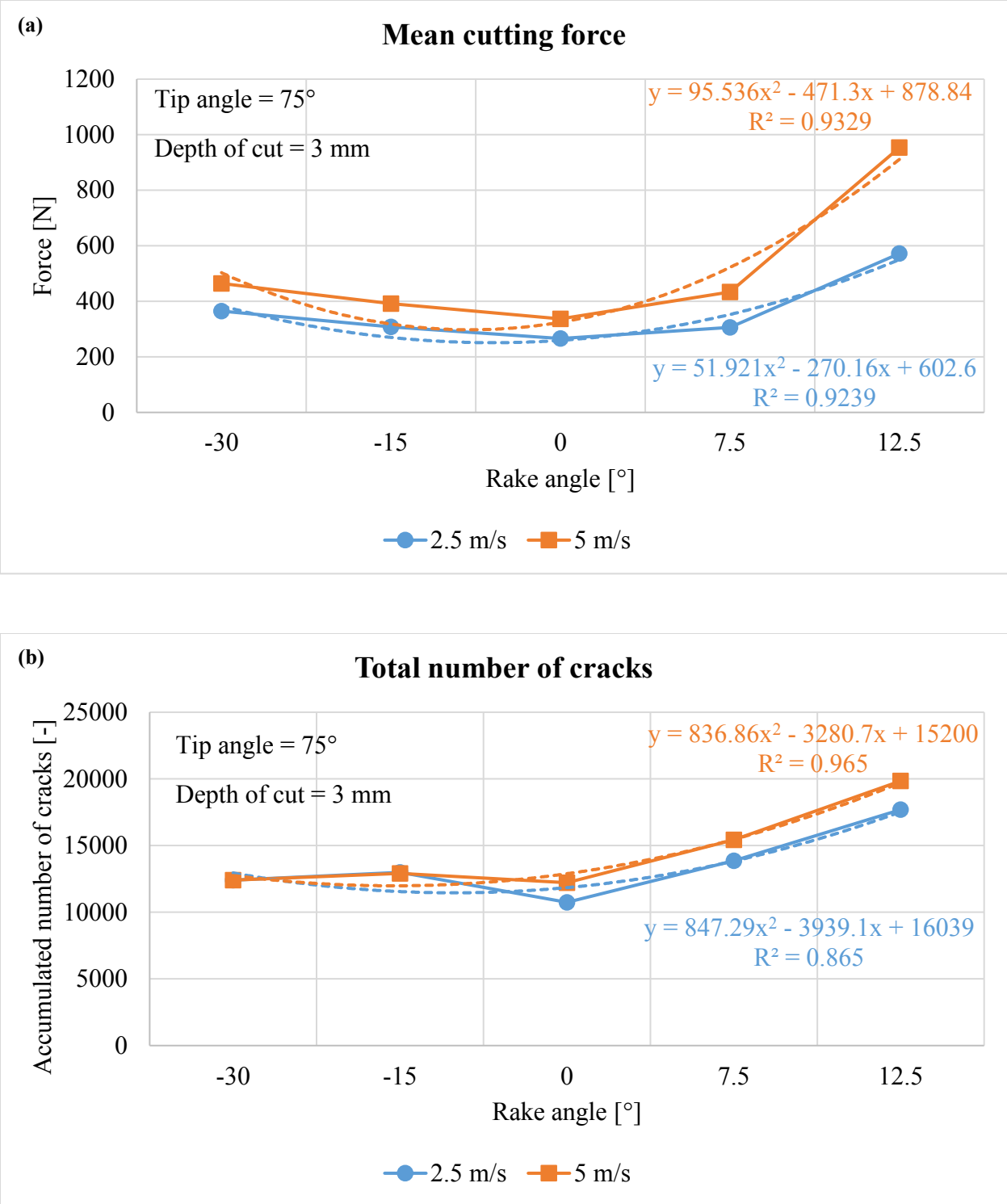

Figure 5-21 Variation of (a) mean cutting force and (b) total number of cracks for different rake angles (tip angle and depth of cut constant, cutting velocity varies)

5.5 Influence of rock type on cutting force and crack pattern

Besides the tool geometry and cutting parameters, as discussed above, it should be noted that the applied tool force depends also on the type of rock material and its mineralogical and mechanical properties. It can be envisaged that the mean cutting force is comparatively different, or more exactly, is higher for - for example - the basalt or granite due to its higher strength compared to the sandstone used in the present work, as well as the induced cracks can also be reduced in such strong rock materials. However, the simulation of the influence of rock type on the mechanical behavior of rocks is beyond this thesis.

6. Conclusions and outlooks

6.1 Conclusions

In this work, Cerchar abrasivity tests are conducted by using a special instrumented West apparatus, in which the sliding distance can be controlled and measured, the scratching velocity can be specified with different values and kept constant, and the applied scratching force can be monitored.

Various Cerchar abrasivity correlated parameters are determined and related to the intrinsic properties of rocks, such as rock fabric and strength. Table 6-1 summarizes diverse parameters and their effecting factors.

Table 6-1 Summary of Cerchar abrasivity correlated parameters and their effecting factors

Parameter	**Data type**	**Application**	**Pro and con**	**Effecting factor**
Wt [mm] CAI [-] Vs [mm^3]	Raw data From Wt From Wt	Abrasivity	Simple, fast	Abrasive mineral, quartz content and its equivalence, rock strength
Ds [mm] Vm [mm^3]	Raw data Raw data	-	-	Grain size, shape and hardness, rock microstructure, strength and porosity
Fs [N] MSF [N] SE [mJ]	Raw data From Fs From Fs	Abrasivity	Complex, slow	Mineral constituents, quartz content, grain size, shape and hardness, rock strength
SSE [mJ/mm^3]	From SE and Vm	Efficiency	More complex, slower	-
CAR [mm^3/mm^3]	From Vm and Vs	Abrasivity, effectivity	More complex, slower	-

The conventional indexes, such as Cerchar abrasivity index and tip wear volume, focus only on the abrasion of the stylus, no attention is paid to what happens on the tested rock. As usual, both indexes can be used to determine the rock abrasivity. They are dependent on the rock strength and abrasive minerals and quartz content or its equivalence within the rock.

The evolution of recorded scratching force shows different regimes for the considered rocks. This phenomenon can be related to the rock fabric, particularly important are the constituent minerals with respect to their type, size, shape and hardness. Similar, the mean and mean peak scratching forces differ in magnitude for the tested rocks, which can be attributed to rock strength, such as compressive strength, tensile strength and Young's modulus. Since the scratching energy and specific energy are determined based on the recorded scratching force, it is considered to use the mean scratching force, scratching energy and specific energy to assess the rock abrasivity. Based on the eight tested rocks, no meaningful correlation is found between these abrasive parameters and the corresponding Cerchar index, while a medium relationship is identified by ignoring the soft sandstone.

The newly proposed abrasive index, named Cerchar abrasion ratio, considers not only the wear on the stylus tip, but also the material removal on the rock surface. Therefore, this abrasion ratio has an ability to quantify the rock abrasivity. According to the definition, the ratio of these two quantities specifies the efficiency of the scratching process and then can be used to evaluate the effectivity of cutting or drilling processes. The determination of Cerchar abrasion ratio demands in addition to the classical Cerchar test the determination of the groove volume. The corresponding testing procedure is more complex and more time consuming.

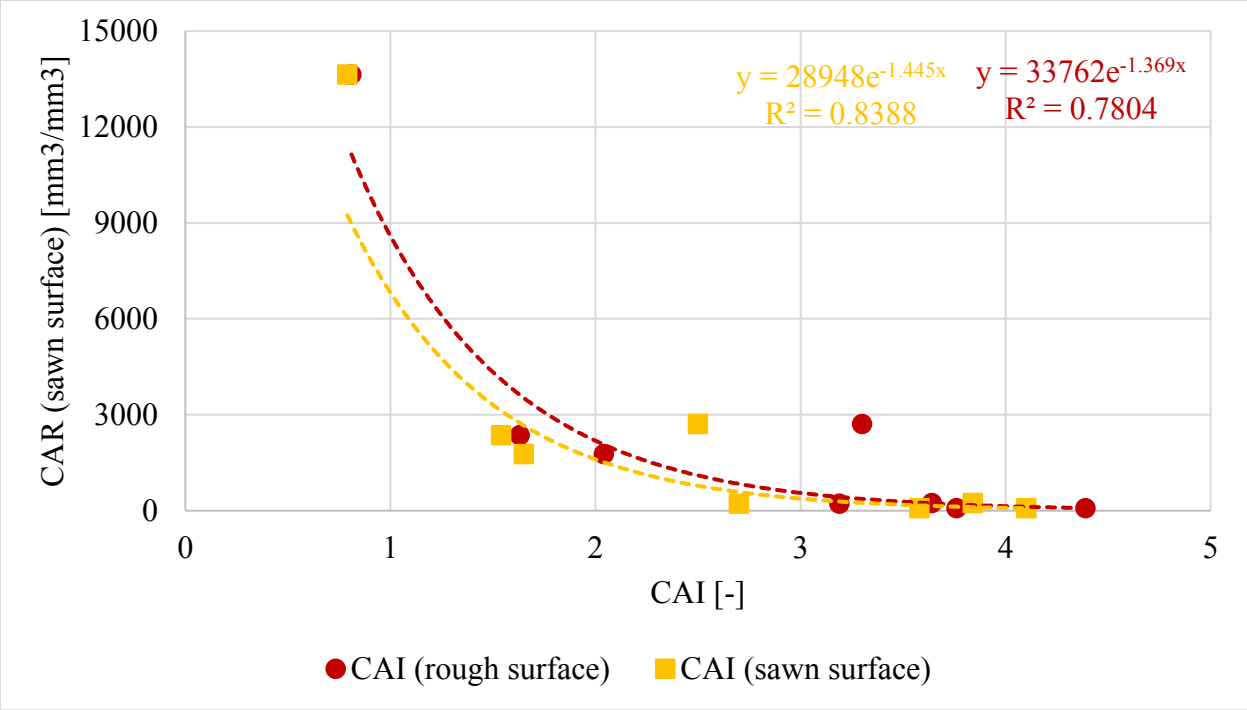

Figure 6-1 Relation of Cerchar abrasion ratio and Cerchar abrasivity index based on the eight tested rocks

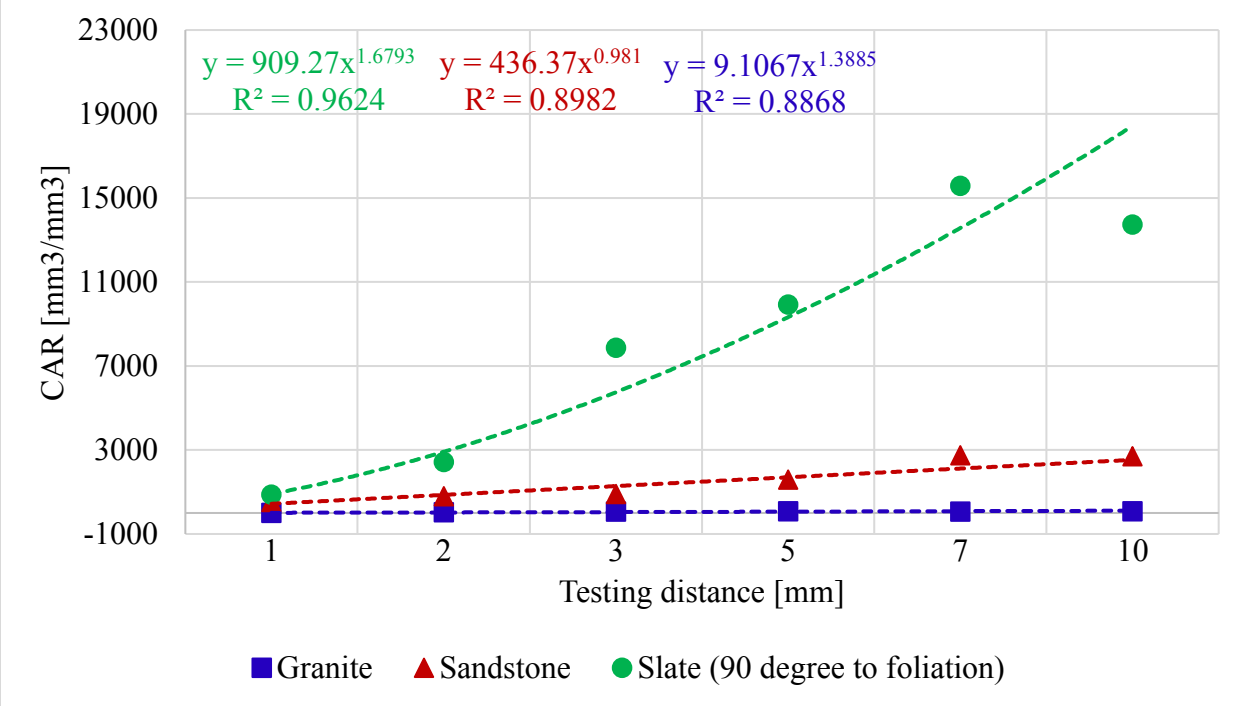

Figure 6-2 Development of Cerchar abrasion ratio versus testing distance for the three tested rocks

By observing the damaged surface produced on the tested rock samples, it is concluded that, for deeper penetration, the abrasive behavior is significantly affected by the rock microstructure, such as grain size, rock porosity and mineral composition, especially the amount of hard or abrasive minerals within the rock. During the scratching process, mineral grains are detached from damaged surface by fracturing after plastic deformation on stressed surface. Transition from plastic deformation-induced to cracking-induced wear can be related to the rock microstructure.

Several testing condition-based factors including surface condition, testing distance and velocity, as well as rock anisotropy affecting the Cerchar abrasivity index are studied based on granite, sandstone, slate and gneiss. The surface roughness has an obvious influence on harder and/or inhomogeneous rocks like granite compared to the softer and homogeneous rocks like sandstone and slate. The standard sliding distance of 10 mm can be kept as defined for the Cerchar test. However, this predefined distance should be exactly maintained in soft rocks like sandstone. The stylus penetrates into the rock progressively during the entire testing distance due to low strength of sandstone. The abrasion occurs not on the tip but on the conical sides of the stylus. A decrement of wear flat of 0.1 mm leads to a decrement of index value of 1. According to the test result, the scratching velocity does not affect the Cerchar index. The influence of rock anisotropy on the Cerchar index is not significant for the two tested intact metamorphic rocks (slate and gneiss). Despite that, to get a more accurate abrasivity result on anisotropic rocks, Cerchar measurements should be performed three times for one rock sample: the stylus scratching inclined, and parallel or orthogonal to the discontinuous planes, as well as on the discontinuity of the layered rocks. To reduce errors in the Cerchar measurement, some recommendations are given in Table 6-2.

Table 6-2 Recommendations for conducting the Cerchar abrasivity test

Factor	**Comment**
Test apparatus	A modern apparatus is recommended, which allows exact control of testing velocity and distance.
Stylus hardness	Styli with HRC 54-56 are predominantly used for hard rocks, while styli with HRC 40-43 are suggested for rocks with low strengths.
Surface condition	CAI can be measured under two surface conditions and a linear relationship is established ($\mathrm{CAI}_{\mathrm{rough}} = \mathrm{CAI}_{\mathrm{sawn}} + 0.3$).
Sliding distance	A lengthening of sliding distance is not necessary, but standard testing length of 10 mm should be carefully watched on soft and abrasive rocks like sandstone.
Scratching velocity	It is not necessary to change the scratching velocity of 10 mm/s.
Testing repetition	Five scratches are defined to determine the CAI for one rock sample, but the amount of scratches could be increased for rocks with larger grain sizes.
Tip wear measurement	A digital binocular is recommended to measure the tip wear.
Rock anisotropy	Cerchar measurement on anisotropic rocks should be repeated three times with different testing angles to obtain a more accurate result.

With respect to the mineralogical-mechanical properties of sandstone, numerical simulations of the Cerchar scratch test are conducted using PFC^{3D}, in which a bonded-particle model associated with the parallel bonds is used. The time-dependent damage due to the scratching is expressed by the separation of bonded particles. The scratching force-displacement curve derived from numerical simulation develops in the same as observed in the experimental study. The applied scratching force obtained numerically matches well with that measured in the laboratory. The discrepancy can be related to the testing condition-based factors, such as rock mineralogy and microstructure, scratching velocity, depth of scratch, abrasion of tools and temperature. The crack initiation and propagation beneath the rock surface can be detected by means of the numerical simulation. Results show that the rock fragmentation process during rock scratching is predominantly caused by the propagation of tensile cracks.

Based on the calibrated model, the influence of tool geometry and cutting parameters on the resultant cutting force and rock fracturing and fragmentation is studied. The cutter geometry, especially tip shape and angle, are one of the major factors affecting the cutting force. Results indicate that a cutter with rounded tip requires more force and produces more cracks than with sharp tip. A larger tip angle enhances the requirement of cutting force and induces more cracks than a smaller tip angle. It is found that the wear on the cutter tip can also affect the cutting force significantly. Cutters with blunt tip obviously require more force than with sharp tip. The cutting velocity associated with the depth of cut have a significant influence on the cutting forces and crack patterns. Especially at a greater cutting depth, the increase of cutting velocity leads to an enhancement of cutting forces. The rake angle effect on the variation of cutting forces reveals that the resulting cutting force decreases firstly with increased negative rake angle and then increases with increased positive rake angle. The lowest force value is obtained for a rake angle of 0°. Note that the numerical simulation can be used instead of the experimental works, if an actual rock cutting test is more expensive and time-consuming, as well as a trial-and-error test should be conducted during the rock excavations in more complex geological situations.

Numerical study of simulation condition-based factors indicates that: (1) the cutting force increases with increasing particle size. (2) More cutting force is required when the damping coefficient is increased. (3) The higher the friction coefficient, the more the required force used for the cutting. (4) The higher the wall stiffness, the lower the resulting cutting force.

6.2 Main contributions of the thesis

The main contributions of this thesis are the following:

1. Study of different Cerchar abrasive parameters and their dependency on the rock mineralogical-mechanical properties.

2. Proposal of a new index to characterize cutting effectivity, named Cerchar abrasion ratio (CAR), which relates abrasion of the cutting tool to excavated rock volume.

3. Investigation of Cerchar abrasive wear mechanism.

4. Investigation of the influence of surface condition, testing velocity and distance and rock anisotropy on the Cerchar abrasivity index.

5. Numerical simulation of Cerchar scratch test based on a quasi-homogeneous and isotropic sandstone model under different scratching scenarios.

6. Applying of calibrated numerical model for simulation of rock cutting and investigation of tool geometry (pick type, tip angle and tip wear) and cutting parameters (cutting velocity, depth of cut and rake angle) affecting the resultant cutting force and crack pattern.

7. Investigation of simulation condition-based factors, such as particle size, damping coefficient, friction coefficient and contact deformability, affecting the applied cutting force.

6.3 Recommendations for future work

Further works should be focused on:

1. More laboratory tests are needed to investigate the Cerchar abrasivity correlated parameters, especially the new proposed Cerchar abrasion ratio (CAR). CAR values should be related to lifetime and wear information obtained from in-situ data of cutting machines to verify this parameter.

2. Enhanced numerical simulation of rock cutting with respect to Cerchar scratch tests should be conducted under consideration of rock anisotropy and also verified by experiments.

3. Magnitude of cutting forces as well as amount of cracking are also affected by the rock types. These effecting factors should be studied by modeling different rock samples with regard to their material properties in further works.

7. References

Abu Bakar, M.Z., Majeed, Y., Rostami, J. (2016) Effects of rock water content on CERCHAR Abrasivity Index. Wear 368-369, 132-145.

Al-Ameen, S.I., Waller, M.D. (1994) The influence of rock strength and abrasive mineral content on the Cerchar abrasive index. Engineering Geology 36, 293-301.

Alber, M. (2008) Stress dependency of the Cerhcar abrasivity index (CAI) and its effects on wear of selected rock cutting tools. Tunnelling and Underground Space Technology 23, 351-359.

Alber, M., Yarali, O., Dahl, P., Bruland, A., Käsling, H., Michalakopoulos, T.N., Cardu, M., Hagan, P., Aydin, H., Özarslan, A. (2014) ISRM suggested method for determining the abrasivity of rock by the Cerchar abrasivity test. International Journal of Rock Mechanics and Rock Engineering 47, 261-266.

Altindag, R., Sengun, N., Sarac, S., Mutluturk, M., Guney, A. (2010) Evaluating the relations between brittleness and Cerchar Abrasion index of rocks. Proceedings of the ISRM Regional Symposium EUROCK 2009, 29-31 October 2009, Cavtat, Croatia, 6 pp.

Archard, J.F. (1953) Contact and Rubbing of flat surfaces. Journal of Applied Physics 24, 981-988.

Arnell, R.D., Davies, P.B., Halling, J., Whomes, T.L. (1991) Tribology - Principles and Design Applications. Macmillan, London.

ASTM D7625-10 (2010) Test method for laboratory determination of abrasiveness of rock using the Cerchar method. American Society for Testing and Materials, 6 pp.

Atkinson, T., Cassapi, V.B., Singh, R.N. (1986) Assessment of abrasive wear resistance potential in rock excavation machinery. International Journal of Mining and Geological Engineering 3, 151-163.

Atkinson, R.H. (1993) Hardness tests for rock characterization. In: Hudson J (ed.): Comprehensive rock engineering - Principles, Practice and Projects 3: Rock testing and site characterization. Pergamon, UK, 982 pp.

Balci, C., Bilgin, N. (2007) Correlative study of linear small- and full-scale rock cutting tests to select mechanized excavation machines. International Journal of Rock Mechanics and Mining Sciences 44, 468-476.

Baumgarten, L. (2015) Gesteinsmechanische Versuche und petrophysikalische Untersuchungen – Laborergebnisse und numerical simulation. Ph.D. Dissertation, Institut fuer Gentechnik, TU Bergakademie Freiberg, Freiberg, Germany. (in German)

Bilgin, N., Demircin, M.A., Copur, H., Balci, C., Tuncdemir, H., Akcin, N. (2006) Dominant rock properties affecting the performance of conical picks and the comparison of some experimental and theoretical results. International Journal of Rock Mechanics and Mining Sciences 43, 139-156.

Bruland, A. (1998) Drillability Test Methods. Ph.D. Dissertation, Norwegian University of Science and Technology, NTNU Trondheim.

Bruland, A., Nilsen, B. (1995) Tunnelling performance estimation based on drillability testing. Proceeding of the 8th International Society for Rock Mechanics and Rock Engineering (ISRM) Congress, 25-29 September 1995, Tokyo, Japan.

Burwell, J.T. (1957/58) Survey of possible wear mechanisms. Wear 1, 119-141.

Cerchar - Centre d'Études et des Recherches des Charbonages de France (1986) The Cerchar abrasiveness index. Verneuil, 8 pp.

Chaput, E.J. (1992) Observations and analysis of hard rock cutting failure mechanisms using PDC picks. M.Sc. thesis, Imperial College, London, UK.

Cundall, P.A. (1971) A computer model for simulating progressive large scale movements in blocky rock systems. Proceedings of the Symposium of the International Society for Rock Mechanics, Society for Rock Mechanics (ISRM), France, pp. 128-132.

Cundall, P.A. (1988) Formulation of a three-dimensional distinct element model – Part I. A scheme to detect and represent contacts in a system composed of many polyhedral blocks. International Journal of Rock Mechanics and Mining Sciences & Geomechanics 25(3), 107-116.

Dahl, F., Bruland, A., Jakobsen, P.D., Nilsen, B., Grov, E. (2012) Classifications of properties influencing the drillability of rocks based on the NTNU/SINTEF test method. Tunnelling and Underground Space Technology 28, 150-158.

Deketh, H.J.R. (1995) Wear of rock cutting tools - Laboratory experiments on the abrasivity of rock. A.A. Balkema, Rotterdam, Brookfield.

Evans, I. (1964) The force required to cut coal with blunt wedges. International Journal of Rock Mechanics and Mining Sciences 2, 1-12.

Evans, I. (1984) A theory of the cutting force of point-attack picks. International Journal of Mining and Geological Engineering 2, 63-71.

Fowell, R.J. (1993) The mechanics of rock cutting. In: Hudson, J.A. (ed.): Comprehensive rock engineering, Principles, Practice and Projects 4: Excavation, Support and Monitoring. Oxford, Pergamon Press Ltd., 155-176.

Fowell, R.J., McFeat-Smith, I. (1976) Factors influencing the cutting performance of a selective tunneling machine. In: Jones, M.J. (ed.): Proceeding of the tunneling symposium '76, IMM, London, pp. 301-309.

Fowell, R.J., Richardson, G., Gollick, M.J. (1994) Prediction of boom tunneling machine excavation rates. In: Nelson & Laubach (eds): Rock Mechanics, Balkema, Rotterdam, 8 pp.

Ghasemi, A. (2010) Study of Cerchar abrasivity index and potential modifications for more consistent measurement of rock abrasion. M.Sc. Thesis, Department of Energy and Mineral Engineering, Pennsylvania State University.

Goektan, R.M. (1990) Effect of cutter pick rake angle on the failure pattern of high-strength rocks. Mining Science and Technology 11, 281-285.

Goektan, R.M. (1997) A suggested improvement on Evans' cutting theory for conical bits. Proceeding of the 4th International Symposium on Mine Mechanization and Automation. Brisbane, Queensland, Australia, 57-61.

Gray, K.E., Armstrong, F., Gatlin, C. (1962) Two-dimensional study of rock breakage in drag-bit drilling at atmospheric pressure. Journal of Petroleum Technology 14, 93-98.

Guo, H. (1990) Rock cutting studies using fracture mechanics principles. Ph.D. Dissertation, Department of Civil and Mining Engineering, University of Wollongong, New South Wales, Australia.

Guo, H., et al. (1992) Rock cutting study using linear elastic fracture mechanics. Engineering Fracture Mechanics 41, 771-778.

Goektan, R.M., Guenes, N. (2005) A semi-empirical approach to cutting force prediction for point-attack picks. Journal of the South Africa Institute of Mining and Metallurgy 105, 257-263.

Hamzaban, M.T., Memarian, H., Rostami, J. (2014) Continuous monitoring of pin tip wear and penetration into rock surface using a new Cerchar abrasivity testing device. International Journal of Rock Mechanics and Rock Engineering 47, 689-701.

Hamzaban, M.T., Memarian, H., Rostami, J., Ghasemi-Monfared, H. (2014) Study of rock-pin interaction in Cerchar abrasivity test. International Journal of Rock Mechanics and Mining Sciences 72, 100-108.

Hamzaban, M.T., Memarian, H., Rostami, J. (2018) Determination of scratching energy index for Cerchar abrasion test. Journal of Mining and Environment 9(1), 73-89.

Hart, R.D., Cundall, P.A., Lemos, J. (1988) Formulation of a three-dimensional distinct element model – Part II. Mechanical calculations for motion and interaction of a system composed of many polyhedral blocks. International Journal of Rock Mechanics and Mining Sciences & Geomechanics 25(3), 117-125.

He, X.Q., Xu, C.S. (2015) Discrete element modelling of rock cutting: from ductile to brittle transition. International Journal for Numerical and Analytical Methods in Geomechanics 39, 1331-1351.

Hondros, G. (1959) The evaluation of Poisson's ratio and the modulus of materials of a low tensile resistance by the Brazilian (indirect tensile) test with a particular reference to concrete. Australian Journal of Applied Science 10, 243-268.

Huang, H. (1999) Discrete element modeling of tool-rock interaction. Ph.D. Dissertation, University of Minnesota, Minneapolis, USA.

Huang. H., Detournay, E., Bellier, B. (1999) Discrete element modelling of rock cutting. In Amadei, Kranz, Scott & Smeallie (eds.): Rock Mechanics for Industry. A.A. Balkema, Rotterdam, 8 pp.

Huang, H., Lecampion, B., Detournay, E. (2013) Discrete element modeling of tool-rock interaction I: rock cutting. International Journal for Numerical and Analytical Methods in Geomechanics 37, 1913-1929.

Huang, H., Detournay, E. (2013) Discrete element modeling of tool-rock interaction II: rock indentation. International Journal for Numerical and Analytical Methods in Geomechanics 37, 1930-1947.

Hurt, K.G., MacAndrew, K.M. (1985) Cutting efficiency and life of rock-cutting picks. Mining Science and Technology 2, 139-151.

Iliescu, D., Gehin, D., Iordanoff, I., Girot, F., Gutierrez, M.E. (2010) A discrete element method for the simulation of CFRP cutting. Composites Science and Technology 70, 73-80.

Itasca (2016): Itasca Consulting Group Inc. PFC (Particle Flow Code), Version 5.0. Minneapolis: ICG.

Jacobs, N., Hagan, P. (2009) The effect of stylus hardness and some test parameters on Cerchar abrasivity index. Proceedings of the 43rd US Rock Mechanics Sympoisum and 4th U.S.-Canada Rock Mechanics Symposium, 28 Juni-01 July 2009, Acheville, 8 pp.

Käsling, H., Thiele, I., Thuro, K. (2007) Abrasivitätsuntersuchung mit dem Cerchar-Test - eine Evaluierung der Versuchungsbedingungen. Veröffentlichung der 16. Tagung für Ingenieurgeologie, 7-10 März 2007, Bochum, 229-235. (in German)

Khruschov, M.M. (1974) Principles of abrasive wear. Wear 28, 69-88.

Käsling, H. (2009) Bestimmung der Gesteinsabrasivität - Grundlagen, Anwendung und Einsatzgrenzen bei machinellen Tunnelvortrieben. Ph.D. Dissertation, Lehrstuhl für Ingenieurgeologie, TU München. München, 123 S. **(in German)**

Kou, S.Q., Lindqvist, P.A., Tang, C.A., Xu, X.H. (1999) Numerical simulation of the cutting of inhomogeneous rocks. International Journal of Rock Mechanics and Mining Sciences 36, 711-717.

Kou, S.Q., Liu, H.Y., Lindqvist, P.A., Tang, C.A. (2004) Rock fragmentation mechanisms induced by a drill bit. International Journal of Rock Mechanics and Mining Sciences 41(3), 6 pp.

Lassnig, K., Latal, C., Klima, K. (2008) Impact of grain size on the Cerchar abrasiveness test. Geomechanik and Tunnelbau 1, 71-76.

Lei, S., Kaitkay, P. (2003) Distinct element modeling of rock cutting under hydrostatic pressure. Key Engineering Materials 250, 110-117.

Lei, S., Kaithkay, P., Shen, X. (2004) Simulation of rock cutting using distinct element method – PFC2D. In: Shimizu, Y., Hart, R.D. and Cundall, P.A. (eds.): Numerical Modeling in Micromechanics via Particle Methods. London, CRC Press, 63-72.

Lunow, C. (2014) Simulation von gesteinsmechanischen Bohr- und Schneidprozessen mittels der Diskreten-Elemente-Methode. Dissertation, Institut fuer Gentechnik, TU Bergakademie Freiberg, Freiberg, Germany. (in German)

Lunow, C., Konietzky, H. (2009): Two dimensional simulation of the pressing and the cutting rock destruction. Proceeding of 2nd International Conference on Computational Methods in Tunneling, Aedificatio Publishers 1, 223-230.

Maidl, B., Schmid, L., Ritz, W., Herrenknecht, M. (2001) Tunnelbohrmaschinen im Hartgestein. Berlin, Ernst & Sohn Verlag, 350 S. (in German)

McFeat-Smith, I., Fowell, R.J. (1977) Correlation of rock properties and the cutting performance of tunnelling machines. Proceeding of Conference on Rock Engineering, 4-7 April 1977, Newcastle-upon-Tyne, 581-602.

McKinnon, S.D., Barra, I.G. (1998) Fracture initiation, growth and effect on stress field: a numerical investigation. Journal of Structural Geology 20(12), 1673-1689.

Mellor, M. (1972) Normalization of specific energy values. Journal of Rock Mechanics and Mining Sciences 9, 661-663.

Mendoza, J.A., Gamwo, I., Zhang, W., Lin, J.S. (2010) Discrete element modeling of rock cutting using crushable particles. Presentation of 44th US Rock Mechanics Symposium and 5th U.S.-Canada Rock Mechanics Symposium, 27-30 June 2010, Salt Lake City, USA.

Menezes, P.L., Lovell, M.R., Avdeev, I.V., Higgs III, C.F. (2014) Studies on the formation of discontinuous rock fragments during cutting operation. Journal of Rock Mechanics and Mining Sciences 71, 131-142.

Michalakopoulos, T.N., Anagnostou, V.G., Bassanou, M.E., Panagiotou, G.N. (2006) The influence of steel styli Hardness on the Cerchar abrasiveness value. International Journal of Rock Mechanics and Mining Sciences 43(2), 321-327.

Moore, M.A. (1974) A review of two-body abrasive wear. Wear 27, 1-17.

Moore, M.A., King, F.S. (1980) Abrasive wear of brittle solids. Wear 60, 123-140.

Moradizadeh, M., Cheshomi, A., Ghafoori, M., TrighAzali, S. (2016) Correlation of equivalent quartz content, Slake durability index and Is_{50} with Cerchar abrasiveness index for different types of rock. International Journal of Rock Mechanics and Mining Sciences 86, 42-47.

NF P18-579 (1990) Granulats - Essai d'abrasivité et de broyabilité. Association française de normalization (AFNOR), Paris.

NF P94-430-1 (2000) Roches - Détermination du pouvoir abrasive d'une roche - Partie 1: Essai de rayure avec une pointe. Association française de normalization (AFNOR), Paris, 7 pp.

Nishimatsu, Y. (1972) The mechanics of rock cutting. International Journal of Rock Mechanics and Mining Sciences 9, 261-270.

Piazzetta, G.R., Lagoeiro, L.E., Figueira, I.F.R., Rabelo, M.A.G., Pintaude, G. (2018) Identification of abrasion regimes based on mechanisms of wear on the steel stylus used in the Cerchar abrasiveness test. Wear 410-411, 181-189.

Plinninger, R.J. (2002) Klassifizierung und Prognose von Werkzeugverschleiß bei konventionellen Gebirgslösungsverfahren im Festgestein. Münchner Geologische Hefte, Reihe B: Angewandte Geologie, B17. München, 146 S. (in German)

Plinninger, R.J., Käsling, H., Thuro, K., Spaun, G. (2003) Testing conditions and geomechanical properties influencing the Cerchar abrasiveness index (CAI) value. International Journal of Rock Mechanics and Mining Sciences 40, 259-263.

Plinninger, R.J., Käsling, H., Thuro, K. (2004) Wear prediction in hardrock excavation using the Cerchar abrasiveness index (CAI). Proceedings of the ISRM Regional Symposium EUROCK 2004 and 53rd Geomechanics Colloquy, 06-08 October 2004, Salzburg, Austria, 6 pp.

Plinninger, R.J. (2010) Hardrock abrasivity investigation using rock abrasivity index (RAI). Proceedings of the 11th International Association of Engineering Geology (IAEG) Congress, 5-10 September 2010, Auckland, New Zealand, 3445-3452.

Potyondy, D.O., Cundall, P.A. (2004) A bonded-particle model for rock. International Journal of Rock Mechanics and Mining Sciences 41, 1329-1364.

Restner, U., Pichler, J. (2007) Mont cenis tunnel modification project - lowering of tunnel invert with sandvik tunnel miner MT620. In Bilgin, N. (ed.): Proceeding of the 2nd Symposium on Underground Excavations for Transportation. 15-17 November 2007, Istanbul, Turkey.

Richard, T. (1999) Determination of rock strength from cutting tests. M.Sc. Thesis, University of Minnesota, Minneapolis, USA.

Richard, T., Detournay, E., Drescher, A., Nicodeme, P., Fourmaintraux, D. (1998) The scratch test as a means to measure strength of sedimentary rocks. Proceeding of the SPE/ISRM Eurock '98, 08-10 July 1998, Trondheim, Norway, 15-22.

Rojek, J., Onate, E., Labra, C., Kargl, H. (2011) Discrete element simulation of rock cutting. Journal of Rock Mechanics and Mining Sciences 26, 996-1010.

Romero, S.U., Gomez, B.B. (1970) Brittle and plastic failure of rocks. International Society for Rock Mechanics 1.

Rostami, J., Ozdemir, L., Bruland, A., Dahl, F. (2005) Review of issues related to Cerchar abrasivity testing and their implications on geotechnical investigations and cutter cost estimates. Proceedings of the 2005 Rapid Excavation and Tunneling Conference (RETC), Seattle, USA, 738-751.

Rostami, J., Ghasemi, A., Gharahbagh, E.A., Dogruoz, C., Dahl, F. (2014) Study of dominant factors affecting Cerchar abrasivity index. International Journal of Rock Mechanics and Rock Engineering 47, 1905-1919.

Roxborough, F.F., Liu, Z.C. (1995) Theoretical considerations on pick shape in rock and coal cutting. Proceeding of the 6th Underground Operators' Conference, 13-14 November 1995, Kalgoorlie, Australia, 189-193.

Sarwary, E., Hagan, P.C. (2016) The effect of changes in tool tip angle on the cutting performance of a pointed pick. Mining Technology 125(3), 184-190.

Schimazek, T., Knatz, H. (1970) Der Einfluss des Gesteinsaufbaus auf die Schnittgeschwindigkeit und den Meißelverschleiß von Streckenvortriebsmaschinen. Glückauf 106(6), 274-278. (in German)

Schimazek, T., Knatz, H. (1976) Die Beurteilung der Bearbeitbarkeit von Gestein durch Schneid- und Rollenbohrwerkzeuge. Erzmetall 29(3), 113-119. (in German)

Schormair, N., Thuro, K., Plinninger, R.J. (2006) The influence of anisotropy on hard rock drilling and cutting. Proceeding of the 10th International Association of Engineering Geology (IAEG) Congress, 6-10 September 2006, Nottingham, UK, 11 pp.

Souissi, S., Hamdi, E., Sellami, H. (2015) Microstructure effect on hard rock damage and fracture during indentation process. Geotechnical and Geological Engineering 33, 1539-1550.

Stanford, J., Hagan, P. (2009) An assessment of the impact of stylus metallurgy on Cerchar abrasiveness index. Proceedings of the 2009 Coal Operators Conference, 12-13 February 2009, University of Wollongong, Australia, 348-355.

Stavropoulou, M. (2006) Modeling of small-diameter rotary drilling tests on marbles. International Journal of Rock Mechanics and Mining Sciences 26, 1034-1051.

Su, O., Akcin, N.A. (2011) Numerical simulation of rock cutting using the discrete element method. Journal of Rock Mechanics and Mining Sciences 48, 434-442.

Suana, M., Peters, T. (1982) The Cerchar abrasivity index and its relation to rock mineralogy and petrography. Rock Mechanics 15, 1-7.

Tan, X., Konietzky, H., Frühwirt, T., Dan, D.Q. (2015) Brazilian Tests on Transversely Isotropic Rocks: Laboratory Testing and Numerical Simulation. International Journal of Rock Mechanics and Rock Engineering 48, 1341-1351.

Tan, X.C., Kou, S.Q., Lindqvist, P.A. (1998) Application of the DDM and fracture mechanics model on the simulation of rock breakage by mechanical tools. Engineering Geology 49, 277-284.

Tan, Y.Q., Yang, D.M., Sheng, Y. (2009) Discrete element method (DEM) modeling of fracture and damage in the machining process of polycrystalline SiC. Journal of European Ceramic Society 29, 1029-1037.

Thiele, I. (2006) Zur Standardisierung des Cerchar-Abrasivitäts-Index-Tests - Vergleichende Untersuchungen an zwei Gerätetypen. Diplomarbeit, Lehrstuhl für Ingenieurgeologie, TU München. München, 89 S. (in German)

Tiryaki, B., Dikmen, A.C. (2006) Effects of rock properties on specific cutting energy in linear cutting of sandstone by picks. International Journal of Rock Mechanics and Rock Engineering 39(2), 89-120.

Thuro, K. (1996) Bohrbarkeit beim konventionellen Sprengbetrieb geologisch-felsmechanische Untersuchungen anhand sieben ausgewählter Tunnelprojekte. Münchner Geologische Hefte, Reihe B: Angewandte Geologie, B1. München, 145 S. (in German)

Thuro, K. (2002) Geologisch-felsmechanische Grundlagen der Gebirgslösung im Tunnelbau. Münchner Geologische Hefte, Reihe B: Angewandte Geologie, B18. München, 160 S. (in German)

Valantin, A. (1973) Test Cerchar pour la mesure de la dureté et de l'abrasivité des roches. Centre d'Études et Recherches des Charbonages de France. Luxembourg, 5 pp.

Van Wyk, G., Els, D.N.J., Akdogan, G., Bradshaw, S.M., Sacks, N. (2014) Discrete element simulation of tribological interactions in rock cutting. International Journal of Rock Mechanics and Mining Sciences 65, 8-19.

Verhoef, P.N.W. (1997) Wear of rock cutting tools: implications for the site investigation of rock dredging projects. Ph.D. Dissertation, Technical University Delft, Netherlands.

Vivek K. Prajapati, B.T. (2011) Modeling of rock failure under PDC cutter based on lab experiments. M.Sc. Thesis, Texas Tech University, USA, 139 pp.

Wang, Y.S., Hsu, S.M. (1996) Wear and wear transition mechanisms of ceramics. Wear 195, 112-122.

Wei, X., Wang, C.Y., Yuan, H.L., Xie, Z.H. (2003) Study of fracture mechanism of rock cutting. Machining of Natural Stone Materials 250, 200-208.

West, G. (1981) A review of rock abrasiveness testing for tunneling. Proceeding of the International Symposium on Weak Rock, 21-24 September 1981, Tokyo, Japan, 585-594.

West, G. (1986) An observation on Mohs' scale of hardness. Quarterly Journal of Engineering Geology and Hydrogeology 19(2), 203-205.

West, G. (1986) A relation between abrasiveness and quartz content for some coal measures sediments. International Journal of Mining and Geological Engineering 4, 73-78.

West, G. (1989) Rock abrasiveness testing for tunneling. International Journal of Rock Mechanics and Mining Sciences 26(2), 151-160.

Yarali, O., Yasar, E., Bacak, G., Ranjith, P.G. (2008) A study of rock abrasivity and tool wear in Coal Measures Rocks. International Journal of Goal Geology 74, 53-66.

Yarali, O., Aydin, H., Duru, H., Özarslan, A. (2013) Effect of scratch length on the Cerchar abrasivity index. Proceedings of the 2013 ISRM International Symposium EUROCK 2013, 21-26 September 2013, Poland.

Yasar, S., Yilmaz, A.O. (2018) Drag pick cutting tests: A comparison between experimental and theoretical results. International Journal of Rock Mechanics and Mining Sciences 10, 893-906.

Zeuch, D.H., Finger, J.T. (1985) Rock breakage mechanisms with a PDC cutter. Proceeding on the SPE Annual Technical Conference and Exhibition, Las Vegas, Nevada, 22-25 Sep. 1985, 11 pp.

Zhang, Q.Q., Han, Z.N., Ning, S.H., Liu, Q.Z. (2015) Numerical simulation of rock cutting in different cutting mode using the discrete element method. Journal of GeoEngineering 10(2), 35-43.

Zum Gahr, K.H. (1987) Microstructure and wear of materials. Elsevier, North Holland.

Zum Gahr, K.H. (1998) Wear by hard particles. Tribology International 31, 587-596.